

**Observation and Modeling –  
An Integrated Study of Transport through the Strait of Bab al Mandab**

Masamichi Inoue

Coastal Studies Institute

Louisiana State University

Baton Rouge, LA 70803-7527

phone: (225) 578-2521, fax: (225) 578-2520, e-mail: [minoue@redsea.csi.lsu.edu](mailto:minoue@redsea.csi.lsu.edu)

Grant Number: N00014-96-1-1227

All field components of the project have been successfully completed, and various modeling efforts have been carried out. The modeling efforts address various phenomena with differing time scales ranging from tidal to seasonal variations in the throughflow transport at the strait. The field program has generated vast amount of very useful data that shed light on various aspects of throughflow transport at the strait, providing guidance in the modeling component of this project. So far, three related journal articles have been published, and a Ph. D. dissertation has been completed. Modeling efforts so far have answered some of the questions raised in the field program. However, many questions remain unanswered especially related to low-frequency transport. Therefore, we plan to continue our modeling efforts toward understanding the dynamics at the strait in the next few years.

### **Observational Component**

The entire project consisted of three deployment phases. During the first phase, 17 Aanderra and 3 upward-looking ADCP current meters with a sampling interval of 4 m, 12 Seacats, and 5 subsurface pressure gauges were located in the Strait. The majority of the instruments were deployed at the Harnish Sill (mooring line B) and a few kilometers north from Perim Narrows (mooring line A). Moorings along A and B lines were maintained during the second phase; however, for the third phase, only the B line instruments and pressure gauge near the Harnish Sill were redeployed. A total of four cruises were carried out in order to service the moorings; cruise 1-May/June 1995, Cruise 2-March/April 1996, Cruise 3-November/December 1996, Cruise 4-July/August 1997. During the cruises, CTD casts were made and shipboard ADCP data were collected; Cruise 1 (51 CTD stations and 6 days of shipboard ADCP), Cruise 2 (42 CTD stations), Cruise 3 (41 CTD stations and 11 days of shipboard ADCP), Cruise 4 (17 CTD stations).

### **Results**

#### Tides

Tidal characteristics of the Strait were examined by analyzing the observations collected during this project and using a two-dimensional finite element model (ADCIRC-2DDI). The Bab el Mandab Strait is where the transition occurs between two noticeably different

### **DISTRIBUTION STATEMENT A**

Approved for Public Release  
Distribution Unlimited

20021122 119

tidal regimes: the Gulf of Aden, where tidal fluctuations are mixed and have a range in excess of 2 m, and the Red Sea, where the tides are principally semidiurnal and their range is less than 1 m. Within the Strait, our observations indicate that tidal currents are a mixed type and dominant constituents are K1 and M2. The vertical structure of the tidal currents is complicated, differs between semidiurnal and diurnal constituents, and varies with location and stratification. The stratification appears to impact the vertical structure of the diurnal tidal currents more. The major part of this signal is barotropic but energetic baroclinic currents are observed near Perim Narrows and the Harnish Sill during the winter stratification. Results of the EOF analysis and internal velocity modes estimated from the observed stratification reveal that the baroclinic currents of diurnal frequency have vertical structure, which is a combination of the second and third baroclinic modes near Perim Narrows and of the first and second modes near the Harnish Sill. Results from the modeling indicate that the largest elevations and most energetic currents are observed in the region located between Perim Narrows and Assab-Mocha line. They also imply that residual circulation induced by the barotropic tides is generally weak in the Strait and consists of a mean and fluctuating component. Average barotropic energy fluxes over a tidal period are small and their direction depends on the constituent. The k1 component has one source of energy, which is the flux from the Gulf of Aden, while there are two sources of energy for the M2: one from the Gulf of Aden and another from the Red Sea. In addition, these results show that the major part of the tidal energy for both constituents is dissipated within the Strait itself.

#### Low-Frequency Flow

Seasonal cycle in throughflow currents at the Strait has been confirmed by this study. Specifically, there are two seasonal phases, the winter-regime where the inflow layer from the Gulf of Aden is overlain on top of the salty outflow layer from the Red Sea, and the summer-regime where a three layer system develops with outflowing top and bottom layers sandwiching a fresher intermediate inflow from the Gulf of Aden. The observation component of this study allow an unprecedented look at the magnitude and seasonal evolution of the inflow layer from the Gulf of Aden, and the high salinity outflow layer from the Red Sea. The timing, structure, and evolution of the summer season mid-depth intrusion of cold, low salinity water into the Red Sea from the Gulf of Aden is measured for the complete intrusion cycle of 1995. We unexpectedly find the deep outflow still strong in June 1995, with speeds of 0.6 m/sec and transport of 0.4 Sv. From July to mid-September, the deep outflow persists but is attenuated to speeds of 0.2 m/sec and transport of 0.05 Sv. The dominant summer feature, the cold low salinity intermediate layer intrusion, persists for 3 months, occupies 70% of the water column in the Strait and carries approximately  $1.7 \times 10^{12} \text{ m}^3$  of cold nutrient-rich water into the red Sea. The winter regime begins in mid-September, is fully developed by early November, and continues to the end of our first observation interval in March 1996. Speeds in the lower layer are 0.8-1.0 m/sec and 0.4-0.6 m/sec in the upper layer. At maximum exchange in mid-February, outflow transport reaches 0.7 Sv. Ubiquitous oscillations in current and salinity at synoptic and intraseasonal periods appear closely related to fluctuations in the along-channel wind forcing and perhaps to coastally-trapped waves.

In order to study exchange flow through the Strait, the Princeton Ocean Model (POM) was configured to the bottom bathymetric configuration at the Strait. ETOP05 world topography data with its 1/12 degree resolution was judged to be too coarse to provide sufficiently accurate bottom bathymetric data for the model grid. In order to obtain the best available topographic data, the nautical charts published by Defense Mapping Agency (available from NOAA National Ocean Service) was digitized for the domain extending from 11.3°N to 14.4°N and from 41.7°E to 45°E with a resolution of 500m. Comparison of the digitized data to the bottom profiles measured during the cruises for this study confirmed the accuracy of the digitization. A curvilinear coordinate grid was used for the model grid, and the model dimensions used are 240 by 70 by 30. The model has two open boundaries located along the northern and southern boundaries. Radiation open boundary conditions were used for velocities at the open boundaries, while temperature and salinity values at inflow along the open boundaries were relaxed toward the initial boundary conditions. Characteristic temperature and salinity values representing the region including the Red Sea, the Strait and the Gulf of Aden were extracted from the Levitus climatology supplemented by the CTD data collected for this study. They were used to specify the initial as well as open boundary conditions. All the experiments run so far are “relaxation experiment (or dam experiment)” whereby the model stratification was initially set to some realistic values, and the model was then allowed to develop its own dynamics while applying the open boundary conditions. Both summer and winter stratifications were used to initialize the model. Typically, during relaxation, the model develops a distinct two-layer flow for the winter-regime, while a three-layer flow would result for the summer-regime. One prominent feature identified in the model is the time-dependent nature of the flow even after long simulation time (e.g., 200 days). Some of those time-dependent motions appear to be associated with active eddy shedding due to the topographic constriction at the strait. In particular, energetic motions with 12~15 day period are observed under the summer-regime. There are still some unresolved issues remaining in modeling the low-frequency flow at the Strait. They include: (1) Impact of the advection scheme used in POM as was recently pointed out; (2) Influence of the model domain size; (3) sensitivity of model results to stratifications used. Currently, those remaining issues are being pursued in order to interpret the model results in the light of the observations collected in this study.

## LIST OF PUBLICATIONS

Murray, S. P., and W. Johns, 1997: Direct observations of seasonal exchange through the Bab al Mandab Strait. *Geophys. Res. Lett.*, 24, 2557-2560.

Pratt, L. J., W. Johns, S. M. Murray, and K. Katsumata, 1999: Hydraulic interpretation of direct velocity measurements in the Bab al Mandab. *J. Phys. Oceanogr.*, 29, 2769-2784.

Pratt, L. J., H. E. Deese, S. P. Murray, and W. Johns, 2000: Continuous dynamical modes in straits having arbitrary cross sections, with applications to the Bab al Mandab. *J. Phys. Oceanogr.*, 30, 2515-2534.

Ewa Jarosz, 2002: Tides in the Bab El Mandab Strait. Ph. D.dissertation, Louisiana State University, Baton Rouge, LA., 139 pp.

**TIDAL DYNAMICS IN THE BAB EL MANDAB STRAIT**

**A Dissertation**

**Submitted to the Graduate Faculty of the  
Louisiana State University and  
Agricultural and Mechanical College  
in partial fulfillment of the  
requirements for the degree of  
Doctor of Philosophy**

**in**

**The Department of Oceanography and Coastal Sciences**

**by  
Ewa Jarosz  
M.S., Louisiana State University, 1997**

## TABLE OF CONTENTS

LIST OF TABLES .....	iv
LIST OF FIGURES.....	vii
ABSTRACT .....	xiii
CHAPTERS	
1. INTRODUCTION.....	1
2. SURFACE TIDE IN THE BAB EL MANDAB STRAIT .....	8
3. TIDAL CURRENTS IN THE BAB EL MANDAB STRAIT .....	11
3.1. Tidal current variance.....	12
3.2. Fortnightly modulations .....	14
3.3. Major diurnal and semidiurnal tidal current constituents.....	19
3.3.1. Diurnal current constituents .....	19
3.3.2. Semidiurnal current constituents .....	28
3.3.3. Comparison of the vertical distributions of tidal currents observed in the Bab el Mandab Strait with the existing models.....	31
3.4. Relation between tidal elevation and currents.....	36
3.5. Tidal transport .....	38
3.6. Barotropic tidal current components.....	41
3.7. Barotropic tidal balance .....	43
3.8. Long period tidal constituents .....	47
3.9. Higher tidal harmonics .....	50
4. BAROCLINIC TIDAL MOTION IN THE BAB EL MANDAB STRAIT ..	52
4.1. Baroclinic tidal currents .....	53
4.2. Density fluctuations.....	59
4.3. Empirical orthogonal function analysis of baroclinic tidal currents .....	62
4.4. Modal structure of the tides.....	68
4.5. Baroclinic responses to tidal forcing in other regions.....	73
5. TWO-DIMENSIONAL FINITE ELEMENT MODEL OF BAROTROPIC TIDES IN THE BAB EL MANDAB STRAIT.....	75
5.1. Model equations .....	75
5.2. Model domain .....	78
5.3. Boundary conditions and model parameters .....	79
5.4. Model-data comparison.....	79
5.5. Tidal model elevations .....	84
5.6. Tidal model currents.....	88
5.7. Residual circulation.....	93

5.8. Momentum balance .....	94
5.9. Energy flux and dissipation estimates.....	101
5.10. Summary .....	106
6. SUMMARY AND CONCLUSIONS .....	109
REFERENCES.....	114
APPENDIX A: DATA SETS.....	121
APPENDIX B: CURRENT ELLIPSE PARAMETERS.....	124
APPENDIX C: NUMERICAL DISCRETIZATION OF THE MODEL (ADCIRC -2DDI) EQUATIONS .....	139
VITA .....	140

## LIST OF TABLES

1. Amplitudes (A) and phases (g, GMT) of tidal elevation constituents .....	9
2. Ellipse parameters and the 95% errors of barotropic currents for the diurnal tidal constituents.....	42
3. Ellipse parameters and the 95% errors of barotropic currents for the semidiurnal tidal constituents.....	43
4. Harmonic constants for the cross-strait and along-strait balance.....	44
5. Latitudes and longitudes of the water level stations used for the model verification .....	80
6. The correlation coefficients (Corr) and standard deviations (SD) between the computed and measured tidal amplitudes and phases; N is the number of the stations; rms is the root mean square error.....	81
7. Comparison of computed (Com) and observed (Obs) $K_1/O_1$ and $M_2/S_2$ amplitudes (A) and phases (g, GMT) at the coastal stations .....	81
8. Comparison between observed (Obs) and computed (Com) tidal current ellipse parameters: semimajor axis (M), semiminor axis (Mn), inclination angle ( $\theta$ ), and phase (g, GMT) .....	83
9. Vertically integrated power flux (in Gigawatts, $1\text{ GW} = 10^9\text{ Watts}$ ) normal to the transects shown in Figure 46.....	103
10. Information for instruments deployed during the first phase of the BAM project .....	121
11. Information for instruments deployed during the second phase of the BAM project.....	122
12. Information for instruments deployed during the third phase of the BAM project .....	122
13. The $K_1$ ellipse parameters and their 95% errors for A2b mooring and winter stratification.....	124
14. The $K_1$ ellipse parameters and their 95% errors for A2b mooring and summer stratification.....	124
15. The $M_2$ ellipse parameters and their 95% errors for A2b mooring and winter stratification.....	125

16. The $M_2$ ellipse parameters and their 95% errors for A2b mooring and summer stratification.....	126
17. The $K_1$ ellipse parameters and their 95% errors for B2b mooring and winter stratification.....	127
18. The $K_1$ ellipse parameters and their 95% errors for B2b mooring and summer stratification.....	127
19. The $M_2$ ellipse parameters and their 95% errors for B2b mooring and winter stratification.....	128
20. The $M_2$ ellipse parameters and their 95% errors for B2b mooring and summer stratification.....	128
21. The $K_1$ ellipse parameters and their 95% errors for C mooring and winter stratification.....	129
22. The $K_1$ ellipse parameters and their 95% errors for C mooring and summer stratification.....	130
23. The $M_2$ ellipse parameters and their 95% errors for C mooring and winter stratification.....	130
24. The $M_2$ ellipse parameters and their 95% errors for C mooring and summer stratification.....	131
25. The $K_1$ ellipse parameters and their 95% errors for AA1 mooring and winter stratification.....	132
26. The $K_1$ ellipse parameters and their 95% errors for AA1 mooring and summer stratification.....	132
27. The $M_2$ ellipse parameters and their 95% errors for AA1 mooring and winter stratification.....	133
28. The $M_2$ ellipse parameters and their 95% errors for AA1 mooring and summer stratification.....	133
29. The $K_1$ ellipse parameters and their 95% errors for AA2b mooring and winter stratification.....	134
30. The $K_1$ ellipse parameters and their 95% errors for AA2b mooring and summer stratification.....	135

31. The $M_2$ ellipse parameters and their 95% errors for AA2b mooring and winter stratification.....	136
32. The $M_2$ ellipse parameters and their 95% errors for AA2b mooring and summer stratification.....	136
33. $K_1$ and $M_2$ ellipse parameters and their 95% errors – AA0 mooring.....	137
34. $K_1$ and $M_2$ ellipse parameters and their 95% errors – AA3 mooring.....	137

## LIST OF FIGURES

1. Map of the Bab el Mandab Strait (depth contours are in meters); locations of the subsurface pressure gauges (triangles) and the current meter moorings (solid circles) deployed during the first phase of the BAM project, and locations of the water level stations are also shown.....	2
2. Vertical profiles of the along-strait velocity component (means) for the winter two-layer and summer three-layer flow regimes at (a) Perim Narrows (A2b mooring), (b) C mooring located in the middle of the Bab el Mandab Strait, and (c) the Hanish Sill (B2b mooring); thin continuous and dotted lines indicate the 95% confidence intervals of the means for the summer and winter flow regimes, respectively .....	3
3. Examples of density ( $\sigma_0$ ) distributions in the Bab el Mandab Strait during (a) winter flow and (b) summer flow regimes; dots denote depth levels of the measurements.....	5
4. Examples of water level fluctuations in the Gulf of Aden (G14), at Perim Narrows (G89), and the Hanish Sill (G108) .....	8
5. Examples of along-strait current component time series collected at Perim Narrows (A2b mooring; depths of 30 m and 140 m), C mooring (depths of 30 m and 140 m), and the Hanish Sill (B2b mooring; depths of 30 m and 80 m) .....	11
6. Vertical distributions of the total variance and variance associated with the semidiurnal, diurnal, and low frequency (< 0.6 cpd) bands at (a) Perim Narrows (A2b mooring), (b) C mooring, and (c) the Hanish Sill (B2b mooring); the 95% confidence interval is $0.79s^2(f) < \sigma^2(f) < 1.29s^2(f)$ where $s^2(f)$ is the variance estimate and $\sigma^2(f)$ is the true variance at frequency f .....	12
7. Vertical distributions of the total current variance and variance associated with the semidiurnal and diurnal frequency bands for (a) the winter stratification (the 95% confidence interval: $0.72s^2(f) < \sigma^2(f) < 1.43s^2(f)$ ) and (b) the summer stratification (the 95% confidence interval: $0.67s^2(f) < \sigma^2(f) < 1.60s^2(f)$ where $s^2(f)$ is the variance estimate and $\sigma^2(f)$ is the true variance at frequency f) near the Hanish Sill (B2b mooring) .....	13
8. Spectrum ( $cm^2/s^2/cpd$ ) of the along-strait currents for spring tides calculated for the two-layer and three-layer flow regimes at A2b (a, b), C (c, d), and B2b (e, f) moorings.....	15
9. Spectrum ( $cm^2/s^2/cpd$ ) of the along-strait currents (A2b mooring) for neap tides computed for the two-layer flow regime .....	19

10. Spectral estimates ( $\text{cm}^2/\text{s}^2/\text{cpd}$ ) of the along-strait current component for the diurnal band centered at 1 cpd computed from 29 day non-overlapping subsets obtained from data collected at the Hanish Sill; the 95% confidence interval is between $0.67S(f)$ and $1.64S(f)$ where $S(f)$ is the spectra estimate at frequency $f$ .....	20
11. The vertical distribution of the semimajor axis of the $K_1$ , $O_1$ , and $P_1$ tidal constituents at (a) Perim Narrows (A2b mooring), (b) C mooring, and (c) the Hanish Sill (B2b mooring).....	21
12. The vertical distribution of (a) semimajor axis, (b) semiminor axis, (c) inclination of the semimajor axis, and (d) phase for the $K_1$ tidal constituent at Perim Narrows (A2b mooring), C mooring, and the Hanish Sill (B2b mooring) for the winter stratification.....	22
13. The vertical distribution of (a) semimajor axis, (b) semiminor axis, (c) inclination of the semimajor axis, and (d) phase for the $K_1$ tidal constituent at Perim Narrows (A2b mooring), C mooring, and the Hanish Sill (B2b mooring) for the summer stratification .....	24
14. Contours of (a) the semimajor axis and phase, and (b) the semiminor axis and inclination angle of the $K_1$ tidal constituent for the winter stratification at the Perim Narrows cross-section (dots denote depth levels of the measurements) .....	26
15. Contours of (a) the semimajor axis and phase, and (b) the semiminor axis and inclination angle of the $K_1$ tidal constituent for the summer stratification at the Perim Narrows cross-section (dots denote depth levels of the measurements) .....	27
16. The vertical distribution of (a) the semimajor axis, (b) semiminor axis, (c) inclination of the semimajor axis, and (d) phase for the $M_2$ tidal constituent at Perim Narrows (A2b mooring), C mooring, and the Hanish Sill (B2b mooring) for the winter stratification.....	28
17. The vertical distribution of (a) semimajor axis, (b) semiminor axis, (c) inclination of the semimajor axis, and (d) phase for the $M_2$ tidal constituent at Perim Narrows (A2b mooring), C mooring, and the Hanish Sill (B2b mooring) for the summer stratification .....	30
18. Contours of (a) the semimajor axis and phase, and (b) the semiminor axis and inclination angle of the $M_2$ tidal constituent for the winter stratification at the Perim Narrows cross-section (dots denote depth levels of the measurements) .....	32
19. Contours of (a) the semimajor axis and phase, and (b) the semiminor axis and inclination angle of the $M_2$ tidal constituent for the summer stratification	

at the Perim Narrows cross-section (dots denote depth levels of the measurements) .....	33
20. Amplitudes of the clockwise and anticlockwise rotary current components of the $K_1$ tidal component computed from the observations collected at A2b mooring during the winter stratification period .....	34
21. Current and water level fluctuations (40-hour high passed-filtered data) at (a) Perim Narrows and (b) the Hanish Sill.....	37
22. Distribution of the along-strait tidal velocity component predicted from the $K_1$ , $O_1$ , $P_1$ , $M_2$ , $S_2$ , and $N_2$ constituents (a) 4 hours after HHW, (b) 4 hours after LLW, (c) 3 hours after LHW, and (d) 3 hours after HLW at the coast (the Perim Narrows cross-section).....	39
23. Example of time series of (a) the principle terms in the cross-strait momentum balance and (b) differences (residuals) between balance terms for the Perim Narrows cross-section .....	45
24. Example of time series of (a) the principle terms in the along-strait momentum balance and (b) differences (residuals) between balance terms for the Perim Narrows cross-section.....	46
25. The along-strait current component at 60 m - B2b mooring (10-40 day band passed data).....	47
26. The vertical distribution of (a) semimajor axis, (b) semiminor axis, (c) inclination of the semimajor axis, and (d) phase for the $M_m$ , $M_{sm}$ , $M_f$ , and $M_{sf}$ tidal constituents at the Hanish Sill (B2b mooring) .....	48
27. Vertical distributions of rms and maximum contribution (max) of the along-strait currents generated by the $M_m$ , $M_{sm}$ , $M_f$ , and $M_{sf}$ tidal constituents.....	49
28. The vertical distribution of (a) semimajor axis, (b) semiminor axis, (c) inclination of the semimajor axis, and (d) phase for the $MK_3$ , $SO_3$ , and $M_4$ tidal constituents at Perim Narrows (AA1 mooring) .....	51
29. Examples of buoyancy frequency distributions near (a) Perim Narrows, (b) C mooring, and (c) the Hanish Sill for the winter and summer stratifications .....	53
30. Examples of vertical distributions of the baroclinic along-strait current components for the winter stratification during (a) flood and (b) ebb tides .....	54
31. Examples of vertical distributions of the baroclinic along-strait current components for the summer stratification during (a) flood and (b) ebb tides.....	55

32. Water level fluctuations (G89) and baroclinic along-strait current component (A2b mooring) at 120 m observed near Perim Narrows - winter stratification .....	56
33. Variance-preserving plots of (a) along-strait and (b) cross-strait baroclinic current components observed in the pycnocline region at three different locations - winter stratification .....	57
34. Variance-preserving plots of (a) along-strait and (b) cross-strait baroclinic current components observed at three different locations - summer stratification (current components at 160 m for A2b and C moorings, and at 100 m for B2b mooring) .....	57
35. The vertical distribution of energy spectra ( $\text{cm}^2/\text{s}^2/\text{cpd}$ ) of the along-strait baroclinic current components near the Hanish Sill for the winter stratification .....	58
36. Time series of $\sigma_0$ from four different depths at the Hanish Sill.....	59
37. Variance-preserving plots of $\sigma_0$ time series (a) for the winter and (b) summer stratifications .....	60
38. Interpolated $\sigma_0$ time series for (a) the winter and (b) summer stratifications; thick horizontal lines indicate the depth of the instruments .....	61
39. Current ellipse parameters for (a) the first and (b) second EOF modes of the diurnal band at Perim Narrows for the winter stratification (major and minor axes are on the left side; these axes were moved slightly to the right for odd depths for clarity; phases are denoted as arrows on the right of each panel, and they are relative to the along-strait velocity at 20 m) .....	63
40. Current ellipse parameters for (a) the first and (b) second EOF modes of the diurnal band at C mooring for the winter stratification (major and minor axes are on the left side; phases are denoted as arrows on the right, and they are relative to the along-strait velocity at 30 m) .....	64
41. Current ellipse parameters for (a) the first and (b) second EOF modes of the diurnal band at the Hanish Sill for the winter stratification (major and minor axes are on the left side; phases are denoted as arrows on the right, and they are relative to the along-strait velocity at 20 m) .....	65
42. Current ellipse parameters for (a) the first and (b) second EOF modes of the diurnal band at the Hanish Sill for the winter stratification period between 12/02/1996 – 01/02/1997 (major and minor axes are on the left side; phases are denoted as arrows on the right, and they are relative to the along-strait velocity at 20 m) .....	66

43. Amplitudes and phases of density for (a) the first and (b) second EOF modes of the diurnal band at the Hanish Sill for the winter stratification period between 12/02/1996 - 01/02/1997 (phases are relative to the along-strait velocity at 20 m) .....	67
44. Amplitudes of the semimajor axes of barotropic (mode 0), first baroclinic (mode 1), second baroclinic (mode 2), and third baroclinic (mode 3) modes of the semidiurnal tidal currents for the winter stratification at (a) Perim Narrows (A2b mooring), (b) C mooring, and (c) the Hanish Sill (B2b mooring); amplitudes of this axis computed from the measurements are denoted by pluses and amplitudes obtained from fitting the first four modes (modes 0 through 3) are shown as a thick continuous line .....	71
45. Amplitudes of the semimajor axes of barotropic (mode 0), first baroclinic (mode 1), second baroclinic (mode 2), and third baroclinic (mode 3) modes of the diurnal tidal currents for the winter stratification at (a) Perim Narrows (A2b mooring), (b) C mooring, and (c) the Hanish Sill (B2b mooring); amplitudes of this axis computed from the measurements are denoted by pluses and amplitudes obtained from fitting the first four modes (modes 0 through 3) are shown as a thick continuous line .....	72
46. A location of the water level stations, transects, and model open boundary (dotted line); depth contours are in meters .....	77
47. Triangular grid for the ADCIRC-2DDI model .....	78
48. Model coamplitudes (in cm; solid line) and cophases (degrees, GMT; dashed line) for the K <sub>1</sub> constituent.....	84
49. Model coamplitudes (in cm; solid line) and cophases (degrees, GMT; dashed line) for the M2 constituent.....	85
50. Distribution of the spring tide water elevation generated by the K <sub>1</sub> , O <sub>1</sub> , P <sub>1</sub> , Q <sub>1</sub> , M <sub>2</sub> , S <sub>2</sub> , N <sub>2</sub> , and K <sub>2</sub> constituents in the Bab el Mandab Strait at the time of (a) LLW, (b) LHW, (c) HLW, and (d) HHW at Perim Narrows .....	86
51. Distribution of the neap tide water elevation generated by the K <sub>1</sub> , O <sub>1</sub> , P <sub>1</sub> , Q <sub>1</sub> , M <sub>2</sub> , S <sub>2</sub> , N <sub>2</sub> , and K <sub>2</sub> constituents in the Bab el Mandab Strait at the time of (a) the high water, and (b) the low water at Perim Narrows .....	88
52. Distribution of amplitudes (cm/s) of the semimajor axis for the K <sub>1</sub> constituent.....	89
53. Distribution of amplitudes (cm/s) of the semimajor axis for the M <sub>2</sub> constituent.....	90
54. Speeds (in cm/s; a shade scale) and direction (arrows) of the currents generated by the K <sub>1</sub> , O <sub>1</sub> , P <sub>1</sub> , Q <sub>1</sub> , M <sub>2</sub> , S <sub>2</sub> , N <sub>2</sub> , and K <sub>2</sub> constituents in the Bab	

el Mandab Strait during spring tides (a) 4 h after LLW, (b) 4 h after LHW, (c) 3 h after HLW, and (d) 4 h after HHW at Perim Narrows .....	91
55. Speeds (in cm/s; a shade scale) and direction (arrows) of the currents generated by the $K_1$ , $O_1$ , $P_1$ , $Q_1$ , $M_2$ , $S_2$ , $N_2$ , and $K_2$ constituents in the Bab el Mandab Strait during neap tides (a) 4 h after the high water, and (b) 4 h after the low water at Perim Narrows .....	92
56. Time-averaged residual tidal flow in the Bab el Mandab Strait .....	93
57. Snapshots of the fluctuating residual at two-day intervals (a) day 81, (b) day 83, (c) day 85, (d) day 87, (e) day 89, (f) day 91,(g) day 93, and (h) day 95 .....	95
58. The distribution of the amplitudes of the semimajor axis for (a) the fluctuations generated by the interactions of the $K_1$ and $O_1$ , and (b) $M_{sf}$ constituent.....	99
59. Terms of the momentum equations for the deep-water grid points located near the ADCP moorings (see Figure 1 and Table 10 for the mooring locations) at Perim Narrows (a and b), in the middle of the Strait (C mooring) (c and d), and the Hanish Sill (e and f) .....	100
60. Terms of the momentum equations for the shallow-water grid points (see Figure 58b for their locations): point 1 (a and b) and point 2 (c and d) .....	101
61. Mean tidal energy flux per unit length for the $K_1$ constituent.....	102
62. Mean tidal energy flux per unit length for the $M_2$ constituent.....	103
63. Tidal energy dissipation rate ( $\text{W}/\text{m}^2$ ) for the $K_1$ constituent.....	104
64. Tidal energy dissipation rate ( $\text{W}/\text{m}^2$ ) for the $M_2$ constituent .....	105

## ABSTRACT

The Bab el Mandab Strait is where the transition occurs between two noticeably different tidal regimes: the Gulf of Aden, where tidal fluctuations are mixed and have a range in excess of 2 m, and the Red Sea, where the tides are principally semidiurnal and their range is less than 1 m. Within the Strait, observations collected between May of 1995 and July of 1997 indicate that tidal currents are a mixed type and dominant constituents are the  $K_1$  and  $M_2$ . The vertical structure of the tidal currents is complicated, differs between semidiurnal and diurnal constituents, and depends on the location and stratification. In addition, the stratification impacts more the vertical distribution of the diurnal tidal currents. The major part of this signal is barotropic but energetic baroclinic currents are observed near Perim Narrows and the Hanish Sill during the winter stratification. Results of the EOF analysis and internal velocity modes estimated from observed density profiles indicate that the baroclinic currents of diurnal frequency have vertical structure, which is a combination of the second and third baroclinic modes near Perim Narrows and of the first and second modes near the Hanish Sill.

To examine in more details the barotropic tides in the Strait, a two-dimensional finite element model (ADCIRC-2DDI) was implemented. Results from this model indicate that the largest elevations and most energetic currents are observed in the region located between Perim Narrows and Assab-Mocha line. They also imply that residual circulation induced by the barotropic tides is generally weak in the Strait and consists of mean and fluctuating components. Average barotropic energy fluxes over a tidal period are small and their direction depends on the constituent. The  $K_1$  component has one source of energy, which is the flux from the Gulf of Aden, while there are two sources of energy for the  $M_2$ : one from the Gulf of Aden and another from the Red Sea. In addition, these results show that the major part of the tidal energy for both constituents is dissipated within the Strait itself.

## 1. INTRODUCTION

Sea straits, which connect semi-enclosed basins with larger water bodies, have drawn the attention of the oceanographic community for many decades. They have been of such high interest because, in the majority of cases, these straits solely control the water mass exchange between two adjacent basins. These exchange processes depend on the flow dynamics that are usually very complex in straits as a result of a shallow sill, such as in the case of the Gibraltar Strait or the Bab el Mandab Strait.

The Bab el Mandab Strait, whose tides are the subject of this dissertation, is located at the southern end of the Red Sea, and is its major link with the Gulf of Aden and Indian Ocean (Figure 1). This Strait is over 150 km long and extends from Hanish Islands in the northwest to Perim Island in the south. It is easily distinguishable from the Red Sea proper and Gulf of Aden because of its shallow depths. At about 15°N, the floor of the Red Sea rises fairly rapidly from more than 1000 m to less than 500 m. Farther south, the sea bottom rises more slowly, and off Great Hanish Island lies a shallow sill (Hanish Sill) at 13° 41' N, where the greatest depth is only about 154 m. South of the Hanish Sill, the depth increases again, and between Mocha and Assab there is an elongated but isolated trench more than 200 m deep. Farther south, the bottom again becomes shallow but furrowed in the central part by an incision with very steep sides forming a narrow throat parallel to the axis of the Strait where the maximum depths vary between 180 m and 200 m. Between Ras Bab el Mandab and Ras Siyan, the Strait is divided into two channels: the small strait on the eastern side that is about 4 km wide and no more than 26 m deep, and the second larger strait located southwest of Perim that is about 20 km wide and up to 230 m deep. This part of the Bab el Mandab Strait is also called Perim Narrows.

It has been recognized for some time that high salinity waters form in the Red Sea (where there is a high net evaporation over precipitation), and then exit into the Indian Ocean through the Bab el Mandab Strait. The volume transport of the Red Sea waters of 0.37 Sv (Murray and Johns, 1997) is very small, yet observations taken throughout the Indian Ocean show these waters to have a distinctive and far-reaching signal. They extend from about 16°N to 32°S (Gründlingh, 1985; Toole and Warren, 1993; Beal et al., 2000), and eastward to Sumatra (Wyrtki, 1971). Remnants of the Red Sea waters even have been observed in the Agulhas retroflection region to the south of South Africa (Gordon et al., 1987; Valentine et al., 1993). The widespread presence of these waters indicates that they are an important component of the thermohaline circulation in the Indian Ocean; therefore, the understanding of the flow dynamics in the Bab el Mandab Strait is crucial since this Strait is the only passage for the Red Sea waters to the Indian Ocean.

The horizontal velocity field in straits is generally dominated by low frequency and tidal motions. Previous and present studies have demonstrated that the low frequency flow in the Bab el Mandab Strait shows seasonal variability (Vercelli, 1931; Thompson, 1939; Smeed, 1997; Murray and Johns, 1997). This variability is characterized by two flow regimes: winter and summer. The winter flow regime is generally observed between October and May, and it is characterized by a two-layer inverse estuarine flow (relatively fresh inflow from the Gulf of Aden on the top of a deep hypersaline outflow of the Red Sea waters). This pattern is usually replaced between June and September by a three-

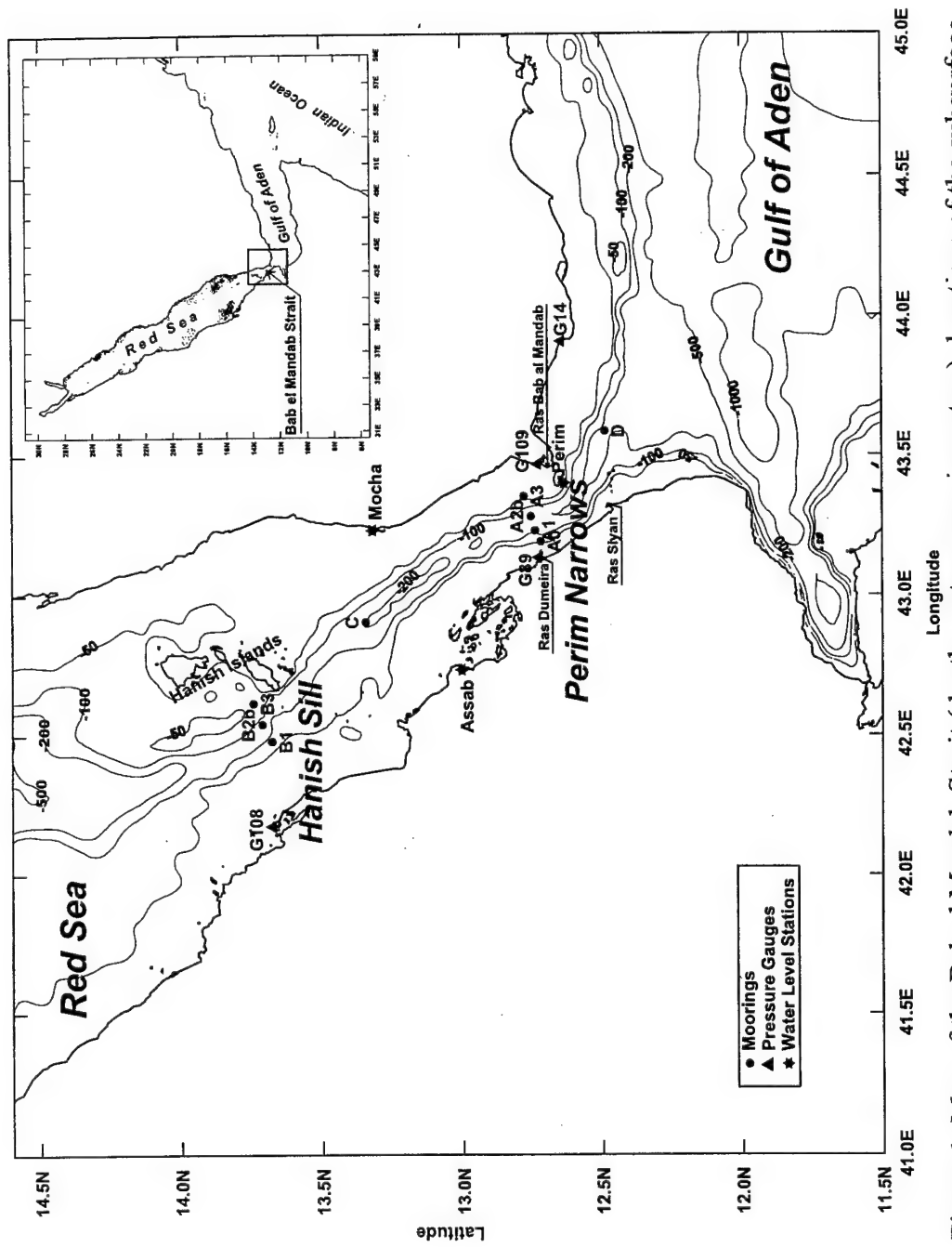


Figure 1. Map of the Bab el Mandab Strait (depth contours are in meters); locations of the subsurface pressure gauges (triangles) and the current meter moorings (solid circles) deployed during the first phase of the BAM project, and locations of the water level stations are also shown.

layer flow (a summer flow regime) comprised of a shallow outflow of the Red Sea surface waters, an intrusion of the relatively fresh and cold Gulf of Aden intermediate waters, and a deep hypersaline outflow of the Red Sea waters. Figure 2 illustrates these two circulation patterns at three different locations: Perim Narrows (A2b mooring), in the middle of the Strait (C mooring), and the Hanish Sill (B2b mooring) (see Figure 1 and Table 10 for mooring locations). It displays means of the along-strait velocity component at different depth levels that were computed from current data collected between June 1995 and March 1996 in the Strait.

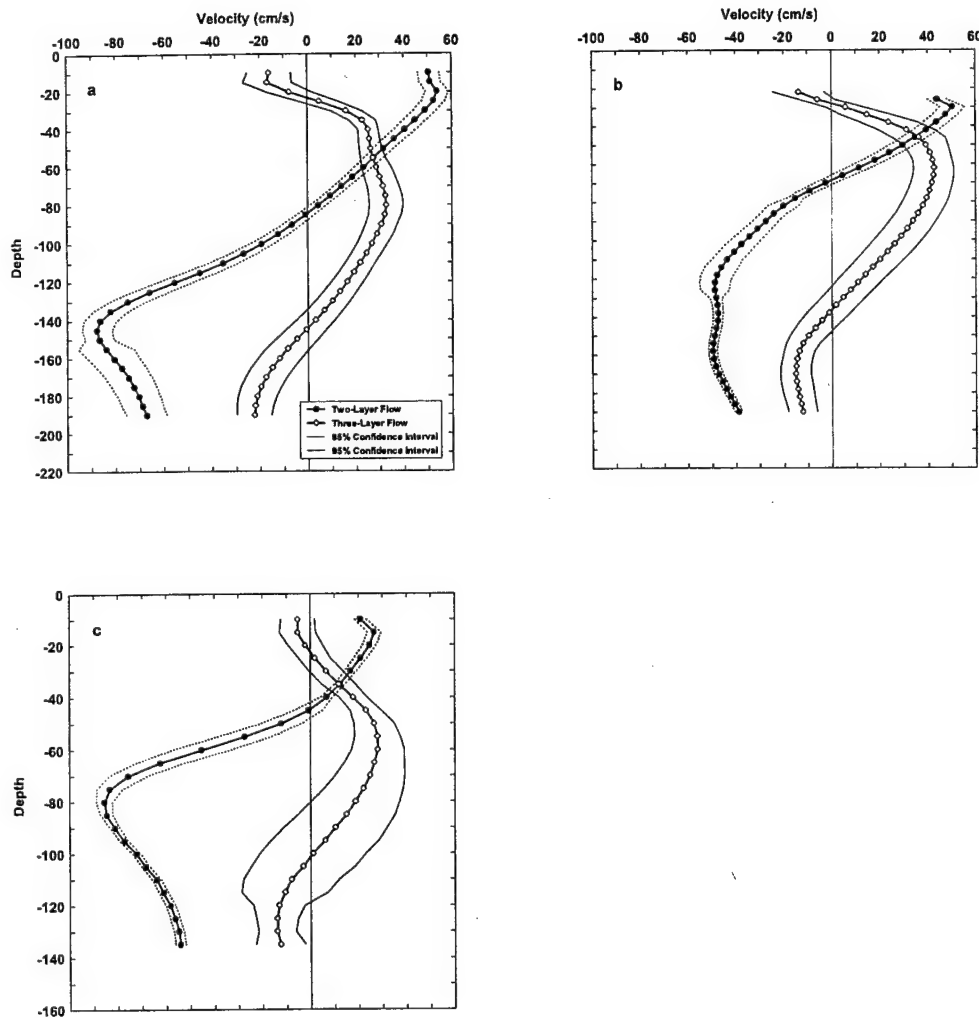


Figure 2. Vertical profiles of the along-strait velocity component (means) for the winter two-layer and summer three-layer flow regimes at (a) Perim Narrows (A2b mooring), (b) C mooring located in the middle of the Bab el Mandab Strait, and (c) the Hanish Sill (B2b mooring); thin continuous and dotted lines indicate the 95% confidence intervals of the means for the summer and winter flow regimes, respectively.

As a result of changing water masses flowing into the Red Sea from the Gulf of Aden, stratification in the Bab el Mandab Strait changes throughout the year. Smeed (1997) estimated the average properties of the water masses observed in the Strait from data presented by Siedler (1969), Patzert (1974), and Maillard and Soliman (1986). He summarized that during the two-layer flow in the Strait two water types dominate: (1) surface waters with temperature of 26°C, salinity of 37 psu and potential density ( $\sigma_0$ ) of 24.5 kg/m<sup>3</sup> inflowing from the Gulf of Aden and (2) Red Sea outflow waters with temperature of 22.5°C, salinity of 40 psu and potential density of 27.9 kg/m<sup>3</sup>. When the three-layer flow is present there are three water types in the Strait: (1) surface waters with temperature of 32°C, salinity of 37 psu and potential density of 22.5 kg/m<sup>3</sup> flowing into the Gulf of Aden; (2) Gulf of Aden intermediate waters with temperature of 18°C, salinity of 36 psu and potential density of 26 kg/m<sup>3</sup> flowing into the Strait; (3) Red Sea outflow waters with average values of 22.5°C, 40 psu, and 27.9 kg/m<sup>3</sup>. Similar values of the water mass properties were also reported by Murray and Johns (1997) who analyzed the salinity and temperature time series gathered at the Hanish Sill.

Although we nominally speak about two or three layer structures of the water column, there are in fact significant pycnocline zones whose thickness might be comparable to the thickness of the surrounding nearly homogeneous layers. In the Bab el Mandab Strait, during the winter flow regime (Figure 3a), there is one pycnocline layer, while during the summer flow regime there might be two pycnocline zones (Figure 3b), if the Red Sea and/or surface outflows are not shut down. Figures 3a and 3b show  $\sigma_0$  distributions in the Bab el Mandab Strait for the winter and summer stratifications, respectively. The data used to construct these plots come from CTD casts that were gathered in the Strait between May 30 and June 4, 1995, and between July 28 and August 1, 1997. During the winter regime, the thickness of the pycnocline zone decreases from about 100 m in the southern part of the Strait to about 50 m at its northern end, and this zone extends approximately between 50 m and 160 m near Perim Narrows, and between 50 m and 100 m at the Hanish Sill. During the summer flow regime, the pycnocline between the Red Sea surface and Gulf of Aden intermediate waters is roughly 20 m thick and located generally between 30 m and 50 m throughout the Strait. The thickness of the pycnocline layer between the Gulf of Aden intermediate and Red Sea deep waters is also about 20 m but its depth varies in the Strait, and the largest density gradients are found approximately between 150 m and 170 m near Perim Narrows and between 90 m and 110 m near the Hanish Sill.

The tidal motion in the Bab el Mandab Strait has not received as much recognition as the low frequency flow. This Strait is a transitional region between two noticeably different tidal regimes: the Gulf of Aden, where tidal fluctuations are mixed and have a range in excess of 2 m, and the Red Sea, where the tides are principally semidiurnal and their range is less than 1 m. A few analytical analyses were done to determine tides in this Strait, and they were used to explain tidal dynamics in the entire Red Sea. Results from these analyses (Harris, 1904; Chandon, 1930; Defant, 1961) showed that the tides in the Red Sea should be considered as a superposition of a tide co-oscillating with those observed in the Gulf of Aden and an independent tide.

Historical observations and descriptions of tides, especially tidal currents, are very limited and restricted to the southern end of the Bab el Mandab Strait. Gedge (Defant, 1961) was the first who described the tidal currents in the Strait as diurnal only. This

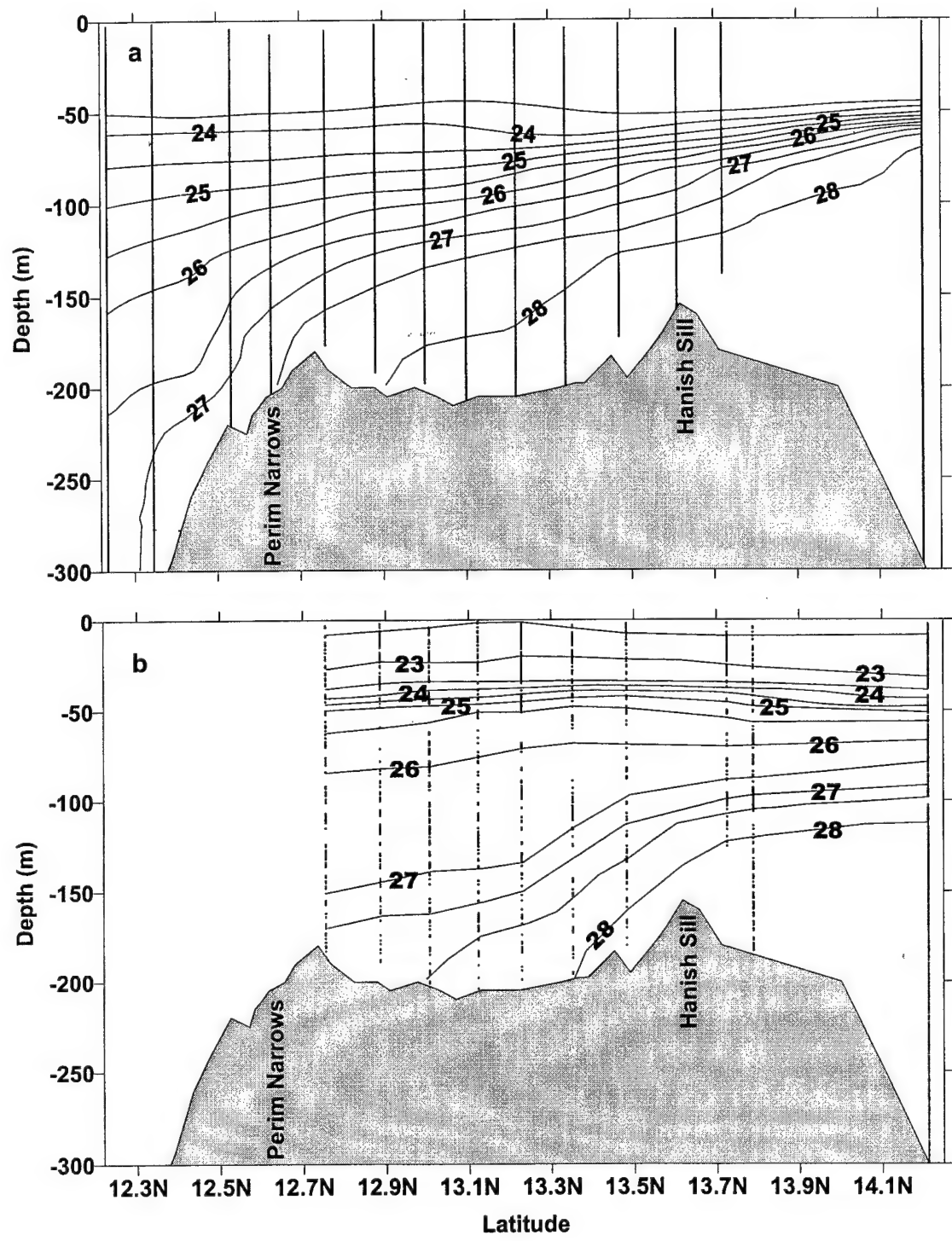


Figure 3. Examples of density ( $\sigma_0$ ) distributions in the Bab el Mandab Strait during (a) winter flow and (b) summer flow regimes; dots denote depth levels of the measurements.

description was based on a short series of measurements (one day) taken during neap tides when amplitudes of the semidiurnal tides are minimal, and it was later dismissed by Vercelli (1925). Based on a 15-day series of current measurements from five depths collected in March 1924, Vercelli (1925) characterized the tidal currents in the southern part of the Bab el Mandab Strait as exceptionally strong with clear diurnal and semidiurnal oscillations. He estimated amplitudes and phases of the tidal currents and concluded that  $M_2$  and  $K_1$  constituents had the largest amplitudes. He also pointed out that the strength of the semidiurnal current constituents decreased with depth, and that at and below 130 m, the tidal currents had a clear diurnal character. Vercelli's discovery of the changing character of the tidal currents with depth is somewhat puzzling considering the fact that, based on the tidal elevation amplitudes, he identified the tidal regime near Perim Narrows (see Figure 1 for the location) as mixed, predominantly semidiurnal. He found the extremely diurnal tidal regime only in the nodal zone of the semidiurnal tide, and this nodal zone, which was deduced from distributions of the observed amplitudes and phases of the tidal elevation, is located farther north near Assab (see Figure 1 for the location). Vercelli (1927) also analyzed a 15-day time series (March 1924) of temperature and salinity at the surface, 100 m and 170 m near Perim Narrows, and pointed out that variations of temperature and salinity were not appreciable at the surface but increased rapidly with depth below 100 m. He indicated that there might be internal tides in the Strait because the large fluctuations of temperature and salinity, when analyzed together with the current measurements, follow the rhythm of the tidal currents. In addition, Defant (1961), who analyzed the same data set as Vercelli (1925, 1927), pointed out that the oscillations in the density transition layer may have amplitudes up to 100 m, and that the extreme changes in temperature and salinity occur at the times of the tidal current reversal. Tidal fluctuations in the density transition layer were also reported by Siedler (1969); however, he did not indicate that these fluctuations may have amplitudes as large as 100 m. He pointed out only that these fluctuations were generally observed in the upper part of the transition layer, and that their period was mainly diurnal. He also analyzed a two-week current time series at two different depths and confirmed the existence of the semidiurnal and diurnal tidal currents near Perim Narrows.

It is apparent that our knowledge about tides in the Bab el Mandab Strait is extremely limited, considering its important location. The question then arises why one should learn more about this motion. The answer is quite simple. Tides are everyday features and because of their everyday presence a proper estimation of their currents and elevations is crucial for the successful prosperity of coastal communities and infrastructures. Extensive knowledge about tides is also important to understand such phenomena as migration patterns of fish or zonation of organisms in coastal regions or on the seabed. From a physical oceanographer's point of view, tides are interesting because a part of tidal energy may be available for vertical mixing of the water column. Interactions of the tides with existing topography and stratification also may create internal waves of large amplitudes at pycnocline depth such as those observed in the Gibraltar Strait (Armi and Farmer, 1986; Pettigrew and Hyde, 1990). Currents produced by tides in a sea strait may interact with the mean flow, and these interactions may lead to a modification of water mass exchange between two basins (Armi and Farmer, 1986; Helffrich, 1995; Pratt et al., 2000). Tidal currents may be also an important component in

sediment transport as well as in pollutant dispersion. These are just a few among many other examples of why we should study and learn more about tides.

The overall purpose of this dissertation is to improve our understanding of the tidal frequency motion in the Bab el Mandab Strait. The specific objectives are: (1) to identify dominant tidal constituents in the entire Strait; (2) to investigate how the tidal elevation and currents vary in this region; (3) to examine effects of stratification on the observed tidal currents; and (4) to study distributions of energy fluxes, energy dissipation, and residual circulation generated by the barotropic tides in the Strait. This will be done by means of analyzing measurements collected in the Strait as well as by numerical modeling. The majority of data analyzed here originate from a project entitled "Observation and Modeling – an Integrated Study of the Transport through the Strait of Bab el Mandab" (the BAM project) that was primarily designed to investigate subinertial transport and its variability in the Strait (a more detailed description of the data sets can be found in Appendix A). The barotropic tides are numerically simulated with the two-dimensional finite element hydrodynamic model named Advanced Two-Dimensional Depth-Integrated CIRCulation Model for Shelves, Coasts and Estuaries (ADCIRC-2DDI) developed by Luettich et al., (1992) and Westerink et al. (1994).

The outline of the dissertation is as follows: in Chapters 2 and 3, a description of the most energetic constituents of the tidal elevation and currents and their variability in the Bab el Mandab Strait is presented. In Chapter 4, features of the baroclinic motion with tidal frequency are analyzed. In Chapter 5, results from a two-dimensional barotropic tidal model are examined.

## 2. SURFACE TIDE IN THE BAB EL MANDAB STRAIT

Prior to the BAM project, the only available data to study tidal elevations in the Bab el Mandab Strait were tidal constants from three locations (Perim, Assab, and Mocha; see Figure 1 for their locations). For the duration of the BAM project, three additional subsurface pressure gauges were deployed in the Strait (see Figure 1 for their locations). Although all water level stations and gauges are confined to the coastal region and their spatial distribution is not ideal, they should, however, give considerable insight to how the tidal parameters vary in the region.

Three characteristic observations of the water level fluctuations for the Gulf of Aden (G14), Perim Narrows (G89), and the Hanish Sill (G108) are illustrated in Figure 4 for a period extending from June 5 to August 14, 1995. These time series clearly exhibit a change in the tidal regime and range. At G14 and G89 sites, surface tides have a mixed character with diurnal and semidiurnal fluctuations clearly visible. However, farther north (G108) the semidiurnal fluctuations dominate the record. These time series also show a reduction in range between the southern and northern ends of the Strait; for instance, at G89 the tidal range exceeds 1.5 m whereas, at the Hanish Sill, it is less than 1 m. In addition, all records clearly indicate the presence of fortnightly modulations.

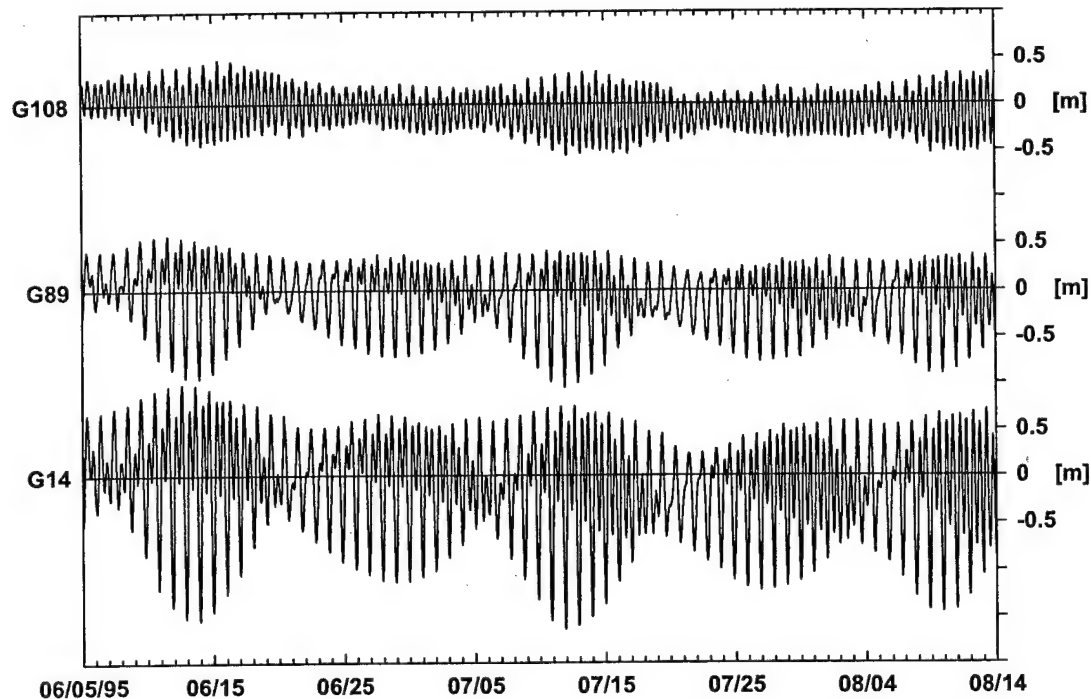


Figure 4. Examples of water level fluctuations in the Gulf of Aden (G14), at Perim Narrows (G89), and the Hanish Sill (G108).

The observed differences in the tidal surface fluctuations between the southern and northern ends of the Strait are also indicated by a partition of tidal variance between semidiurnal ( $1.90 \pm 0.22$  cpd; degrees of freedom - 116) and diurnal ( $0.99 \pm 0.22$  cpd; degrees of freedom - 116) frequency bands. At Perim Narrow (G89), the percentage of

the total variance contained in both tidal bands is almost identical: 46% and 50% for the semidiurnal and diurnal frequency bands, respectively. At the Hanish Sill (G108), however, the semidiurnal band accounts for 90% of the variance, while the diurnal band accounts for only 3%. As expected, the tidal regime at Perim Narrows is similar to that observed in the Gulf of Aden (mixed type), while near the Hanish Sill, the tides are dominated by semidiurnal fluctuations as they are in the Red Sea (Vercelli, 1925; Defant, 1961). In the middle of the Strait (Assab, Mocha), lack of water level time series prevents us from computing the tidal variance but, based on the form factor, which is defined as an amplitude ratio:  $(A_{K_1} + A_{O_1})/(A_{M_2} + A_{S_2})$ , Vercelli (1925) described the tidal regime as a mixed, predominantly diurnal due to the existence of the node for the  $M_2$  component.

Table 1. Amplitudes (A) and phases (g, GMT) of tidal elevation constituents.

Station	$M_2$		$S_2$		$K_1$		$O_1$	
	A (cm)	g (deg)						
G14	47	119	22	139	39	340	20	344
Perim*	37	136	17	159	35	350	18	351
G109	29	125	16	144	30	340	15	345
G89	23	121	14	142	27.5	337	14	340
Assab*	6.9	259	4	170	18	335	8.5	344
Mocha*	8	244	4.5	188	7	335	6.1	352
G108	24	286	5	299	6	321	2	335

\*Water level stations

Results from harmonic analysis (Foreman, 1977) of the data collected by the pressure gauges, as well as the tidal constants obtained from the International Hydrographic Office, indicate that among diurnal tidal constituents, the  $K_1$  (principal luni-solar with a period of 23.93 h),  $O_1$  (principle lunar with a period of 25.82 h), and  $P_1$  (principle solar with a period of 24.07 h) components have the largest amplitudes. Among semidiurnal components, the  $M_2$  (principal lunar with a period of 12.42 h),  $S_2$  (principle solar with a period of 12.00 h), and  $N_2$  (larger lunar elliptic with a period of 12.66 h) constituents are the strongest. Table 1 lists amplitudes and phases for the  $M_2$ ,  $S_2$ ,  $K_1$ , and  $O_1$ .

The amplitude and phases again seem to confirm the changing tidal character in the Bab el Mandab Strait. There is a strong attenuation of the amplitudes of both diurnal constituents ( $K_1$  and  $O_1$ ). Similar to these two components, the  $S_2$  constituent also displays a decreasing trend from 22 cm at the Gulf of Aden site to 5 cm at the Hanish Sill. However, another semidiurnal component,  $M_2$ , behaves differently. The  $M_2$  amplitudes decrease by more than 80% from the Gulf of Aden to Mocha and Assab, but then increase again to 24 cm at G108 site. The phase of the diurnal tides varies slightly in the Strait, and the maximum observed difference between the southern and northern ends is  $\sim 15^\circ$ . In contrast,  $M_2$  and  $S_2$  tidal constituents exhibit a considerable increase in phase, implying a time difference of  $\sim 6$  h for  $M_2$  and  $\sim 5$  h for  $S_2$  between the time of the maximum amplitude at G109 and G108 sites. In contrast to variability along the Strait, there is generally little variability in phases and amplitudes of the constituents in the cross-strait direction.

The Bab el Mandab Strait is considered a narrow strait in the sense that its width (the width of the Strait varies between 20 km and 110 km) is much smaller than an external Rossby radius of deformation ( $\sim 1300$  km), and it can be also said that the tides

at both ends of this Strait differ noticeably. Rocha and Clarke (1987) considered theoretically the tidal behavior in a strait connecting two basins and they concluded that in narrow straits: (1) sea level tidal constants change linearly from one end to the other; (2) if the tides in each basin differ, steep sea level gradients occur in the strait; (3) when the tide in one basin is much larger than the tide in the other, the tide in a strait propagates towards the low tide end with some turning in the Kelvin wave sense. These conclusions seem to explain fairly well the behavior of the diurnal tidal constituents in the Bab el Mandab Strait, except for the turning in the Kelvin wave sense, but the limited data set does not allow us to say definitely whether such a turning exists or not; but the semidiurnal components, especially the  $M_2$  component, do not fit well to the theory, probably as a result of the node located near Assab.

### 3. TIDAL CURRENTS IN THE BAB EL MANDAB STRAIT

Currents in the Bab el Mandab Strait exhibit strong diurnal and semidiurnal fluctuations as well as fortnightly modulations. There is also a decrease in range, as illustrated in Figure 5 for the time period between November 1, 1995 and March 20, 1996 (winter circulation regime). The figure displays only the along-strait current components because the currents in the Strait are highly polarized in this direction. The data come from three moorings: the first is located just north of Perim Narrows (A2b mooring), the second is in the middle of the Strait (C mooring), and the third is near the Hanish Sill (B2b mooring). For each mooring, the currents from two different depths, where the maxima of the subtidal flow (see Figure 2) are usually observed, are shown. The top three curves display the along-strait velocity component from the upper layer and the bottom three show the same component for the lower layer.

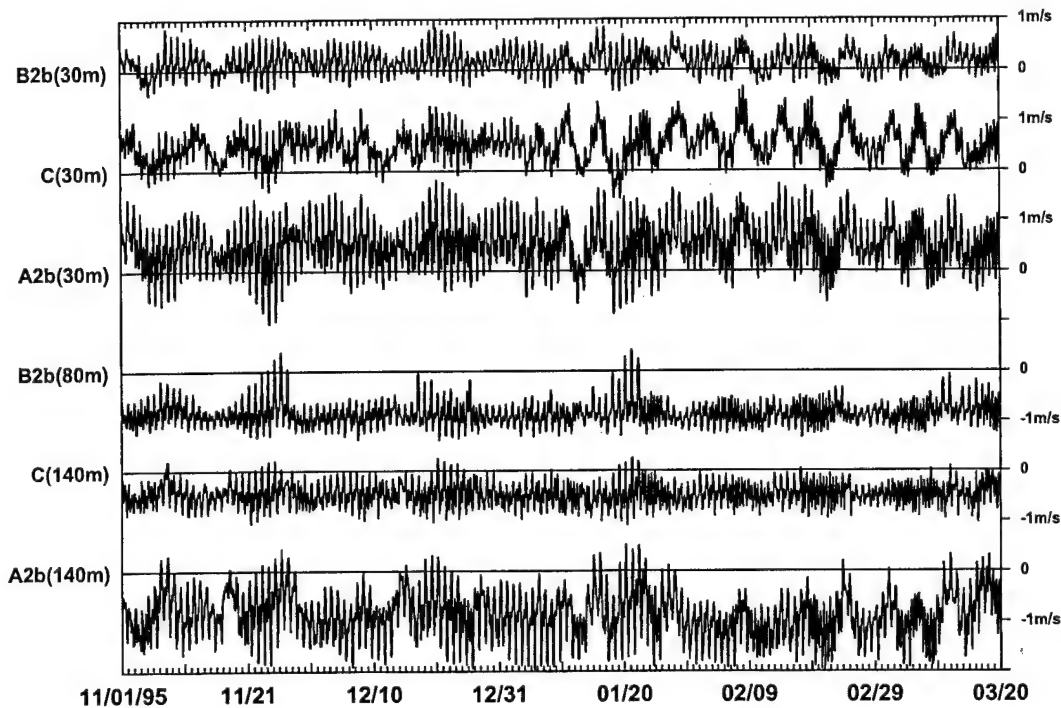


Figure 5. Examples of along-strait current component time series collected at Perim Narrows (A2b mooring; depths of 30 m and 140 m), C mooring (depths of 30 m and 140 m), and the Hanish Sill (B2b mooring; depths of 30 m and 80 m).

It is apparent that over each tidal cycle, the flow in the upper layer is usually reversed at the Hanish Sill and Perim Narrows during the ebbing tide (tidal flow towards the Gulf of Aden); however, at C mooring such a flow reversal appears only when strong subtidal fluctuations are not superimposed on the tidal currents. By contrast, the reversal of the lower layer flow at all sites is rare and occurs only during a flood stage (tidal flow towards the Red Sea) of spring tides. When the summer circulation regime (data not shown) is present in the Bab el Mandab Strait, the reversal of the flow is generally observed in all three layers at all sites during each 24-hour period.

### 3.1. Tidal current variance

To determine whether the tidal fluctuations dominate the flow field observed in the Strait and to evaluate how strong diurnal or semidiurnal fluctuations are in this area, variance contained in three different frequency bands was estimated. These computations show that the current variance depends on location, depth, and frequency band. Figure 6 shows the distribution of the total variance as well as the distribution of variance contained in low frequency flow (frequencies less than 0.6 cpd), diurnal ( $1 \pm 0.22$  cpd) and semidiurnal ( $1.94 \pm 0.22$  cpd) bands. Variance estimates were computed from the data collected at A2b, C, and B2b moorings during the first deployment. At Perim

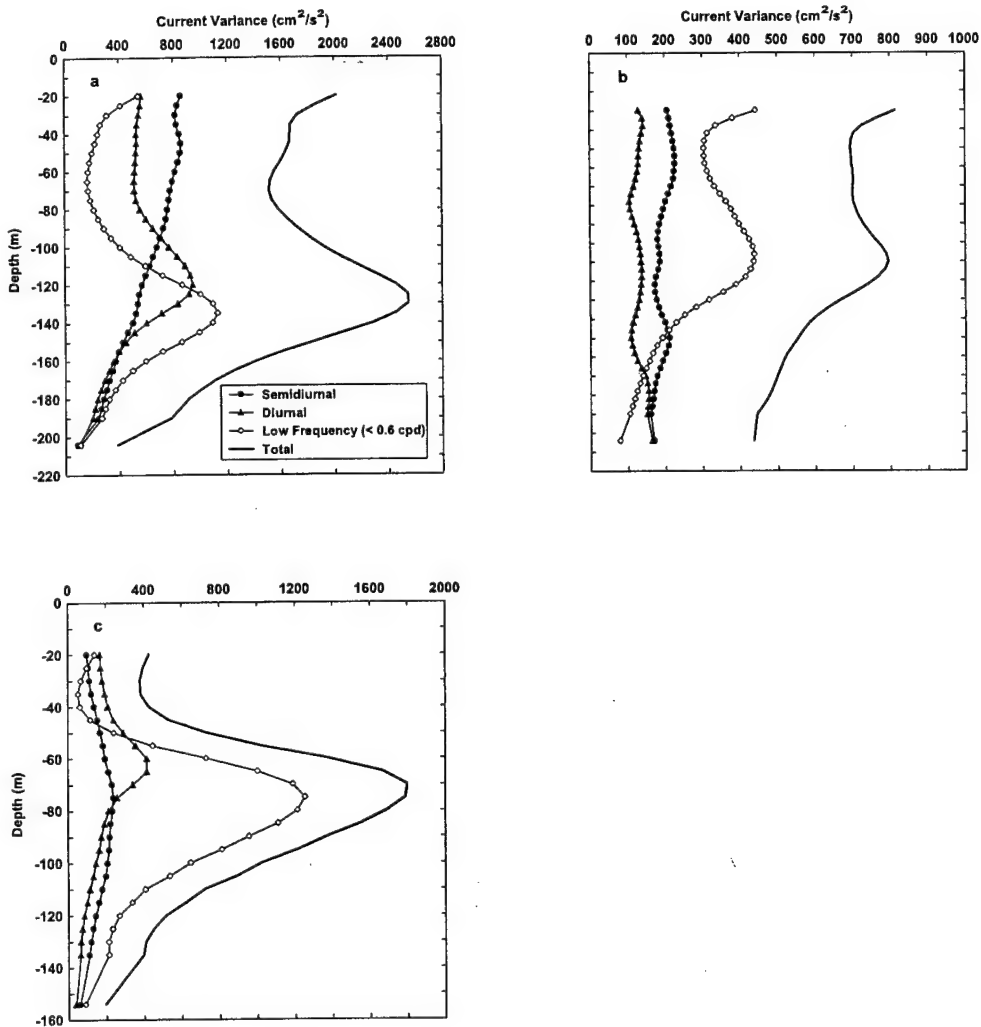


Figure 6. Vertical distributions of the total variance and variance associated with the semidiurnal, diurnal, and low frequency ( $< 0.6$  cpd) bands at (a) Perim Narrows (A2b mooring), (b) C mooring, and (c) the Hanish Sill (B2b mooring); the 95% confidence interval is  $0.79s^2(f) < \sigma^2(f) < 1.29s^2(f)$  where  $s^2(f)$  is the variance estimate and  $\sigma^2(f)$  is the true variance at frequency  $f$ .

Narrows (Figure 6a), more than 50% of the current variance at depths between 20 m and 120 m and below 160 m occurs in the tidal frequencies. However, at depths below 120 m and above 160 m, the low frequency flow shows as much variability as the tidal currents. In the middle of the Strait (Figure 6b), in the upper 130 m of the water column, 50% or more variance occurs at the low frequencies (< 0.6 cpd) and no more than 45% is associated with the semidiurnal and diurnal tides together. Below 130 m, the variability of the subtidal flow decreases and drops to 25% at 190 m, and at the same time, the tidal variance increases, and below 150 m is at least equal to 60% of the total variance. Finally, at the Hanish Sill (Figure 6c), more than 50% of the current variance occurs at the tidal frequencies in the upper 55 m; however, below this depth, the low frequency currents show much more variability than that of the tidal currents and, on average, 63% of the total variance is associated with these currents. Similar distributions of the current variance at the Hanish Sill and Perim Narrows are observed when the data from the second and third deployments are used.

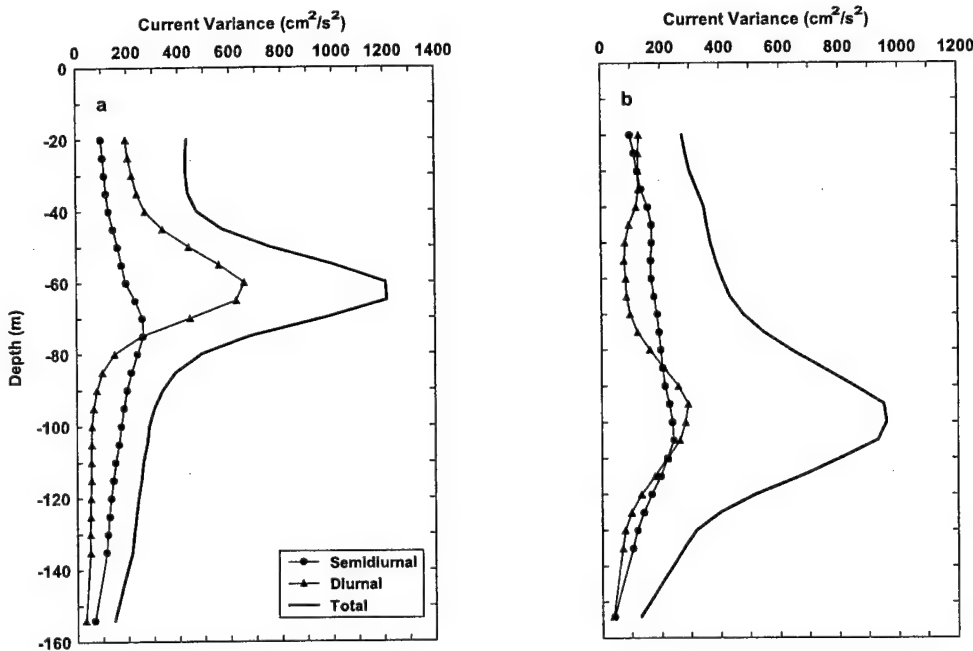


Figure 7. Vertical distributions of the total current variance and variance associated with the semidiurnal and diurnal frequency bands for (a) the winter stratification (the 95% confidence interval:  $0.72s^2(f) < \sigma^2(f) < 1.43s^2(f)$ ) and (b) the summer stratification (the 95% confidence interval:  $0.67s^2(f) < \sigma^2(f) < 1.60s^2(f)$  where  $s^2(f)$  is the variance estimate and  $\sigma^2(f)$  is the true variance at frequency  $f$ ) near the Hanish Sill (B2b mooring).

Figure 6 also shows that the character of the tidal fluctuations depends strongly on depth and location. At Perim Narrows (Figure 6a), semidiurnal tides dominate in the upper part of the water column (above 80 m) whereas the diurnal fluctuations are stronger below 100 m and above 140 m. At other depths, though, energy at both tidal bands is

almost identical. At mooring C (Figure 6b), vertical distribution of the current variance at the tidal frequencies is more uniform than that at mooring A2b, with the semidiurnal fluctuations being a little more energetic than those with the diurnal period. On average, at this location, 29% and 20% of the current variance is associated with the semidiurnal and diurnal frequency bands, respectively. At the Hanish Sill (Figure 6c), however, the variance distribution is again not uniform with the diurnal fluctuations dominating at depths between 50 m and 70 m. At other depths, the variance associated with both tidal bands is comparable.

In addition, the current variance also has the different vertical distributions for the summer and winter stratifications. The most apparent differences between the summer and winter stratification distributions of the variance associated with the tidal bands are observed at Perim Narrows and the Hanish Sill. Figure 7b illustrates the variance distribution at the Hanish Sill when the summer stratification is present in the Strait. It shows that the amount of variance associated with both tidal bands is fairly comparable throughout the water column, and it is, on average, equal to 29% of the total variance for each tidal band. By contrast, when the winter stratification is observed (Figure 7a) the diurnal fluctuations clearly dominate at and above 70 m (40% or more of the total variance is associated with the diurnal band), whereas the semidiurnal fluctuations are dominant below 80 m (40% or more of the total variance is associated with the semidiurnal band).

In summary, it is apparent that the tidal bands contain a significant portion of the variance, and that at some depth they may even dominate the fluctuations, which are superimposed on the mean flow. When percentages of the total variance contained in semidiurnal and diurnal bands are compared, the tidal currents in the Bab el Mandab Strait can be simply classified as mixed; however, to say whether they are predominantly semidiurnal or diurnal, one needs to examine separately different location and depths for each seasonal stratification phase.

### 3.2. Fortnightly modulations

Fortnightly modulations in tidal amplitudes are mainly due to differences in the configuration of the sun, moon and earth (Pugh, 1987). These fortnightly modulations (clearly evident in the current records displayed in Figure 5) cover a possible range of maximal (spring) and minimal (neap) tidal currents that are observed in the Strait (for convenience of this discussion, I refer to the largest tides in the fortnightly cycle as spring tides as opposed to the lowest tides that I refer to as neap tides). Furthermore, when the tidal current range is known, a range of horizontal kinetic energy might be estimated as well.

To explore the fortnightly variability of the tidal current and energy associated with them, spectra for spring and neap tides were calculated separately for the two-layer and three-layer flow regimes from the data collected at three ADCP moorings deployed between June 1995 and March 1996. Results for the spring tides are shown in Figure 8. All spectra were computed from the 125-hour time series that were centered on the spring or neap tide, and then for each depth, average spectra of 8 (the 95% confidence interval is between  $0.56S(f)$  and  $2.29S(f)$  where  $S(f)$  is the spectra estimate at frequency  $f$ ) for the spectra estimates for the winter flow regime and 6 (the 95% confidence interval is between  $0.46S(f)$  and  $2.72S(f)$  where  $S(f)$  is the spectra estimate at frequency  $f$ ) for the

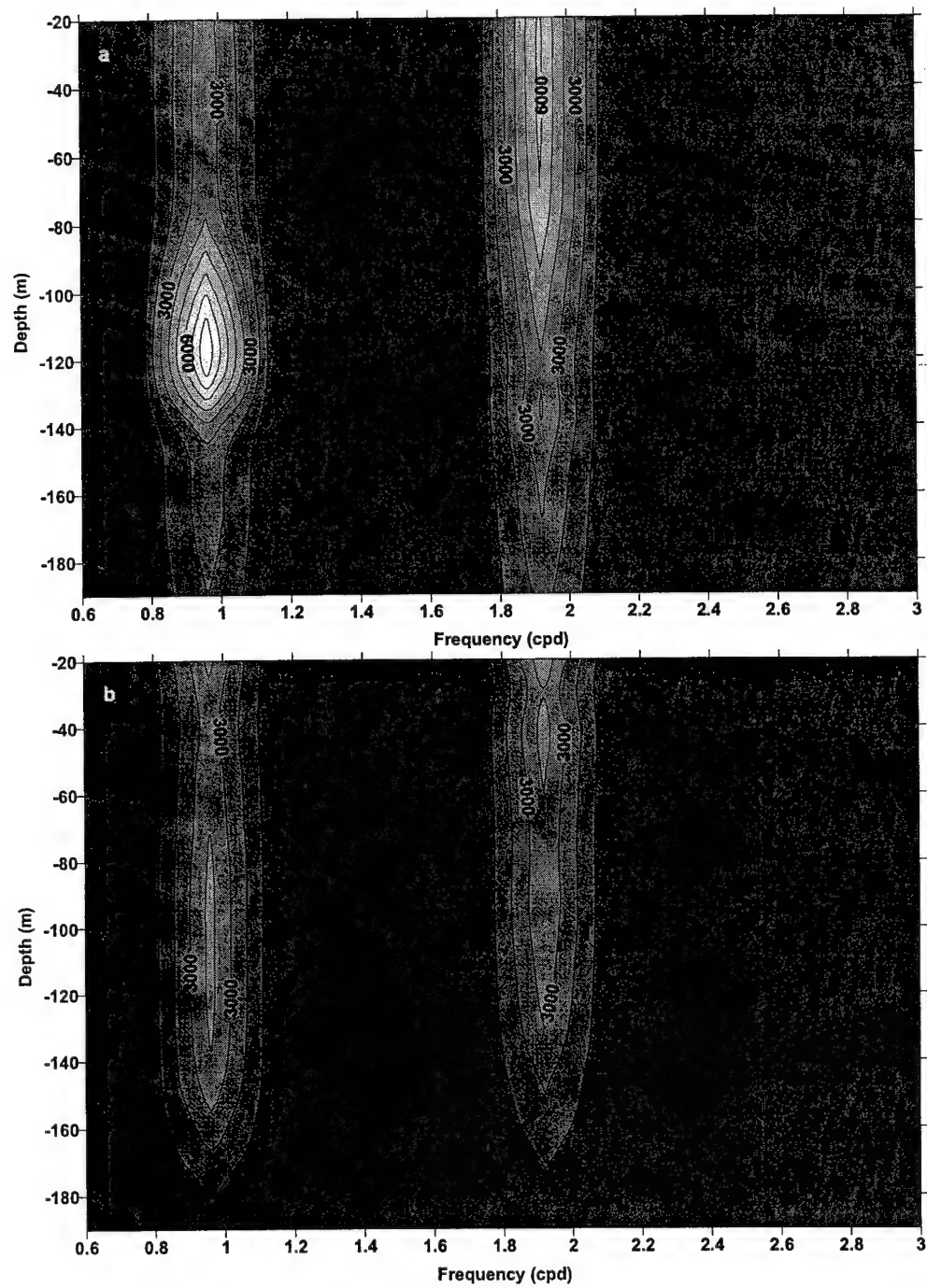
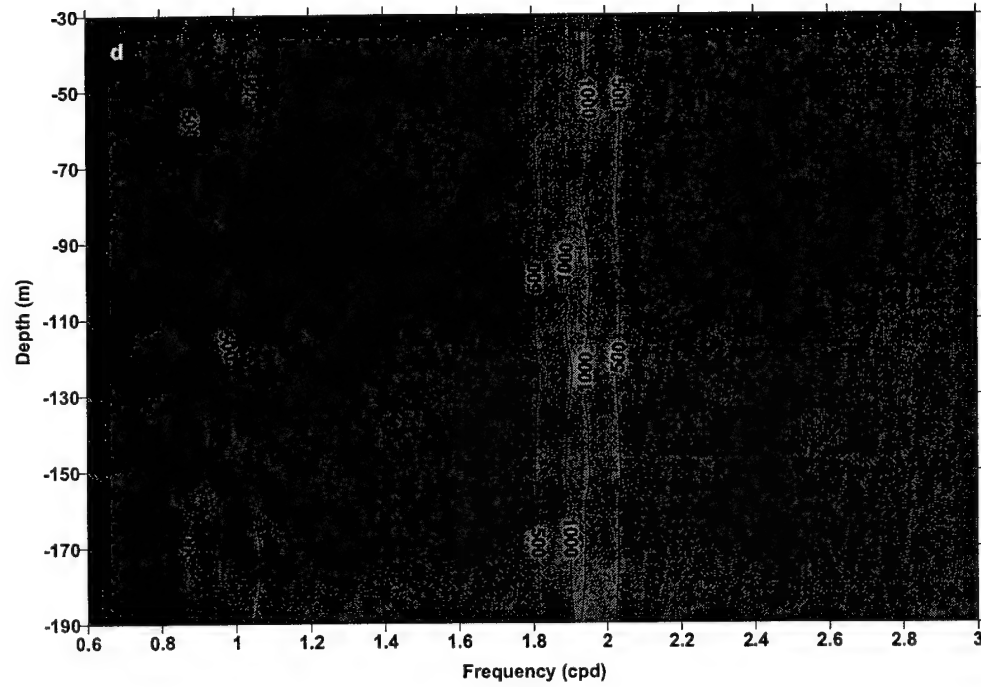
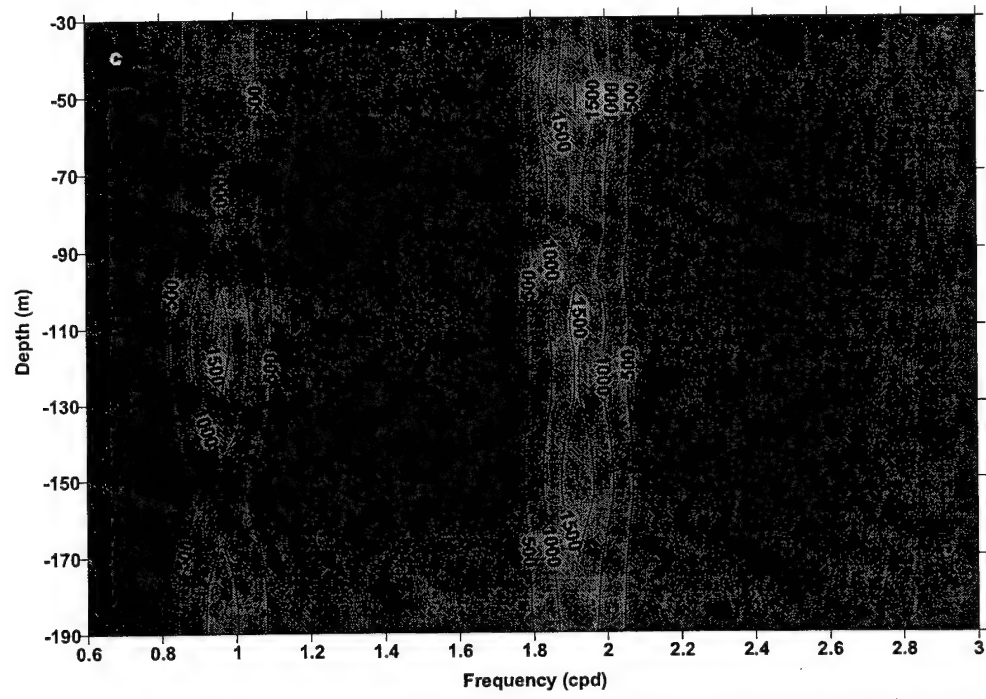
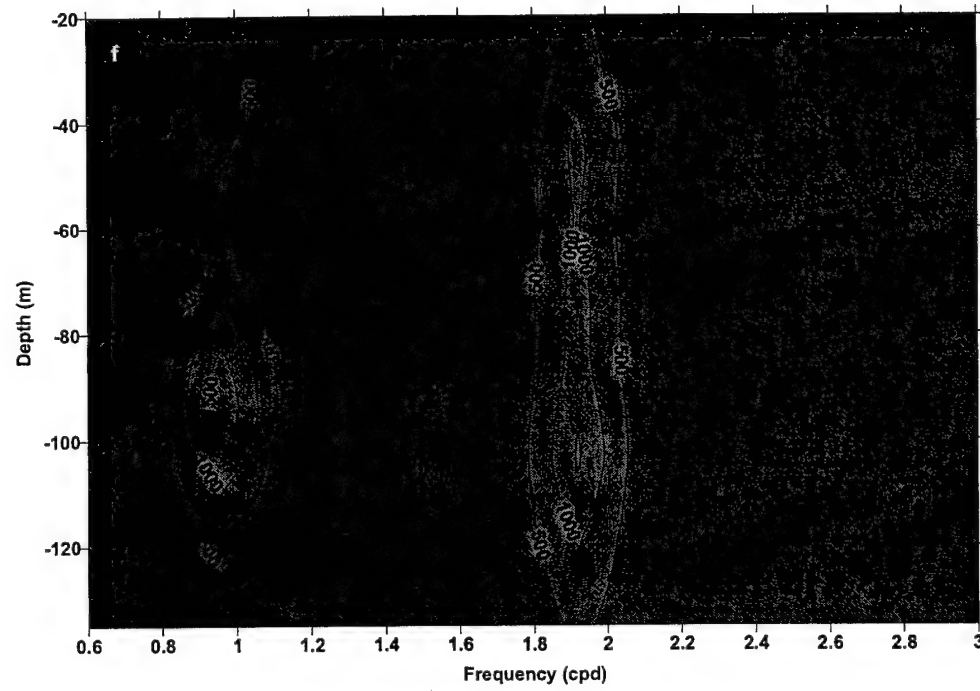
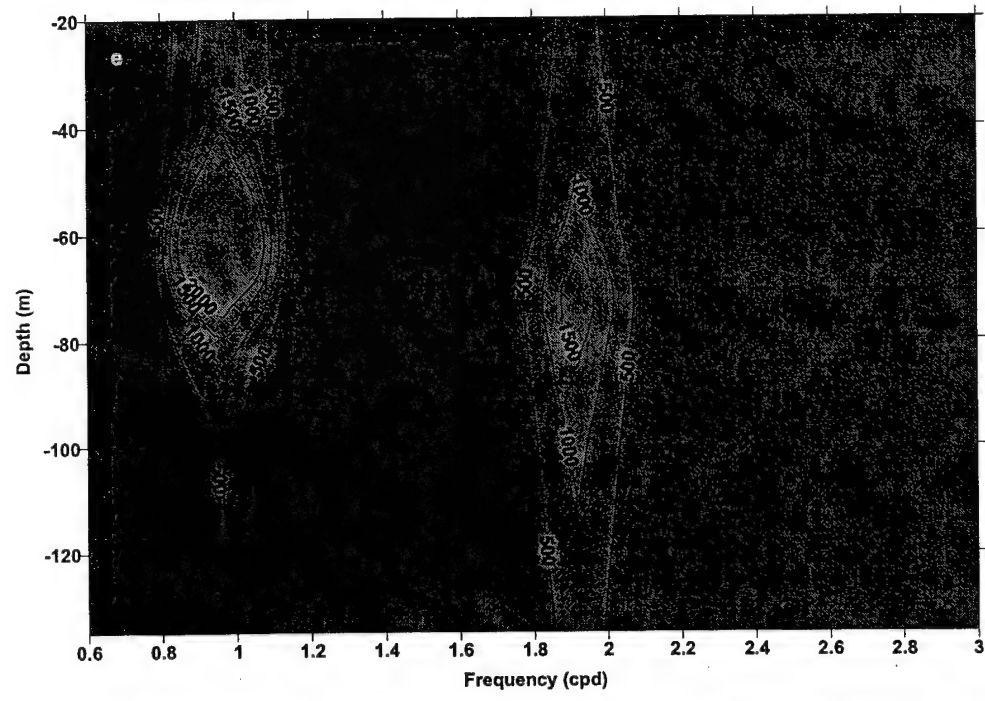


Figure 8. Spectrum ( $\text{cm}^2/\text{s}^2/\text{cpd}$ ) of the along-strait currents for spring tides calculated for the two-layer and three-layer flow regimes at A2b (a, b), C (c, d), and B2b (e, f) moorings.



(Figure 8 cont.)



(Figure 8 cont.)

summer flow regime neap-spring cycles were calculated. Figure 8 displays only frequencies between 0.6 cpd and 3 cpd because a limited length of the time series does not allow computing any reliable estimates for frequencies lower than 0.6. As for the higher frequencies ( $> 3$  cpd), they do not have spectra estimates that are higher than  $50 \text{ cm}^2/\text{s}^2/\text{cpd}$ .

The results displayed in Figure 8 clearly show that regardless of the seasonal flow and stratification phase, energy associated with the diurnal and semidiurnal tides at Perim Narrows (Figure 8a and 8b) is always much higher than that estimated in the middle of the Strait (Figure 8c and 8d) and near the Hanish Sill (Figure 8e and 8f). Furthermore, it is also evident that the energy distribution computed from the winter flow regime differs from that calculated from the summer flow regime, especially the distribution associated with the diurnal band.

For the winter flow, the diurnal energy distribution is fairly similar in the vertical at all three locations (Figures 8a, 8c, and 8e), and it has a distinct maximum located at about 120 m, 110 m, and 60 m (in the respective pycnocline layers) for A2b, C, and B2b moorings, respectively. Additionally, the lowest energy estimates are found near the bottom at A2b and B2b moorings; however, at C mooring, the minimum values are found near the surface. The energy distribution in the semidiurnal band differs between locations. At Perim Narrows, the maximum is near the surface. At C mooring, the energy is almost uniformly distributed with depth, while at the Hanish Sill, the semidiurnal energy has a distinct maximum at about 70 m. When the energy estimates are compared between the bands, the diurnal frequencies have larger values, especially at depths of the maxima at Perim Narrows and the Hanish Sill, whereas they are very similar at C mooring.

The diurnal energy computed from the current data collected during the three-layer flow regime is smaller than that found for the two-layer flow at all locations. Furthermore, this energy is fairly uniformly distributed with depth at the Perim Narrows (Figure 8b). At C mooring (Figure 8d), there is an indication of higher energy near the surface and at about 180 m, while at the Hanish Sill (Figure 8e) the energy associated with the diurnal frequency band shows a distinct maximum at about 90 m. A profile of the vertical distribution of the semidiurnal energy is quite similar to that found from the two-layer flow data subset whereas the actual values are slightly lower, especially at A2b and C moorings. At Perim Narrows, the energy maximum is again located near the surface, while at C mooring the energy is uniformly distributed with depth. Finally, at the Hanish Sill there is an indication of higher energy at about 100 m. The energy estimates compared between the principle tidal bands have similar values at Perim Narrows and the Hanish Sill, whereas they are slightly higher for the semidiurnal band at C mooring.

Figure 9 shows an example of the energy spectra for the neap tides computed from data at A2b mooring collected when the winter circulation prevailed in the Bab el Mandab Strait. It is very apparent that profiles of the vertical energy distribution at diurnal and semidiurnal frequencies are quite similar to those observed for the spring tide, but at the same time, there is a strong reduction in tidal energy for both principle tidal bands due to weaker forcing. Such a strong reduction of energy (50% or more) and almost identical vertical distributions to those found for the spring tides are also observed at this mooring for the energy estimates obtained from the summer flow and at the two other locations for both flow regimes.

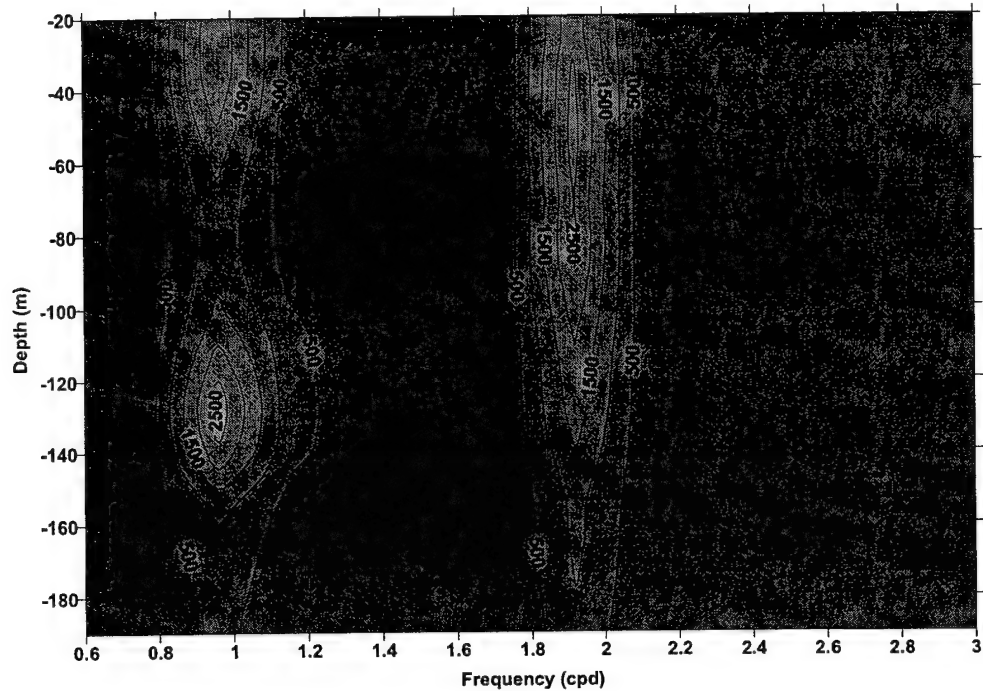


Figure 9. Spectrum ( $\text{cm}^2/\text{s}^2/\text{cpd}$ ) of the along-strait currents (A2b mooring) for neap tides computed for the two-layer flow regime.

### 3.3. Major diurnal and semidiurnal tidal current constituents

This section gives a description of tidal current ellipse parameters, which have been deduced by the use of harmonic analysis (Foremen, 1978) and verified by admittance calculations (Munk and Cartwright, 1966; Cartwright et al., 1969). The admittance computations used as an input reference pressure time series that were obtained from amplitudes and phases of the tidal elevations. The tidal elevation amplitudes and phases were computed from data gathered by nearby pressure gauges where more than 6 months of data were available, such that all the major constituents in the diurnal and semidiurnal bands are resolved. In the cases of Mocha and Assab, the reference series were computed from the tidal constants provided by the International Hydrographic Office. Both methods give very comparable results even for the short current time series.

### 3.3.1. Diurnal current constituents

Results of the harmonic analysis, as well as admittance, show that among diurnal components,  $K_1$ ,  $O_1$ , and  $P_1$  are the strongest tidal current constituents at all mooring sites. Among these three, the  $K_1$  is the most energetic constituent, with the  $O_1$  component next. To investigate changes of the diurnal components in the vertical and along-strait directions, the current ellipse parameters, which were obtained from harmonic analysis, such as the semimajor axis, semiminor axis, inclination angle of the semimajor axis (measured counterclockwise from East), and phase of the semimajor axis for these constituents will be examined next. In addition, the sign of the semiminor axis defines a sense of rotation of the tidal currents with a negative sign defining clockwise rotation and

a positive sign implying anticlockwise rotation. These parameters were computed from the data collected at A2b, C and B2b moorings. At each location, the analyzed data come from two different instruments: an ADCP current meter, which sampled the major part of the water column and an Aanderaa meter that was deployed below the ADCP current meter.

The average spectra of the neap-spring cycle suggest that the strength of the diurnal currents vary with depth, and this variability is very apparent, especially at Perim Narrows and the Hanish Sill where the strongest currents are observed in the respective pycnocline layers. In general, at these two locations, the strength of the diurnal currents not only varies with depth but also changes with time at the same depth. Figure 10 illustrates this variability, showing a series of the spectral estimates of the along-strait current components centered at 1 cpd and computed from 29-day non-overlapping subsets obtained from the data collected during three deployments near the Hanish Sill. It is very apparent that during the winter months (October through May), the highest energy

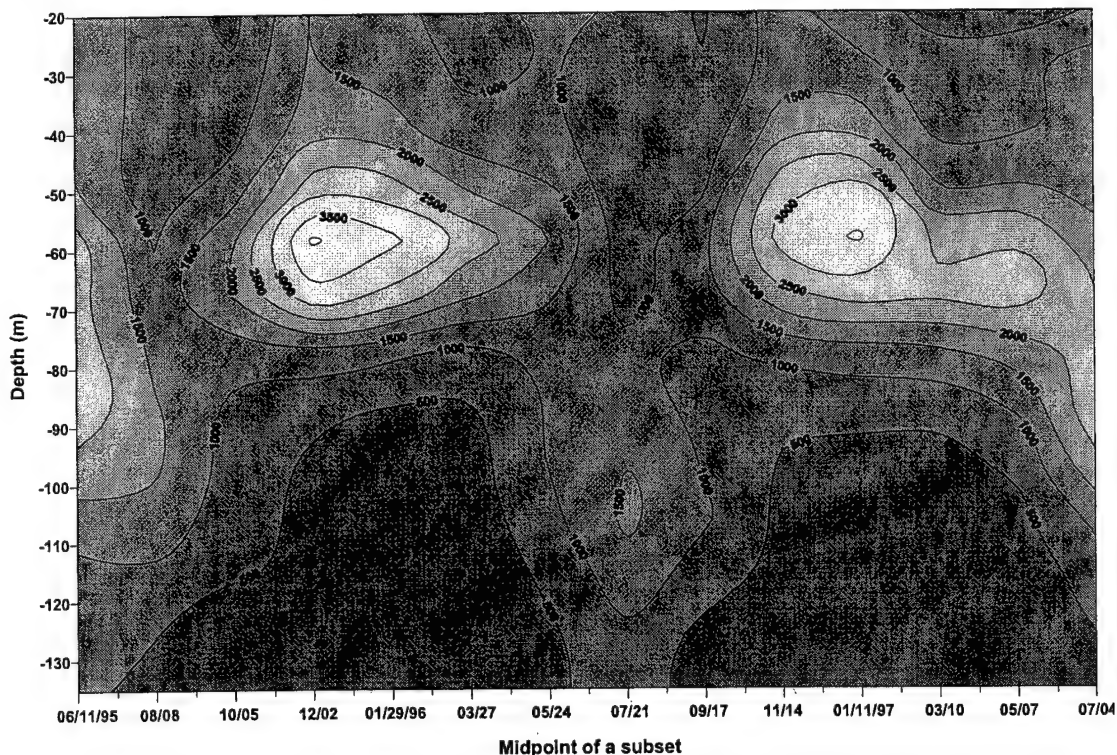


Figure 10. Spectral estimates ( $\text{cm}^2/\text{s}^2/\text{cpd}$ ) of the along-strait current component for the diurnal band centered at 1 cpd computed from 29 day non-overlapping subsets obtained from data collected at the Hanish Sill; the 95% confidence interval is between  $0.67S(f)$  and  $1.64S(f)$  where  $S(f)$  is the spectra estimate at frequency  $f$ .

(strongest currents) is found at  $\sim 60$  m whereas during the summer months (June through September), the maximum energy is usually located approximately between 95 m and 105 m. Similar changes with time and depth are observed for the spectra estimates at A2b mooring while at C mooring, seasonal variability is less pronounced but still present.

A similar conclusion about depth dependence of the diurnal current strength may be drawn when profiles of the semimajor axis of three diurnal constituents are scrutinized (Figures 11a through 11c). These profiles are fairly similar in shape at the same location, and they clearly show non-uniform distribution in the vertical with a distinct maximum at about 120 m and 60 m at Perim Narrows and the Hanish Sill, respectively. At C mooring, the distribution of the semimajor axis (Figure 11b) is rather uniform with depth. It is also apparent that the  $K_1$  constituent has the highest amplitudes in all three locations, which on average, are  $\sim 50\%$  and  $\sim 70\%$  larger than those found for  $O_1$  and  $P_1$ , respectively.

The mid-depth maxima at Perim Narrows and the Hanish Sill indicate that currents generated by the diurnal constituents are not barotropic in the Bab el Mandab

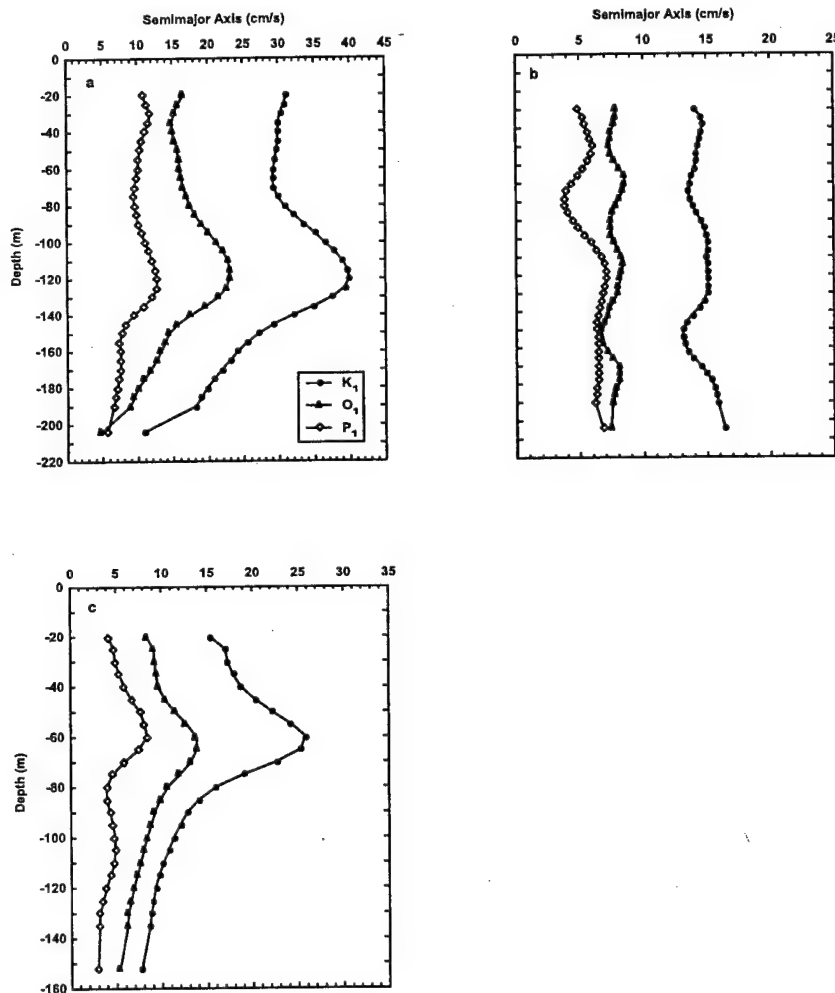


Figure 11. The vertical distribution of the semimajor axis of the  $K_1$ ,  $O_1$ , and  $P_1$  tidal constituents at (a) Perim Narrows (A2b mooring), (b) C mooring, and (c) the Hanish Sill (B2b mooring).

Strait, but they are a superposition of the barotropic and baroclinic current components. Figures 3a and 3b illustrate the density distribution changes with the changing seasonal

circulation. To investigate whether this seasonal variability of the stratification influences the ellipse parameters of the diurnal currents, these parameters will be examine separately for the two-layer (winter stratification) and three-layer flow (summer stratification) stratifications, and a discussion will be limited to the  $K_1$  constituent for two reasons: (1) this component is the most energetic in the Strait, and (2) profiles of the next two most energetic diurnal components ( $O_1$  and  $P_1$ ) display similar features to those observed for the  $K_1$  constituent.

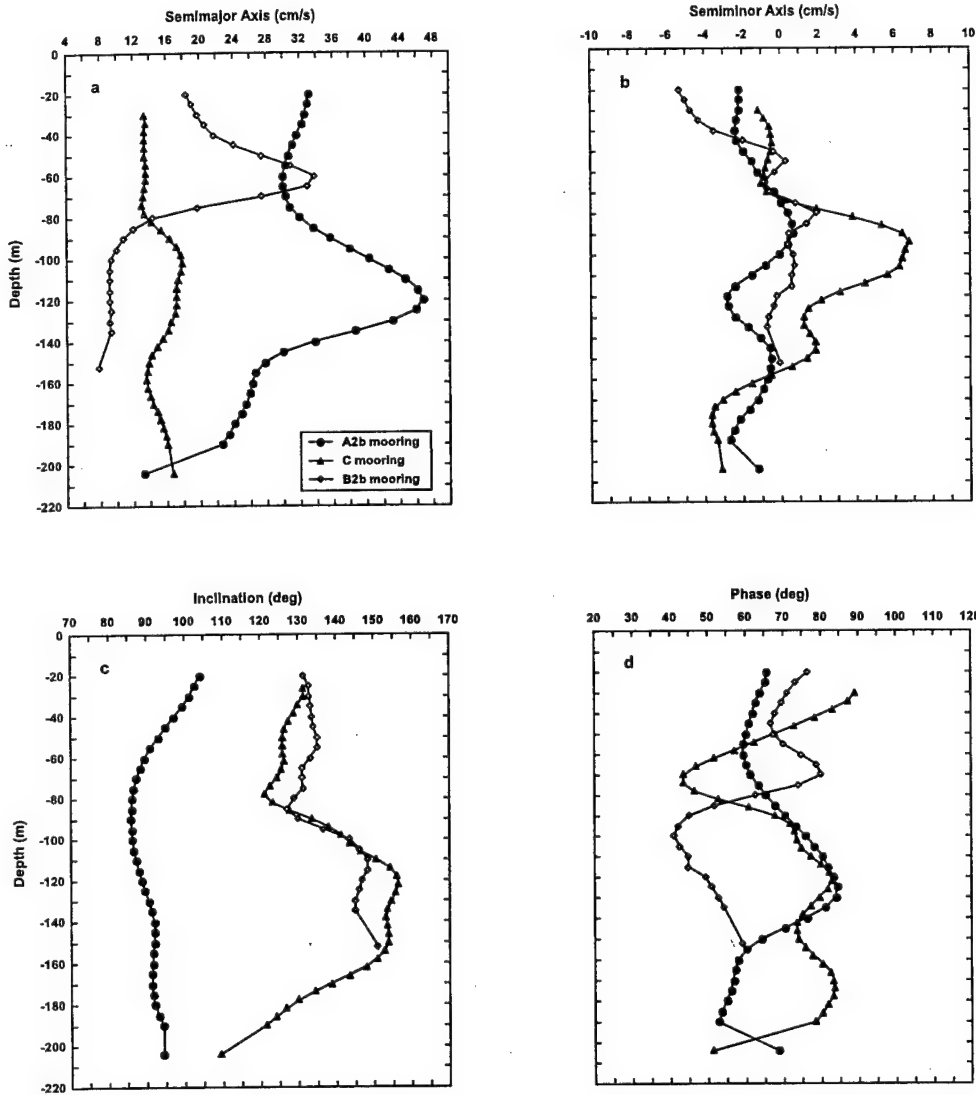


Figure 12. The vertical distribution of (a) semimajor axis, (b) semiminor axis, (c) inclination of the semimajor axis, and (d) phase for the  $K_1$  tidal constituent at Perim Narrows (A2b mooring), C mooring, and the Hanish Sill (B2b mooring) for the winter stratification.

Figure 12 illustrates the ellipse parameters of the  $K_1$  constituent computed from the data at the locations listed above for the time period from November 1, 1995 to March 28, 1996 (for the Aanderaa current meters the time series may be shorter) when the winter stratification associated with the two-layer circulation was present in the Strait. The semimajor axis distribution (Figure 12a) clearly shows that there is an attenuation of tidal amplitudes between Perim Narrows (A2b mooring) and C mooring. This decrease in amplitudes is probably due to an increasing width of the Strait, and it can be also partly due to dissipation of the tidal currents by bottom friction. Farther north, at the Hanish Sill, the amplitudes are generally smaller than those found at Perim Narrows; however, when they are compared with those of C mooring, the amplitudes of the semimajor axis have much larger values, between 40 m and 80 m. In the vertical, the profiles share common features: they all show that the semimajor axis is non-uniformly distributed with depth, and the largest amplitudes are found in the pycnocline regions at all locations considered. The non-uniform distributions are particularly noticeable at Perim Narrows and the Hanish Sill where the maximum computed values are 47 cm/s at 120 m and 34 cm/s at 60 m, respectively. In the middle of the Strait (C mooring), enhanced amplitudes with a maximum of 18 cm/s at 100 m are also present in the pycnocline region, but they are smaller than those at the other two locations. Above the pycnocline, the amplitudes of the semimajor axis are nearly constant, and this is very evident at A2b and C moorings where the layer with the inflowing Gulf of Aden waters is thick and consequently well-resolved by the presented data. Below the pycnocline, the semimajor axis either decreases with depth as observed at Perim Narrows or it is almost constant as observed at C mooring and the Hanish Sill.

The semiminor axis values of the  $K_1$  constituent (Figure 12b) are generally much smaller than those of the semimajor axis. The largest amplitudes for this axis are found at mid-depths at C mooring where they may be as high as 7 cm/s and in the upper part of the water column at B2b mooring where they vary between 5.5 cm/s at 20 m and 3.5 cm/s at 40 m. At the other depths at the same locations and at A2b mooring, the amplitudes of this axis are equal to 20% or less of the semimajor axis length. This large difference between semimajor and semiminor axes implies that the currents generated by  $K_1$  are nearly rectilinear. Furthermore, the inclination angle of the semimajor axis (Figure 12c) displays some variability that may be partly caused by the local topography, but, in general, these variations are rather small and it can be concluded that the maximum currents are aligned with the along-strait axis.

The phase distribution of the semimajor axis differs greatly from an idealistic progressive wave model in which an incoming tidal wave from the Gulf of Aden would produce the maximum tidal currents at Perim Narrows followed in turn at C mooring, and then at the Hanish Sill. Figure 12d illustrates that the phases at all locations are variable with depth, but they also share important characteristics, e.g. (1) the shape of their vertical profiles is very similar in the respective pycnocline regions, and (2) the maximum currents occur almost simultaneously in these pycnocline layers at all locations. Below the pycnocline layers, however, the profiles look dissimilar. In general, at these depths one rather expects to see a phase decrease due to friction as the currents approach the bottom. Such behavior is present at C mooring and Perim Narrows if the phase at 204 m is disregarded at Perim Narrows. In contrast, at the Hanish Sill, the phase is nearly constant.

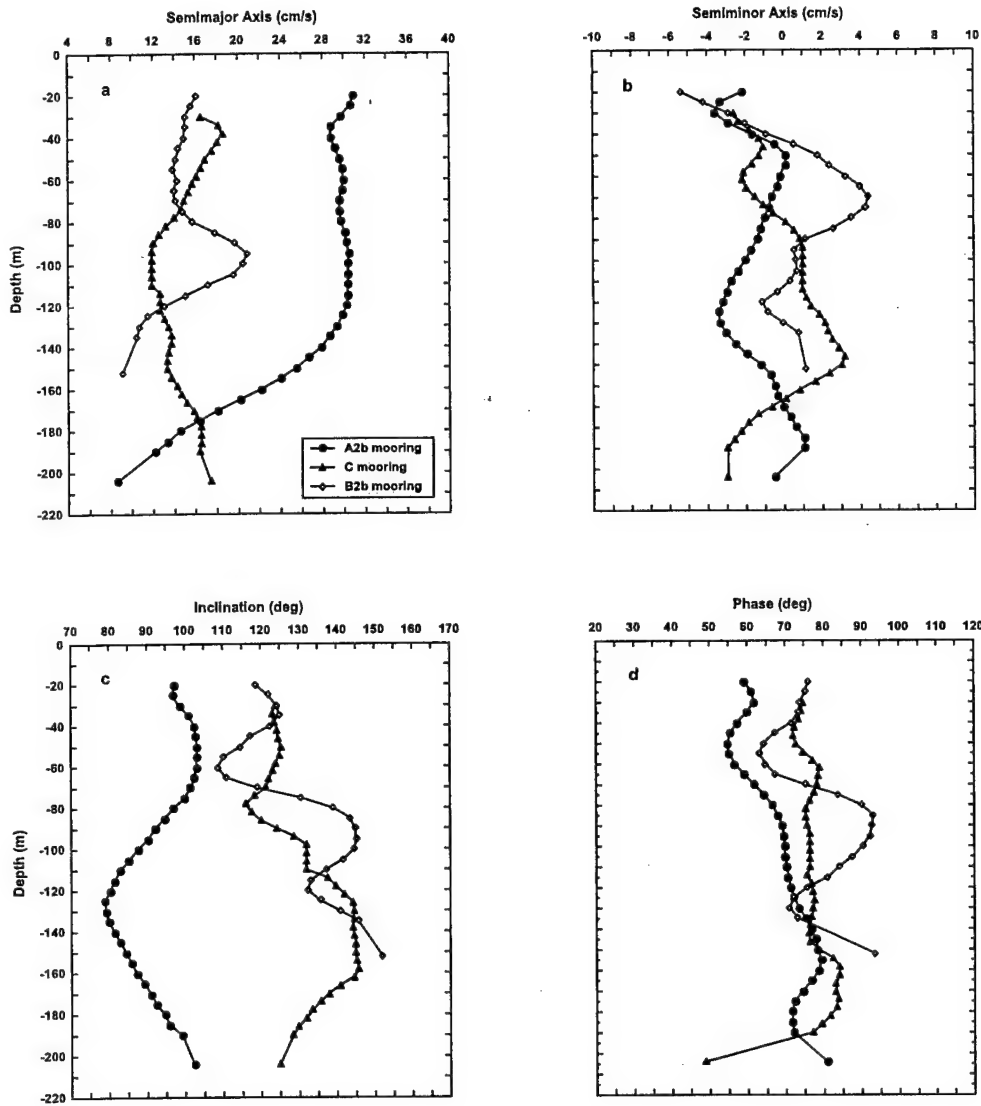


Figure 13. The vertical distribution of (a) semimajor axis, (b) semiminor axis, (c) inclination of the semimajor axis, and (d) phase for the  $K_1$  tidal constituent at Perim Narrows (A2b mooring), C mooring, and the Hanish Sill (B2b mooring) for the summer stratification.

The next figure (Figure 13) displays the ellipse parameters for the time period from June 30, 1995 to September 30, 1995 when the summer stratification associated with the three-layer circulation was observed in the Bab el Mandab Strait. Major changes are apparent in the vertical profiles of the semimajor axis at all moorings (Figure 13a). At Perim Narrows and C mooring, the mid-depth amplitude maxima observed during the winter stratification are not present for the summer stratification. At the Hanish Sill, the highest amplitudes with a maximum of  $\sim 21$  cm/s at 95 m are located deeper in the water column than they are for the winter stratification, and these enhanced currents are

confined to the depths of the lower pycnocline region (the pycnocline between the Red Sea waters and Gulf of Aden intermediate waters). In addition, at C mooring, the currents have larger amplitudes above 50 m and below 150 m, while at Perim Narrows, the amplitudes of the semimajor axis are almost constant and equal, on average, to 30 cm/s between 20 m and 120 m before being reduced to 8 cm/s near the bottom.

Similar to the semiminor axis values observed for the winter stratification, the amplitudes of this axis (Figure 13b) for the summer stratification are smaller than those of the semimajor axis at all moorings. When the amplitudes from the respective locations are compared for these two stratifications there is a little difference in length of this axis at Perim Narrows; however, this axis is reduced especially at mid-depths at C mooring, and it has larger amplitudes between 50 m and 90 m at the Hanish Sill for the summer stratification.

The inclination angle (Figure 13c) shows fairly similar distributions in the vertical to those presented earlier for the winter stratification. Furthermore, the phase of the semimajor axis (Figure 13d) differs significantly, especially at Perim Narrows where the phase generally increases with depth, and then below 160 m it diminishes with the exception at 204 m as the currents approach the bottom. At C mooring, there are also changes in a vertical profile of the phase that has nearly constant values between 30 m and 150 m and is equal, on average, to  $76^\circ$ . Between 160 m and 180 m (the lower pycnocline region) it has a maximum of  $\sim 85^\circ$  before being again reduced near the bottom to  $48^\circ$ . At the Hanish Sill, the phase profile is very comparable to that of the winter stratification, i.e., in the lower pycnocline regions the currents have larger phases.

To further investigate variability in the distribution of the  $K_1$  constituent in the Strait, the next two figures (Figures 14 and 15) show cross-sectional distributions of the ellipse parameters for this component at the section located just north of Perim Narrows. Results from the harmonic analysis done only on records from the second deployment were used in drawing these figures since this section, when compared with other sections available, had the best instrument coverage and data return. Figure 14 shows contours of all ellipse parameters for the winter stratification. It is apparent that in the deep channel (AA1 and AA2b moorings), these parameters show little variability. Features such as amplitude maximum and phase minimum in the pycnocline layer or small amplitudes of the semiminor axis are present at both moorings. The only major difference is present in the phase distribution; the phase at AA1 mooring seems to be  $10^\circ$  to  $15^\circ$  larger than the phase at the same depth at AA2b mooring.

The amplitudes of the semimajor axis for the summer stratification (Figure 15a, solid line) seem to be more evenly distributed in the section than those found for the winter stratification. There is an indication of the larger amplitudes with a maximum of 35.5 cm/s at depths below 140 m, and slightly higher amplitudes at depths above 40 m, which, as indicated by CTD casts, coincide with the upper and lower pycnocline regions, but these larger amplitudes are present only at AA1 mooring. The phase (Figure 15a, dashed line) shows similar features to those observed in the winter with earlier phases near the bottom and on the eastern side of the section, and later phases in the lower pycnocline layer that are even observed at AA2b mooring where the amplitudes do not display any enhancement. The inclination angle (Figure 15b, dashed line) and the length of the semiminor axis (Figure 15b, solid line) show some minor changes, but, in general, they both are fairly similarly distributed to those for the winter stratification.

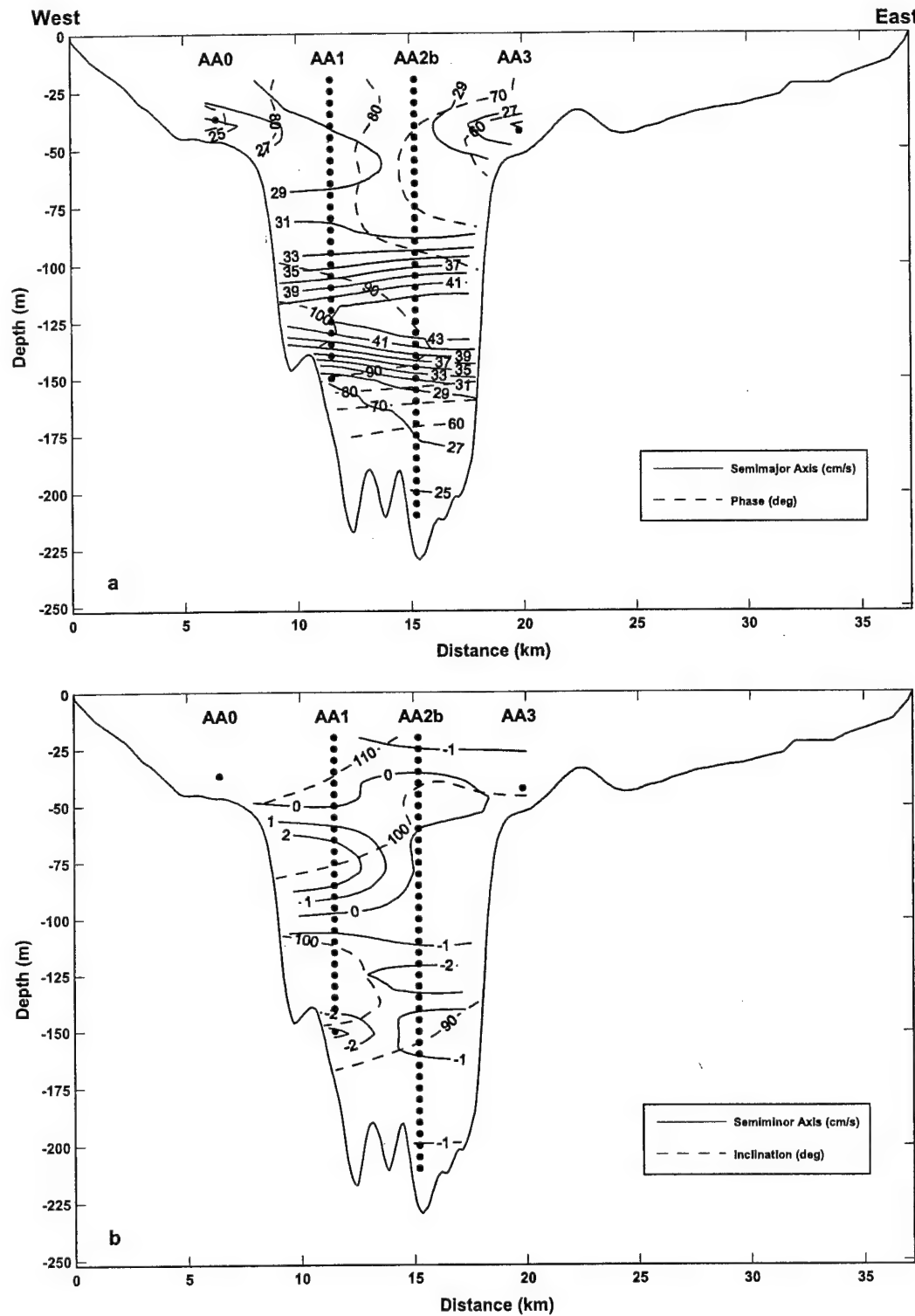


Figure 14. Contours of (a) the semimajor axis and phase, and (b) the semiminor axis and inclination angle of the  $K_1$  tidal constituent for the winter stratification at the Perim Narrows cross-section (dots denote depth levels of the measurements).

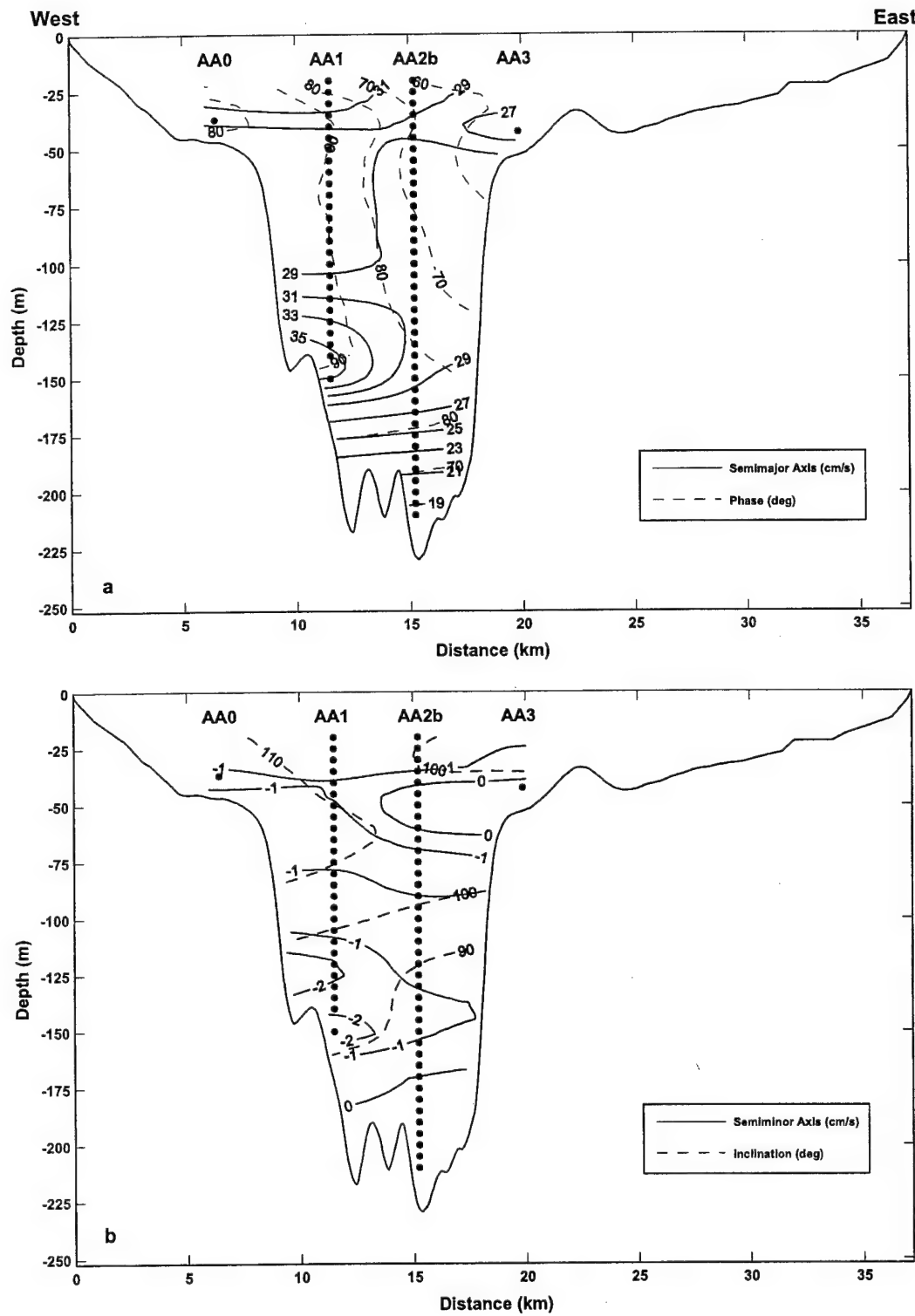


Figure 15. Contours of (a) the semimajor axis and phase, and (b) the semiminor axis and inclination angle of the  $K_1$  tidal constituent for the summer stratification at the Perim Narrows cross-section (dots denote depth levels of the measurements).

### 3.3.2. Semidiurnal current constituents

Among semidiurnal components, the  $M_2$ ,  $S_2$ , and  $N_2$  are the strongest tidal current constituents at all mooring sites. Among these three, the  $M_2$  is the most energetic component with the  $S_2$  and  $N_2$  being comparable to each other and much less energetic than the  $M_2$  (amplitudes of the  $M_2$  semimajor axis are, on average, 63% and 73% larger than those of the  $S_2$  and  $N_2$ , respectively). In addition, the spectra estimates from the 29-day non-overlapping subsets show some variability with depth and time for the semidiurnal band; therefore, vertical, along- and cross-strait distributions of the ellipse

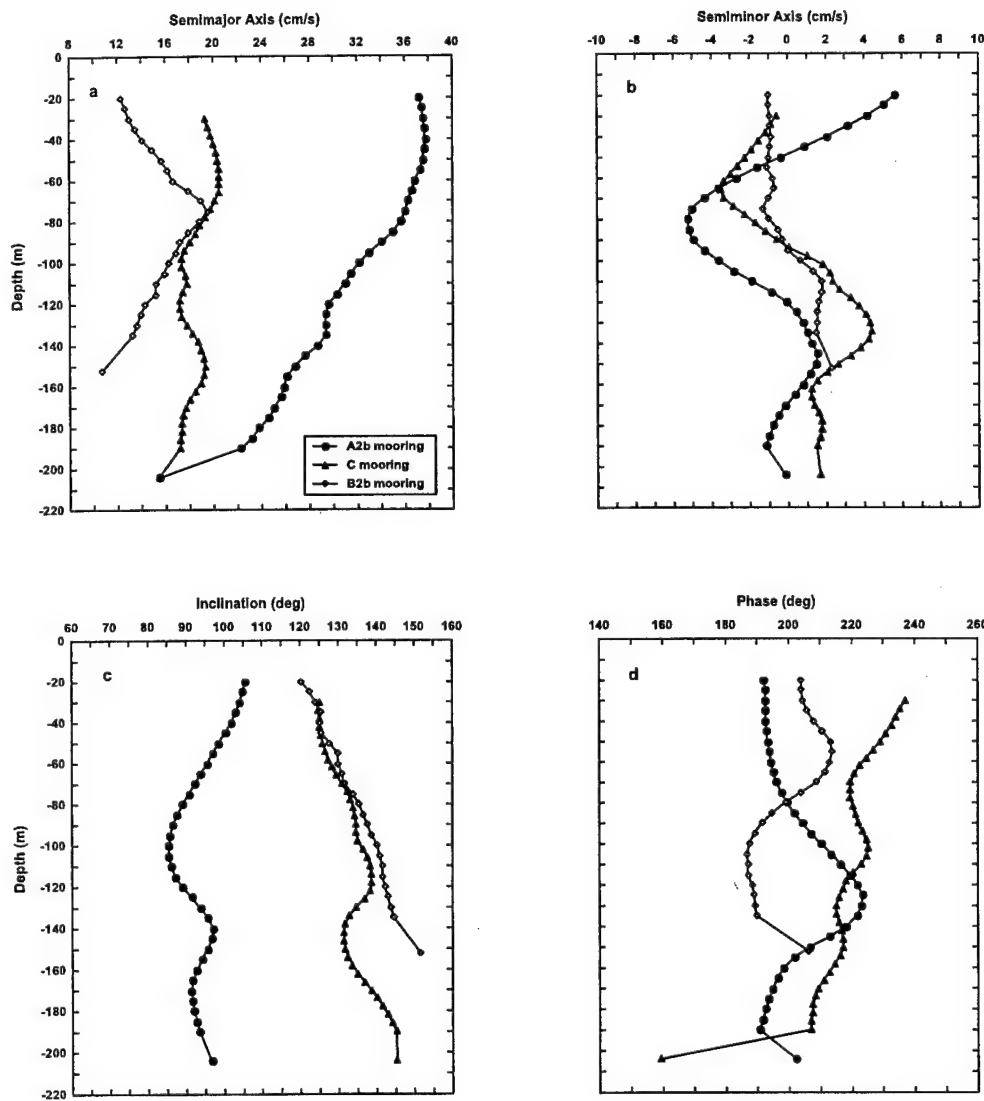


Figure 16. The vertical distribution of (a) the semimajor axis, (b) semiminor axis, (c) inclination of the semimajor axis, and (d) phase for the  $M_2$  tidal constituent at Perim Narrows (A2b mooring), C mooring, and the Hanish Sill (B2b mooring) for the winter stratification.

parameters will be examined separately for the stratifications associated with the two-layer and three-layer flow regimes. The discussion will be limited to the  $M_2$  component since the other two show similar features to those observed for the  $M_2$ .

The semimajor axes of the  $M_2$  component (Figure 16a) for the winter stratification show generally an attenuation of the current amplitudes from Perim Narrows to the Hanish Sill. In the vertical, the profiles of this axis exhibit a different distribution with depth at each location. At Perim Narrows, the amplitudes diminish with depth from their maximum value of 37 cm/s near the surface to 15 cm/s near the bottom, whereas at C mooring, they are nearly uniform with depth and, on average, equal to 18.5 cm/s throughout a major part of the water column before decreasing to their minimum of 15 cm/s near the bottom. Near the Hanish Sill, the vertical profile of the  $M_2$  semimajor axis is similar to the vertical profile of the  $K_1$  constituent for the same stratification configuration rather than to the semimajor axis profiles of the  $M_2$  component found at the two remaining locations. This profile shows a maximum of 19.5 cm/s at a depth of 75 m.

Values of the semiminor axis (Figure 16b) are at all depths much smaller than the corresponding values of the semimajor axis. They are only equal to 15% or less of the semimajor axis amplitudes at all three locations with the exception of the mid-depths at C mooring and near the bottom at the Hanish Sill where they are slightly higher and equal to 20% of those found for the semimajor axis. Such small amplitudes of this axis indicate that the currents generated by the  $M_2$  constituent, similar to those associated with the  $K_1$  component, are nearly rectilinear in the Bab el Mandab Strait. Furthermore, the inclination angle vertical profiles (Figure 16c) display little variability with depth and the values of these angles generally fluctuate around angles that the along-channel axis makes with the east at each location. In contrast, the phase (Figure 16d) is quite variable with depth. In the vertical, a shape of the phase profiles are very similar at Perim Narrows and the Hanish Sill showing that the currents have later phases in the pycnocline regions as opposed to those present above and below this layer with the exception of the phase at the last depth level at both moorings. In the middle of the Strait the phase profile is quite different, showing some variability, but, in general, the phase decreases gradually with increasing depth.

For the summer stratification, there are a few minor changes in vertical profiles of the  $M_2$  semimajor axis (Figure 17a). At A2b mooring, the major change is observed below 150 m where the amplitudes decrease more rapidly than those observed during the winter stratification. At C mooring, they are even more uniformly distributed with depth, and they are, on average, equal to 16 cm/s. At B2b mooring, the shape of the profile is fairly similar to that for the winter stratification; however, the highest amplitudes with a maximum of 19 cm/s are located lower in the water column at depths of the lower pycnocline layer. The semiminor axis amplitudes (Figure 17b) vary differently with depth for the summer stratification; however, similar to those observed in the winter, they are again much smaller than those of the semimajor axis at all respective depths and locations. Furthermore, the inclination (Figure 17c) is more variable with depth particularly at C mooring and the Hanish Sill locations; but, in general, these variations are rather small and it may be concluded that the maximum currents are aligned with the direction of the along-channel axis as they are for the winter stratification. The main changes in the phase vertical profiles (Figure 17d) are found at Perim Narrows where the phase does not have any mid-depth maximum but rather slightly fluctuates around 200°

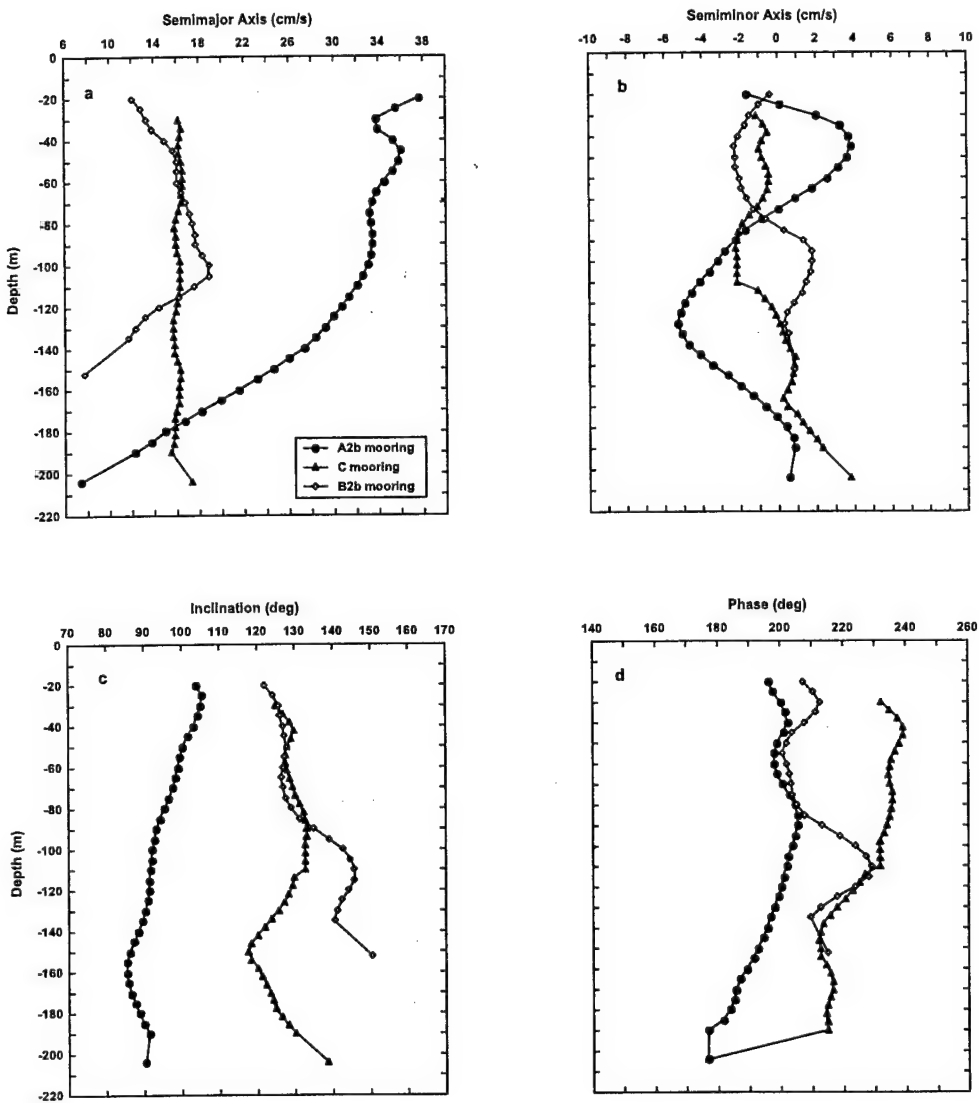


Figure 17. The vertical distribution of (a) semimajor axis, (b) semiminor axis, (c) inclination of the semimajor axis, and (d) phase for the  $M_2$  tidal constituent at Perim Narrows (A2b mooring), C mooring, and the Hanish Sill (B2b mooring) for the summer stratification.

between 20 m and 90 m before diminishing to  $176^\circ$  near the bottom. The phase distribution at C mooring is fairly similar to that associated with the winter stratification. Finally, at the Hanish Sill, the phase maximum is located in the lower pycnocline region.

Figures 18 and 19 display ellipse parameters of the  $M_2$  constituent along the Perim Narrows cross-section for the winter and summer stratifications, respectively. Similar to the figures of the  $K_1$  component, these plots are constructed from results obtained from data gathered during the second deployment. Figure 18a (solid line) shows that, for the winter stratification, the semimajor axis in the section does not diminish with depth as expected from the amplitude distribution of this constituent at A2b mooring but

instead it has a maximum of ~39 cm/s at 110 m. This maximum, however, is present only at AA1 mooring. From this maximum, the amplitudes diminish towards the bottom and with decreasing depth before increasing again near the surface. At another deep mooring (AA2b mooring), the amplitudes decrease with increasing depth from their maximum values (35 cm/s) near the surface to a minimum (> 25 cm/s) near the bottom. The  $M_2$  phase (Figure 18a, dashed line) displays similar features (maximum values in the pycnocline layer, minimum values near the surface and bottom) as the phase observed at A2b mooring. Furthermore, this distribution of the phase also indicates that currents on the east side of the Strait lead those on the west by ~ 1 hour, and this feature is especially clearly visible between 20 m and 150 m at AA1 and AA2b moorings. The semiminor axis (Figure 18b, solid line) of the  $M_2$  has again much lower values than those of the semimajor at all depths with a maximum computed value of 5.5 cm/s. Finally, the inclination angle (Figure 18b, dashed line) does not vary much in the cross-section, and the currents are generally aligned with the along-strait axis.

For the summer stratification, as opposed to the winter stratification distribution, the amplitudes of the semimajor axis do not show any mid-depth maximum (Figure 19a, solid line). These amplitudes vary between 22 cm/s and 38 cm/s, and they diminish with depth from their maximum value near the surface to their minimum values near the bottom in the deepest part of the section. This decrease is more gradual at AA2b mooring than that observed at another mooring located in the deep part of the section (AA1 mooring). The phases (Figure 19a, dashed line) display similar behavior to those found for the winter stratification in the sense that the earlier (lower) phases are present near the bottom, and later (higher) phases on the west side of the section, as well as slightly higher values, are found at ~ 130 m, especially apparent at AA1 mooring. Furthermore, the amplitudes of the semiminor axis (Figure 19b, solid line) are small and do not exceed 5.5 cm/s. The inclination (Figure 19b, dashed line) shows very similar behavior to that found for the winter stratification.

### **3.3.3. Comparison of the vertical distributions of tidal currents observed in the Bab el Mandab Strait with the existing models**

The vertical structure of tidal current ellipses in a homogeneous unbounded sea under conditions of various friction and eddy viscosity formulations was analyzed in terms of the bottom Ekman layer dynamics by Prandle (1982). He showed that as the height above the bottom increases: (1) the semimajor axis increases rapidly near the bottom and progressively less rapidly in the upper part of the flow; (2) the eccentricity, which is a ratio of the semiminor axis to the semimajor one, becomes progressively smaller, and then it is almost constant higher in the water column; (3) the phase of the maximum current becomes gradually greater for tidal frequencies larger than the inertial, and smaller if the tidal frequency is smaller than the inertial; (4) the rotation of the inclination angle depends highly on a parameterization of eddy viscosity; (5) the sense of rotation of the tidal currents near the bottom is anticlockwise; however, higher in the water column, it again depends on the parameterization of eddy viscosity.

Yasuda (1987) used a similar linear model to study tidal ellipse parameters in homogeneous waters; however, in his studies, he also included horizontal boundaries. In

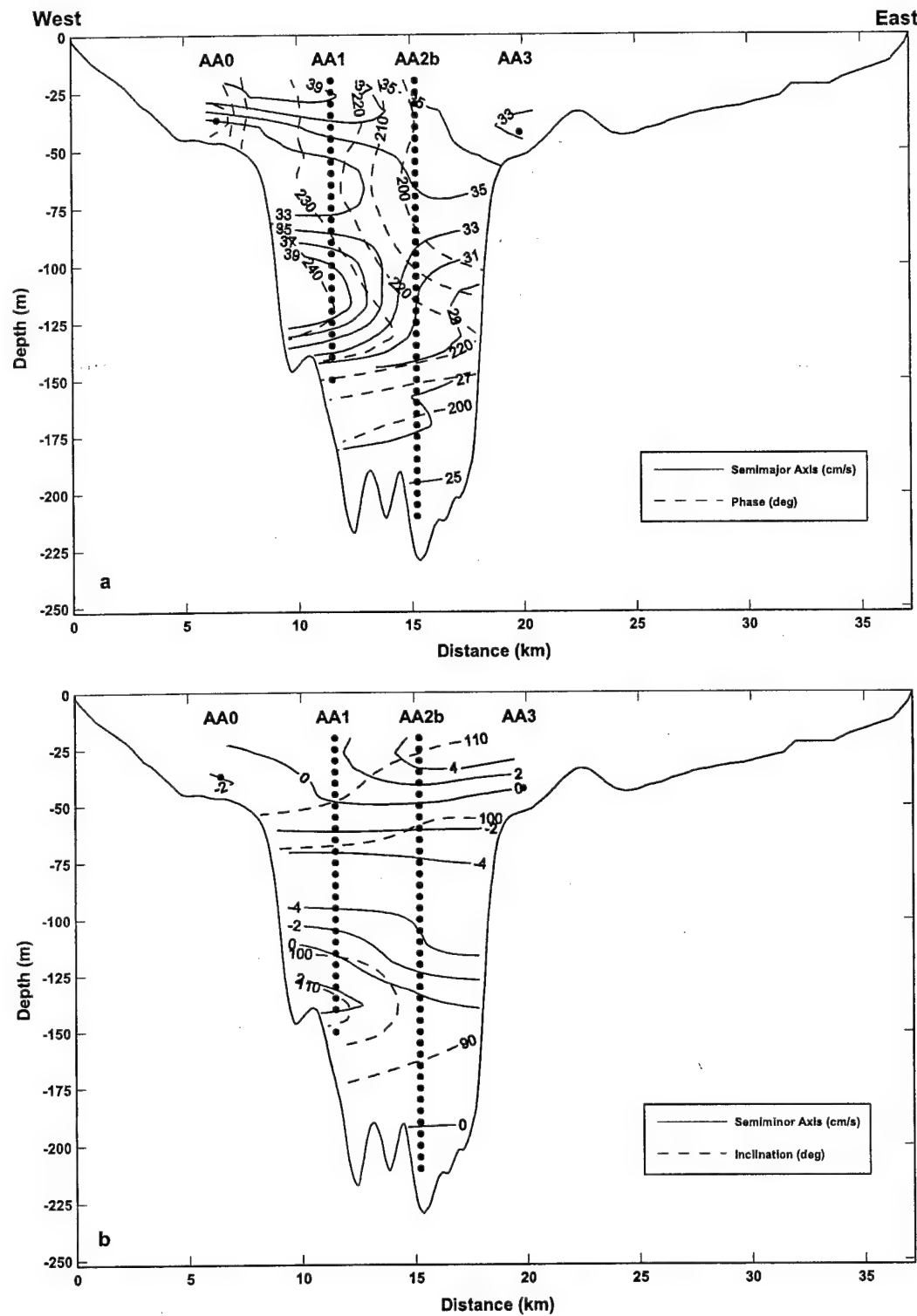


Figure 18. Contours of (a) the semimajor axis and phase, and (b) the semiminor axis and inclination angle of the  $M_2$  tidal constituent for the winter stratification at the Perim Narrows cross-section (dots denote depth levels of the measurements).

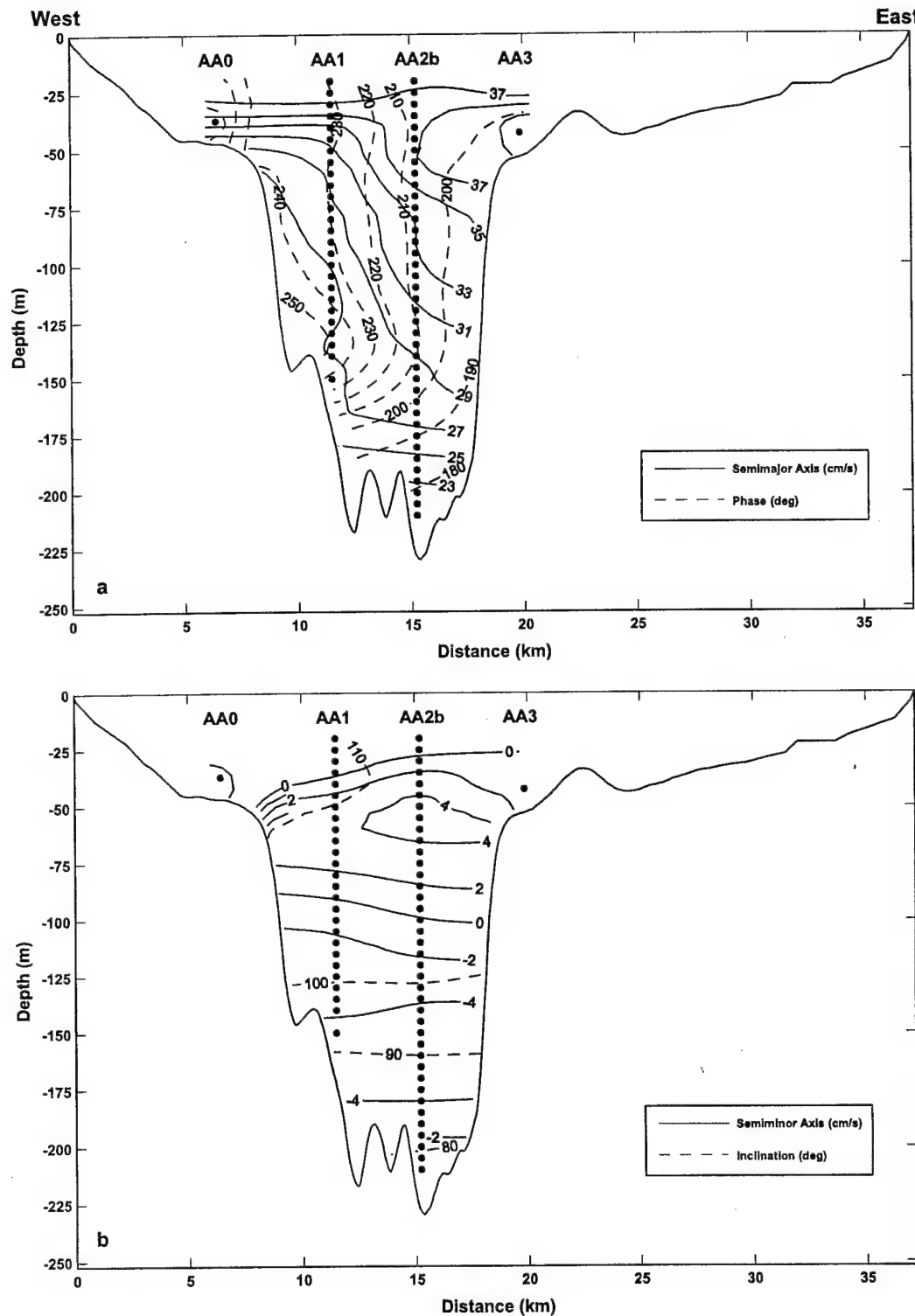


Figure 19. Contours of (a) the semimajor axis and phase, and (b) the semiminor axis and inclination angle of the  $M_2$  tidal constituent for the summer stratification at the Perim Narrows cross-section (dots denote depth levels of the measurements).

general, his findings regarding the distribution of the semimajor axis and phase for the narrow basin are very similar to those reported for the open ocean by Prandle (1982) in the case of a tidal frequency higher than the inertial frequency and constant eddy viscosity. The rotation of the inclination near the bottom, though, is different; in the case of a bounded basin, this angle rotates anticlockwise as opposed to the clockwise rotation found by Prandle (1982) for an open basin. There is also a difference in the current rotation; for a bounded basin case, currents rotate anticlockwise near the bottom and clockwise away from it. Yasuda also concluded that the eccentricity is larger near the bottom than away from it so the currents are nearly rectilinear above the bottom boundary layer.

Mass and van Haren (1987) examined effects of friction in stratified and unstratified open oceans on rotary tidal current components (anticlockwise and clockwise). The amplitude sum and difference of these components are equal to the semimajor and semiminor axis, respectively; whereas the inclination and phase are equal to half of the sum and difference of the phases of the clockwise and anticlockwise components, respectively. They showed that in the case of a stratified ocean there is a maximum of the  $M_2$  current amplitude and phase in the interior of the pycnocline; however, these changes are only found for the clockwise rotary component of the tidal

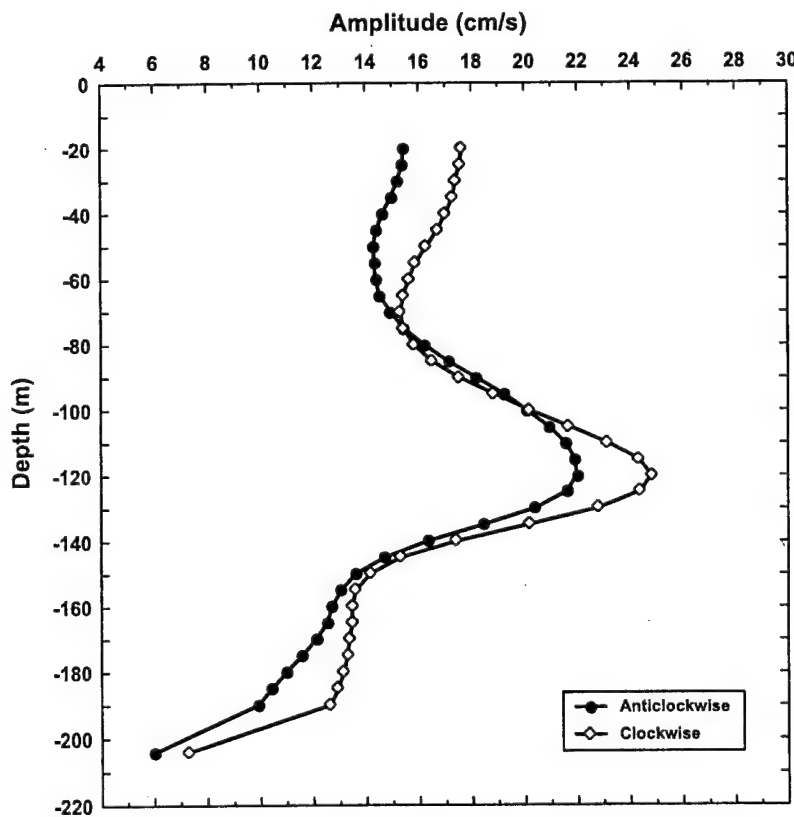


Figure 20. Amplitudes of the clockwise and anticlockwise rotary current components of the  $K_1$  tidal component computed from the observations collected at A2b mooring during the winter stratification period.

current. The anticyclonic component is unaffected by the stratification because its thin bottom boundary layer lies well below the pycnocline. Similar conclusions regarding maxima of the tidal currents occurring at the depth of the interface in the case of a two-layer ocean were obtained by Prinsenberg and Bennett (1989).

It is rather difficult to choose one model from the existing models and compare its results to the observed vertical profiles of the ellipse parameters of the  $K_1$  or  $M_2$  constituents in the Bab el Mandab Strait because none of them includes simultaneously lateral boundaries and changing vertical density distribution. It would be informative, however, to compare common model results with the vertical profiles observed in the Strait. To begin with, the model considered by Mass and van Haren (1987) seems to be a good approximation for the  $K_1$  component and the winter stratification, but, as Figure 20 shows, both  $K_1$  rotary components (A2b mooring) have a maximum in the pycnocline region so they both appear to be affected by the stratification. The stratification also appears to have an effect on the phases of both components. This different behavior from that reported by Mass and van Haren (1987) may result, for instance, from the fact that their model does not include horizontal boundaries and/or that the bottom boundary layer of the anticyclonic rotary component is thick enough to interact with the pycnocline region. The latter reason may be the proper explanation of the different (than expected) distribution of the  $K_1$  anticyclonic rotary component at Perim Narrows where the thickness of its bottom boundary layer is on the order of 100 m (if estimated for the eddy viscosity of  $0.55 \text{ m}^2/\text{s}$  that was calculated from the formula given by Csanady (1976)).

A common finding for all models is a sharp decrease of the semimajor axis in the bottom boundary layer due to friction. Such behavior of the semimajor axis is observed, for example, for the  $K_1$  and  $M_2$  at Perim Narrows central moorings or for the  $M_2$  at the Hanish Sill where their bottom boundary layers are probably well resolved by the measurements. The sharp decrease is not present for both tidal constituents at C mooring or the  $K_1$  component at the Hanish Sill where the currents generated by these constituents are rather weak in the lower part of the water column. Prandle (1982) showed that less energetic flows are modified by the friction closer to the bottom so their bottom boundary layer may not be resolved by the present observations.

All these models show that the phase of the tidal currents with frequency higher than the inertial decreases rapidly near the bottom. This seems to agree fairly well with the observations for both tidal components at C and Perim Narrows moorings (A2b, AA1, AA2b) if the phase at the last depth level, which shows a sharp increase near the bottom, is excluded at A2b mooring. This unexpected increase may be partly caused by the fact that the phase at this depth was computed from a time series that is shorter than those used for the phase computation at depths above, and that the observations were collected by a different instrument (an Aanderaa meter not an ADCP current meter). Additionally, the phase standard errors for both constituents at this depth are larger than those found for the phase at all depths above, and for the winter stratification, they are  $8^\circ$  and  $3^\circ$  for the  $K_1$  and  $M_2$  constituents, respectively. Therefore, phase confidence intervals are quite large and, for instance, a 95% confidence interval for the  $K_1$  is between  $53^\circ$  and  $85^\circ$  with the lower limit fitting fairly well to the expected decrease of the phase with depth. Large errors are also found for the phases computed from the time series collected by another Aanderaa meter deployed at B2b mooring. At the Hanish Sill, even if the phase at the last depth level is disregarded due to the large errors, the phase decrease for

the  $K_1$  is still not present, and this may be partly due to the fact that the bottom boundary layer is not well resolved by the observations at this location.

Yasuda's model (1987) predicts anticlockwise rotation of the currents near the bottom (the bottom boundary layer) and clockwise above. It is rather difficult to discuss the sense of rotation of the tidal current in the Strait because the semiminor axis is often very small ( $< 3$  cm/s) and, additionally, its error can be as large as the length of this axis (see Appendix B for errors); however, at depths where this axis is much larger than its error, the sense of rotation is quite variable, and it seems to depend on the location, constituent, and stratification so such a current rotation as reported by Yasuda is not consistently present in the Bab el Mandab Strait. Yasuda also concluded that currents are nearly rectilinear in a bounded basin, and this agrees very well with the observations. However, his conclusion regarding the eccentricity does not agree with the observations because it can be as high away from the bottom as it is near it. Finally, he pointed out that the inclination angle veers anticlockwise near the bottom. In the Bab el Mandab Strait such a rotation is not observed for the majority of the analyzed profiles.

### 3.4. Relation between tidal elevation and currents

Results presented earlier clearly show that, regardless of the frequency, the elevation amplitudes of the major tidal constituents vary in the Bab el Mandab Strait with the greatest amplitudes found at its southern end. Similar behavior is observed for the amplitudes of the tidal currents. However, phase variability, especially for tidal elevation components, depends on frequency. For the diurnal constituents of the elevation and currents, phases vary little between different locations; this is also true for the semidiurnal components of the currents; however, the elevation phase of the same constituents changes greatly indicating approximately a six-hour difference between a maximum elevation at Perim Narrows and the Hanish Sill.

To investigate the relationship between tidal elevations and currents, coherence and phase between the water elevation and along-strait current components at Perim Narrows and the Hanish Sill were estimated. Results from this analysis indicate that, regardless of the stratification, the tidal elevations and currents are very coherent for both tidal bands and, at all depths, coherence squared is higher than 0.80 (the 95 % confidence level is equal to 0.1 for all computed coherence squared values) at Perim Narrows. At the Hanish Sill, higher values of coherence squared ( $> 0.80$ ) are found in the upper 80 m and below 140 m for both tidal bands. Between these two depths, however, coherence squared drops to 0.70 and 0.75 for the diurnal and semidiurnal frequencies, respectively. In addition, these results also indicate that, at Perim Narrows (A2b and AA2b moorings), the elevation leads the currents for the diurnal band and the time lag is between 4 and 9 hours (the average time lag is 6.5 hours). For the semidiurnal frequency, the elevation precedes again the currents at Perim Narrows with a time lag between 2.8 and 4.5 hours (the average time lag is 3.5 hours). At the Hanish Sill, the currents in the diurnal band lag the elevation and the time lag varies between 3.9 and 8 hours (the average time lag is 5.1 hours). For the semidiurnal band, however, the relation is reversed and the currents lead the elevation with the time lead, on average, equal to 3.1 hours.

The phase lag between the semidiurnal elevations and currents, small differences between current phase, nearly a  $\sim 180^\circ$  phase difference between the elevations at Perim Narrows and the Hanish Sill, and the existence of the nodal zone for the semidiurnal tides

(Vercelli, 1925; Defant, 1961) seem to imply that the semidiurnal tidal wave has the nature of a standing wave in the Bab el Mandab Strait. Based solely on the phase relationship between the elevation and currents, a similar conclusion can be drawn about the diurnal tides; however, such an interpretation can be erroneous. Tejedor, et al. (1999) showed that in the Strait of Gibraltar, variable geometry can be partly responsible for

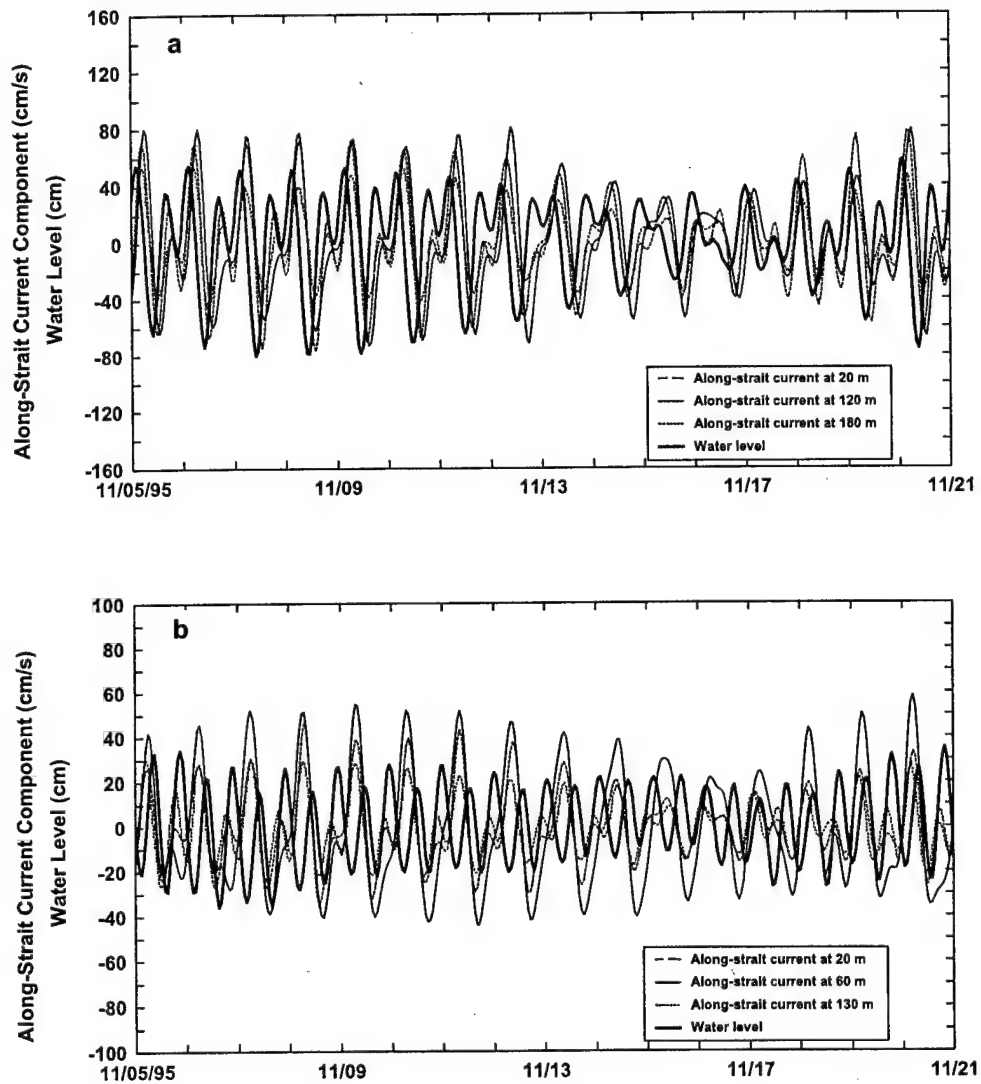


Figure 21. Current and water level fluctuations (40-hour high passed-filtered data) at (a) Perim Narrows and (b) the Hanish Sill.

modifying characteristics of a progressive wave of the  $M_2$  frequency so that a phase difference between tidal velocity and elevation is  $\sim 90^\circ$  ( $\approx 3$  hours). They used a dimensionless parameter, which depends on tidal frequency and variability of the cross-sectional area and width along a strait, to show that geometry can be responsible for this phase difference. This parameter was estimated for the  $K_1$  frequency in the Bab el

Mandab Strait. Its absolute values vary between 1 and 28.33 in the Strait, and they are usually much larger than 1 (there are only two cases when they are equal to 1) as they should be if the effects of geometry are important; therefore, it can be concluded that the geometry of the Bab el Mandab Strait might be partly responsible for the observed phase lag between the diurnal currents and elevations, and that the diurnal tide should not be characterized as a standing wave.

Figures 21a and 21b display the current (A2b and B2b moorings) and elevation (G109 and G108) data. Based on the variance calculations, the fluctuations of the tidal elevation and currents near Perim Narrows can be characterized as a mixed type. Near the Hanish Sill, however, the elevation variations are strongly semidiurnal, but the current regime is mixed. These different regimes of the elevations and currents can be explained by a simple model. This model assumes that the currents in the Bab el Mandab Strait are solely driven by the along-strait elevation gradient. This gradient contains both semidiurnal and diurnal fluctuations because the diurnal oscillations are very strong in the southern part of the Strait, and they are able to generate a large enough gradient so that one can observe quite strong diurnal tidal currents at the northern end even if the elevation fluctuations are dominated by the semidiurnal tides.

Finally, Figures 22a through 22d show examples of the tidal current velocity distribution for the Perim Narrows cross-section. It displays the along-strait tidal currents that, superimposed on the subtidal flow, might be observed at this cross-section at four different times of the spring tides: 4 hours after HHW (higher high water) and LLW (lower low water), 3 hours after LHW (lower high water) and HLW (higher low water) at the coast, and are generated by the major tidal components ( $K_1$ ,  $O_1$ ,  $P_1$ ,  $M_2$ ,  $S_2$ , and  $N_2$ ). The along-strait components for this plot were calculated from the ellipse parameters obtained from the data gathered during the winter stratification. Four hours after HHW at the coast, the currents are in a maximum flood stage flowing into the Strait (Figure 22a). The highest speeds of the along-strait component are observed near the surface (80 cm/s) and approximately in the middle of the water column with maximum values a little above 100 cm/s at 120 m. Four hours after LLW (Figure 22b), the flow is reversed in the entire cross-section, and the outflow speeds are lower than those of the previous stage; however, similar to the previous stage, the strongest currents are located at mid-depths. In addition, there is also an indication that during the first ebb, the currents above 150 m are stronger on the west side of the Strait. During the second flood (Figure 22c), the flow is not reversed in the entire section. There is inflow in the upper 90 m and below 150 m; however, between these depths the currents flow out of the Strait. The exact depths where the outflow is present differ between the east and west sides of the cross-section. These negative speeds are weak, but the flow consistently keeps the direction as drawn in Figure 22c until the next ebb (Figure 22d) when the currents in the entire cross-section flow out of the Strait.

### 3.5. Tidal transport

The good data coverage of the Perim Narrows cross-section allowed computing estimates of the tidal transport associated with the major diurnal and semidiurnal constituents. The transport was found for a slightly narrower section that extends between the 6th and 21st km. The narrowing of the section was dictated by a lack of data from its shallowest parts. The total section area, including these shallow parts is  $2.4 \text{ km}^2$  and the

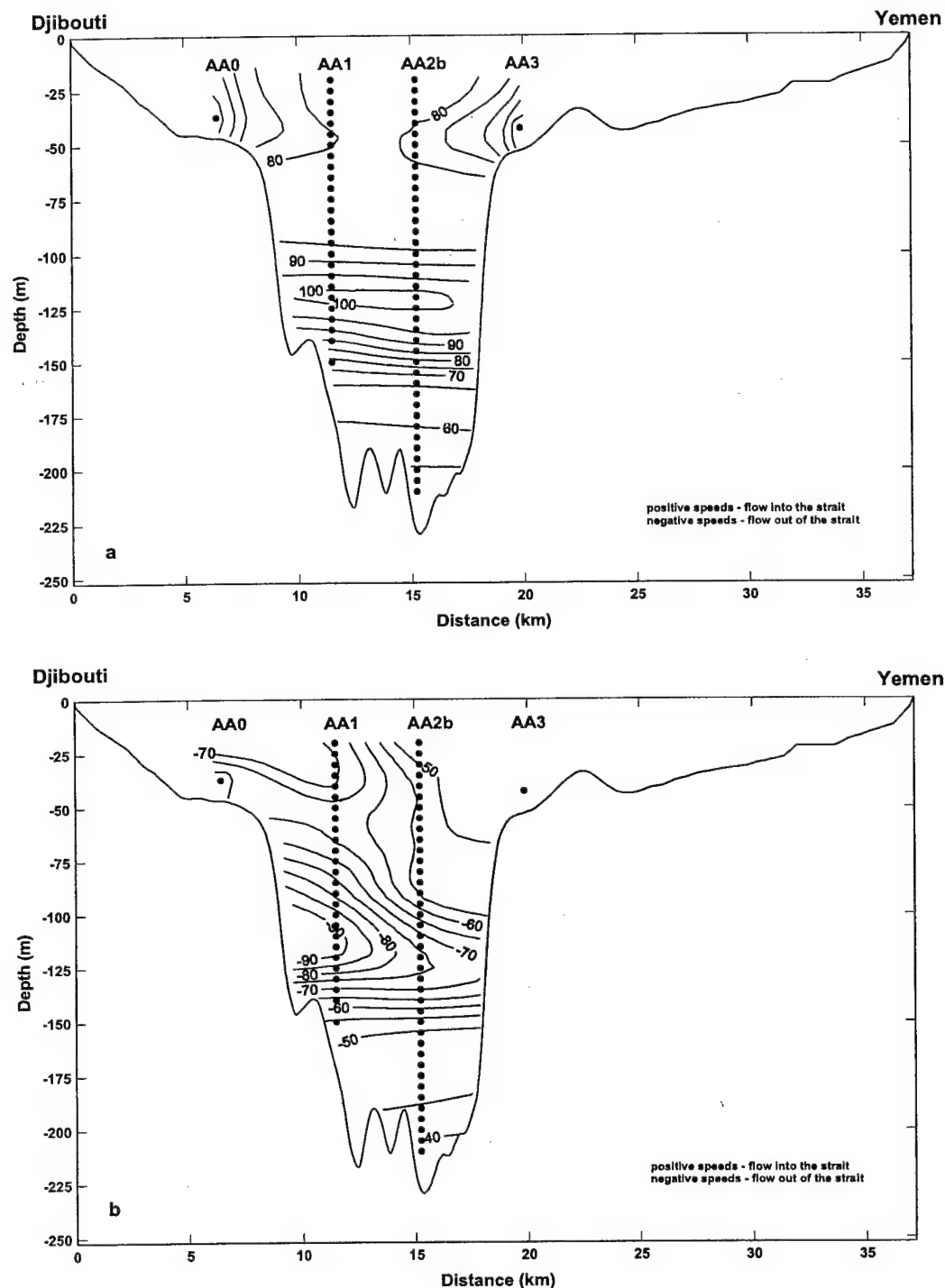
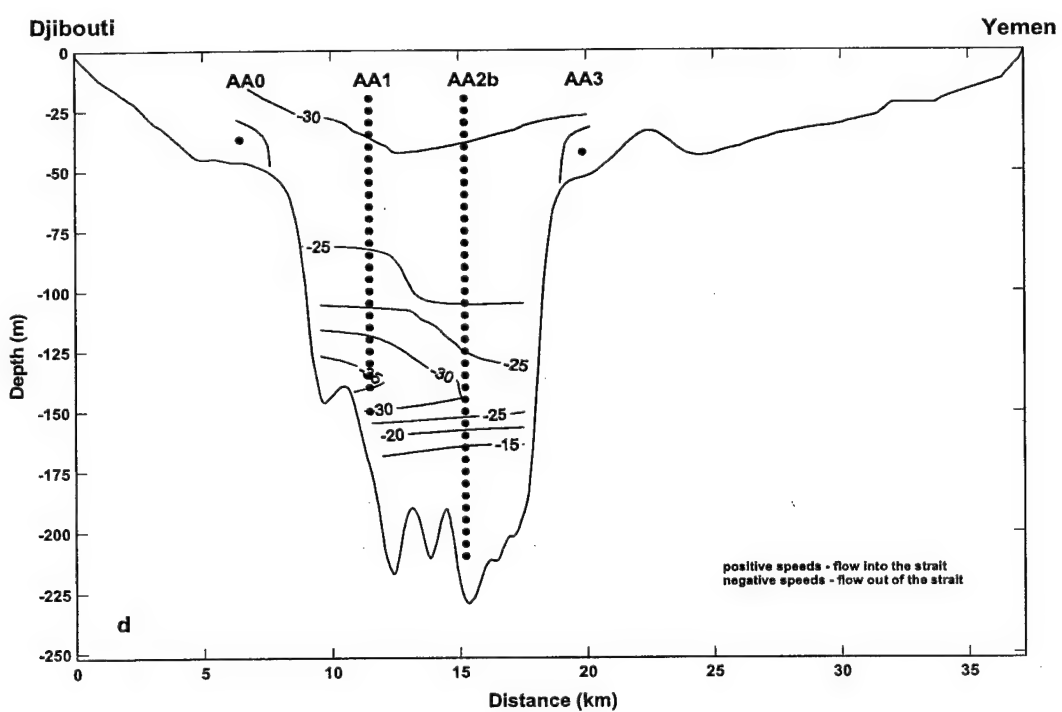
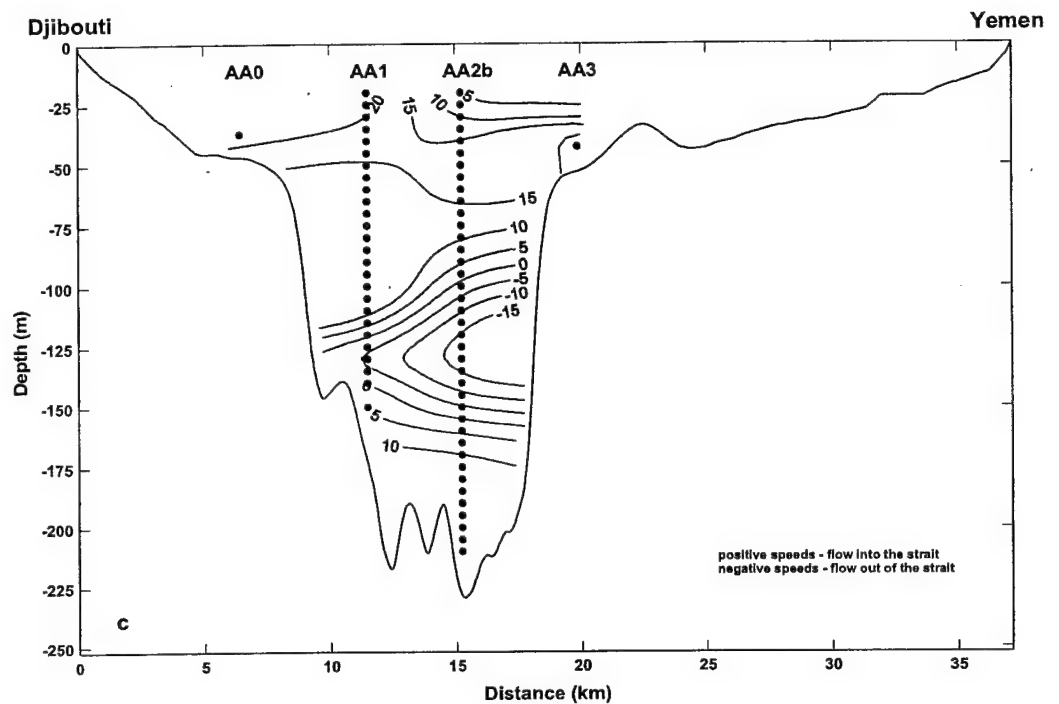


Figure 22. Distribution of the along-strait tidal velocity component predicted from the  $K_1$ ,  $O_1$ ,  $P_1$ ,  $M_2$ ,  $S_2$ , and  $N_2$  constituents (a) 4 hours after HHW, (b) 4 hours after LLW, (c) 3 hours after LHW, and (d) 3 hours after HLW at the coast (the Perim Narrows cross-section).



(Figure 22 cont.)

area considered in calculations is  $1.945 \text{ km}^2$  so the transport estimates were found for a major part of the section (above 81%); therefore, these estimates should be reasonable.

The lack of salinity and temperature observations does not allow defining the interface between the layers and finding the transport estimates separately for each layer so only the transport through the entire section was computed.

As expected, for the diurnal constituents, the largest transport is associated with the  $K_1$  whose amplitudes and phases are 0.61 Sv ( $1\text{Sv}=10^6 \text{ m}^3/\text{s}$ ) and  $66^\circ$ , and 0.59 Sv and  $91.0^\circ$  for the winter and summer stratifications, respectively. The  $M_2$  signal has similar amplitudes and they are 0.61 Sv ( $219.2^\circ$ ) for the winter season and 0.57 Sv ( $218^\circ$ ) for the summer season. In addition, regardless of the stratification season the transport amplitudes are very comparable to the average Red Sea outflow transport for the winter season, which, as reported by Murray and Johns (1997), is 0.6 Sv so it would be of high interest to evaluate tidal transport in different layers to determine whether there is a net tidal transport of the Red Sea waters. However, as indicated earlier, one needs simultaneous measurements of density (or salinity) and currents to answer this question.

### 3.6. Barotropic tidal current components

It is very apparent, particularly at Perim Narrows and the Hanish Sill, that the tidal currents are depth dependent, and therefore, they are not strictly barotropic but they are a superposition of barotropic and baroclinic tides. Characteristics of the baroclinic tidal currents in the Strait will be discussed in the next chapter. The barotropic tides correspond to depth-independent currents related to long wave motion that is not modified by friction. To estimate a contribution of the barotropic component to the tidal currents at the locations discussed earlier, first the current observations for the longest possible time period at each mooring were depth averaged using the following equations:

$$u_{bt}(t) = \frac{\sum_{k=1}^n h_k u_k(t)}{\sum_{k=1}^n h_k} \quad (1a)$$

$$v_{bt}(t) = \frac{\sum_{k=1}^n h_k v_k(t)}{\sum_{k=1}^n h_k} \quad (1b)$$

where  $u_{bt}$ ,  $v_{bt}$  and  $u$ ,  $v$  are the cross-strait and along-strait components of the barotropic and measured currents at time  $t$ , respectively,  $h_k$  is the layer thickness, and  $n$  is the total number of levels with current data. Then the ellipse parameters were computed. Since at all locations measurements sampled at least 80% of the total water column, the computed estimates should be a good approximation of the barotropic current ellipse parameters.

As expected, among all resolved tidal current constituents, the most energetic barotropic ones are the  $K_1$ ,  $O_1$ ,  $P_1$ ,  $M_2$ ,  $S_2$ , and  $N_2$  components. Similar to the distributions of tidal current axes discussed earlier, there is ~50% reduction in the barotropic amplitude of the semimajor axis between Perim Narrows (A2b, AA1, and AA2b moorings) and C mooring (Tables 2 and 3). Such a reduction is not present

between C mooring and the Hanish Sill where the amplitudes are comparable. The semiminor axes are again much smaller than the respective semimajor ones so the barotropic currents are nearly rectilinear. With the exception of  $P_1$  at C mooring, the phase does not vary much between different diurnal constituents at the same location or at the different moorings located along the central axis of the Strait. This lack of phase variation means that the maximum tidal currents generated by these three diurnal components occur almost simultaneously at all locations. Along the same axis, the phase for the same semidiurnal component shows some variability but the phase differences between the locations are generally small and rarely reach  $30^\circ$ . Furthermore, the  $N_2$  has the earliest phase, and the barotropic currents generated by this constituent are observed at the same location approximately half an hour earlier than those generated by the  $M_2$  and about 1 hour before the  $S_2$  currents. Finally, similar to the results discussed earlier (cross-sectional variability of the phase in the section near Perim Narrows), the phase of the barotropic component also seems to suggest that the tidal currents generated by the diurnal and semidiurnal constituents on the east side lead ( $\sim 1$  hour) those on the west (compare the phases at AA2 and AA1 moorings) at Perim Narrows.

When the barotropic amplitudes of the semimajor axis of the diurnal and semidiurnal components are compared with the observed amplitudes of the semimajor axis at depths, where effects of the bottom friction are negligible and the tidal currents can be simply defined as a sum of the barotropic and baroclinic components, it is obvious that the barotropic amplitudes are usually very comparable to the observed ones at the majority of depth levels. The baroclinic component, especially that associated with the diurnal components, is generally important in the pycnocline layer during the winter

Table 2. Ellipse parameters and the 95% errors of barotropic currents for the diurnal tidal constituents.

Tide	Semimajor Axis (cm/s)	Semiminor Axis (cm/s)	Inclination Angle (deg)	Phase (deg, GMT)
A2b mooring				
$K_1$	$29.7 \pm 2.0$	$-1.5 \pm 0.2$	$91.3 \pm 0.4$	$68.3 \pm 1.2$
$O_1$	$16.4 \pm 0.6$	$-0.5 \pm 0.2$	$92.5 \pm 0.6$	$68.5 \pm 3.5$
$P_1$	$9.6 \pm 0.6$	$-0.5 \pm 0.1$	$91.9 \pm 0.4$	$66.7 \pm 1.2$
AA1 mooring				
$K_1$	$31.9 \pm 1.6$	$-0.9 \pm 0.5$	$104.4 \pm 0.9$	$88.6 \pm 1.2$
$O_1$	$18.7 \pm 0.7$	$-0.1 \pm 0.4$	$104.3 \pm 0.9$	$89.2 \pm 2.2$
$P_1$	$10.5 \pm 0.5$	$-0.4 \pm 0.2$	$102.7 \pm 0.9$	$96.3 \pm 1.2$
AA2b mooring				
$K_1$	$29.0 \pm 0.9$	$-0.7 \pm 0.3$	$94.6 \pm 0.4$	$71.3 \pm 2.0$
$O_1$	$16.7 \pm 0.4$	$-0.3 \pm 0.2$	$94.2 \pm 0.6$	$74.6 \pm 2.9$
$P_1$	$8.7 \pm 0.3$	$-0.3 \pm 0.1$	$94.7 \pm 0.4$	$78.2 \pm 2.0$
C mooring				
$K_1$	$13.8 \pm 0.7$	$1.2 \pm 0.5$	$133.5 \pm 6.9$	$73.4 \pm 2.7$
$O_1$	$7.2 \pm 0.9$	$0.6 \pm 0.3$	$132.0 \pm 5.5$	$74.4 \pm 4.1$
$P_1$	$5.5 \pm 0.3$	$-0.2 \pm 0.2$	$135.9 \pm 6.9$	$64.1 \pm 2.7$
B2b mooring				
$K_1$	$15.6 \pm 0.7$	$-0.6 \pm 0.6$	$133.0 \pm 1.6$	$73.9 \pm 4.9$
$O_1$	$9.4 \pm 0.5$	$-0.4 \pm 0.6$	$134.2 \pm 2.5$	$77.6 \pm 8.2$
$P_1$	$4.9 \pm 0.2$	$-0.1 \pm 0.2$	$137.2 \pm 1.6$	$73.9 \pm 4.9$

Table 3. Ellipse parameters and the 95% errors of barotropic currents for the semidiurnal tidal constituents.

Tide	Semimajor Axis (cm/s)	Seminor Axis (cm/s)	Inclination Angle (deg)	Phase (deg, GMT)
A2b mooring				
M <sub>2</sub>	29.2 ± 1.2	-1.0 ± 0.2	94.3 ± 0.4	200.8 ± 1.4
S <sub>2</sub>	10.2 ± 1.4	-0.3 ± 0.2	94.3 ± 1.1	227.0 ± 5.1
N <sub>2</sub>	8.4 ± 0.8	-0.2 ± 0.1	93.8 ± 1.0	182.8 ± 7.8
AA1 mooring				
M <sub>2</sub>	32.5 ± 2.7	-0.9 ± 0.6	105.4 ± 1.7	234.0 ± 1.3
S <sub>2</sub>	11.2 ± 1.1	-0.6 ± 0.2	105.2 ± 2.2	258.5 ± 5.3
N <sub>2</sub>	9.7 ± 0.6	-0.2 ± 0.3	105.2 ± 2.2	215.2 ± 6.1
AA2b mooring				
M <sub>2</sub>	29.6 ± 0.7	-0.5 ± 0.2	96.9 ± 0.6	200.6 ± 1.8
S <sub>2</sub>	9.3 ± 1.7	-0.2 ± 0.1	96.9 ± 2.3	223.4 ± 4.7
N <sub>2</sub>	8.5 ± 1.2	-0.1 ± 0.1	95.2 ± 1.8	182.5 ± 7.1
C mooring				
M <sub>2</sub>	16.2 ± 1.2	0.2 ± 0.2	128.3 ± 7.8	220.9 ± 5.5
S <sub>2</sub>	6.2 ± 0.6	0.2 ± 0.5	124.7 ± 9.6	248.1 ± 9.0
N <sub>2</sub>	4.5 ± 0.5	-0.1 ± 0.3	128.0 ± 4.9	206.7 ± 8.4
B2b mooring				
M <sub>2</sub>	15.0 ± 0.4	-0.3 ± 0.2	133.9 ± 0.8	204.6 ± 3.5
S <sub>2</sub>	6.0 ± 0.8	-0.1 ± 0.2	133.4 ± 2.1	230.3 ± 9.4
N <sub>2</sub>	3.9 ± 0.4	-0.1 ± 0.1	132.8 ± 2.3	193.0 ± 6.4

stratification period at Perim Narrows and the Hanish Sill. However, this larger baroclinic contribution is confined just to a fraction of the total water depth at each location; therefore, it can be concluded, just by such simple comparison that the tidal flow is dominated by the barotropic tidal currents in the Bab el Mandab Strait. As will be shown later (Chapter 4) a similar conclusion can be drawn from results of the dynamic mode decomposition.

### 3.7. Barotropic tidal balance

In the Bab el Mandab Strait, where barotropic tides are a dominant component of the tidal flow, the tidal motion may be described as a first order approximation by the Laplace tidal equations. A Cartesian coordinate system can be defined as follows: the x-axis is a cross-strait axis, y is an axis along the center of the strait, and z is a vertical axis positive upward with 0 at the free surface. The cross-strait and along-strait momentum equations are:

$$\frac{\partial u}{\partial t} - fv = -g \frac{\partial \zeta}{\partial x} \quad (2a)$$

$$\frac{\partial v}{\partial t} + fu = -g \frac{\partial \zeta}{\partial y} \quad (2b)$$

where u and v are cross-strait and along-strait velocity components, f is the Coriolis parameter, g is the acceleration due to gravity,  $\zeta$  is the surface elevation, h is the water depth, and t is time.

Based on measurements, it has been shown that, for instance, in the Strait of Gibraltar (Candela et al., 1990; Lafuente et al., 2000) or in the Strait of Belle Isle (Garrett

and Petrie, 1981), the tidal flow balance is reduced to two terms in both along- and cross-strait directions. In the case of the cross-strait equation (2a), the Coriolis term is balanced by the cross-strait surface elevation gradient (geostrophic balance) whereas the along-strait equation is reduced to the balance between the local acceleration and along-strait surface elevation gradient terms.

Scaling analysis (with typical values of a cross-strait length  $X=10^4$  m, an along-strait length  $Y=10^5$  m, cross-strait velocity  $U=10^{-1}$  m/s, along-strait velocity  $V=1$  m/s, Coriolis parameter  $f=10^{-6}$  1/s, tidal period  $T=10^5$  s, water elevation differences  $\Delta\zeta_c=10^{-2}$  m for the cross-strait direction and  $\Delta\zeta_a=10^{-1}$  m for the along-strait direction) seems to suggest that in the Perim Narrows cross-section, the along-strait balance of the tidal flow is indeed between the local acceleration and along-strait surface elevation gradient terms. However, the cross-strait momentum is not geostrophic because the local acceleration term is of the same order as the Coriolis term. Therefore, for this section, the momentum equations (2a and 2b) can be simplified and rewritten as:

$$\frac{\partial u}{\partial t} - fv = -g \frac{\partial \zeta}{\partial x} \quad (3a)$$

$$\frac{\partial v}{\partial t} = -g \frac{\partial \zeta}{\partial y} \quad (3b)$$

To verify the validity of these equations, each term was evaluated from current and water level measurements. The cross-strait elevation gradient ( $\frac{\partial \zeta}{\partial x}$ ) was evaluated as a difference between G109 and G89 sites ( $\Delta x=32$  km) whereas the along-strait gradient ( $\frac{\partial \zeta}{\partial y}$ ) was estimated as the water level difference between G109 and Mocha locations ( $\Delta y=70$  km; very comparable results were obtained when the same gradient was estimated between G89 and Assab). The velocity components in equations 3a and 3b were approximated by averages of the vertically averaged velocities from AA1 and AA2b moorings. Columns 2 and 3 of Table 4 show left and right hand terms of equation 3a, and columns 4 and 5 of the same table contain the terms of equation 3b computed for the major tidal constituents.

Table 4. Harmonic constants for the cross-strait and along-strait balance.

Constituent	Cross-Strait Balance				Along-Strait Balance			
	$\frac{\partial u}{\partial t} - fv$		$-g \frac{\partial \zeta}{\partial x}$		$\frac{\partial v}{\partial t}$		$-g \frac{\partial \zeta}{\partial y}$	
	Amp*	Phase	Amp*	Phase	Amp*	Phase	Amp*	Phase
K <sub>1</sub>	9.73	40°	9.41	7°	21.34	351°	16.14	323°
O <sub>1</sub>	5.79	48°	5.59	17°	11.60	349°	11.41	338°
P <sub>1</sub>	3.41	48°	2.70	11°	6.55	356°	4.40	322°
M <sub>2</sub>	16.83	157°	17.90	139°	41.58	129°	49.89	109°
S <sub>2</sub>	5.89	174°	6.20	162°	14.27	153°	19.19	132°
N <sub>2</sub>	4.31	142°	4.31	124°	11.85	112°	14.59	91°

\*Amp – amplitudes of the respective terms in  $10^{-6}$  m/s<sup>2</sup>

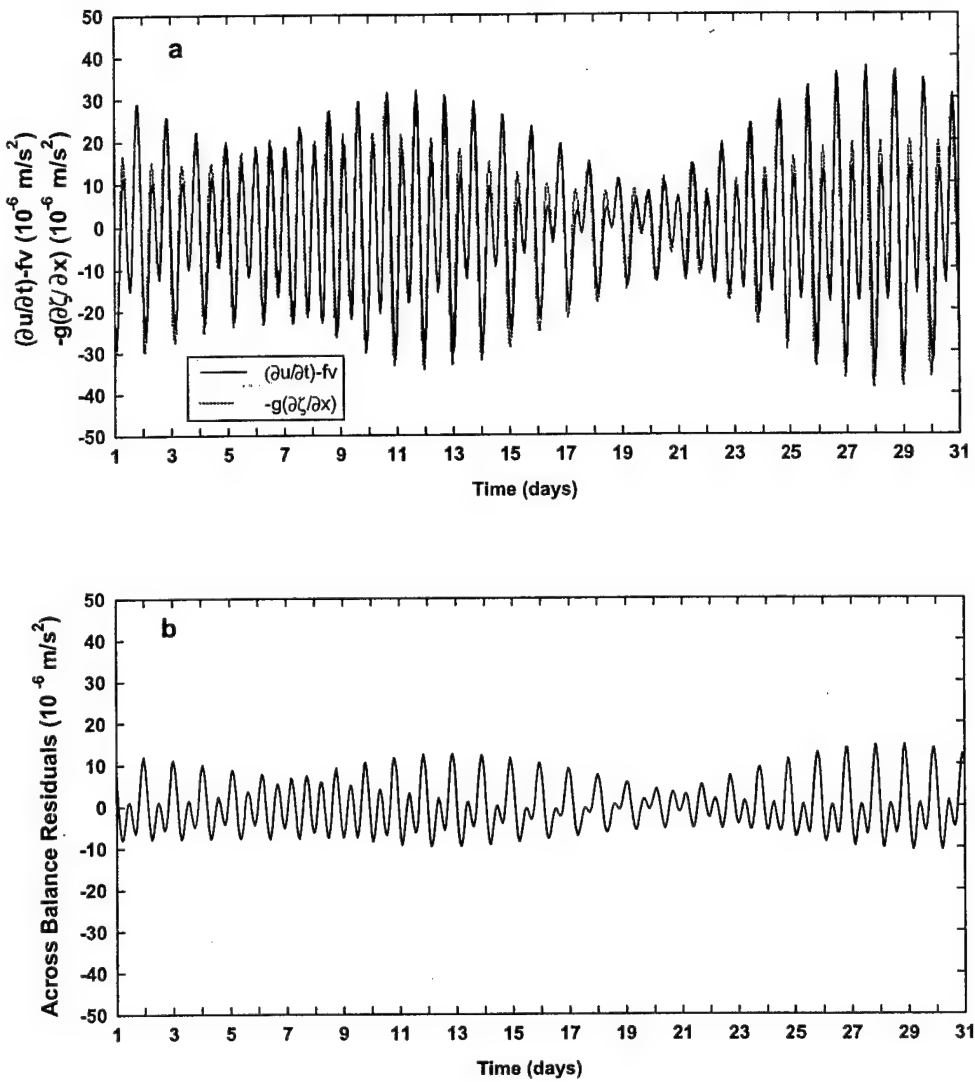


Figure 23. Example of time series of (a) the principle terms in the cross-strait momentum balance and (b) differences (residuals) between balance terms for the Perim Narrows cross-section.

The amplitudes of the terms from the cross-strait momentum equation are generally in very good agreement for all major tidal constituents; however, there is a discrepancy between the phases with the elevation gradient showing consistently lower phases than those associated with the combined effect of the local acceleration and Coriolis term. Furthermore, the phase differences of the diurnal components are larger than those of the semidiurnal components. In addition, Figure 23 shows the terms of the cross-strait balance and their residuals for all tidal constituents combined together. It displays a month-long times series for a better visual comparison. These short series, as well as the series generated for the longer time period, show that the comparison between the terms is rather remarkable (a correlation coefficient is equal to 0.93). The elevation

gradient term generally has slightly larger magnitudes than those of the local acceleration and Coriolis terms combined together. The root mean squared (rms) of the residuals is small and equal to  $4.8 \times 10^{-6} \text{ m/s}^2$ . Therefore, it might be concluded that, based on the observations, the cross-strait balance of the tidal flow as described by equation 3a is not perfectly satisfied at Perim Narrows; however, the equation terms evaluated by the measured currents and elevations agree fairly well with each other, and if the balance is scrutinized separately for different constituents the results are better for the semidiurnal tidal components.

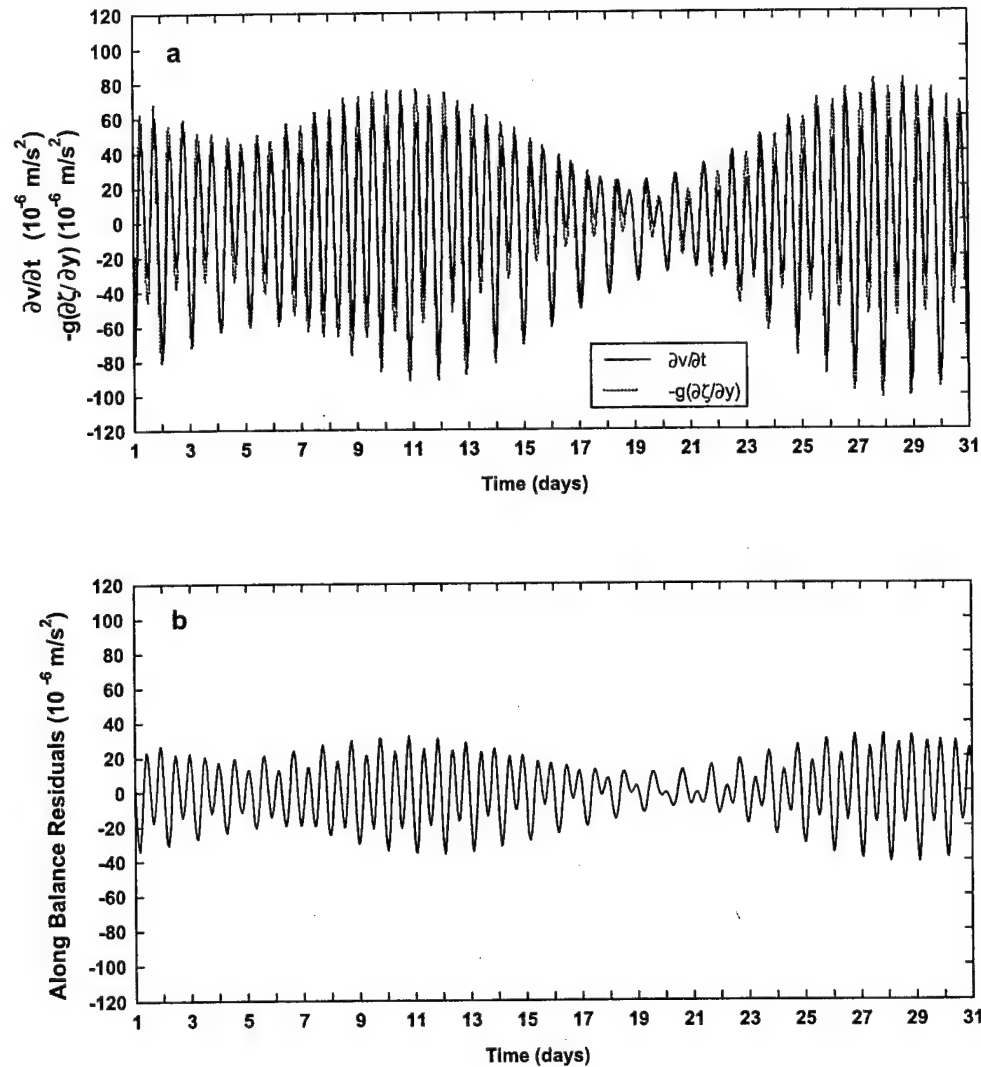


Figure 24. Example of time series of (a) the principle terms in the along-strait momentum balance and (b) differences (residuals) between balance terms for the Perim Narrows cross-section.

The terms of the along-strait balance for the considered tidal components also correspond fairly well to each other (Table 4). There is poorer agreement between the amplitudes, but the phases of the diurnal constituents agree better than those found for the

cross-strait tidal balance. In addition, for all tidal components, the elevation gradient again shows lower phases than those of the local acceleration. The terms for all major semidiurnal and diurnal constituents combined together are displayed in Figure 24 (only one month is shown for a better visual comparison, but conclusions are also valid for the longer time series). The comparison between the terms is again reasonable; the correlation coefficient between the series is 0.92. However, it is also apparent that the along-strait elevation gradient term has consistently higher magnitudes and that the residuals with an rms of  $13.7 \times 10^{-6}$  m/s<sup>2</sup> are fairly large (Figure 24b). These large residuals suggest that perhaps other terms, such as a bottom friction and/or advection, should be included in the along-strait momentum balance equation. If one, for instance, assumes that the variance contained in the residual could be solely explained by a linear frictional term of the form  $rv$  where  $r$  is the linear drag coefficient then from the regression between residual and current velocity  $r$  is equal to  $4.3 \times 10^{-5}$  1/s. Furthermore, if the friction term with  $r = 4.3 \times 10^{-5}$  1/s is included in the along-strait momentum balance the magnitude of the residuals is reduced approximately 50%, and their rms is much lower and equal to  $7.1 \times 10^{-6}$  m/s<sup>2</sup>.

In addition, the terms of the along-strait balance are approximately twice as large as those of the cross-strait balance. This implies that the variability of at least those currents observed in the deep channel (the barotropic part of the flow) in the Strait can be well described just by the balance between the along-strait elevation gradient and local acceleration.

### 3.8. Long period tidal constituents

Long period tidal currents are either a direct response to astronomical forcing or they result from nonlinear dynamics in the short period tidal flow. With periods up to several months, the primary astronomical forcing constituents are  $M_f$  (lunar fortnightly) with a period of 13.66 days, and  $M_m$  (monthly lunar) with a period of 27.55 days. A

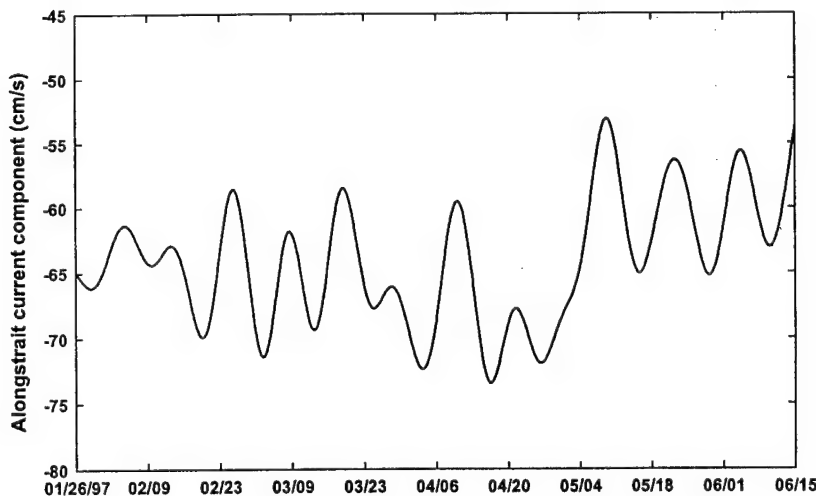


Figure 25. The along-strait current component at 60 m - B2b mooring (10 - 40 day band passed data).

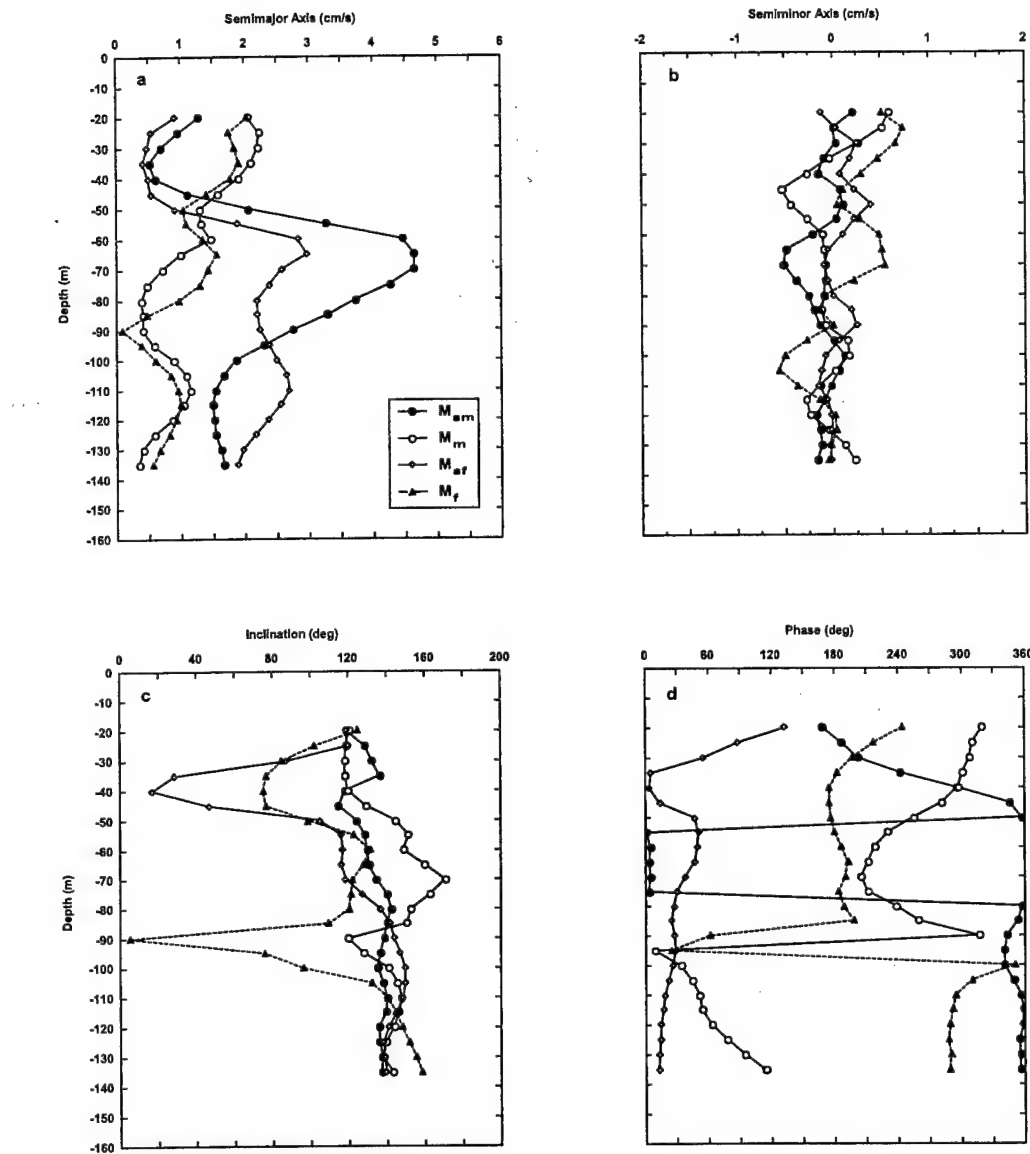


Figure 26. The vertical distribution of (a) semimajor axis, (b) semiminor axis, (c) inclination of the semimajor axis, and (d) phase for the  $M_m$ ,  $M_{sm}$ ,  $M_f$ , and  $M_{sf}$  tidal constituents at the Hanish Sill (B2b mooring).

major component, which results from nonlinear effects, is  $M_{sf}$  (a period of 14.75 days), and it is produced through  $M_2$  and  $S_2$  interactions. These long period fluctuations are present in the current measurements collected in the Bab el Mandab Strait as illustrated in Figure 25. This figure displays the filtered along-strait current component (10–40 day band) from B2b mooring. The filtering, of course, does not isolate only the tidal signal; the data also contain oscillations with similar periods that are created by other forcing mechanisms. However, the long period fluctuations superimposed on mean currents are

very well visible in these data, especially those with periods of about two weeks. Such fortnightly fluctuations are also easily detected at other moorings located in the Strait.

To obtain reliable estimates of the long period tidal constituents, a long data record is required, and one of the longest records available from the BAM project is that collected at B2b mooring (the Hanish Sill). Results of the harmonic analysis for the long period components computed from this data set indicate that the  $M_m$ ,  $M_{sm}$  (lunar-evectional with a period of 31.81 days),  $M_f$ , and  $M_{sf}$  constituents have the largest amplitudes. Figure 26 displays the ellipse parameters for these four components.

The semimajor axis amplitudes of all components (Figure 26a) are much smaller than those of the major semidiurnal or diurnal constituents, and they lie between 0.2 cm/s and 4.7 cm/s. All of them are not uniformly distributed with depth and, except perhaps for some similarities between the  $M_m$  and  $M_f$ , their vertical distributions are not as comparable as they are for the shorter period tides. The  $M_m$  and  $M_f$  have maximum amplitudes in the upper 50 m, which vary approximately between 1.5 cm/s and 2 cm/s. The amplitudes of the same axis of the  $M_{sm}$  and  $M_{sf}$ , however, have their minimum in the upper 50 m. Below 50 m they increase, and for the  $M_{sm}$ , there is a distinct maximum of 4.7 cm/s at 70 m. The  $M_{sf}$  also reaches its maximum value of 3 cm/s at the same depth. The semiminor axis amplitudes (Figure 26b) of all long period tides are even smaller than those of the semimajor axis and they do not exceed 0.7 cm/s. The inclination angle (Figure 26c) varies quite widely, especially at depths where the major axis is very small. The vertical distribution of the phase (Figure 26d) shows that there is a phase difference of  $\sim 180^\circ$  between 20 m and 50 m for the  $M_{sm}$ , and between 80 m and 90 m for the  $M_m$  and  $M_f$  constituents, indicating that the maximum inflowing current (at these frequencies)

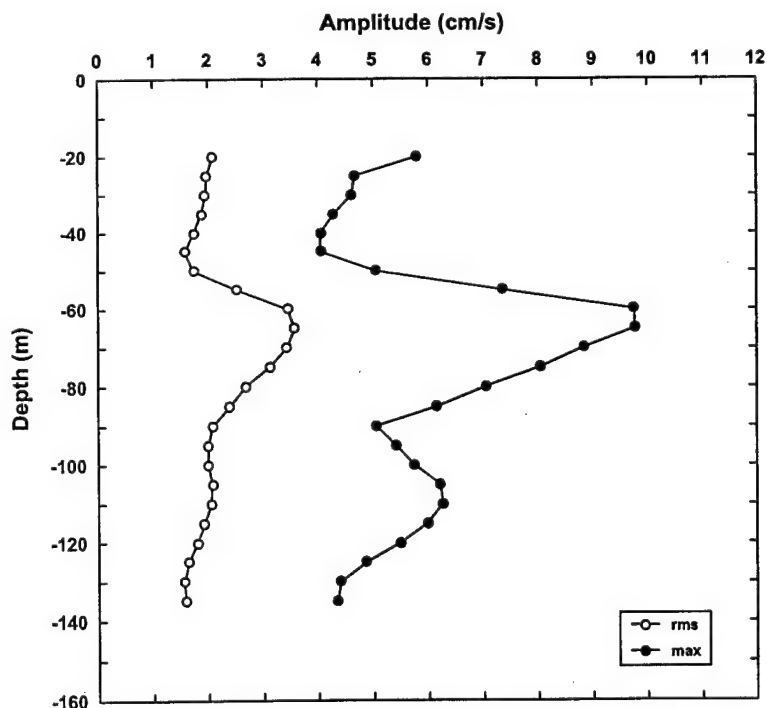


Figure 27. Vertical distributions of rms and maximum contribution (max) of the along-strait currents generated by the  $M_m$ ,  $M_{sm}$ ,  $M_f$ , and  $M_{sf}$  tidal constituents.

coincides with the maximum outflowing current, i.e. the flow structure is strongly two-layered. The phase profile of the  $M_{sf}$  shows a difference of  $\sim 120^\circ$  between 20 m and 40 m and an almost constant phase of  $\sim 25^\circ$  below 40 m.

To estimate the net contribution, which the long period tides may add to the low frequency flow, the tidal currents generated by these four long period tides were computed from the tidal constants, and then the rms of the along-strait component was calculated. Figure 27 shows a vertical distribution of this quantity together with the maximum possible long period tidal current speed (max) at each depth. The distribution of the rms values clearly shows that regardless of the depth, the average contribution of the long period tides to the mean flow is very small and does not exceed 4 cm/s. However, on a few occasions, when all long period components reach maximum simultaneously (max values), their input may be quite significant, and, for example, at 60 m this contribution can reach 10 cm/s.

### 3.9. Higher tidal harmonics

In coastal areas, the astronomical tides are usually distorted by the presence of higher harmonics. The appearance of these additional components is due to wave-wave interactions associated with nonlinearities of the tidal motion in shallow waters (Le Provost, 1991). If these harmonics have large amplitudes this could mean that the nonlinear terms such as friction and advection are important terms in tidal dynamics. The Bab el Mandab Strait is rather a shallow strait with extensive shoals (depths less than 50 m) present on both sides of a deep trench located in the middle. Therefore, one expects that the higher tidal harmonics could play a significant role in tidal circulation there. The majority of moorings from the BAM project are located in deep sections of the Bab el Mandab Strait, hence, it may not be appropriate to discuss whether these harmonics are an important part of the tidal dynamics in this Strait. However, there are a few instruments, which were deployed in the waters where depths are between 45 m and 60 m, and these instruments together with the deep moorings may at least help to identify which shallow water tidal harmonics are the most energetic.

Results of the harmonic analysis, which was applied to the entire time series, show that the high frequency tidal currents are much less energetic than those generated by the major tidal constituents. Maximum computed amplitudes of the major axis of any high frequency component rarely reach 4 cm/s. Furthermore, among all of these components, third-diurnal harmonics such as the  $MK_3$  and  $SO_3$  seem to be dominant ones. Other harmonics that often have the semimajor axis equal to or larger than 1 cm/s are the  $M_3$ ,  $MO_3$ ,  $SK_3$ ,  $M_4$ ,  $MS_4$ , and  $MK_4$ .

Figure 28 shows vertical profiles of the tidal current constants of the  $MK_3$ ,  $SO_3$ , and  $M_4$  obtained from the harmonic analysis of measurements collected at AA1 mooring. This mooring was chosen because the  $MK_3$ ,  $SO_3$ , and  $M_4$  have the highest recorded amplitudes of both axes when compared with the amplitudes of these constituents or any other higher harmonics at the remaining moorings. Similar to the constituents discussed earlier, these tidal components are not uniformly distributed in the vertical. Amplitudes of the semimajor axis display maxima for all considered components near  $\sim 110$  m. Additionally, as opposed to the major diurnal, semidiurnal or long period tides, the higher harmonics do not have amplitudes of the semiminor axis much smaller than those of the semimajor axis (Figure 28b). The amplitudes of these two axes are very comparable in

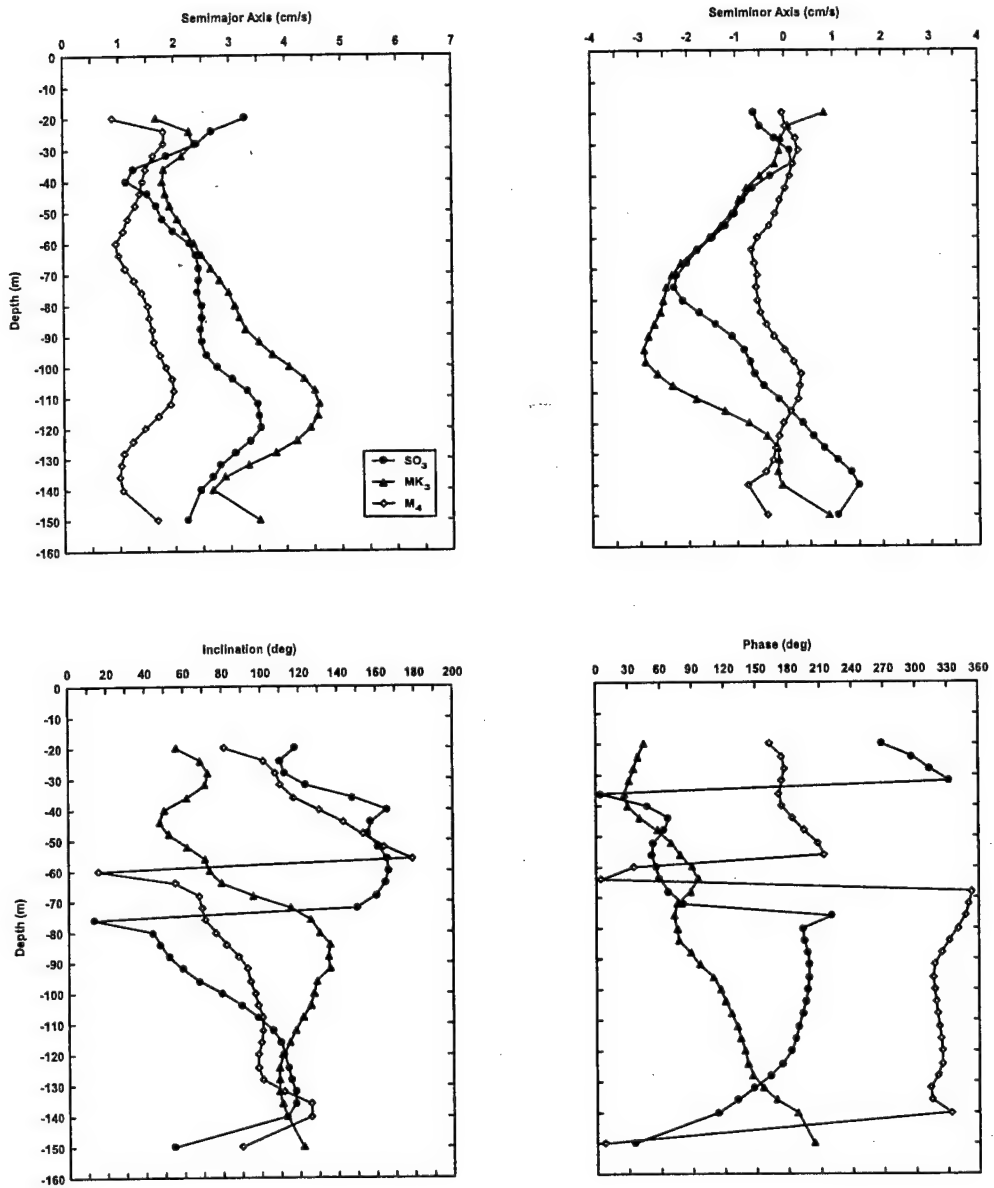


Figure 28. The vertical distribution of (a) semimajor axis, (b) semiminor axis, (c) inclination of the semimajor axis, and (d) phase for the MK<sub>3</sub>, SO<sub>3</sub>, and M<sub>4</sub> tidal constituents at Perim Narrows (AA1 mooring).

length at almost all depths, especially those of the MK<sub>3</sub> and SO<sub>3</sub>. Similar to the amplitudes of the semimajor axis, values of the semiminor axis of all components vary with depth. Furthermore, the inclination angle of all higher harmonics (Figure 28c) is quite variable and changes a great deal with depth. Finally, the phase of the MK<sub>3</sub> and SO<sub>3</sub> major axes (Figure 28d) changes fairly gradually with depth, increasing for the first and decreasing for the second. The M<sub>4</sub> phase, however, first increases with depth in the upper 70 m, then fluctuates around 320° before increasing again to ~360° at 150 m.

#### 4. BAROCLINIC TIDAL MOTION IN THE BAB EL MANDAB STRAIT

Internal tidal fluctuations are frequently observed in straits. They are generated through interactions between barotropic tides with bottom topography in the presence of vertical stratification. These fluctuations generated by tides may assume different forms such as internal bores, finite-amplitude lee waves or solitary wave packets, some may overturn and mix the water column, and some are found as interface fluctuations at tidal frequencies that have consistent phase throughout a strait.

Wunch (1975) pointed out that the dynamics of the internal tides is related to the latitude (inertial frequency) of the measurement location and to the density structure (buoyancy frequency). If the tidal frequency is smaller than the inertial frequency, the internal tides are trapped near a generation area. Conversely, if the tidal frequency is... higher than the inertial frequency tides are freely propagating waves. In the Bab el Mandab Strait, the inertial frequency, which varies between  $3.18 \times 10^{-5}$  1/s and  $3.53 \times 10^{-5}$  1/s, is always lower than the frequency of the semidiurnal ( $1.4 \times 10^{-4}$  1/s) and diurnal ( $7.3 \times 10^{-5}$  1/s) tides, thus, theoretically, progressive internal waves of diurnal and semidiurnal frequencies could be present in this Strait if the buoyancy frequency is different from 0 and higher than their frequencies.

The buoyancy frequency is defined as:

$$N^2 = -\frac{g}{\rho} \frac{\partial \rho}{\partial z} \quad (4)$$

where  $g$  is the acceleration due to gravity, and  $\rho$  is the density at depth  $z$ . It depends strongly on the density structure of the water column and is critical in determining the maximum frequency of the internal wave oscillations versus depth. The depth dependency of this frequency constrains some internal waves to the certain depth range in the water column, i.e., to the depths where the buoyancy frequency is higher than the internal wave frequency. Depths where the buoyancy frequency equals the internal wave frequency are referred to as a "turning points" (Desaubies, 1972). The internal wave energy is reflected off these "boundaries", much like internal wave reflection off the ocean bottom.

With changing stratification (density distribution) one may expect a somewhat different distribution of the buoyancy frequency. Examples of profiles of this parameter for two types of the density distribution observed in the Bab el Mandab Strait are displayed in Figure 29. These profiles were computed from the CTD profiles that were taken near the mooring locations. It is very clear that the profiles have different shapes for the winter and summer stratifications. Throughout the water column, values of the buoyancy frequency for both density distributions are higher than 0 and at the same time, they vary considerably with depth with the maximum values found in the pycnocline regions. In general, the buoyancy frequency is larger throughout the water column than the semidiurnal or diurnal frequencies; therefore, similar to the inertial frequency, it should not be a limiting factor for the internal waves of diurnal or semidiurnal frequencies to be generated in the Bab el Mandab Strait.

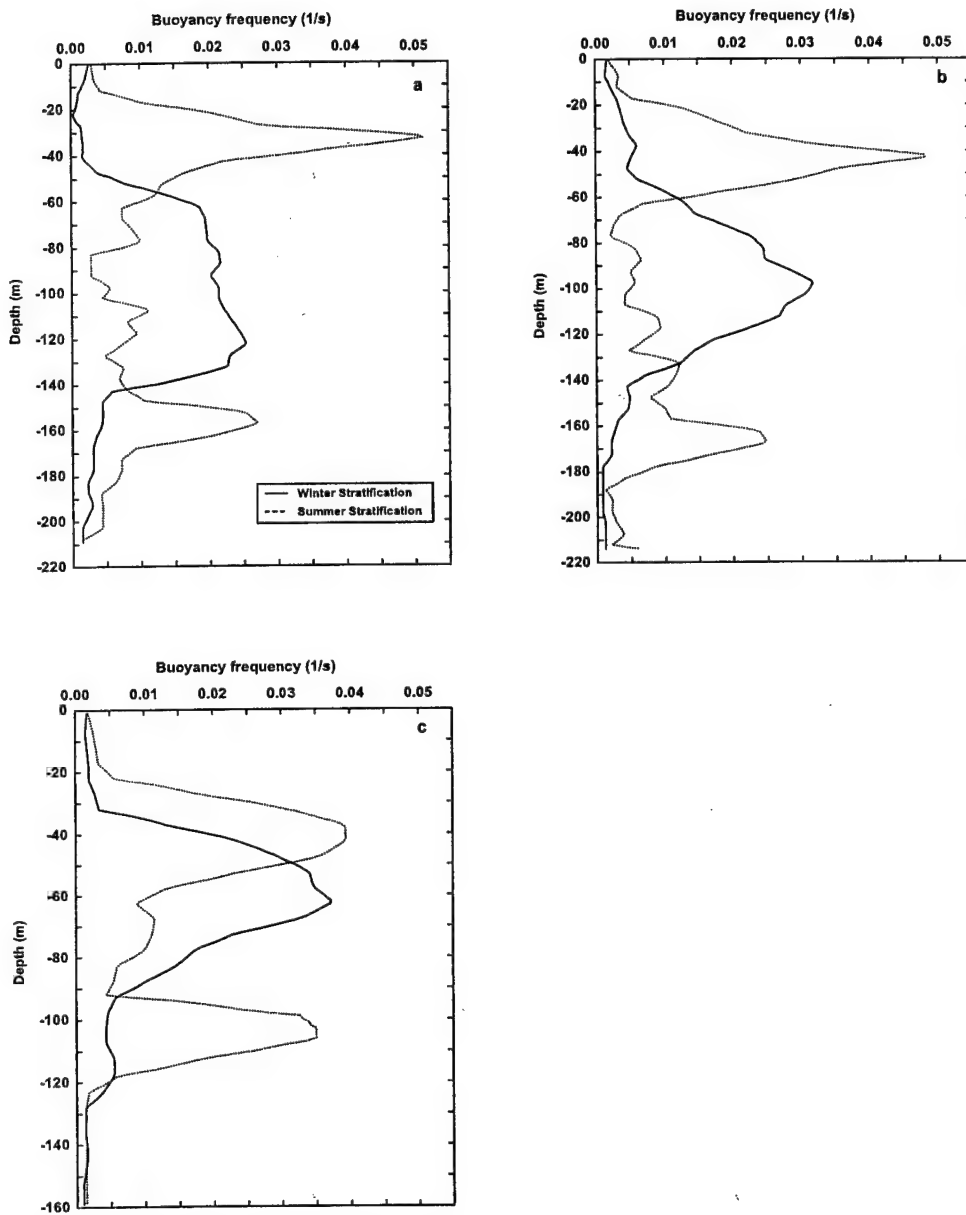


Figure 29. Examples of buoyancy frequency distributions near (a) Perim Narrows, (b) C mooring, and (c) the Hanish Sill for winter and summer stratifications.

#### 4.1. Baroclinic tidal currents

To extract baroclinic tidal currents from the observations, depth-averaged currents were estimated from equations 1a and 1b (page 41) at the moorings with the good vertical instrument coverage. It was assumed that these depth-averaged currents represented the barotropic currents. The baroclinic currents were taken then as a difference between the measured and barotropic currents. The barotropic currents were also estimated as a simple average. The resulting time series of the barotropic and baroclinic current

components are very comparable to those obtained when the barotropic currents are computed from equations 1a and 1b. For further analyses, the baroclinic estimates obtained from the first approach were used.

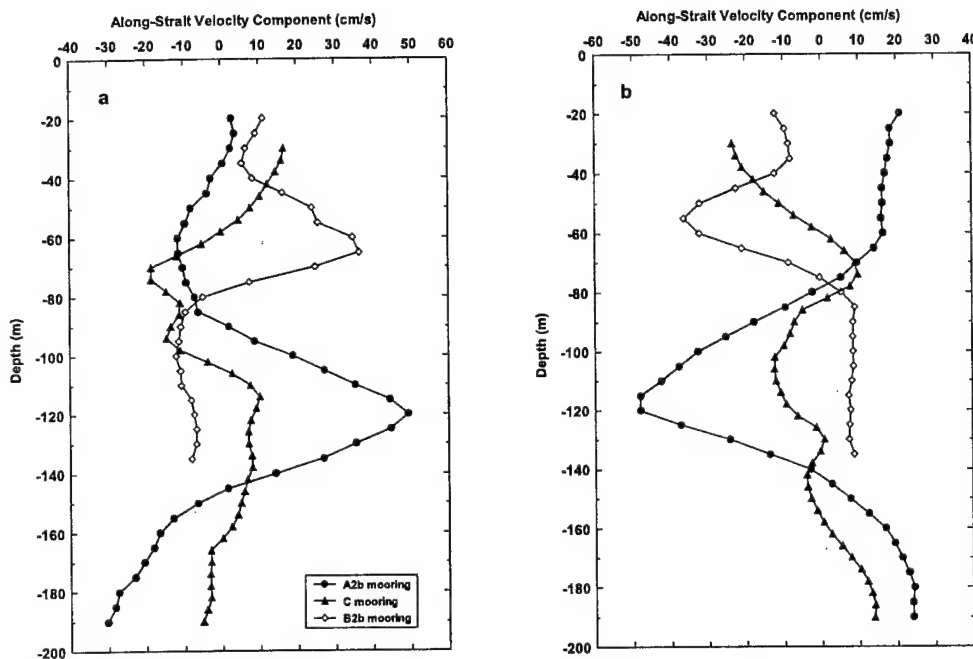


Figure 30. Examples of vertical distributions of the baroclinic along-strait current components for the winter stratification during (a) flood and (b) ebb tides.

Figures 30 and 31 show examples of the vertical distributions of the baroclinic currents of the flood and ebb tides for the winter and summer stratifications. In addition to the removal of the barotropic currents, the displayed data were band-passed (3 – 30 h) to suppress high frequency and subtidal fluctuations. For the two-layer flow stratification (Figure 30), the vertical distributions of the along-strait velocities with distinct maxima at the depth of the pycnocline are very common at Perim Narrows (A2b mooring) and the Hanish Sill (B2b mooring). The baroclinic currents in the middle of the Bab el Mandab Strait (C mooring) are much weaker and the vertical profiles are more intermittent in nature, and consequently the small maximum at ~ 110 m, as shown in Figure 30, is often not observed at all. The maximum rms value of along-strait velocity varies with the depth and location. The largest ones are found at Perim Narrows at the pycnocline depth where they generally vary between 25 cm/s and 50 cm/s. At C mooring, the largest values are found at the depth of 80 m, and they are usually less than 15 cm/s. Over the Hanish Sill, the strongest currents, with maximum speeds usually between 10 cm/s and 35 cm/s, are again present in the pycnocline region.

In summer (Figure 31), the baroclinic currents are weaker at all locations when compared to those observed for the winter stratification. The vertical profiles of these currents are very intermittent at Perim Narrows (A2b mooring) and in the middle of the

Strait (C mooring). At these locations, the strongest currents are usually observed between 160 m and 180 m where their speeds often reach 40 cm/s at Perim Narrows and 20 cm/s at C mooring. Over the Hanish Sill, a vertical structure of the along-strait velocity with a maximum located in the lower pycnocline zone is observed each day. The depth of the maximum may move up or down in the water column but on average, the maximum baroclinic currents are located between 90 m and 100 m where the maximum speeds are usually between 10 cm/s and 25 cm/s.

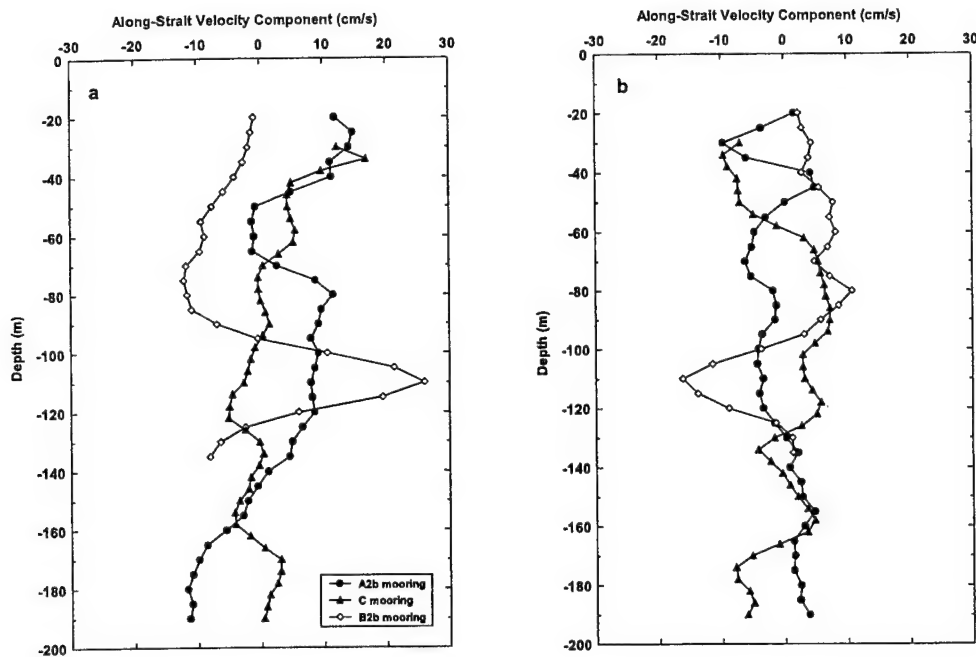


Figure 31. Examples of vertical distributions of the baroclinic along-strait current components for the summer stratification during (a) flood and (b) ebb tides.

In addition to variations in horizontal and vertical directions, the baroclinic currents also exhibit variability on a time scale longer than the tidal period. This time variability is associated with the fortnightly cycle, and it is especially apparent at depths of the enhanced baroclinic tidal currents during the winter at Perim Narrows and the Hanish Sill. These modulations, however, are not so evident for the summer period. Figure 32 shows, as an example, the time series of the currents from the pycnocline layer (120 m) at A2b mooring and the water level from G89 gauge (both located near Perim Narrows). The fortnightly cycle is evident in both time series. The amplitudes of the baroclinic currents are roughly proportional to the surface tidal amplitudes, since the baroclinic currents have larger amplitudes during the spring tide and smaller ones during the neap tide.

To identify major frequencies of the baroclinic currents, variance of the current components were computed from the data collected by the ADCP instruments (first deployment data), and variance preserving plots for the along-strait and cross-strait

components are shown in Figures 33 and 34. Regardless of the stratification configuration, for the motion with frequencies higher than 0.6 cpd there are distinct peaks at diurnal (centered at  $\sim$  1 cpd) and semidiurnal (centered at  $\sim$  1.94 cpd) frequencies as well as at higher frequencies ( $\sim$  3 cpd and  $\sim$  4 cpd). Further discussion will be limited only to the internal motion with diurnal and semidiurnal periods because semidiurnal and diurnal fluctuations are much more energetic than high frequency oscillations.

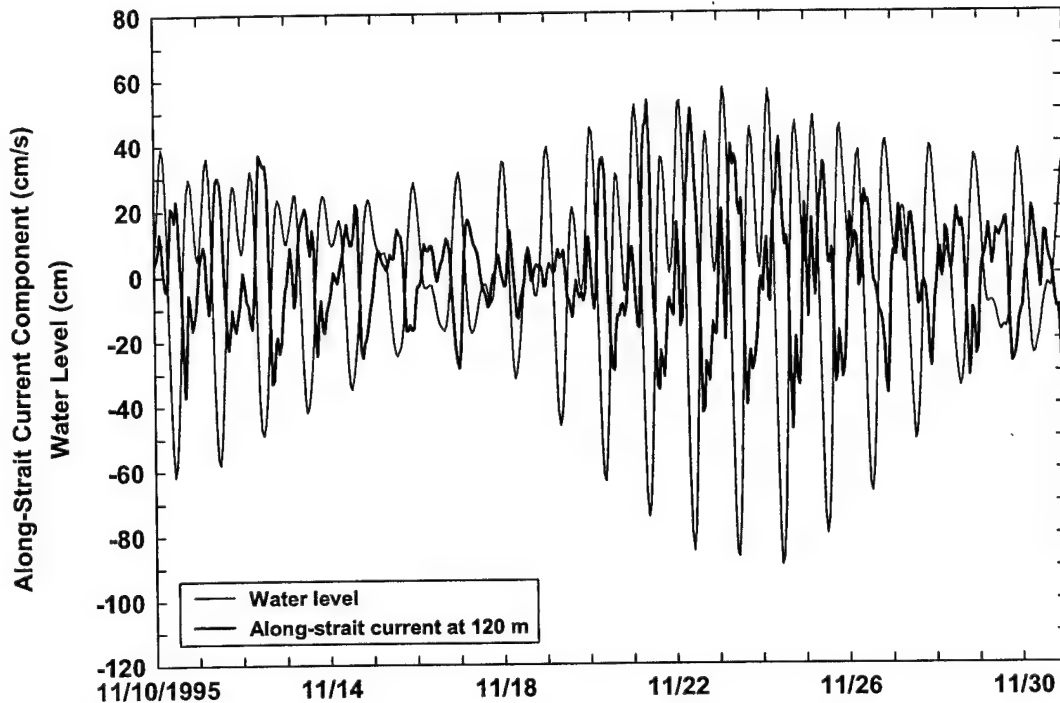


Figure 32. Water level fluctuations (G89) and baroclinic along-strait current component (A2b mooring) at 120 m observed near Perim Narrows - winter stratification.

The energy associated with the semidiurnal and diurnal frequencies varies greatly with depth as it is shown in Figure 35. This figure displays spectra of the along-strait baroclinic currents observed at the Hanish Sill for the winter stratification. For this stratification, the diurnal frequencies generally contain more energy than the semidiurnal ones. Furthermore, the spectra of the diurnal frequency have very distinct maxima located in the pycnocline regions at the Perim Narrows and the Hanish Sill locations. At the same locations, the along-strait component of the diurnal baroclinic currents contains more energy than the across-strait one at depths of the enhanced currents. At C mooring, energy associated with both components is very comparable with the maximum located at 70 m and 100 m for the along- and cross-strait components, respectively. In winter, the baroclinic currents with the semidiurnal period show an increase in energy near the same depths as the diurnal currents at Perim Narrows and the Hanish Sill. For the summer stratification period, the baroclinic current speeds in the Strait are lower compared to those observed in the winter. However, similar to the winter stratification, the energy

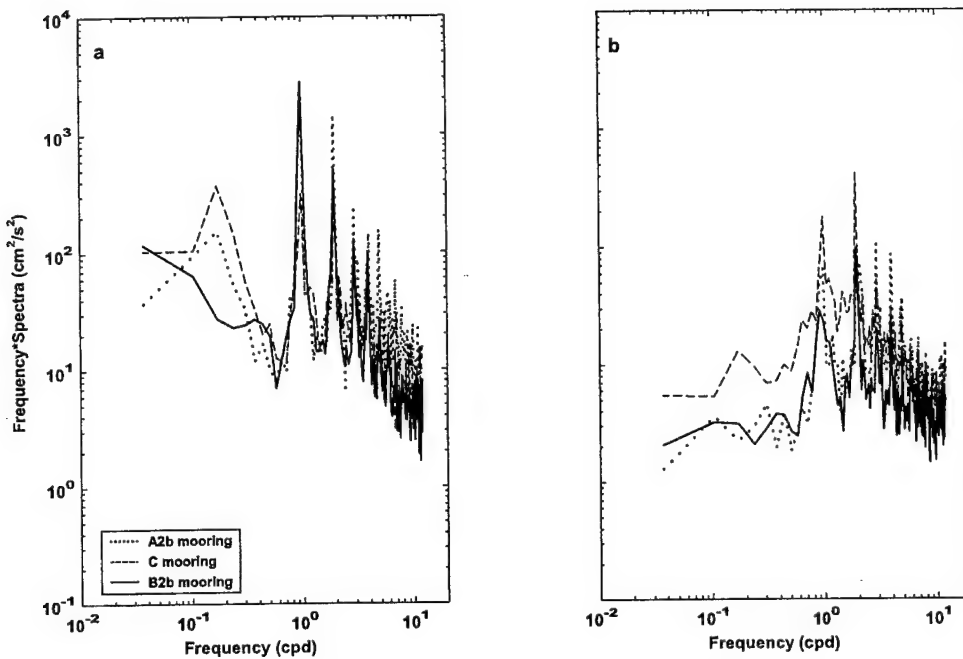


Figure 33. Variance-preserving plots of (a) along-strait and (b) cross-strait baroclinic current components observed in the pycnocline region at three different locations - winter stratification.

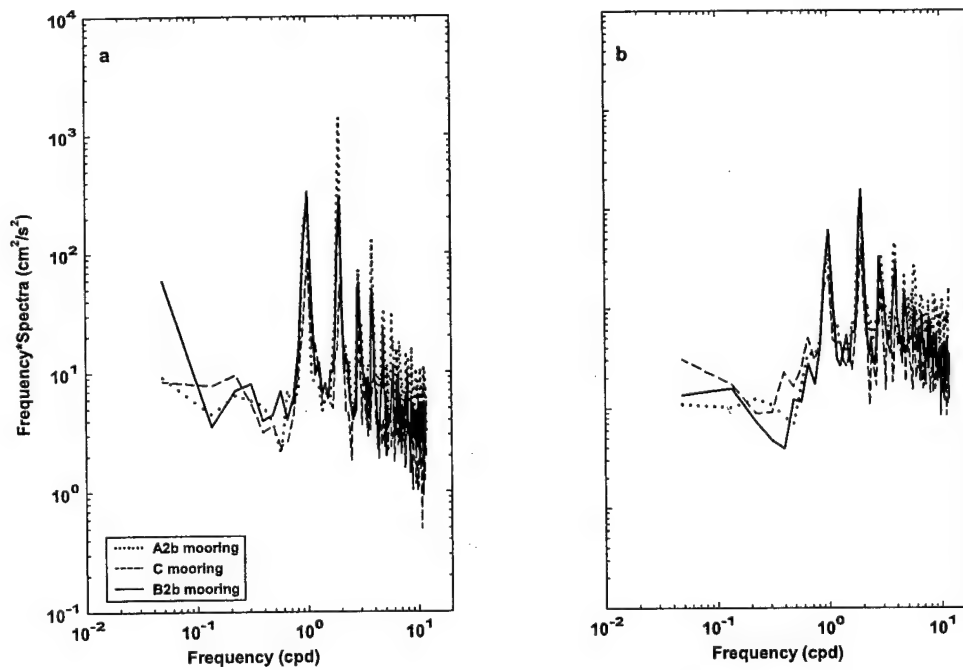


Figure 34. Variance-preserving plots of (a) along-strait and (b) cross-strait baroclinic current components observed at three different locations - summer stratification (current components at 160 m for A2b and C moorings, and at 100 m for B2b mooring).

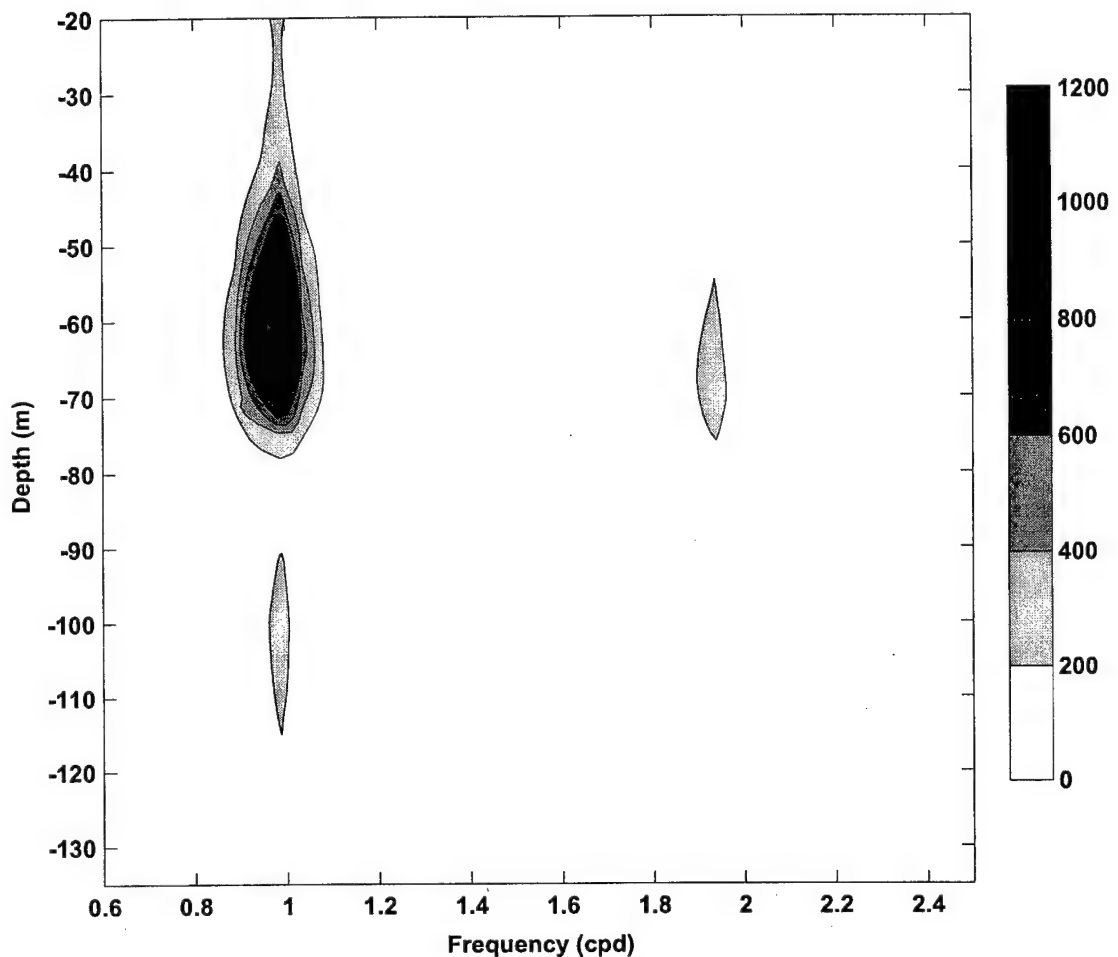


Figure 35. The vertical distribution of energy spectra ( $\text{cm}^2/\text{s}^2/\text{cpd}$ ) of the along-strait baroclinic current components near the Hanish Sill for the winter stratification.

maxima are only observed in the pycnocline regions. At Perim Narrows, the cross-strait component has much lower energy estimates than the along-strait one, which has maxima above 70 m and below 160 m for both semidiurnal and diurnal frequencies. Additionally, this maximum is larger for the semidiurnal currents. At C mooring, the spectra estimates for both frequency bands are very comparable at all depths with the maximum energy located between 40 m and 60 m and below 130 m. Finally, at the Hanish Sill, the diurnal and semidiurnal currents show a distinct energy maximum in the lower pycnocline region (between 90 m and 110 m) and a secondary maximum in the upper one (between 20 m and 40 m). Furthermore, in the lower pycnocline region, the along-strait component contains more energy than the cross-strait component, and energy associated with the diurnal band is higher than that contained in the semidiurnal band.

#### 4.2. Density fluctuations

The continuous time series of density are available only at the Hanish Sill and these series display quite different behavior for the winter and summer stratification. Figure 36 show an example of the  $\sigma_0$  time series at four depth levels. Unfortunately, the displayed data do not resolve the density distribution for the entire water column but they do give its fairly representative distribution for depths between 66 m and 145 m. They illustrate very clearly that for the density distribution associated with the summer stratification (July, August and September of 1995 are the months when the three-layer flow was very well established in the Strait), the largest density fluctuations are observed at 94 m and 117 m, whereas for the winter stratification (after 10/24/1995), they are generally confined to 66 m and 94 m. In both cases they are confined to the pycnocline layers. These fluctuations, of course, are a superposition of subtidal, tidal and higher frequency oscillations, but as long as the tidal fluctuations are considered they appear to be generally diurnal in nature. In the case of the summer stratification, they are only present in the second pycnocline region. This is because there were no data returned from the instrument deployed near the upper pycnocline in the summer of 1995. However, as the density data from the next two deployments seem to suggest, the oscillations exist in this pycnocline as well.

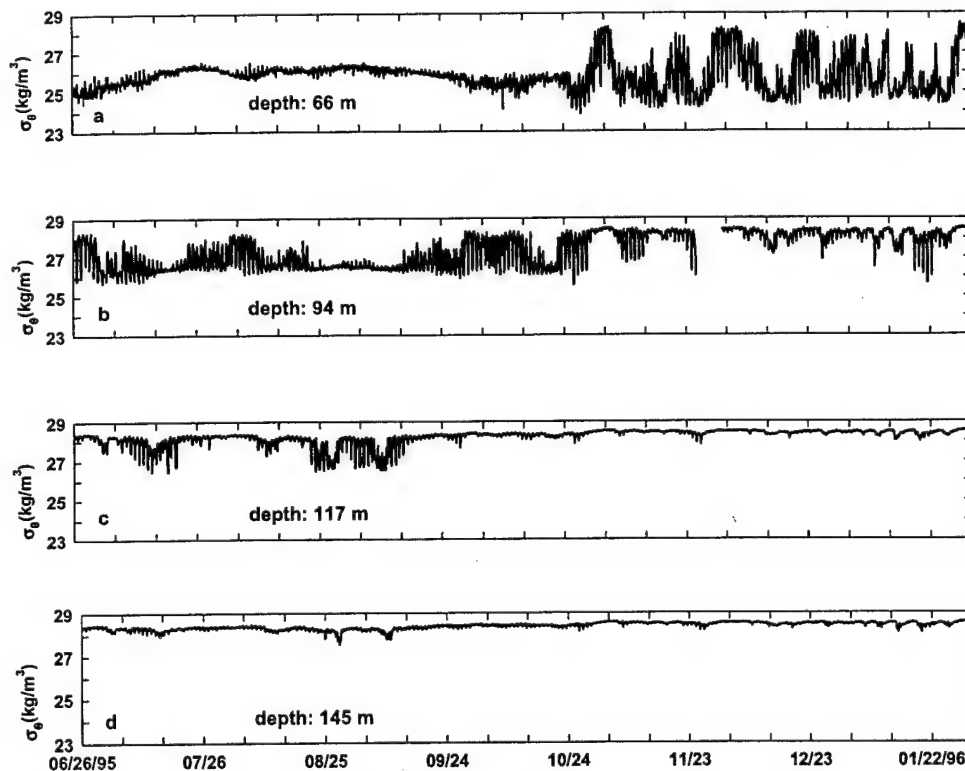


Figure 36. Time series of  $\sigma_0$  from four different depths at the Hanish Sill.

To identify the major periodicities of the density oscillations, variance preserving plots (Figure 37) were constructed separately for the winter and summer stratification

from the data displayed in Figure 36. Regardless of the subtidal flow phase, stratification and depth, all plots show peaks at diurnal, semidiurnal and higher frequencies (at  $\sim 1, 2, 3, 4$ , and  $5$  cpd). They also indicate that the largest variance estimates among principle tidal frequencies are found at  $66$  m for the winter stratification (Figure 37a) while for the summer stratification (Figure 37b), the highest values of the variance estimates are found at  $94$  m. Furthermore, at these depths, the peaks centered approximately at  $1$  cpd are larger than those centered  $\sim 2$  cpd.

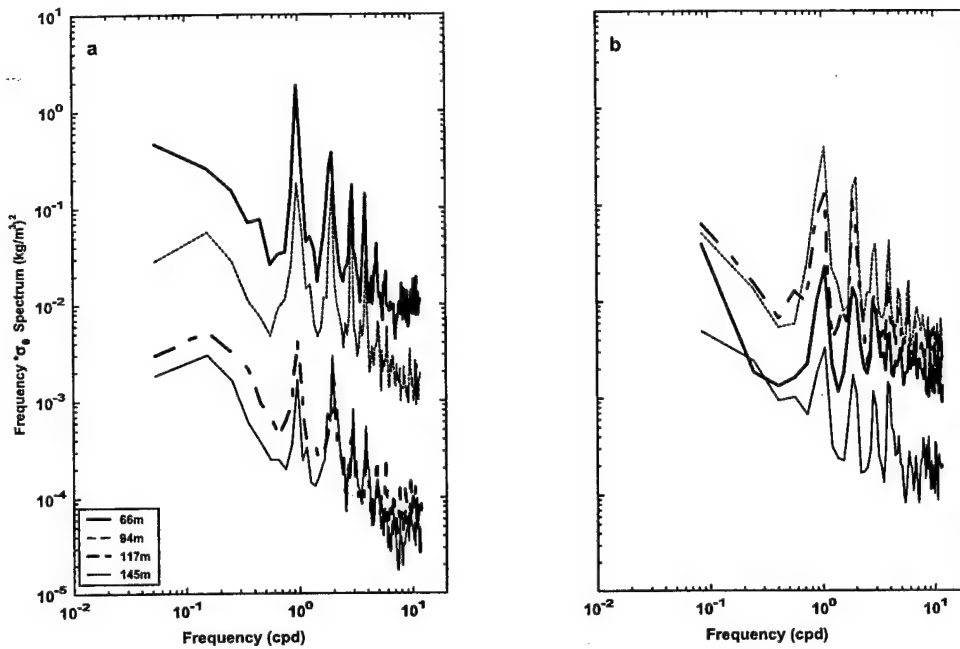


Figure 37. Variance-preserving plots of  $\sigma_\theta$  (a) for the winter and (b) summer stratifications.

The dominance of the diurnal fluctuations is also reflected by the percentage of the variance associated with the principle tidal bands, which for the diurnal tides is at least two times larger than that of the semidiurnal ones at depths of the energetic fluctuations; for instance, 25% of variance occurs in the diurnal frequencies as opposed to only 4% associated with the semidiurnal frequencies for the winter stratification. In summer, between 30% and 46% of variance is contained in the diurnal band and no more than 13% in the semidiurnal band for the time series collected in the region of the second pycnocline. In general, at depths in or near the pycnocline layers the tidal fluctuations are dominated by the diurnal tides, while at depths where the density shows little variability, the principle tidal bands together account for no more than 10% of variance, and this variance is usually equally divided between both bands.

To estimate a possible displacement range of these internal fluctuations, the  $\sigma_\theta$  time series were interpolated, and the results are displayed in Figure 38. For clarity, approximately a month of the interpolated time series for a few isopycnals, which as

indicated by CTD casts should be located at pycnocline regions, are shown for the winter and summer stratifications. Furthermore, for the summer stratification, the measurements resolved fairly well only the lower pycnocline layer; however, as has been mentioned earlier, they seem to exist in the upper pycnocline, but because of poor time and vertical resolutions of the data set, reliable results were not obtained for this region. The interpolated  $\sigma_0$  time series suggest that for both stratifications the minimum displacement range is just a few meters, but the maximum displacement range can be as large as 20 m.

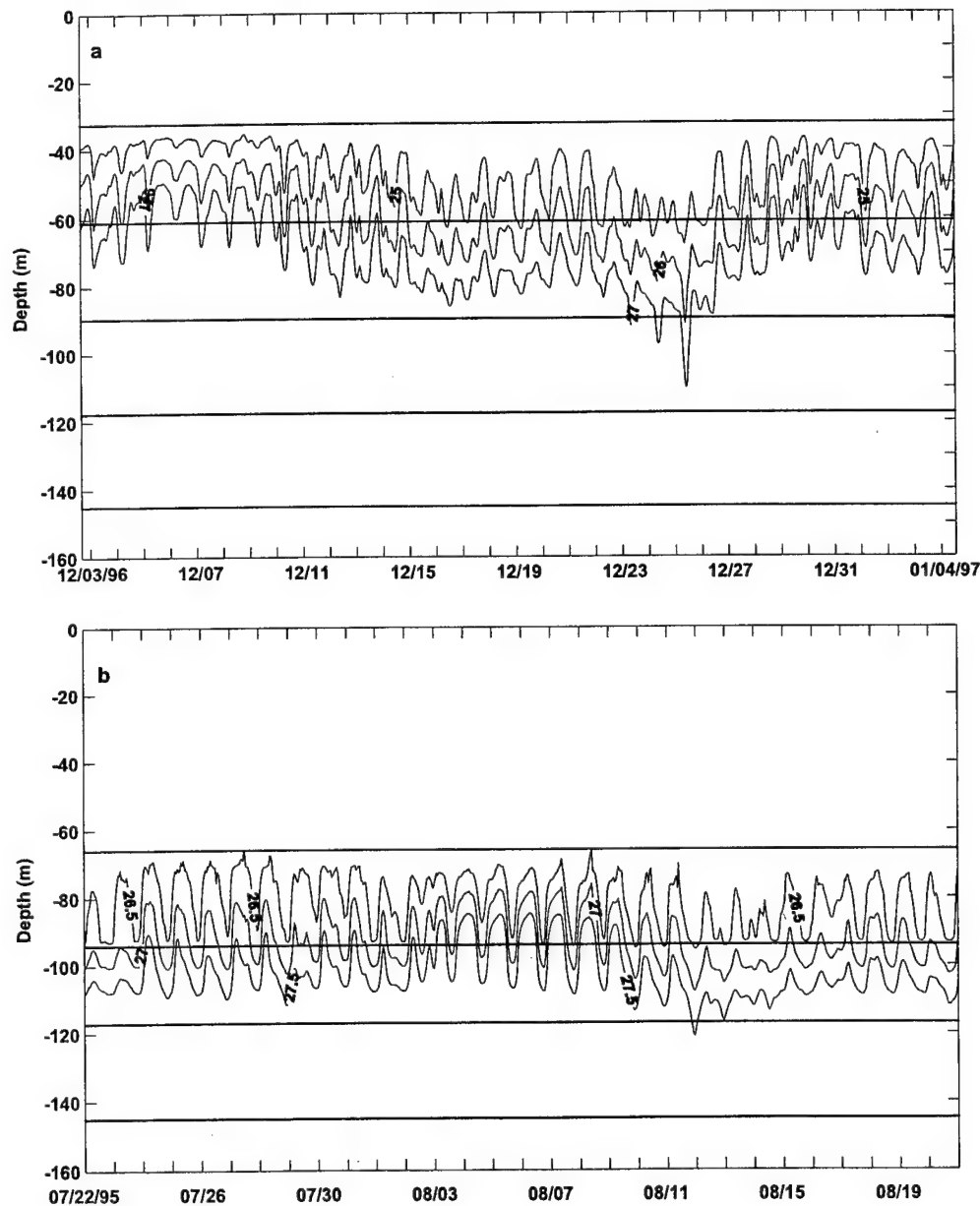


Figure 38. Interpolated  $\sigma_0$  time series for (a) the winter and (b) summer stratifications; thick horizontal lines indicate the depth of the instruments.

#### **4.3. Empirical orthogonal function analysis of baroclinic tidal currents**

To study spatial relationships of the baroclinic motion, empirical orthogonal function analysis (EOF) in the frequency domain was employed. This method assumes that any variable can be considered as a sum of orthogonal empirical functions and residuals. The EOF analysis in the frequency domain was developed for applications in meteorological data analysis by Wallace and Dickinson (1972). It was also successfully applied in oceanography to study internal tides by Denbo and Allen (1984), Bartkovich (1985), and Rosenfeld (1990) among others. A purpose of this approach is to extract the coherent part of the current variance for a given frequency band. The frequency-domain EOF analysis involves computing a band-averaged cross-spectral matrix for real time series and then calculating the eigenvectors and eigenvalues of that matrix. The complex eigenvectors are used to compute EOF amplitudes and phases.

The EOF method was applied separately to data subsets that contained the current measurements (with the barotropic component removed) collected during the winter and summer stratifications (first deployment data from A2b, C, and B2b moorings). Furthermore, the separate cross-spectral matrixes were constructed for the diurnal and semidiurnal bands, defined here as 0.96 – 1.04 cpd for the former and 1.9 – 1.98 cpd for the latter. The advantage of looking at the energy in the frequency band, rather than at the single frequency, is that the internal tidal energy may be spread out in a band around the tidal line due to Doppler shifting by the low frequency flow (Wunsch, 1975). Matrix elements were taken as an average of spectral and cross-spectral estimates obtained from a 14-day non-overlapping subsets (10 and 6 independent estimates of each element for the winter and summer periods, respectively). Included in a given matrix were the average estimates of both along-strait and cross-strait current components.

The EOF results show that regardless of the location, frequency band, and stratification type, 80% or more current variance is accounted for by the first two EOF modes. On average, the first mode always explains more variance (the averaged variance varies between 66% and 91% for all considered cases) than the second EOF mode (5% - 21%). The exact mode variance as well as their amplitudes and phases depend on depth. Finally, at depths where the variance of the first mode is minimal, the second mode usually accounts for the majority of the baroclinic current variance.

Figures 39, 40, and 41 display ellipses of the first two EOF modes of the diurnal band for the winter stratification period at Perim Narrows (A2b mooring), C mooring, and the Hanish Sill (B2b mooring), respectively. As mentioned earlier, during this stratification period, the baroclinic signal is very strong in the Strait, especially near Perim Narrows and the Hanish Sill, and the modes computed from the data collected at these locations show a few interesting features. First of all, the currents associated with each mode are nearly rectilinear and aligned with the along-strait axis, especially at depths where amplitudes of the major axis are large. At both locations, there are one (the second EOF mode at Perim Narrows and the first EOF mode in the Hanish Sill) or two (the first EOF mode at Perim Narrows and the second EOF mode at the Hanish Sill) current minima in the water column. In addition, approximately at depths of these minima, there is a phase shift. This phase shift can be very rapid with the phase difference of  $\sim 180^\circ$  as it is, for instance, at depths between 70 m and 90 m for the first EOF mode in the Hanish Sill or the phase may change gradually with the maximum phase difference of  $145^\circ$  as it is observed for the first mode between 20 m and 140 m.

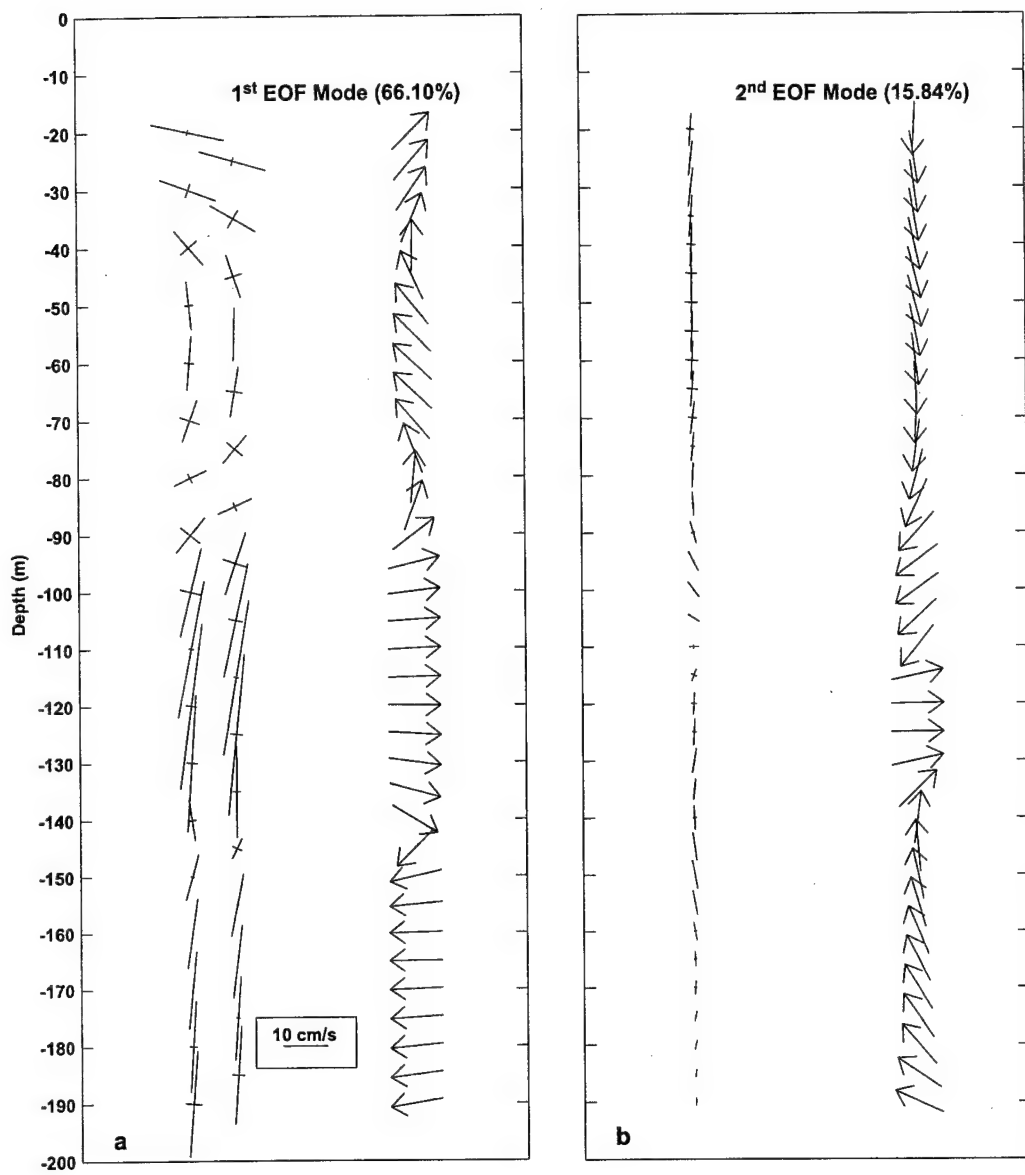


Figure 39. Current ellipse parameters for (a) the first and (b) second EOF modes of the diurnal band at Perim Narrows for the winter stratification (major and minor axes are on the left side; the axes were moved slightly to the right for odd depths for clarity; phases are denoted as arrows on the right of each panel, and they are relative to the along-strait velocity at 20 m).

at Perim Narrows. Either the vertical distribution of the current amplitudes or phases of the EOF modes do not have precise distributions of amplitudes and phases associated with dynamic modes (zero amplitudes at depths of a  $180^\circ$  phase shift); however, they resemble them, i.e., the first EOF mode at Perim Narrows and the second EOF at the

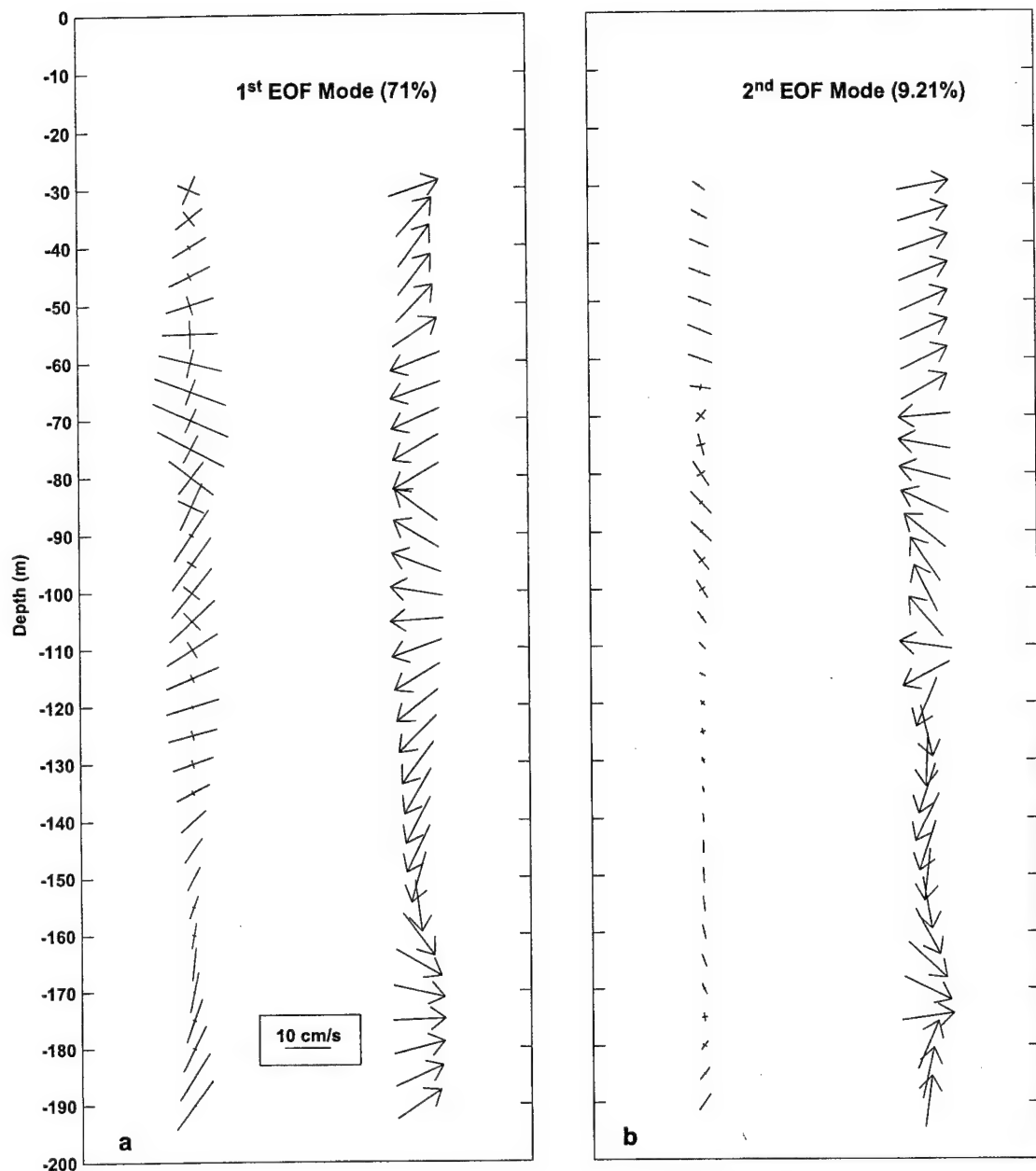


Figure 40. Current ellipse parameters for (a) the first and (b) second EOF modes of the diurnal band at C mooring for the winter stratification (major and minor axes are on the left side; phases are denoted as arrows on the right, and they are relative to the along-strait velocity at 30 m).

Hanish Sill are fairly comparable to the second dynamic mode, while the first EOF mode at the Hanish Sill is analogous to the first dynamic mode. These findings imply that at these two locations, the baroclinic response may be limited to a few lowest baroclinic dynamic modes, and they suggest that it may be in the form of the first and second dynamic modes at the Hanish Sill and the second dynamic mode at Perim Narrows.

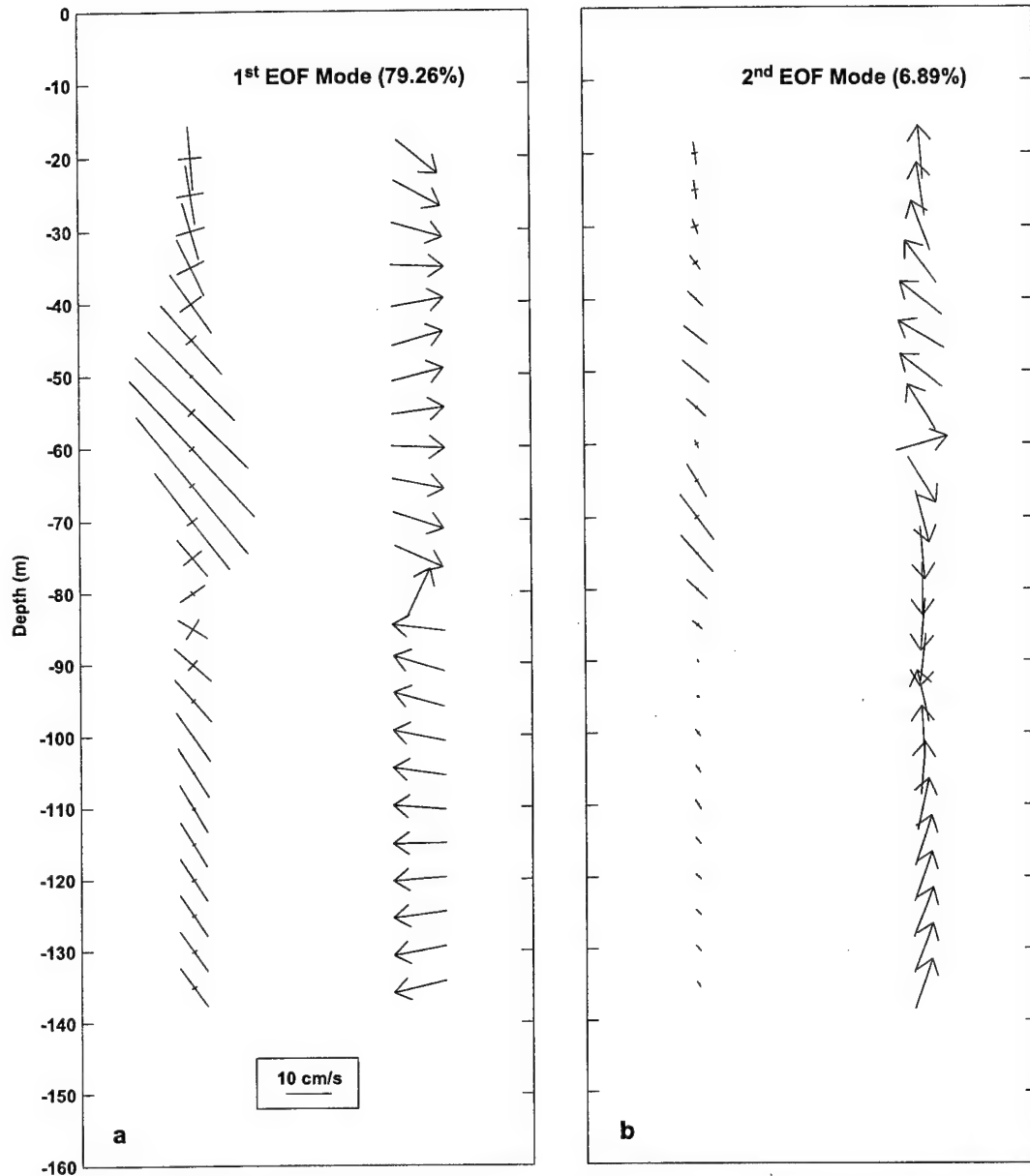


Figure 41. Current ellipse parameters for (a) the first and (b) second EOF modes of the diurnal band at the Hanish Sill for the winter stratification (major and minor axes are on the left side; phases are denoted as arrows on the right, and they are relative to the along-strait velocity at 20 m).

At C mooring, the baroclinic currents are rather weak, and distributions of the ellipse parameters of the diurnal EOF modes are quite variable (Figure 40). This is also true for other analyzed cases (the semidiurnal band for the winter period and both frequency bands for the summer period). In general, the currents seem to be less polarized in the along-strait direction, especially in the upper part of the water column. The phase may shift  $\sim 180^\circ$  or change gradually, but these phase changes are not always accompanied by the current amplitude minimum.

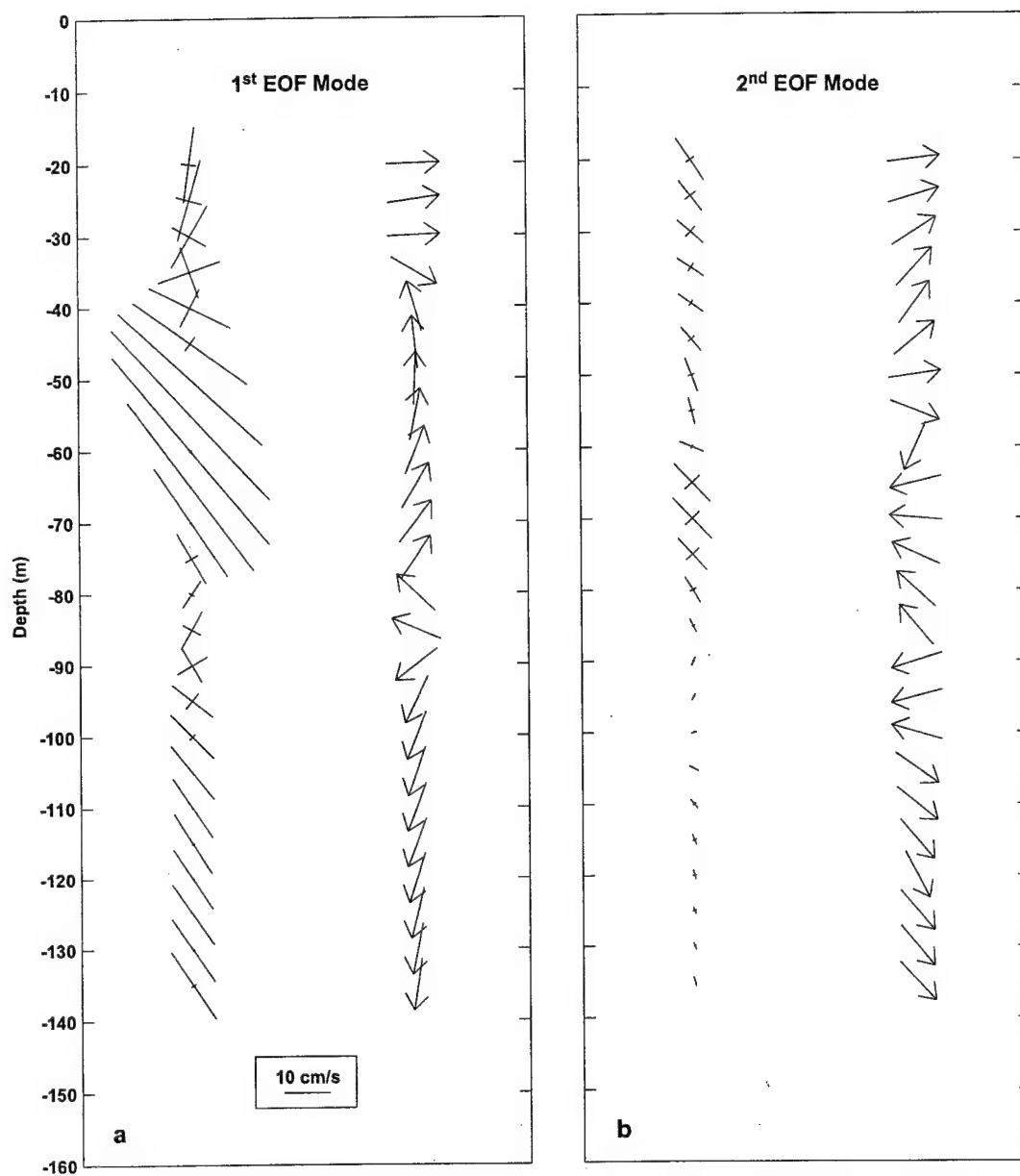


Figure 42. Current ellipse parameters for (a) the first and (b) second EOF modes of the diurnal band at the Hanish Sill for the winter stratification period between 12/02/1996 – 01/02/1997 (major and minor axes are on the left side; phases are denoted as arrows on the right, and they are relative to the along-strait velocity at 20 m).

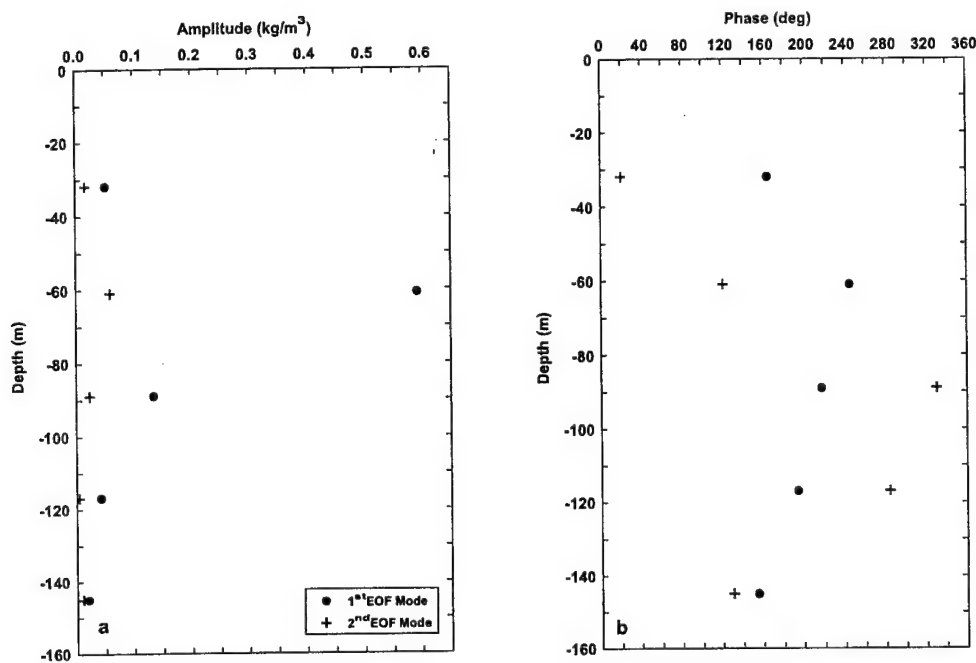


Figure 43. Amplitudes and phases of density for (a) the first and (b) second EOF modes of the diurnal band at the Hanish Sill for the winter stratification period between 12/02/1996 – 01/02/1997 (phases are relative to the along-strait velocity at 20 m).

To extract the coherent part of the velocity and density fluctuations in the diurnal frequency band, the EOF analysis was also applied to the data set that consisted of the velocity components and density measurements collected at the Hanish Sill during the third deployment. The times series used in this analysis were much shorter (December 2, 1996 – January 2, 1997) but covered the time period when density data were simultaneously collected at five different depths, which should give a good approximation of the density distribution for the winter stratification. Results are displayed in Figures 42 and 43. On average, 98% of the variance is accounted for by the first two modes (88% for the first and 10% for the second). The ellipse parameters (Figure 42) of the currents such as major axis, minor axis and direction are very similar to those obtained for the velocity data alone; however, the phase distribution is different and its behavior is not as consistent with the dynamic modes as it is when the velocity data are analyzed alone (Figure 40). In addition, density amplitudes of the first EOF mode (Figure 43a) reach maximum in the pycnocline layer; however, its phase is not constant with depth as one would expect if the first dynamic mode dominated the baroclinic response at the Hanish Sill. Similar conclusions are also true for the second EOF mode. This lack of consistency in the expected behavior may be partly caused by the poor vertical resolution of the density measurements.

#### 4.4. Modal structure of the tides

It is possible to discriminate between barotropic and baroclinic flows, and between the different modes of the baroclinic motions, by examining the modal structure (dynamic mode decomposition) computed from the density distribution. The dynamic mode decomposition starts from hydrodynamics equations with the assumptions that the fluid is horizontally unbounded, linear and Boussinesq, and dissipative effects as well as effects associated with the horizontal inhomogeneity of ambient stratification are negligible. In this case, the initial set of the equations of motion, conservation of density, and continuity reads (LeBlond and Mysak, 1978):

$$\frac{\partial u}{\partial t} - fv = -\frac{1}{\rho_0} \frac{\partial p}{\partial x} \quad (5a)$$

$$\frac{\partial v}{\partial t} + fu = -\frac{1}{\rho_0} \frac{\partial p}{\partial y} \quad (5b)$$

$$\frac{\partial w}{\partial t} = -\frac{1}{\rho_0} \frac{\partial p}{\partial z} - \frac{g}{\rho_0} \rho \quad (5c)$$

$$\frac{\partial \rho}{\partial t} - \frac{N^2 \rho_0}{g} w = 0 \quad (5d)$$

$$\frac{\partial u}{\partial x} + \frac{\partial v}{\partial y} + \frac{\partial w}{\partial z} = 0 \quad (5e)$$

where  $u$  and  $v$  are the horizontal velocity components,  $w$  is the vertical velocity component,  $p$  and  $\rho$  are the perturbations of pressure and density,  $\rho_0$  is the mean sea-water density,  $N$  is the buoyancy frequency,  $f$  is the Coriolis parameter, and  $g$  is the acceleration due to gravity. The system of boundary conditions, for which the solution of equations 5a through 5e is valid, contains the condition of continuity of pressure and the kinematic relation at the free surface ( $z = 0$ )

$$p = g\rho_0 \zeta \quad (5f)$$

$$w = \frac{\partial \zeta}{\partial t} \quad (5g)$$

and the condition of impermeability of the sea bottom ( $z = -H$ )

$$w = 0 \quad (5h)$$

where  $\zeta$  is the free surface elevation.

For a harmonic oscillation with a given tidal frequency  $\omega$ , the  $u$ ,  $v$ ,  $w$ ,  $p$ , and  $\rho$  variables may be represented as

$$u(x, y, z, t) = \frac{1}{\rho_0} \sum_{n=1}^{\infty} P_n(z) U_n(x, y) \exp(i\omega t) \quad (6a)$$

$$v(x, y, z, t) = \frac{1}{\rho_0} \sum_{n=1}^{\infty} P_n(z) V_n(x, y) \exp(i\omega t) \quad (6b)$$

$$w(x, y, z, t) = i\omega \sum_{n=1}^{\infty} P_n(z) \Pi_n(x, y) \exp(i\omega t) \quad (6c)$$

$$p(x, y, z, t) = \sum_{n=1}^{\infty} P_n(z) \Gamma_n(x, y) \exp(i\omega t) \quad (6d)$$

$$\rho(x, y, z, t) = \sum_{n=1}^{\infty} \frac{dP_n(z)}{dz} \Gamma_n(x, y) \exp(i\omega t) \quad (6e)$$

On substituting equations 6a to 6e into equations 5a to 5e, and introducing a separation constant  $|k_n|$  where  $k_n$  is the n mode wavenumber, the following equation is obtained:

$$\frac{d}{dz} \frac{\omega^2 - f^2}{N^2 - \omega^2} \frac{dP_n}{dz} + \frac{N^2}{g} \frac{\omega^2 - f^2}{N^2 - \omega^2} \frac{dP_n}{dz} + |k_n|^2 P_n = 0 \quad (7a)$$

Equation 7a together with the rewritten boundary conditions at the free surface ( $z = 0$ ):

$$\frac{dP_n}{dz} + \frac{N^2 - \omega^2}{g} P_n = 0 \quad (7b)$$

and at the bottom ( $z = -H$ ):

$$\frac{dP_n}{dz} = 0 \quad (7c)$$

are solved to determine the vertical distribution of modal pressure amplitudes (pressure eigenfunctions of mode n)  $P_n(z)$ . For a given buoyancy frequency profile, equation 7a can be solved numerically, and to evaluate the eigenfunctions for the buoyancy frequency profiles observed in the Bab el Mandab Strait, the finite difference approximation proposed by Marchuk and Kagan (1984) was used. Furthermore, horizontal velocities are proportional to the pressure eigenfunctions and are considered as a linear combination of these eigenfunctions plus residuals, so if the pressure eigenfunctions are known one can fit them in a least squares sense to find horizontal velocity modes for a given tidal frequency. To determine the relative importance of different modes for the diurnal and semidiurnal frequencies, the modal fit was applied to average Fourier coefficients (averages of the Fourier coefficients obtained from a 14-day non-overlapping data subsets) of the horizontal velocity components, and these coefficients centered at 1 cpd and 1.94 cpd were considered to be representative for the entire diurnal and semidiurnal frequency bands, respectively. In addition, the fit was performed only for the velocity data collected at A2b, C, and B2b moorings in the winter stratification period for two

reasons: (1) the baroclinic signal is much stronger in the winter and its contribution to the overall tidal flow is very apparent, and (2) the density structure for the summer stratification is much more variable than that observed in the winter, and the number of CTD casts is two small (the maximum is 4 as opposed to at least 10 for the winter stratification) to find the representative buoyancy distribution at different moorings for this season.

The dynamic mode decomposition is only valid if (1) there are no lateral boundaries, (2) the bottom is flat, and (3) the mean flow speed is much smaller than the wave speeds of different modes. For the Bab el Mandab Strait, none of these assumptions is strictly met. However, A2b, C, and B2b moorings are located in the deep channel away from its vertical walls, and local depth variations in the channel near these moorings are rather small, so the first and second assumptions may be assumed to be locally valid. The third assumption is met for the barotropic mode because its speed is always larger than the seasonal flow speed (assuming that the average depth of the Strait is 50 m, the barotropic mode speed is 22 m/s while the seasonal flow speed is on the order of 1 m/s). The speeds of the baroclinic modes are usually less than 1 m/s and decrease as the mode number increases so baroclinic mode amplitudes of the tidal flow are influenced by the mean flow advection as shown, for instance, by Thomson and Huggett (1980) in the Johnstone Strait. However, the purpose of this decomposition is to determine the relative importance of the different modes in the Bab el Mandab Strait, not to evaluate the exact values of the amplitudes for each mode. Therefore, for this purpose, results from the dynamic mode decomposition should be good enough at the moment, but the influence of the seasonal flow on the baroclinic modes in the Strait definitely requires further investigations.

Results of the modal decomposition show that regardless of the frequency and location, the fit of all possible modes in each mooring (34 modes for A2b mooring, 32 modes for C mooring, and 23 for B2b mooring) accounts for from 50% to 90% of the observed variance. The lowest percentage of variance is usually observed for the Fourier coefficients of the cross-strait velocity component, which is not surprising because this component is weak and its coefficients are very small and extremely variable with depth. In addition, if this percentage is compared with the percentage of the explained variance when the barotropic mode and the first three baroclinic modes are only fitted, the difference is, on average, less than 3%; therefore, it can be concluded that the lowest four dynamic modes are needed to describe the observed variability in the diurnal and semidiurnal frequency bands in the Bab el Mandab Strait.

Two examples of barotropic and the first three baroclinic modes of the semimajor axis, which display the largest variations in the Strait and were computed from the respective Fourier coefficients found for tidal currents observed near Perim Narrows, C mooring and the Hanish Sill for the semidiurnal and diurnal frequencies, are shown in Figures 44 and 45. For both tidal frequency bands, the barotropic mode (mode 0) clearly dominates the tidal flow. There is some contribution from the first baroclinic mode (mode 1) at Perim Narrows and from the second mode (mode 2) at the Hanish Sill for the semidiurnal tidal flow but this contribution is rather small in comparison to the barotropic mode (Figure 44). In contrast, the contribution from the baroclinic modes for the diurnal frequency band can be fairly large (Figure 45). At Perim Narrows, the second (mode 2) and third (mode 3) modes clearly dominate. All three baroclinic modes seem to be

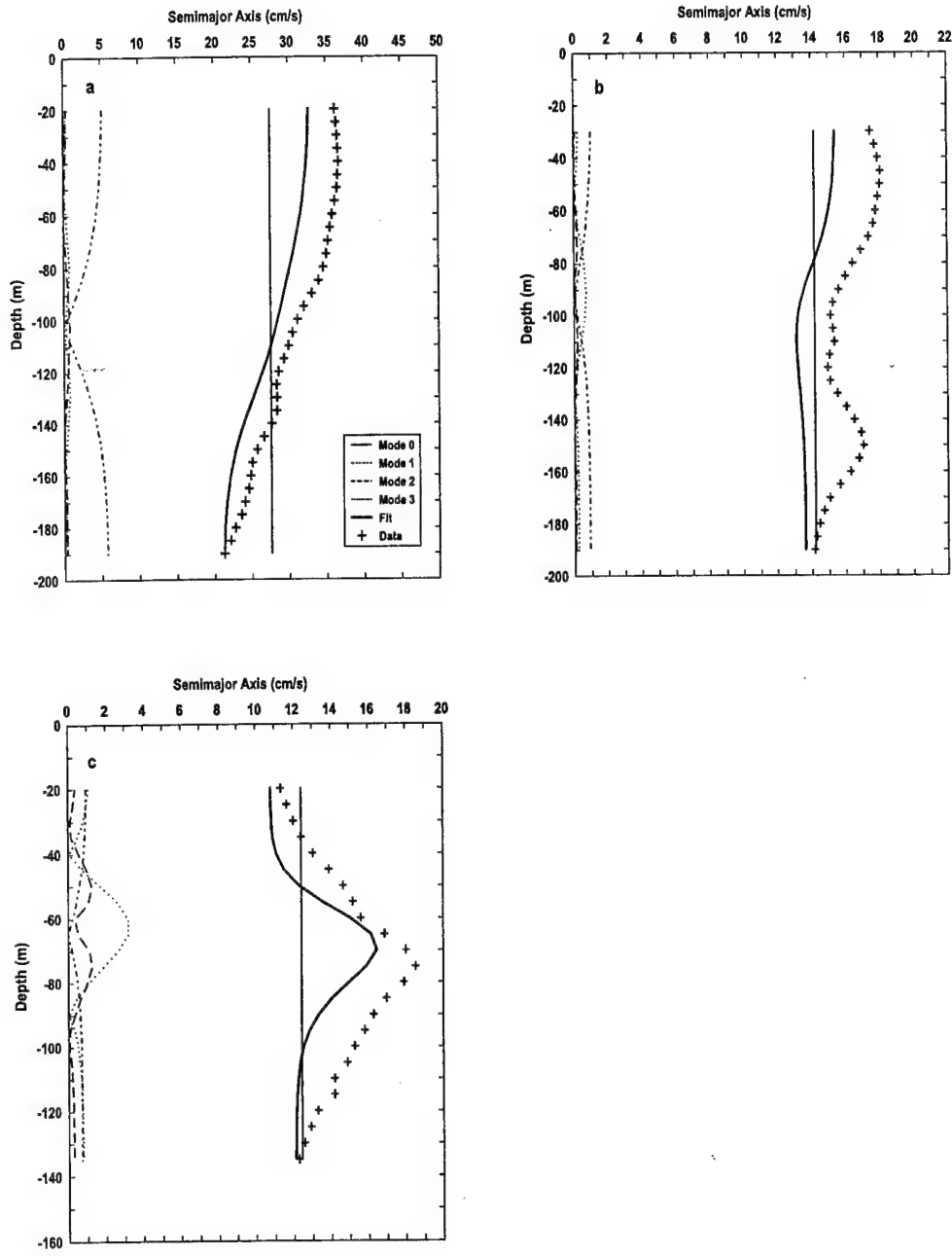


Figure 44. Amplitudes of the semimajor axes of barotropic (mode 0), first baroclinic (mode 1), second baroclinic (mode 2), and third baroclinic (mode 3) modes of the semidiurnal tidal currents for the winter stratification at (a) Perim Narrows (A2b mooring), (b) C mooring, and (c) the Hanish Sill (B2b mooring); amplitudes of this axis computed from the measurements are denoted by pluses and amplitudes obtained from fitting the first four modes (modes 0 through 3) are shown as a thick continuous line.

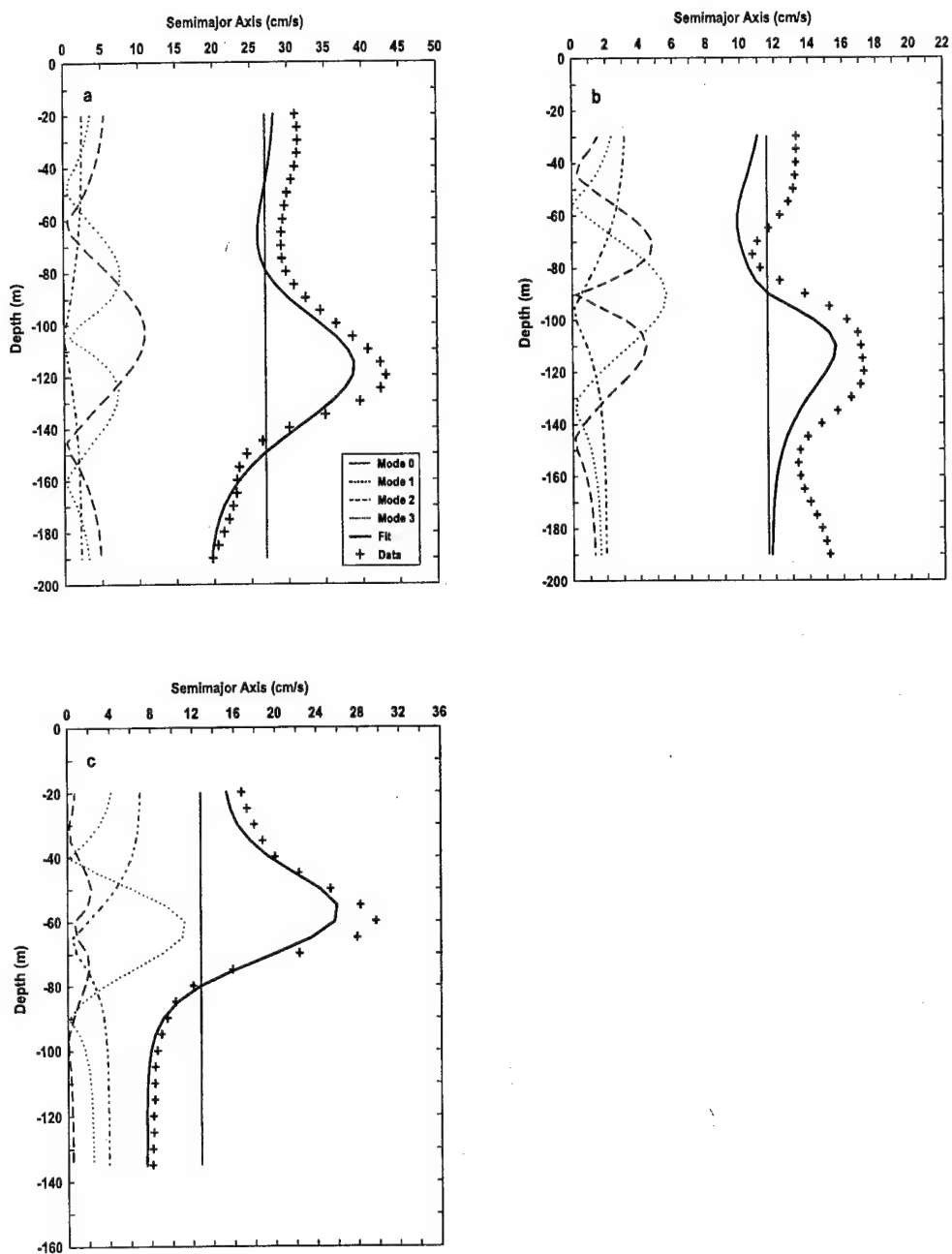


Figure 45. Amplitudes of the semimajor axes of barotropic (mode 0), first baroclinic (mode 1), second baroclinic (mode 2), and third baroclinic (mode 3) modes of the diurnal tidal currents for the winter stratification at (a) Perim Narrows (A2b mooring), (b) C mooring, and (c) the Hanish Sill (B2b mooring); amplitudes of this axis computed from the measurements are denoted by pluses and amplitudes obtained from fitting the first four modes (modes 0 through 3) are shown as a thick continuous line.

important at C mooring, while the baroclinic response near the Hanish Sill is generally dominated by the first and second baroclinic modes. In addition, the results of the dynamic mode decomposition at Perim Narrows and the Hanish Sill concerning the baroclinic modes are very comparable to the results of the EOF analysis: these two methods suggest the importance of the same dynamic modes, and perhaps this agreement makes the results of the dynamic mode decomposition less questionable considering the fact that this decomposition was performed for the region where the required assumptions are not met.

#### 4.5. Baroclinic responses to the tidal forcing in other regions

Different internal baroclinic responses to the tidal forcing have been observed and described, for instance, in the Strait of Gibraltar (Lacomb and Richez, 1982; La Violette and Arnone, 1988; Armi and Farmer, 1988; Pettigrew and Hyde, 1990), the Strait of Georgia (Hughes, 1969; Gargett, 1976), in Knight Inlet (Farmer and Smith, 1980) and the Strait of Messina (Griffa et al., 1986; Di Sarra et al., 1987; Sapia and Saluti, 1987; Brandt et al., 1999).

It has been shown that the tidally-driven flow of stratified water over very variable bottom topography produces a broad variety of different internal responses depending on the degree of stratification and the strength of tidal forcing. In Knight Inlet, for example, Farmer and Smith (1980) have identified three distinct types of time dependent responses: (1) internal tides, (2) traveling internal surges arising from the advance of lee waves or jumps over the sill against the slackening tide, and (3) stationary wave trains formed upstream of the sill crest that subsequently evolve into traveling surges. They have not discussed the generation of internal tides, but, based on time series CTD profiles, they have concluded that internal tides are of the second baroclinic mode because the vertical excursion of isopycnals continues to increase with depth well below 30 m where the first baroclinic mode has its maximum. Based on the 60-hour Bathysonde profiles of temperature and salinity from November, Siedler (1969) has pointed out that near Perim Narrows, the greatest fluctuations of these parameters are generally confined to the upper part of the pycnocline. His salinity measurements also show that isohalines do not go up and down together, but they seem to be out of phase in the upper and lower part of the transition zone. The results of the dynamic mode decomposition, if one assumes that they are valid, for the winter stratification data collected near Perim Narrows, show that in the upper part of the pycnocline the eigenfunctions of the vertical displacement associated with the second and third mode have the largest amplitudes. These findings together with Siedler's observations imply that, if the response is in the form of the internal tide this tide may be of the second baroclinic mode with some contribution from the third mode. However, observations presented by Farmer and Smith (1980) also show that spreading of isopycnals can be also associated with hydraulic jumps or lee waves of the second mode so the spreading of isohalines near Perim Narrows may be generated by these features as well. Additionally, these authors have also described responses such as lee waves and undular bores that are of the first baroclinic mode. They have pointed out that the response is of the first mode if the tidal flow is supercritical with respect to this mode. However, if the flow is approximately critical or subcritical for the first mode and simultaneously supercritical with respect to the second mode the response is of the latter. Later observations from Observatory Inlet

(Farmer and Denton, 1985) have shown that the baroclinic responses can be of the second and first mode successively as the ebb flow accelerates.

Bores of the first and second mode have been observed in the Strait of Gibraltar by Armi and Farmer (1988), and the latter type manifests as a spreading of the isopycnals accompanied by mixing. The large amplitude stationary bores form downstream of Camarinal Sill during tidal outflow (ebb tides), and later they degenerate into a series of large amplitude internal waves with a period of ~1000 s, which propagate eastward. Armi and Farmer (1988) have also observed a small amplitude undular bore formation during flood tides. In the Strait of Messina, Brandt et al. (1999) have reported the presence of internal bores that later degenerate into short period internal solitary waves. Short period internal waves generated by tidal flow have been also observed in the Strait of Georgia (Hughes, 1969; Gargett, 1976).

At present, the only apparent conclusion about the baroclinic flow in the Bab el Mandab Strait is that the velocity and density observations distinctly show that the tidal flow has a baroclinic component. This baroclinic component is primarily of a diurnal period, and the strongest signal is observed in the pycnocline layer. Additionally, this signal is more pronounced for the winter stratification period and it is very distinct at Perim Narrows and the Hanish Sill. Analyses of the data suggest that the baroclinic velocities seem to contain strong contributions from the second and third baroclinic modes at Perim Narrow, and from the first and second modes at the Hanish Sill. However, to decipher what type of baroclinic responses to the tidal forcing are actually present at the Bab el Mandab Strait, more detailed (finer resolution in time and space) observations of density and currents are definitely required considering the fact that this response may have several different forms and that some of them, such as solitary waves, cannot be resolved by the BAM data because of the large sampling interval (0.5 h).

## 5. TWO-DIMENSIONAL FINITE ELEMENT MODEL OF BAROTROPIC TIDES IN THE BAB EL MANDAB STRAIT

To examine in more detail the barotropic tides, which dominate the tidal signal in the Bab el Mandab Strait, a numerical model is implemented. The overall purpose of this numerical study is (1) to describe in more detail the distributions of the barotropic tidal elevation and currents within the Strait; (2) to evaluate whether residual circulation generated by the barotropic tidal currents contributes significantly to the overall circulation in this region; (3) to examine which momentum balance terms are dominant; and (4) to estimate energy fluxes and energy dissipation in the Strait.

The barotropic tides in the Bab el Mandab Strait are numerically simulated with the two-dimensional finite element hydrodynamic model named ADvanced Two-Dimensional Depth-Integrated CIRCulation Model for Shelves, Coasts and Estuaries (ADCIRC-2DDI) developed by Luettich et al., (1992) and Westerink et al. (1994). Selection of a finite element model was justified mainly by its accuracy in modeling of tides and, additionally, as a result of finite element formulation by its grid flexibility. The accuracy in tidal simulations is well documented in the literature (Walters, 1987; Werner and Lynch, 1987; Walters and Werner, 1989; Westerink et al., 1989; Westerink et al., 1992; Foreman et al., 1995). The finite element formulation of the model leads to tremendous grid flexibility and allows easy incorporation of the complex coastline, high levels of refinement near shallow coastal areas and in regions of rapid bathymetric change, while, simultaneously, it allows keeping a less dense grid in areas where depth or flow changes are negligible and high spatial resolution is not required.

### 5.1. Model equations

The ADCIRC-2DDI model is based on vertically integrated equations of motion and continuity. The basic equations in a spherical coordinate system are defined as follows (Gill, 1982):

$$\frac{\partial U}{\partial t} + \frac{U}{R \cos \phi} \frac{\partial U}{\partial \lambda} + \frac{V}{R} \frac{\partial U}{\partial \phi} - fV - \frac{UV \sin \phi}{R \cos \phi} = -\frac{g}{R \cos \phi} \frac{\partial}{\partial \lambda} (\zeta - \alpha \eta) - \frac{\tau_{bx}}{\rho_0 H} \quad (8a)$$

$$\frac{\partial V}{\partial t} + \frac{U}{R \cos \phi} \frac{\partial V}{\partial \lambda} + \frac{V}{R} \frac{\partial V}{\partial \phi} + fU + \frac{UV \sin \phi}{R \cos \phi} = -\frac{g}{R} \frac{\partial}{\partial \phi} (\zeta - \alpha \eta) - \frac{\tau_{by}}{\rho_0 H} \quad (8b)$$

$$\frac{\partial \zeta}{\partial t} + \frac{1}{R \cos \phi} \frac{\partial (UH)}{\partial \lambda} + \frac{1}{R \cos \phi} \frac{\partial (VH \cos \phi)}{\partial \phi} = 0 \quad (8c)$$

where  $t$  represents time,  $\lambda, \phi$  denote degrees of longitude (east of Greenwich positive) and latitude (north of the Equator positive),  $\zeta$  is the free surface elevation,  $U, V$  are the depth-averaged horizontal velocities,  $H = \zeta + h$  is the total water column depth,  $h$  is the bathymetric depth,  $f$  is the Coriolis parameter,  $\rho_0$  is a reference density,  $g$  is the acceleration due to gravity,  $\alpha$  is the Earth elasticity factor,  $\eta$  is the Newtonian equilibrium tidal potential,  $\tau_{bx}, \tau_{by}$  are the bottom stresses in  $x$  and  $y$  directions which are taken as

$$\tau_{bx} = \rho_o C_d U \sqrt{U^2 + V^2}; \quad \tau_{by} = \rho_o C_d V \sqrt{U^2 + V^2} \quad (9)$$

where  $C_d$  denotes the bottom drag coefficient. The equilibrium tidal potential is expressed as (Reid, 1990):

$$\eta(\lambda, \phi, t) = \sum_{n,j} C_{jn} f_{jn}(t_o) L_j(\phi) \cos[2\pi(t - t_o)/T_{jn} + j\lambda + v_{jn}(t_o)] \quad (10)$$

where  $t$  is time relative to  $t_o$ , which is the reference time,  $C_{jn}$  is a constant characterizing the amplitude of a tidal constituent  $n$  of species  $j$ ,  $f_{jn}$  is the time-dependent nodal factor,  $v_{jn}$  is the time-dependent astronomical argument,  $j = 0, 1, 2$  are the tidal species ( $j = 0$  declinational;  $j = 1$  diurnal,  $j = 2$  semidiurnal),  $L_0 = 3\sin^2\phi - 1$ ,  $L_1 = \sin(2\phi)$ ,  $L_2 = \cos^2\phi$ , and  $T_{jn}$  is the period of a constituent  $n$  for species  $j$ .

To account for the Earth's curvature in the finite element discretization (Kolar et al., 1994), the governing equations 8a through 8c are projected onto a planar surface using a Carte Parallelogramatique Projection (CP) (Pearson, 1990), which is defined as:

$$x' = R(\lambda - \lambda_o) \cos \phi_o; \quad y' = R\phi \quad (11)$$

where  $\lambda_o, \phi_o$  are the longitude and latitude of the central point of the projection. An application of the Carte Parallelogramatique Projection to equations 8a through 8c yields the following set of the equations (Blain and Rogers, 1998)

$$\frac{\partial U}{\partial t} + \frac{U \cos \phi_o}{\cos \phi} \frac{\partial U}{\partial x'} + V \frac{\partial U}{\partial y'} - fV - \frac{UV \sin \phi}{R \cos \phi} = -\frac{g \cos \phi_o}{R \cos \phi} \frac{\partial}{\partial x'} (\zeta - \alpha \eta) - \frac{\tau_{bx}}{\rho_o H} \quad (12a)$$

$$\frac{\partial V}{\partial t} + \frac{U \cos \phi_o}{\cos \phi} \frac{\partial V}{\partial x'} + V \frac{\partial V}{\partial y'} + fU + \frac{UV \sin \phi}{R \cos \phi} = -g \frac{\partial}{\partial y'} (\zeta - \alpha \eta) - \frac{\tau_{by}}{\rho_o H} \quad (12b)$$

$$\frac{\partial \zeta}{\partial t} + \frac{\cos \phi_o}{\cos \phi} \frac{\partial (UH)}{\partial x'} + \frac{1}{\cos \phi} \frac{\partial (VH \cos \phi)}{\partial y'} = 0. \quad (12c)$$

Furthermore, the ADCIRC-2DDI model does not solve the momentum and continuity equations given by equations 12a through 12c but is based on the generalized wave continuity equation (GWCE) form of these equations. This is dictated by the fact that models, which solve the equations in a form given by equations 8a through 8c or 12a through 12c and use the finite element method, are plagued with severe spurious mode problems and typically require the use of nonphysical dissipation limiting their usefulness as predictive tools. The GWCE formulation (Lynch and Gray, 1979), however, leads to finite element depth-integrated numerical code that is highly accurate and robust. The GWCE is derived by combining a time-differentiated form of the continuity equation (12c) and a spatially differentiated form of the momentum equations (12a and 12b), and adding the continuity equation multiplied by a nonphysical constant in time and space  $\tau_o$ . These operations lead to the GWCE equation, which is defined in the CP coordinate system (Blain and Rogers, 1998) as follows:

$$\begin{aligned}
& \frac{\partial^2 \zeta}{\partial t^2} + \tau_o \frac{\partial \zeta}{\partial t} + \frac{\cos \phi_o}{\cos \phi} \frac{\partial}{\partial x'} [U \frac{\partial \zeta}{\partial t} - \frac{\cos \phi_o}{\cos \phi} UH \frac{\partial U}{\partial x'} - VH \frac{\partial U}{\partial y'} + \frac{\sin \phi}{R \cos \phi} UVH + fVH \\
& - gH \frac{\cos \phi_o}{\cos \phi} \frac{\partial}{\partial x'} (\zeta - \alpha\eta) - (\frac{\tau_{bx}}{\rho_o H} - \tau_o) UH] + \frac{\partial}{\partial y'} [V \frac{\partial \zeta}{\partial t} - \frac{\cos \phi_o}{\cos \phi} UH \frac{\partial V}{\partial x'} \\
& - \frac{\sin \phi}{R \cos \phi} U^2 H + fUH - gH \frac{\partial}{\partial y'} (\zeta - \alpha\eta) - (\frac{\tau_{bx}}{\rho_o H} - \tau_o) VH] - \frac{\partial}{\partial t} (\frac{\sin \phi}{R \cos \phi} VH) \\
& - \tau_o \frac{\sin \phi}{R \cos \phi} VH = 0
\end{aligned} \tag{13}$$

Equations (13) and (12a and 12b) are the final ones that are solved by the ADCIRC-2DDI model. Numerical discretization of the model equations is described briefly in Appendix C and in detail by Luettich et al. (1992).

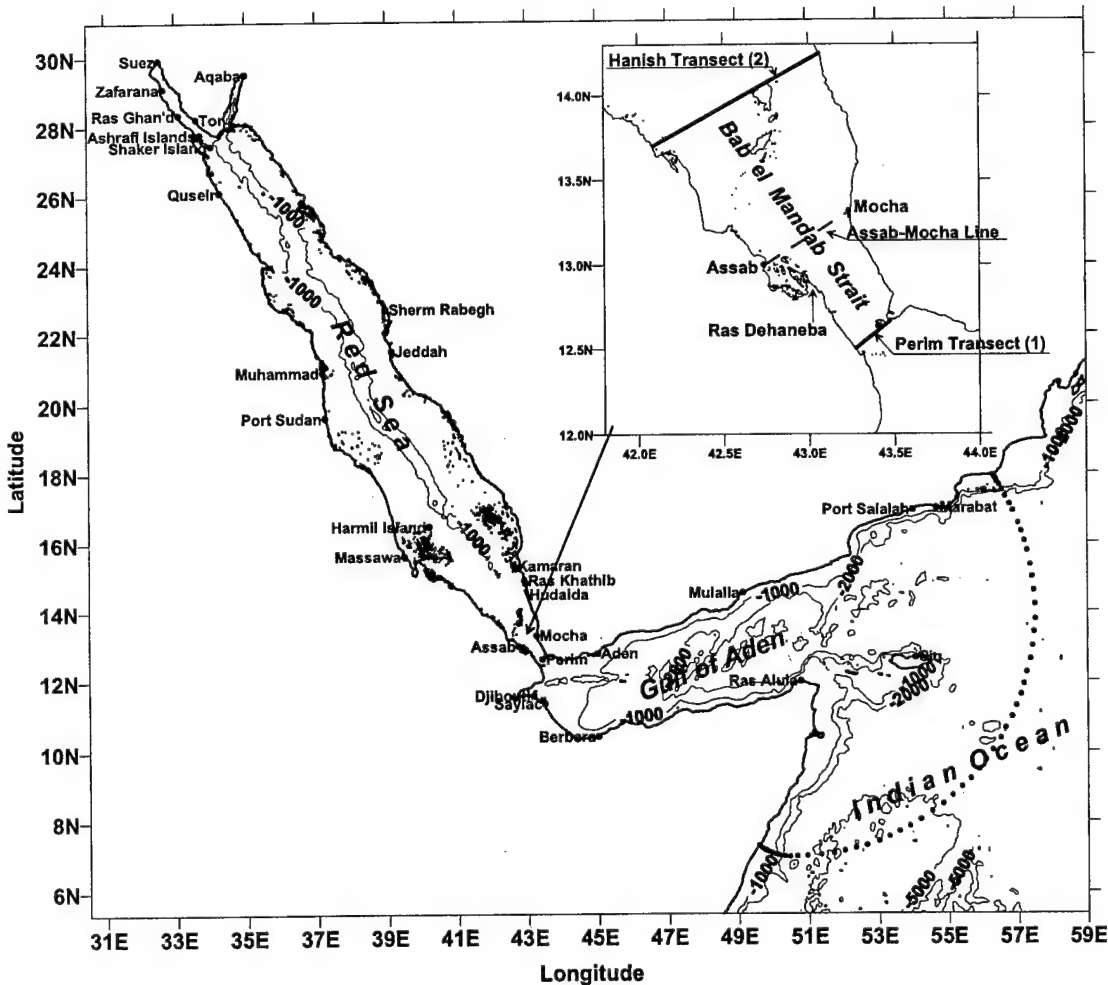


Figure 46. A location of the water level stations, transects, and model open boundary (dotted line); depth contours are in meters.

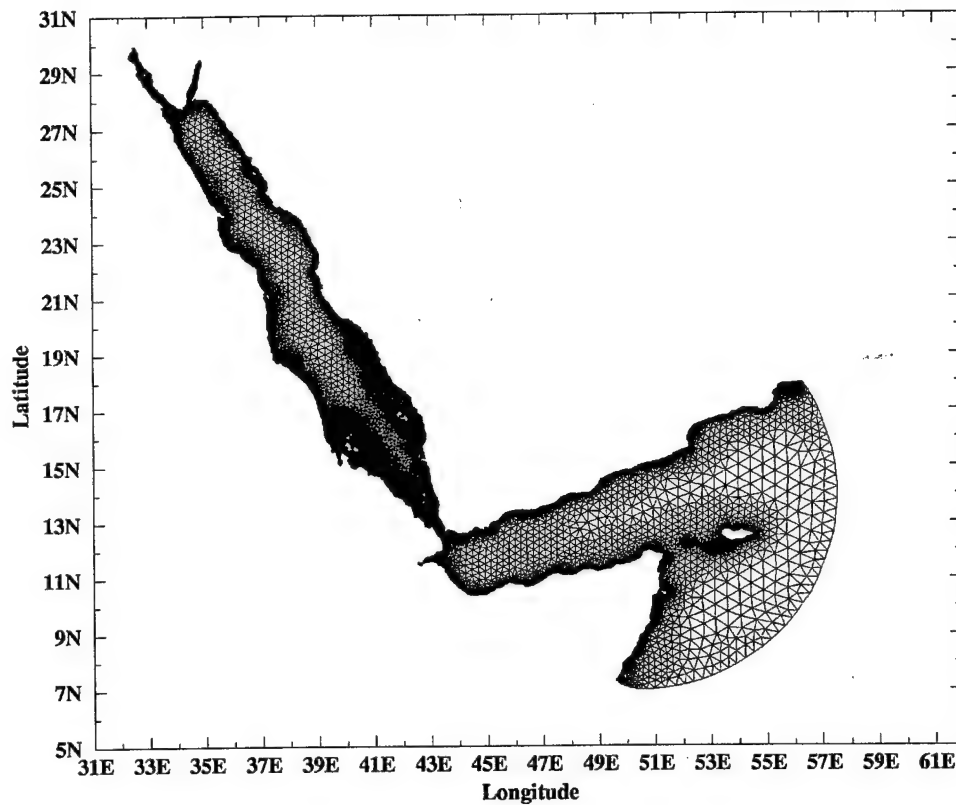


Figure 47. Triangular grid for the ADCIRC-2DDI model.

### 5.2. Model domain

The model domain, shown in Figure 46, includes not only the Bab el Mandab Strait but also the entire Red Sea, Gulf of Aden and northwestern part of the Indian Ocean. Such a large model area was chosen primarily to reproduce tidal waves propagating from the Indian Ocean, which is a major forcing of tidal motion in the Red Sea as well as in the Strait as discussed by Defant (1961). A second reason was to avoid having two open boundaries since the tidal elevation data outside and in the Strait are limited, and it was rather difficult to estimate reliable tidal elevation harmonic constants at open boundaries located near the Strait.

Bathymetry for the model was obtained from two sources: the Naval Oceanographic Office Digital Bathymetric Data Base – Variable Resolution (DBDB-V) and charts published by the Defense Mapping Agency in 1992. The bathymetry from the charts was digitized, and this data set is limited only to an area slightly larger than the Strait itself while DBDB-V data cover the entire model domain.

The finite element grid used in computations is displayed in Figure 47. It consists of 37436 nodes and 70733 elements. Nodal spacing for this mesh varies throughout the domain and ranges between 0.2 km and 55.5 km with the highest refinement present in the Strait where the minimum and maximum nodal spacing are 0.2 km and 2 km, respectively.

### **5.3. Boundary conditions and model parameters**

No-normal flow and free tangential slip conditions were imposed at the land boundary nodes with the exception of the nodes that have an inner angle less than  $45^\circ$ , where both normal and tangential flows were set to 0. Furthermore, at the open boundaries, the tidal elevation generated by four diurnal ( $K_1, O_1, P_1, Q_1$ ) and four semidiurnal ( $M_2, S_2, N_2, K_2$ ) constituents was specified. The tidal harmonic constants, which were used to generate the elevation at the open boundary nodes, were taken from the World Ocean Tide Model database FES95.2 (La Provost et al., 1994), and they were linearly interpolated onto the boundary nodes before they were used in the ADCIRC-2DDI model. In addition, an effective tidal potential forcing within the domain was applied for the same eight constituents.

The Earth elasticity factor was taken as 0.69. A constant value for the bottom friction coefficient, equal to 0.003, was applied throughout the domain. Bottom friction coefficients varying between 0.003 and 0.001 were tried, and a value of 0.003 gave the best agreement with the observations. A time step of 30 seconds was used to ensure model stability. The parameter  $\tau_o$ , which weights the primitive and GWCE form of the continuity equation, was estimated from a formula given by Westerink et al., (1994) and set equal to 0.001. Finally, the minimum depth was assigned to be 2 m to eliminate any drying of computational nodes. The model simulations were carried out for one year to generate the long time series that allow the separation of  $P_1$  and  $K_2$  constituents from  $K_1$  and  $S_2$ , respectively. The amplitudes and phases of the major tidal constituents were obtained through the standard harmonic analysis (Foreman, 1977, 1978).

### **5.4. Model-data comparison**

The model results were verified by sea level observations (33 stations) as well as by estimates of the barotropic tidal currents obtained from the measurements collected by the ADCP instruments (5 moorings; the ADCP mooring locations are listed in Tables 10, 11, and 12). Geographical locations of the water level stations, which were used for the data-model comparison in addition to the pressure gauges (the pressure gauge locations are listed in Tables 10, 11, and 12 and shown in Figure 1) of the BAM project, are listed in Table 5 and displayed in Figure 46. All observed tidal amplitudes and phases come from the coastal areas so there is no possibility of verifying how well the model predicts the tidal elevations away from the shore. In addition, at some stations only a few tidal constituents are available for the comparison; the common constituents for all stations are  $K_1, O_1, M_2$ , and  $S_2$ .

At this point it should be also emphasized that the model captures qualitatively major features of the diurnal tidal elevations, such as larger amplitudes in the Gulf of Aden and smaller in the Red Sea proper, as well as major features of semidiurnal tidal elevations such as the higher amplitudes in the Gulf of Aden, Aquaba and Suez and very small amplitudes near Port Sudan and Jeddah resulting from the presence of an anticlockwise amphidromic system (Defant, 1961). This amphidromic system is also reproduced in the same region by the model; however, the model results suggest that its node is located very close to the east coast of the Red Sea.

To evaluate agreement between the model and observations in terms of calculated and measured amplitudes and phases of the tidal constituents in the coastal areas of the model domain, the correlation coefficients were computed, and they are listed together

with the total number of stations used in the comparison and respective standard deviations of the differences between the model and data in Table 6. In addition, the root mean square (rms) error is listed. This error was estimated from the following expression (Nakamura et al., 2000):

$$\text{rms} = \frac{1}{N} \sum_{i=1}^N \frac{1}{T} \left[ \int_0^T (A_{\text{com}} \cos(\omega t - g_{\text{com}}) - A_{\text{obs}} \cos(\omega t - g_{\text{obs}}))^2 dt \right]^{1/2} \quad (14)$$

where N is total number of the water level stations, T is the tidal period,  $\omega$  is the tidal frequency, A and g are amplitudes and phases, respectively, and suffixes "com" and "obs" denote the calculated and observed harmonic constants, respectively.

Because of high correlation coefficients as well as small rms values and low standard deviations (for both amplitudes and phases) the model performance for the diurnal tidal components is satisfactory. However, the model accuracy is not so good for the major semidiurnal constituents, and this rather poor performance is reflected in the lower correlation coefficients, larger standard deviations and rms (Table 6). Additionally, the large differences between computed and measured tidal constant of the semidiurnal elevation are not uniformly distributed in the model domain. To identify possible sources

Table 5. Latitudes and longitudes of the water level stations used for the model verification.

Station Name	Latitude	Longitude
Aden	12° 47'	44° 59'
Aqaba	29° 31'	35° 00'
Ashrafi Islands	27° 47'	33° 43'
Assab	13° 00'	42° 44'
Berbera	10° 26'	45° 00'
Djibouti	11° 35'	43° 09'
Harmil Island	16° 29'	40° 11'
Hudaida	14° 50'	42° 56'
Jeddah	21° 31'	39° 08'
Kamaran	15° 20'	42° 36'
Marabat	16° 59'	54° 41'
Massawa	15° 37'	39° 28'
Mocha	13° 19'	43° 14'
Muhammad	20° 54'	37° 10'
Mulalla	14° 32'	49° 08'
Perim	12° 38'	43° 24'
Port Salalah	16° 56'	54° 00'
Port Sudan	19° 36'	37° 14'
Quseir	26° 06'	34° 16'
Ras Alula	11° 59'	50° 47'
Ras Ghan'd	28° 21'	33° 07'
Ras Khathib	14° 55'	42° 54'
Saylac	11° 22'	43° 28'
Shaker Island	27° 27'	34° 02'
Sherm Rabegh	22° 44'	38° 58'
Siq	12° 40'	54° 04'
Suez	29° 56'	32° 33'
Tor	28° 14'	33° 37'
Zafarana	29° 07'	32° 40'

Table 6. The correlation coefficients (Corr) and standard deviations (SD) between the computed and measured tidal amplitudes and phases; N is the number of the stations; rms is the root mean square error.

Tidal Constituent	N	Amplitude		Phase		rms (cm)
		Corr	SD(cm)	Corr	SD(deg)	
Q <sub>1</sub>	10	0.97	0.4	0.90	11	0.9
O <sub>1</sub>	33	0.99	0.8	0.99	16	1.1
P <sub>1</sub>	17	0.99	0.6	0.98	22	1.2
K <sub>1</sub>	33	0.99	2.4	0.86	17	2.2
N <sub>2</sub>	23	0.73	3.2	0.85	42	5.1
M <sub>2</sub>	33	0.83	9.3	0.85	39	9.4
S <sub>2</sub>	33	0.94	2.5	0.79	18	3.0
K <sub>2</sub>	20	0.91	1.1	0.75	28	4.5

of error, comparison between computed and observed amplitude and phases of the most energetic tidal constituents (O<sub>1</sub>, K<sub>1</sub>, M<sub>2</sub>, and S<sub>2</sub>) for all locations is given in Table 7. In the Gulf of Aden and southern part of the Bab el Mandab Strait, the agreement between model and observations is very satisfactory for both diurnal and semidiurnal components. This good agreement suggests that the tidal elevation constants taken from the World Ocean Tide Model (Le Provost et al., 1994) represent well the tidal wave incoming from the Indian Ocean. They, therefore, are not likely to be a major source of the errors observed north of Perim Narrows and in the Red Sea where the model does not simulate well semidiurnal waves, especially their phases. The largest phase discrepancies are found in the Strait (Assab, G108, and Mocha) where the difference between the computations and observations can be as large as 140°.

A set of experiments (changes in depth at the model nodes) in the Strait indicates that the phase errors are partly related to the bathymetry. A 10 m increase of depth in the deep channel and a 5 m increase of depth in the shoals between Perim Narrows and Assab-Mocha line resulted in a 15% increase of the M<sub>2</sub> phase and small changes in the K<sub>1</sub> phase. In addition, the errors may be related to the friction term. It was shown by Grenier et al. (1995) that in regions with strong rectilinear currents, the standard quadratic formulation of the friction term may not be good enough to properly describe damping of tidal waves. This problem should be examined in the Bab el Mandab Strait and will be addressed in the future since the model uses the standard quadratic friction formulation to simulate tides in the region where the tidal currents are strong and rectilinear.

Table 7. Comparison of computed (Com) and observed (Obs) K<sub>1</sub>/O<sub>1</sub> and M<sub>2</sub>/S<sub>2</sub> amplitudes (A) and phases (g, GMT) at the coastal stations.

Station	K <sub>1</sub> /O <sub>1</sub>				M <sub>2</sub> /S <sub>2</sub>			
	A (cm)		g (deg)		A (cm)		g (deg)	
	Obs	Com	Obs	Com	Obs	Com	Obs	Com
Aden*	40.0	39.0	350	346	48.0	49.5	134	133
	20.0	20.0	352	350	21.0	21.8	159	148
Aqaba	2.0	1.7	158	160	28.0	16.2	128	134
	1.0	0.5	146	164	8.0	6.2	155	154
Ashrafi Islands	2.0	2.0	167	159	25.0	14.2	118	129
	1.0	0.7	153	154	4.0	5.1	145	151
Assab	18.0	14.5	335	340	6.9	14.3	259	118
	8.5	6.7	344	344	4.0	7.1	170	155
Berbera*	46.0	38.3	349	348	48.0	49.5	135	134
	19.0	19.6	356	351	20.0	21.8	160	161

(Table 7 cont.)

Djibouti*	39.0 19.0	38.7 19.8	354 357	347 351	46.3 20.5	51.4 22.0	139 163	134 160
G14*	39.0 20.0	38.4 19.7	340 344	348 351	47.0 20.0	50.2 22.0	119 139	133 160
G89**	30.0 15.0	27.9 14.2	340 345	346 349	23.0 14.0	34.4 15.6	121 142	131 160
G109**	30.0 15.0	30.0 15.2	340 345	350 354	29.0 16.0	34.0 16.7	125 144	134 162
G108	6.0 2.0	4.4 1.5	321 335	350 354	24.0 5.0	8.0 2.0	286 299	350 15
Harmil Island	2.0 1.0	2.0 0.7	166 180	161 160	13.0 3.0	15.0 6.4	318 334	318 344
Hudaida	1.0 1.0	1.2 0.6	340 92	27 104	30.0 6.0	13.0 4.5	305 351	320 341
Jeddah	2.8 1.0	3.0 2.0	156 161	159 159	6.0 1.0	3.4 1.4	109 132	149 172
Kamaran	2.0 1.0	1.0 1.0	34 140	99 136	33.0 9.0	18.0 6.9	300 334	324 348
Marabat*	33.0 19.0	34.5 18.2	345 346	342 345	32.0 14.0	32.3 12.9	144 170	144 169
Massawa	2.3 2.0	2.8 2.1	164 184	166 163	33.4 12.4	34.4 15.0	328 332	333 3
Mocha	7.0 6.1	16.0 7.8	335 352	352 358	8.0 4.5	14.0 7.2	244 188	134 166
Muhammad	3.0 2.0	2.9 1.7	166 175	160 159	6.0 1.0	2.9 1.2	132 185	176 210
Mulalla*	40.0 20.0	36.8 19.2	349 352	345 348	40.0 12.0	38.6 16.6	136 164	134 159
Perim**	35.0 18.0	34.5 18.1	350 351	350 353	37.0 17.0	42.6 18.9	136 159	136 162
Port Salalah*	36.0 18.0	34.7 18.2	344 347	343 345	31.0 12.0	31.9 12.8	144 168	143 168
Port Sudan	2.0 2.0	2.9 1.7	168 170	157 156	1.0 1.0	1.5 0.8	204 256	246 277
Quseir	2.0 2.0	2.2 1.0	158 192	154 153	22.0 5.0	13.0 4.9	112 139	134 156
Ras Alula*	37.1 18.9	35.6 18.5	348 353	356 350	36.3 15.4	36.5 15.8	139 156	138 163
Ras Ghan'd	2.0 2.0	2.9 0.9	160 157	163 154	18.0 7.0	9.0 3.0	274 302	302 318
Ras Khathib	4.0 1.0	1.2 0.6	69 82	25 82	26.0 7.0	13.0 4.5	294 339	318 339
Saylac*	40.0 20.0	38.9 19.9	348 356	348 351	50.0 20.0	51.6 22.6	137 153	133 161
Shaker Island	2.0 1.0	2.0 0.7	167 178	154 151	25.0 4.0	14.0 5.1	117 144	132 154
Sherm Rabegh	4.0 4.0	2.7 1.4	156 162	160 163	11.0 2.0	6.1 2.5	124 165	142 164
Siq*	35.0 17.0	33.0 17.3	338 339	346 349	23.0 13.0	27.0 11.4	139 156	140 164
Suez	4.5 1.3	3.3 0.8	158 170	162 152	56.0 14.0	26.0 8.7	278 306	300 319
Tor	4.0 2.0	2.6 0.8	164 159	157 152	8.0 1.0	3.2 1.6	205 230	213 211
Zafarana	3.0 1.0	3.3 0.9	165 199	163 152	42.0 12.7	21.0 6.9	280 301	300 320

\*Stations located in the Gulf of Aden; \*\* stations located in the southern part of the Bab el Mandab Strait.

Locations (5) with good estimates of the barotropic tidal currents are limited to the Bab el Mandab Strait. In Table 8, the observed and calculated  $K_1$ ,  $O_1$ ,  $M_2$ , and  $S_2$  tidal currents are described by the parameters of the tidal ellipse. In general, the agreement between computed and measured tidal currents in the Strait is satisfactory for both semidiurnal and diurnal constituents. The largest error for the semimajor axis is found for  $M_2$  at Perim Narrows where the computed amplitudes are, on average, 20% smaller than the measured amplitudes. For other constituents at Perim Narrows as well as for all at C mooring and the Hanish Sill the difference between computed and observed semimajor axis is always less than 20% of that estimated from the observations. Similar to the observed tidal currents, the model results clearly show that the simulated tidal currents are nearly rectilinear (the semiminor axis is much smaller than the semimajor axis for all constituents) in the Bab el Mandab Strait. In addition, the difference between the model and observed inclinations is, on average, 4% of the observed inclination angles. Finally, the phase agreement is better for the diurnal constituents than for the semidiurnal tidal components, and the phase difference is always smaller than 1 h for all considered constituents.

Table 8. Comparison between observed (Obs) and computed (Com) tidal current ellipse parameters: semimajor axis ( $M$ ), semiminor axis ( $Mn$ ), inclination angle ( $\theta$ ), and phase ( $g$ , GMT).

Mooring	M (cm/s)		Mn (cm/s)		$\theta$ (deg)		g (deg)	
	Obs	Com	Obs	Com	Obs	Com	Obs	Com
$K_1$								
A2b	29.7	29.4	-1.5	-1.4	91.3	98.8	68.3	73.2
AA1	31.9	30.0	-0.9	-1.7	104.4	104.6	88.6	72.1
AA2b	29.0	28.9	-0.7	-2.0	94.6	95.0	71.3	72.1
C	13.8	15.1	1.2	0.6	133.5	132.8	73.4	74.6
B2b	15.6	16.5	-0.6	-0.4	133.0	122.0	73.9	78.3
$O_1$								
A2b	16.4	17.3	-0.5	-1.0	92.5	97.9	68.5	74.7
AA1	18.7	17.4	-0.1	-1.0	104.3	104.6	89.2	75.0
AA2b	16.7	16.1	-0.3	-0.9	94.2	94.3	74.6	73.9
C	7.2	8.6	0.6	0.4	132.0	133.3	74.4	76.6
B2b	9.4	9.1	-0.4	-0.3	134.2	123.0	77.6	81.8
$M_2$								
A2b	29.2	25.0	-1.0	-0.7	94.3	99.0	200.8	221.0
AA1	32.5	24.6	-0.9	-0.7	105.4	104.6	234.0	222.3
AA2b	29.6	23.9	-0.5	-0.4	96.9	96.6	200.8	220.0
C	16.2	13.4	0.2	0.3	128.3	132.7	220.9	222.9
B2b	15.0	15.0	-0.3	-0.3	133.9	123.0	204.6	223.0
$S_2$								
A2b	10.2	9.1	-0.3	-0.2	94.3	99.1	227.0	246.0
AA1	11.2	9.5	-0.6	-0.2	105.2	104.3	258.5	246.5
AA2b	9.3	8.8	-0.2	-0.1	96.9	96.0	223.4	246.0
C	6.2	5.5	0.2	0.1	124.7	132.0	248.1	248.9
B2b	6.0	6.4	-0.1	-0.1	133.4	123.8	230.3	250.0

In conclusion, the model performance for the elevation constants of the diurnal tides is very comparable to the performance of other finite difference or finite element models that were used to simulate tides in other regions (see, for example, Kowalik and Proshutinsky, 1993; Foreman et al., 1995; Tsimplis et al., 1995; Kowalik and Polyakov, 1998). However, other numerical models give better agreement between observed and

modeled elevation constants for the semidiurnal tides. As for the tidal current ellipse parameters, the accuracy is again very comparable.

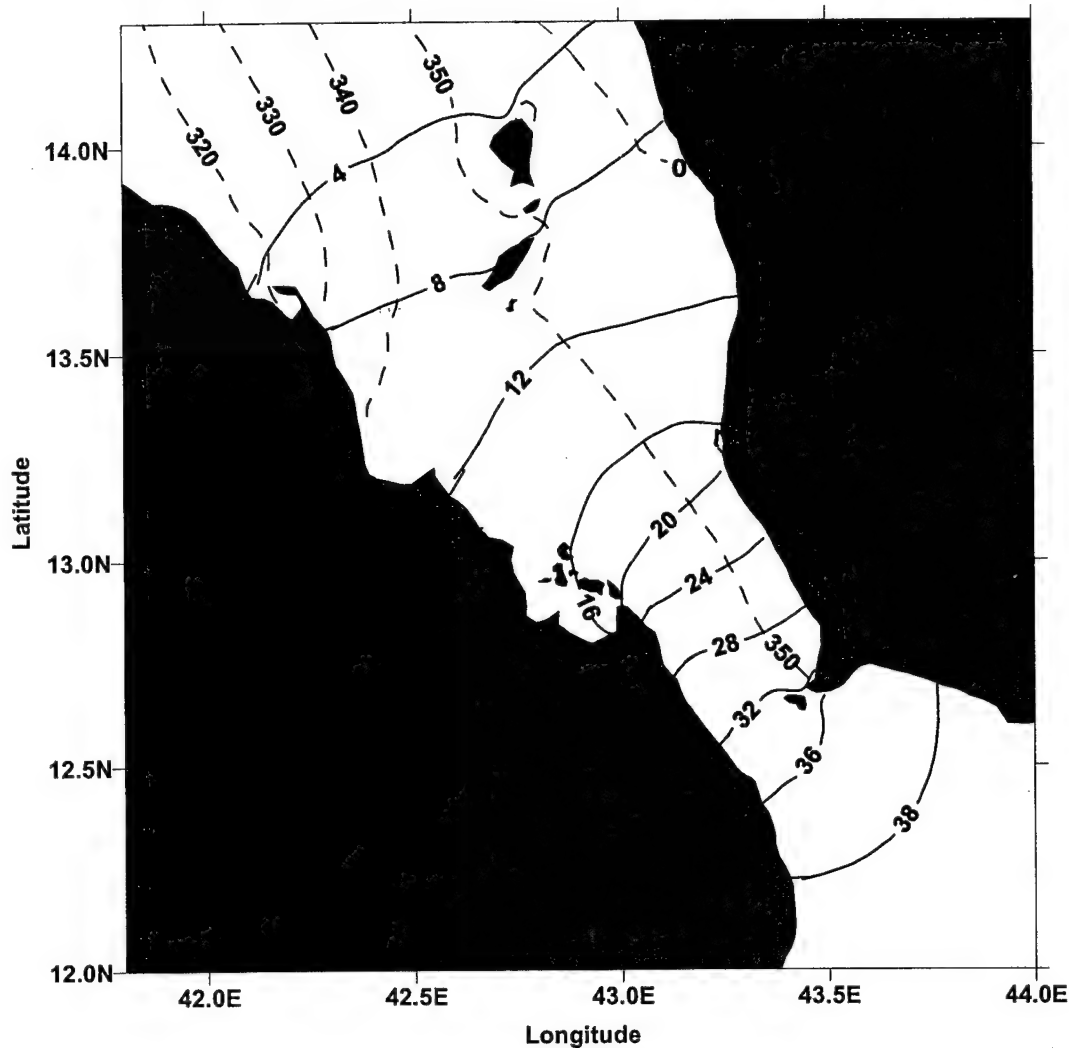


Figure 48. Model coamplitudes (in cm; solid line) and cophases (degrees, GMT; dashed line) for the  $K_1$  constituent.

### 5.5. Tidal model elevations

Figures 48 and 49 display charts of computed coamplitudes and cophases of the tidal elevations for the  $K_1$  and  $M_2$  constituents in the Bab el Mandab Strait. The numbers on the coamplitude lines are given in centimeters. The phase angle is expressed in degrees. In the along-strait direction, the distribution of the coamplitudes displays a rapid attenuation of the  $K_1$  amplitude (Figure 48), which decreases from ~ 32 cm at Perim Narrows to ~ 8 cm near the Hanish Sill, while at the same time, there is little variability in the  $K_1$  amplitude in the cross-strait direction. The phase variation is rather small with the highest differences found near the Hanish Sill where the maximum elevation on the west side occurs approximately 1 h earlier than that on the east side. Additionally, the

phase distribution in the Strait implies an anticlockwise amphidromic system for  $K_1$  constituent located farther north, and, according to the model results, this amphidromic region is centered approximately at  $14^{\circ} 57'N$  and  $41^{\circ} 58'E$ . Though the coamplitudes and cophases for the remaining three diurnal constituents are not shown, constituents  $O_1$ ,  $P_1$  and  $Q_1$  have characteristics similar to the  $K_1$ . Of course, they have smaller amplitudes that are 50 %, 31 %, and 9 %, respectively, of the  $K_1$  amplitudes. Additionally, the amphidromic point of  $P_1$  is positioned almost at the same location as that of  $K_1$ ; however, the  $O_1$  and  $Q_1$  amphidromic systems are centered south (at  $14^{\circ} 24'N$  and  $42^{\circ}E$ ) of that for the  $K_1$ .

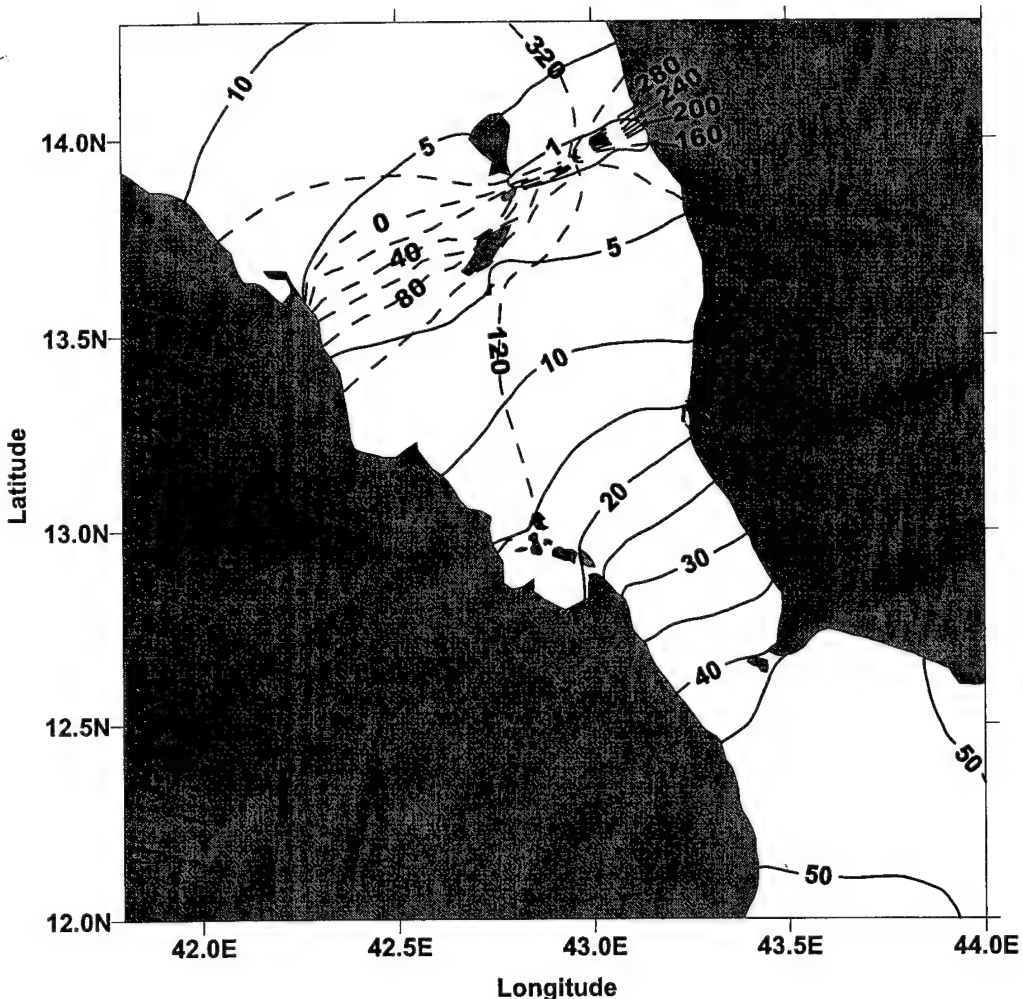


Figure 49. Model coamplitudes (in cm; solid line) and cophases (degrees, GMT; dashed line) for the M2 constituent.

The distributions of the M<sub>2</sub> amplitudes (Figure 49) and phases south of the latitude 13°N are similar to those of the K<sub>1</sub>, i.e., the amplitudes decrease very rapidly in the along-strait direction from 45 cm at the southern end of the Bab el Mandab Strait to 21 cm at approximately 13°N simultaneously showing little variability in the cross-shore

direction, while the phase implies that the  $M_2$  elevation is in phase in this part of the Strait. Farther north, the amplitudes continue decreasing to their minimum values of 1 cm

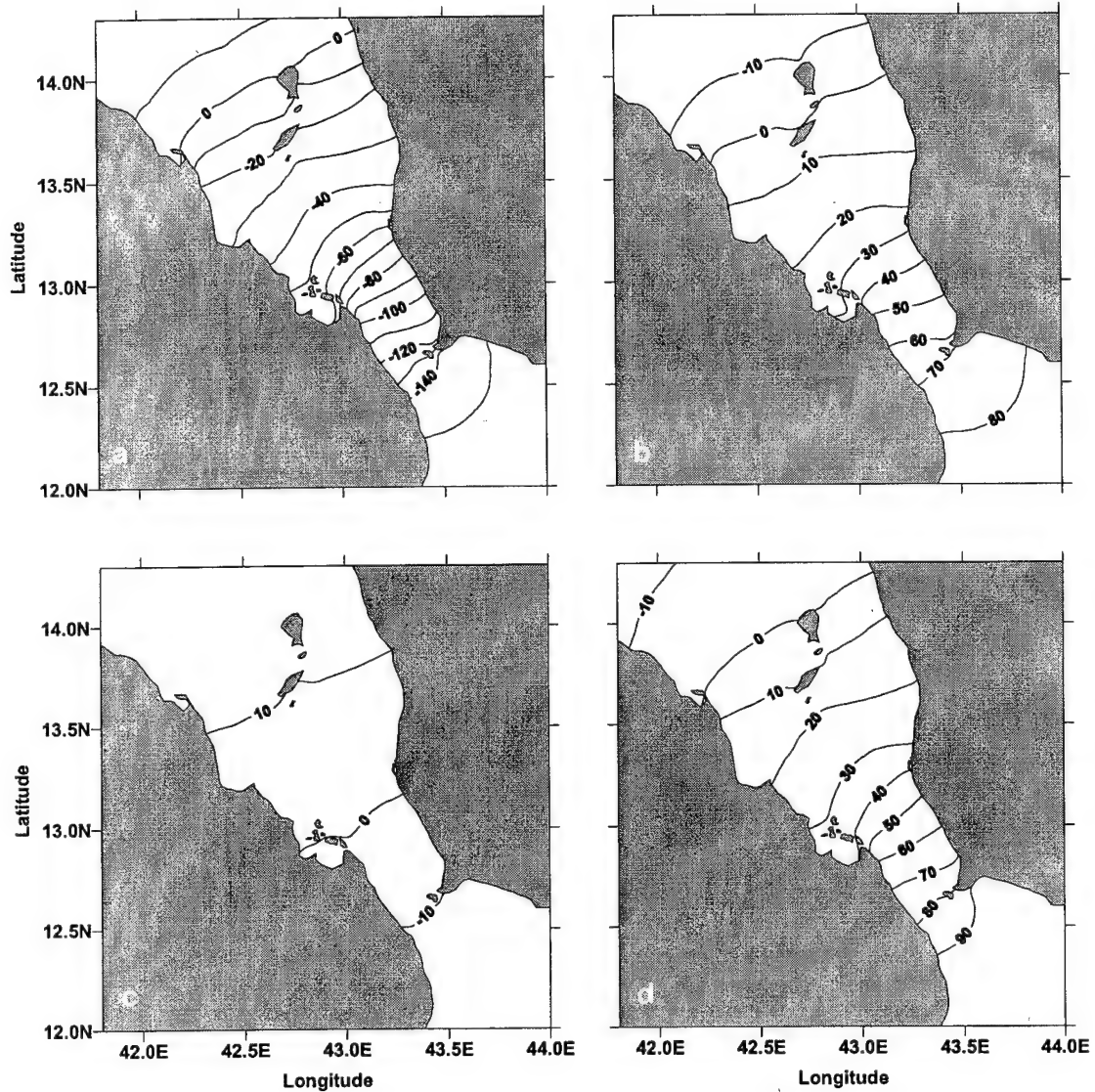


Figure 50. Distribution of the spring tide water elevation generated by the  $K_1$ ,  $O_1$ ,  $P_1$ ,  $Q_1$ ,  $M_2$ ,  $S_2$ ,  $N_2$ , and  $K_2$  constituents in the Bab el Mandab Strait at the time of (a) LLW, (b) LHW, (c) HLW, and (d) HHW at Perim Narrows.

or less found just east of the Hanish Islands. This minimum is associated with a  $M_2$  amphidromic system, which is approximately centered at  $14^{\circ}\text{N}$  and  $43^{\circ}\text{E}$ . Vercelli (1925) and Defant (1961) postulated that, in the Strait, there is a nodal zone of the  $M_2$  tide, where a rapid transition of the phase is observed, but this nodal zone is located southwest (near Assab) of that suggested by the model results. At the northern end of the Strait, the amplitudes are slightly higher than 5 cm.

The variability of the amplitudes and phases of the  $S_2$  and  $N_2$  components is similar to that of the  $M_2$ . Except near the amphidromic systems, where the amplitudes of all three constituents have their minimal values, the amplitudes of the  $S_2$  and  $N_2$  constituents are 45% and 48% of those of the  $M_2$  elevations. The amphidromic systems of the  $S_2$  and  $N_2$  are located southwest of that of the  $M_2$ , and they are centered approximately at  $13^{\circ} 54'N$  and  $42^{\circ} 36'$  and  $13^{\circ} 30'N$  and  $42^{\circ} 18'$ , respectively. The  $K_2$ , the smallest among semidiurnal tidal components, shows a similar distribution pattern of the amplitudes to those discussed above with the largest values found at the southern end (2.5 cm) and smallest (0.5 cm) in the northern part of the Bab el Mandab Strait. The phase, however, has quite different distribution: there is no amphidromic system for this constituent in the Strait and the phase decreases from  $\sim 150^{\circ}$  near Perim Narrows to  $90^{\circ}$  near the Hanish Sill.

The next two figures (Figures 50 and 51) display the modeled tidal elevation distribution of the spring and neap tides in the Bab el Mandab that is generated by a combination of the  $K_1$ ,  $O_1$ ,  $P_1$ ,  $Q_1$ ,  $M_2$ ,  $S_2$ ,  $N_2$ , and  $K_2$ . For all displayed plots the times of the high or low waters are referenced to those observed at Perim Narrows.

The spring tides in the Bab el Mandab Strait are generally characterized by two high and two low waters. Two nearly equal high and low waters are mostly observed just north of the Hanish Islands where the tidal elevation fluctuations are dominated by the semidiurnal tides. Farther south, these maxima and minima are more and more dissimilar due to the changing character of the tides from the semidiurnal type to the mixed type. The distributions of the tidal elevation for both high waters of the spring tides (Figures 50b and 50d) are fairly similar. They both show the largest elevations in the southern part of the Strait, and they are 70 cm and 80 cm near Perim Narrows for LHW and HHW, respectively. Furthermore, the elevation shows large gradients in the along-strait direction while simultaneously showing little or no variability in the cross-strait direction. Two major differences between these two high waters are: (1) in general, the elevations of HHW (Figure 50d) are  $\sim 10$  cm larger than those of LHW (Figure 50b); (2) the zero elevation line is located at the northern end of the Strait for HHW while for LHW it is positioned farther south (between the Hanish Islands). Similar to the high water stages, the low water elevation distributions show little variability in the cross-strait direction and large variations in the along-strait direction. Furthermore, when LLW is observed at Perim Narrows (Figure 50a), the low water (negative values) is generally present in the entire Strait, while for the HLW stage (Figure 50c), only the part of the Strait between Perim Narrows and the Assab-Mocha line is actually in the low water stage whereas farther north, the tidal elevation implies rather high water stage. When the elevation magnitude is compared between these two low water stages, between Perim Narrows and the Assab-Mocha line, the magnitudes associated with HLW are much smaller, and they are 5% or less of those of LLW, while farther north they are comparable.

The elevation variability associated with the neap tides is displayed in Figure 51. In general, over 24 hours of the neap tides, one may see one low and one high water or, similar to the spring tides, two high and two low waters. Figure 51 shows the high and low waters of the 24 h cycle when only one high and low are observed. The general features of the elevation distribution (such as higher magnitudes near Perim Narrows, large gradients in the along-strait direction, little variability in the cross-shore direction and zero tidal elevation at the northern end of the Strait) are identical to those observed

during HHW and LLW of the spring tides. The only difference, as expected, is the magnitude of the tidal elevations, which is always lower as expected in the entire Strait for the neap tides.

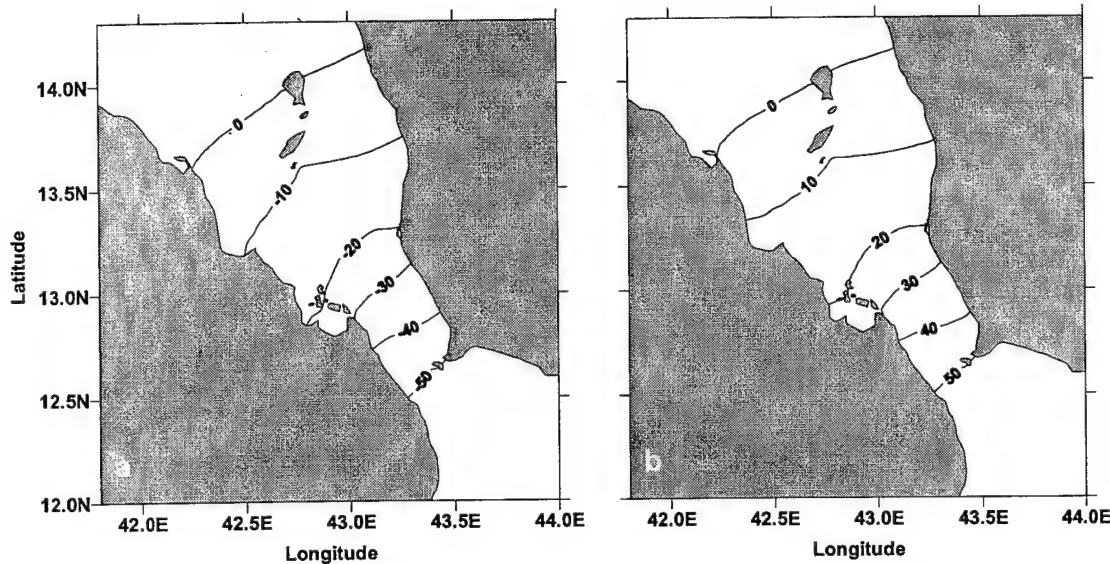


Figure 51. Distribution of the neap tide water elevation generated by the  $K_1$ ,  $O_1$ ,  $P_1$ ,  $Q_1$ ,  $M_2$ ,  $S_2$ ,  $N_2$ , and  $K_2$  constituents in the Bab el Mandab Strait at the time of (a) the high water, and (b) the low water at Perim Narrows.

### 5.6. Tidal model currents

The amplitude distribution of the semimajor axis for the  $K_1$  constituent is displayed in Figure 52. This distribution of the semimajor axis amplitudes shows apparent amplification of the  $K_1$  tidal currents as they flow into the Bab el Mandab Strait from the Gulf of Aden. The strongest currents are present in the narrowest part of the Strait (between Perim Narrows and Assab-Mocha line) with the maximum amplitudes found near the Perim Island where the speeds are between 35 cm/s and 40 cm/s. Farther north, the amplitudes are generally below 20 cm/s. The direction of the maximum flow is usually aligned with the along-strait. Similar to the results from the data analysis, the  $K_1$  tidal currents are nearly rectilinear in the Strait. Values of the semimajor axis (not shown) are not larger than 5 cm/s, and on average, they are equal to 0.8 cm/s. The sense of the rotation is quite variable and does not show any obvious patterns. The phase distribution (not shown) of the currents indicates that the  $K_1$  currents turn earlier in the shallow waters than those observed in the deep parts of the Strait.

The variability of the semimajor axis of the currents induced by the  $M_2$  constituent are very similar to those of the  $K_1$  tidal component (Figure 53). The currents intensify as they flow into the Bab el Mandab Strait. The largest amplitudes are found near Perim Narrows where they reach speeds near 40 cm/s. In general, the enhanced currents are observed south of the Assab-Mocha line. In this part of the Strait, the amplitudes of the semimajor axis are larger than 20 cm/s with the exception of the regions located near the coastline where they are reduced to or below 10 cm/s. Farther north of the Assab-Mocha line, the amplitudes rarely exceed 20 cm/s. The direction of the

maximum flow is generally aligned with the along-strait axis. Furthermore, the amplitudes of the semiminor axis (not shown) are much smaller than those of the semimajor one and on average, are equal to 0.5 cm/s. Finally, the phase (not shown) implies that the currents in the shallow waters turn at least 1 h earlier than those in the deep waters.

The distributions of the tidal ellipse parameters of the other six constituents mimic those of the  $K_1$  and  $M_2$ . The major difference is found in the amplitudes of the semimajor axis, which are reduced. For example, the amplitudes of the  $O_1$ ,  $P_1$ , and  $Q_1$  constituents are, on average, 55%, 38%, and 10%, respectively, of those associated with the  $K_1$  constituent. The amplitudes of the semidiurnal components are also smaller when

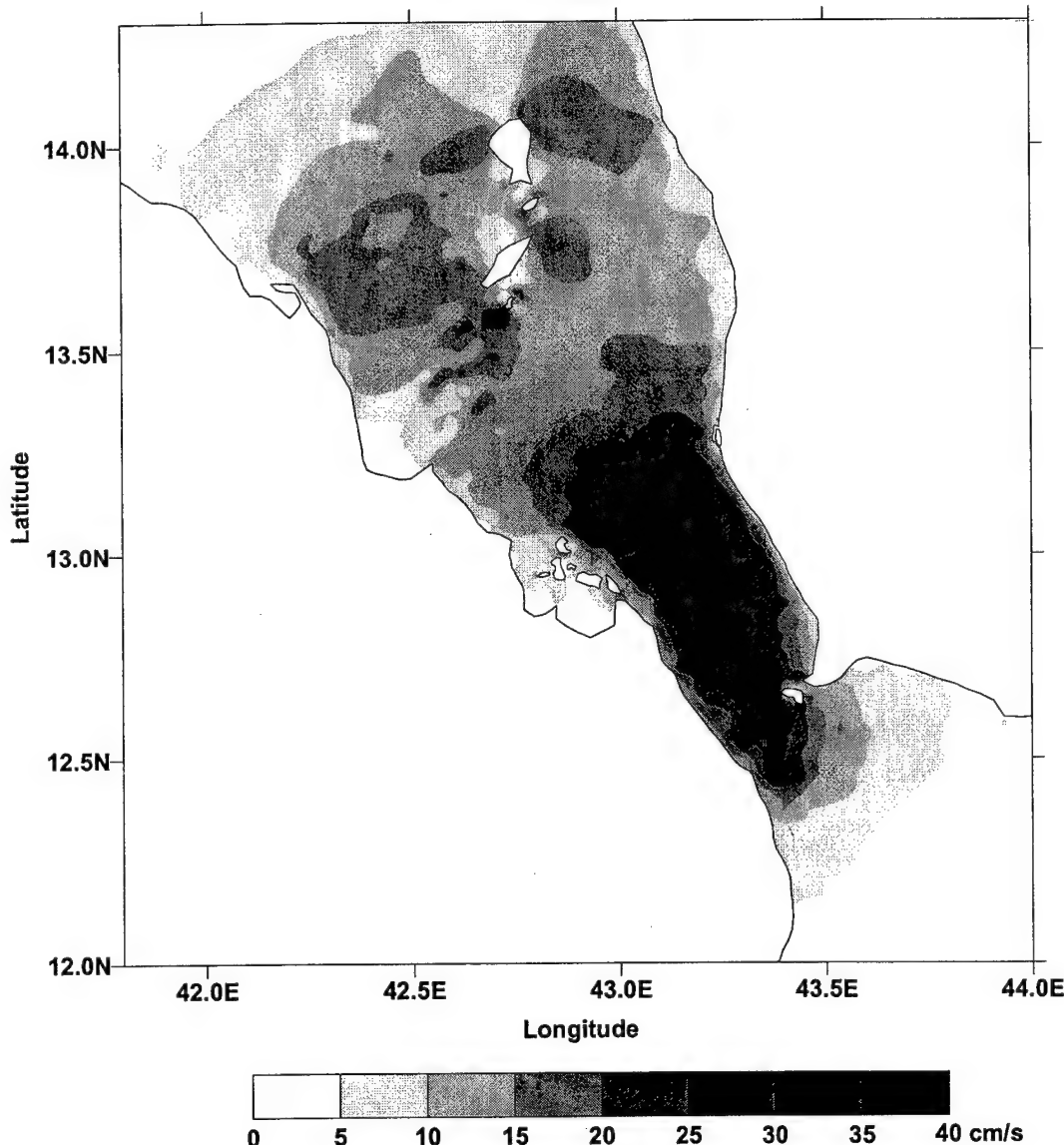


Figure 52. Distribution of amplitudes (cm/s) of the semimajor axis for the  $K_1$  constituent.

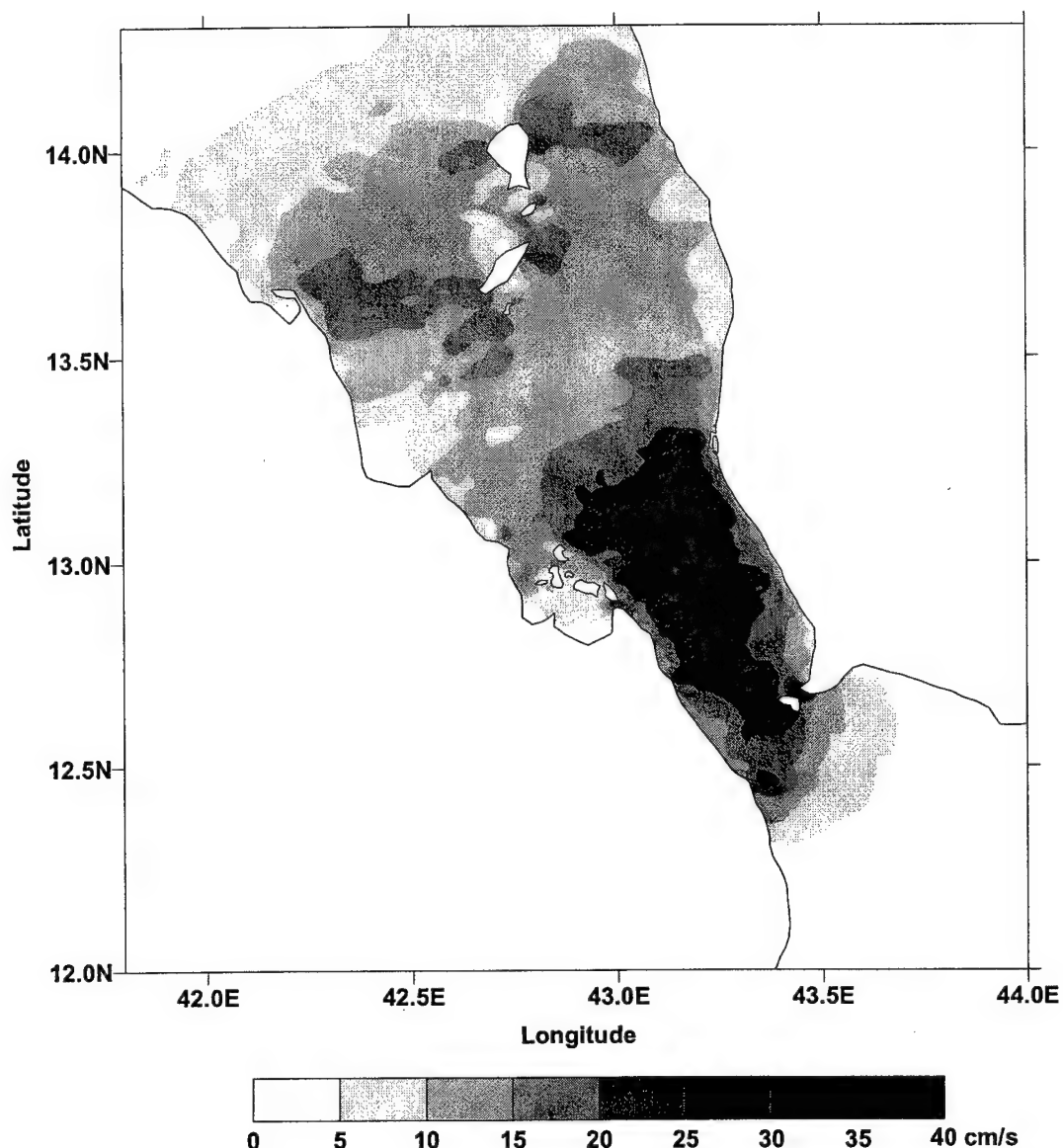


Figure 53. Distribution of amplitudes (cm/s) of the semimajor axis for the  $M_2$  constituent.

compared with the  $M_2$  constituent, and they are 41%, 25%, and 5% of the  $M_2$  amplitudes for  $S_2$ ,  $N_2$ , and  $K_2$ , respectively.

The next two figures (Figures 54 and 55) display the spatial variability of the speed and direction of the tidal flow that is associated with the spring and neap elevations shown in Figures 50 and 51. For all plots displayed the times of the high or low water are again referenced to those observed at Perim Narrows.

During the spring tides, about 4 h after LLW at Perim Narrows (Figure 54a), the currents are at the maximum outflow (ebb). The direction of the flow varies very little and in general, the outflow is observed in the entire Strait. Furthermore, near the Hanish Sill, the maximum speeds are not higher than 60 cm/s. Farther south (between the Assab-

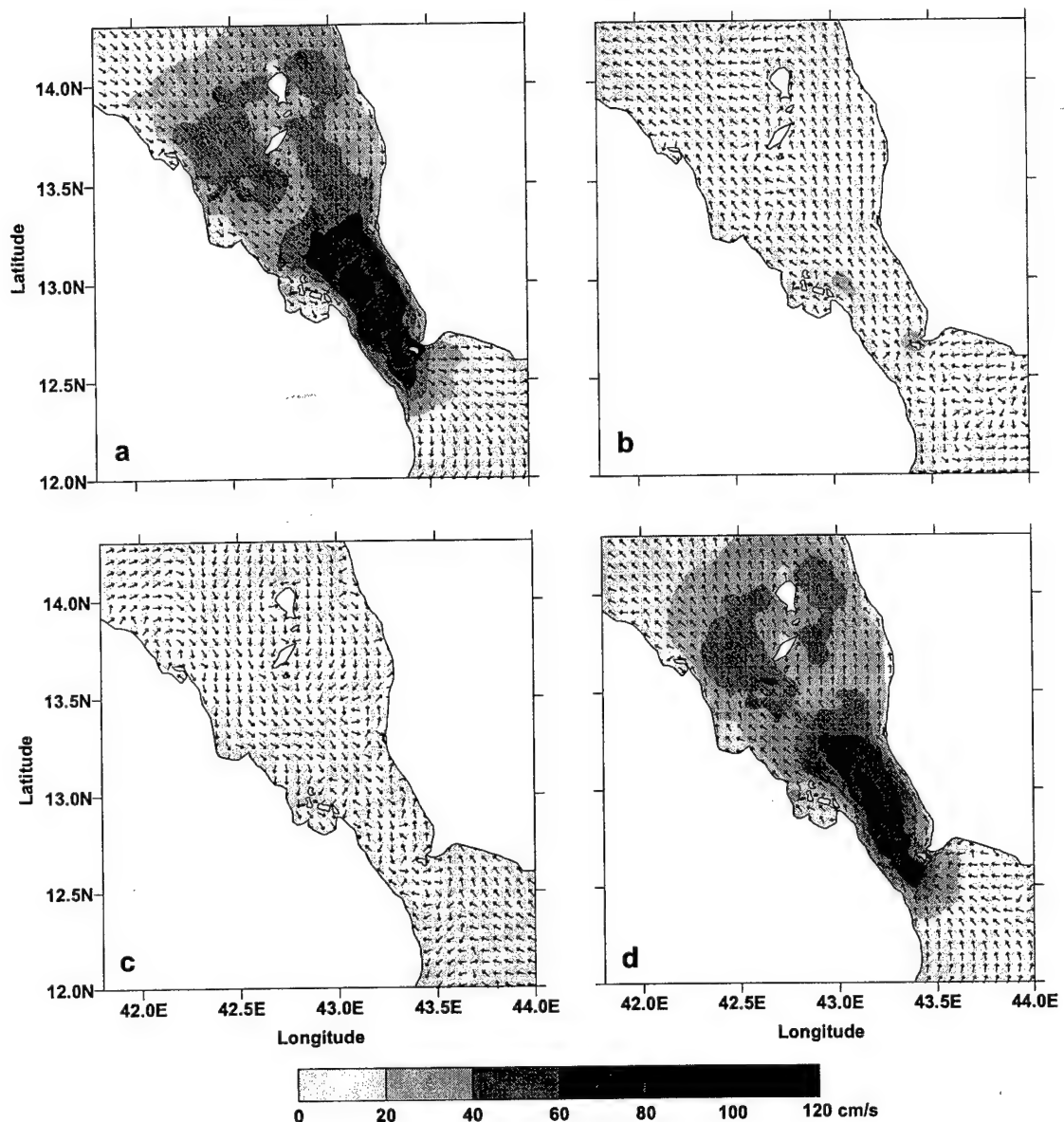


Figure 54. Speeds (in cm/s; a shade scale) and direction (arrows) of the currents generated by the  $K_1$ ,  $O_1$ ,  $P_1$ ,  $Q_1$ ,  $M_2$ ,  $S_2$ ,  $N_2$ , and  $K_2$  constituents in the Bab el Mandab Strait during spring tides (a) 4 h after LLW, (b) 4 h after LHW, (c) 3 h after HLW, and (d) 4 h after HHW at Perim Narrows.

Mocha line and Perim Narrows), however, the flow accelerates and near the Perim Narrows, the maximum speeds may reach over 100 cm/s. Seven hours later or 4 h after LHW at Perim (Figure 54b), the currents are in the flood stage. The direction of the flow is reversed and shows more variability when compared with the previous ebb stage, but the barotropic currents generally flow into the Strait with the speeds rarely exceeding 20 cm/s. Figure 54c displays the speed and direction variability approximately 3 h after HLW at Perim Narrows (second ebb). Similar to the previous stage, the speeds are weak

and rarely reach 15 cm/s. The flow direction varies greatly and the well-defined outflow is generally observed only in the deep channel where the speeds are between 10 cm/s and 15 cm/s. Finally, 4 h after HHW, the tidal currents are at the maximum flood stage (Figure 54d). The speed distribution is comparable to that of the maximum ebb currents with the maximum velocity reaching above 100 cm/s at Perim Narrows. The direction of the flow is nearly uniform showing the well-defined inflow in the entire Strait.

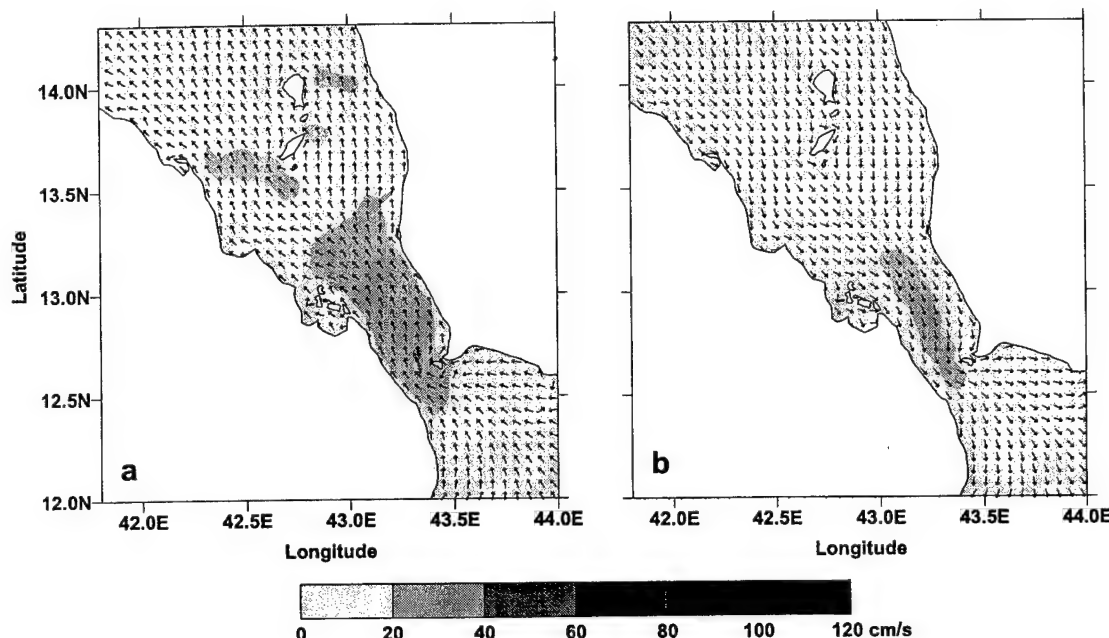


Figure 55. Speeds (in cm/s; a shade scale) and direction (arrows) of the currents generated by the  $K_1$ ,  $O_1$ ,  $P_1$ ,  $Q_1$ ,  $M_2$ ,  $S_2$ ,  $N_2$ , and  $K_2$  constituents in the Bab el Mandab Strait during neap tides (a) 4 h after the high water, and (b) 4 h after the low water at Perim Narrows.

The speed distribution and direction of the flood flow of the neap tide, which is present in the Strait about 4 h after the high water at Perim Narrows, are displayed in Figure 55a. The maximum observed speeds are reduced, and they are about 50% of those of the second flood of the spring tides. They are generally between 25 cm/s and 35 cm/s between the Assab-Mocha line and Perim Narrows with the exception that in the very shallow waters, they are below 10 cm/s and in the vicinity of the Perim Island, they may reach 40 cm/s. Farther north, the maximum speeds do not exceed 20 cm/s. Similar to the maximum flood of the spring tides, there is little variability in the direction of the tidal flow, which generally shows inflow in the entire Strait. As Figure 55b shows for the duration of the ebb of the neap tide, the direction of the flow also varies little, while the speeds are greatly reduced when compared with those observed during the first ebb of the spring tides, and they do not exceed 30 cm/s.

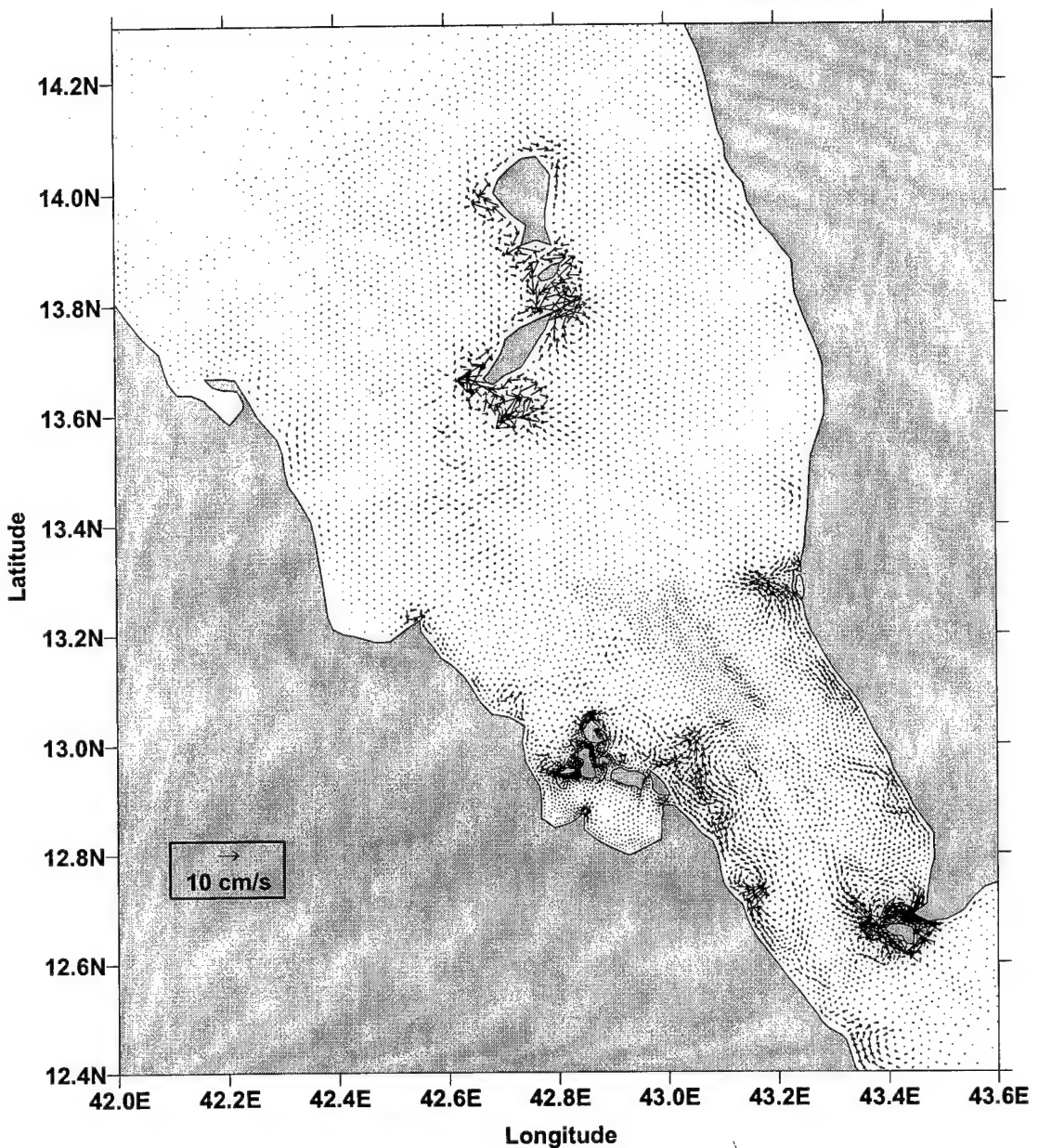


Figure 56. Time-averaged residual tidal flow in the Bab el Mandab Strait.

### 5.7. Residual circulation

Due to variable bathymetry, the tidal currents may generate residual currents through nonlinear interaction (Zimmerman, 1978). These residual currents can play an important role in the local mean circulation. Huthnance (1973) showed that the Coriolis force and bottom drag are the mechanisms responsible for the generation of the residuals, while the role of the advective terms is to transfer properties (e.g. vorticity) from the tides to the mean flow (Zimmerman, 1980; Robinson, 1983).

To extract the time-averaged residual motion, which is induced by the eight tidal constituents ( $K_1$ ,  $O_1$ ,  $P_1$ ,  $Q_1$ ,  $M_2$ ,  $S_2$ ,  $N_2$ , and  $K_2$ ) in the Bab el Mandab Strait, the

computed currents were averaged over a 29-day period, and the results of this averaging are shown in Figure 56. In general, the residual currents in the Strait are weak. Their speeds are, on average, less than 1 cm/s (the mean of the residual current speed for the entire Strait is 0.9 cm/s). The strongest residual flow is generally found near the islands and in the part of the Strait between Perim Narrows and Assab-Mocha line. Near the Perim or Hanish Islands, for instance, the speed of the residual currents can be as high as 20 cm/s. It has to be emphasized here that the strong residual flow observed near the islands and headlands may be partly generated by sharp changes in the coastline associated with the model grid. The time-averaged residual flow also displays several small clockwise and counterclockwise eddies such as those located west of Mocha or east of Ras Dehaneba.

In addition to the time-averaged residual flow, the time-dependent residual flow was also analyzed. These residuals were extracted from the model data by removing motions with periods less than 2 days. Figure 57 shows a series of snapshots of the fluctuating residuals, with mean removed. The amplitudes of these currents are slightly lower than those of the time-averaged residual currents with the maximum amplitudes being below 15 cm/s. Similar to the time-averaged residual flow, the most energetic currents are again observed near the Perim and Hanish Islands. Additionally, small eddies are present in the time-dependent residual flow, and these eddies seem to be better developed during the spring tides (the fluctuations presented in Figure 57 encompass a time period that starts and ends in the middle of the spring tides). Furthermore, the fluctuations are generally dominated by a fortnightly cycle (compare days 81 and 95). Spectral analysis (results not shown) indicates that most of the energy at low frequencies is indeed in the fortnightly frequency; however, there is also some energy in the monthly frequency. None of the low frequency constituents is included in the forcing so they arise through the interaction between those, which are used to force the model. The results indicate that among these long period tidal constituents, the  $M_{sf}$  ( $M_2$  and  $S_2$  interactions) and that with a 13.66-day period and generated by nonlinear interactions of the  $K_1$  and  $O_1$  constituents (Butman et al., 1983; Brink, 1995; Kowalik and Polyakov, 1998) are dominant components in the Bab el Mandab Strait. Figure 58 shows the spatial structure of the semimajor axes of these two components. The amplitudes of this axis vary between 0.01 cm/s and 5.30 cm/s for the  $M_{sf}$  and between 0.01 cm/s and 5.48 cm/s for another component. An interesting feature of these structures is that the amplitudes of the  $M_{sf}$  constituent in the Strait are generally smaller than those associated with the oscillations generated by the  $K_1$  and  $O_1$  tidal components.

### 5.8. Momentum balance

To examine details in tidal dynamics, each term of the momentum equations was evaluated from the model results in order to identify the main balances that generate the tidal circulation in the Bab el Mandab Strait. Figures 59 and 60 show a time series of the terms in the cross-strait ( $u$  equation) and along-strait ( $v$  equation) momentum equations estimated at grid points of the model domain.

Figure 59 displays the momentum terms evaluated at mesh points located in the deep channel of the Strait. These grid points are near the locations of the ADCP moorings deployed for the BAM project. At these locations as well as at other mesh points examined in the deep channel, the barotropic pressure gradient and local acceleration are

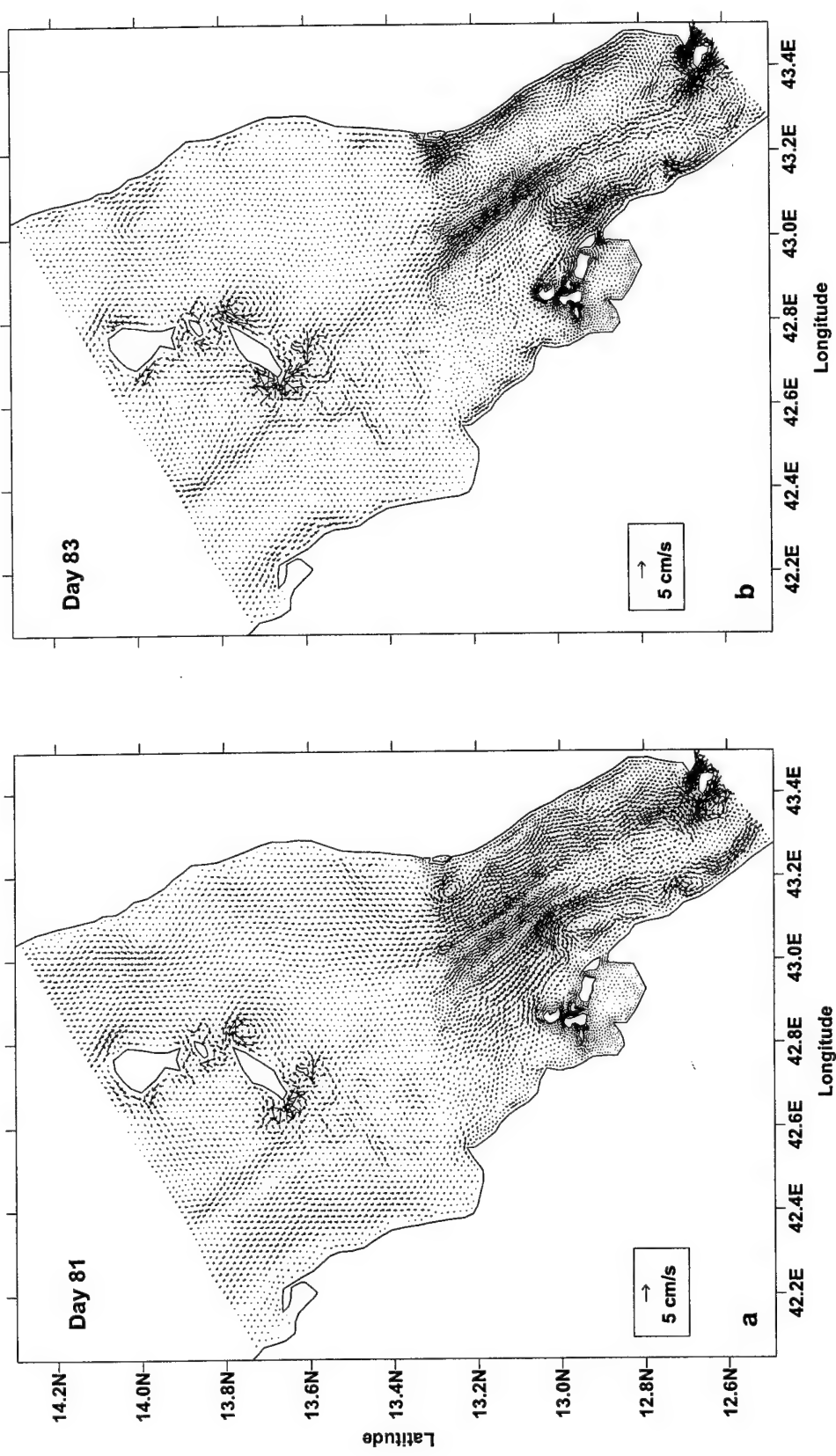
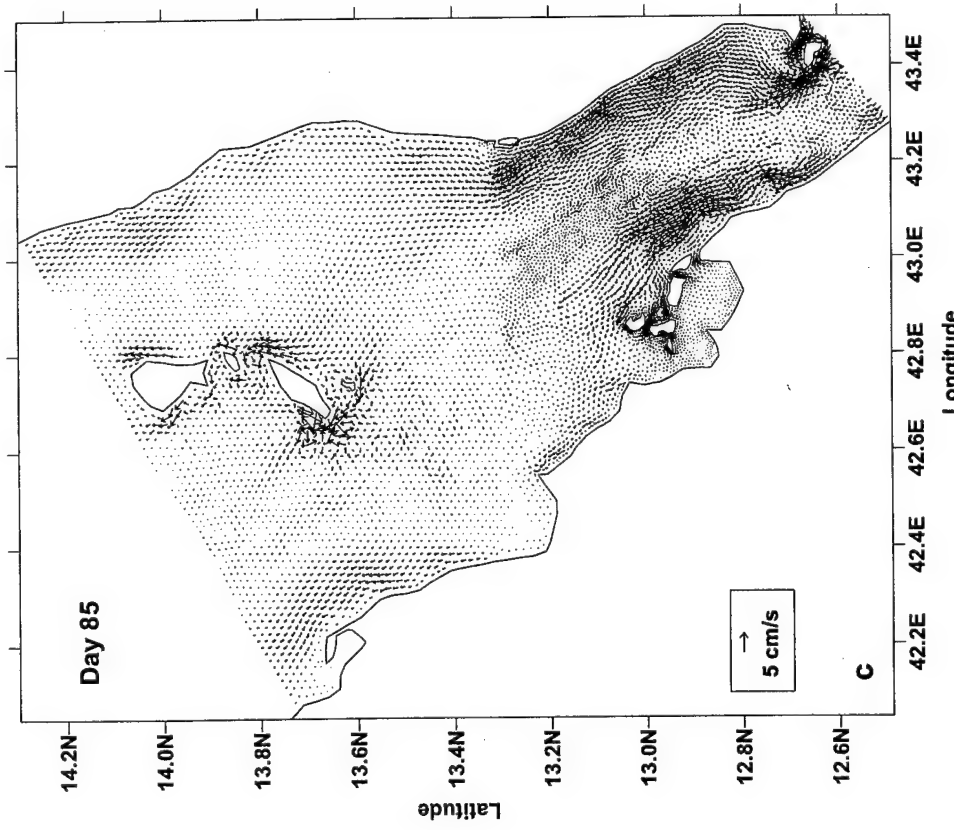
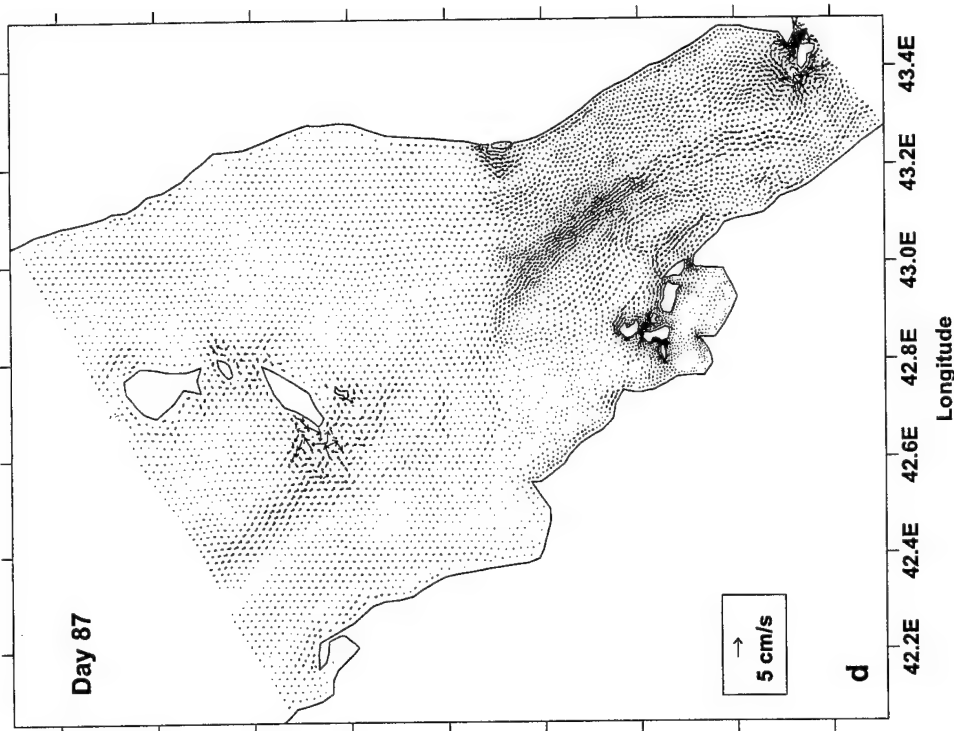
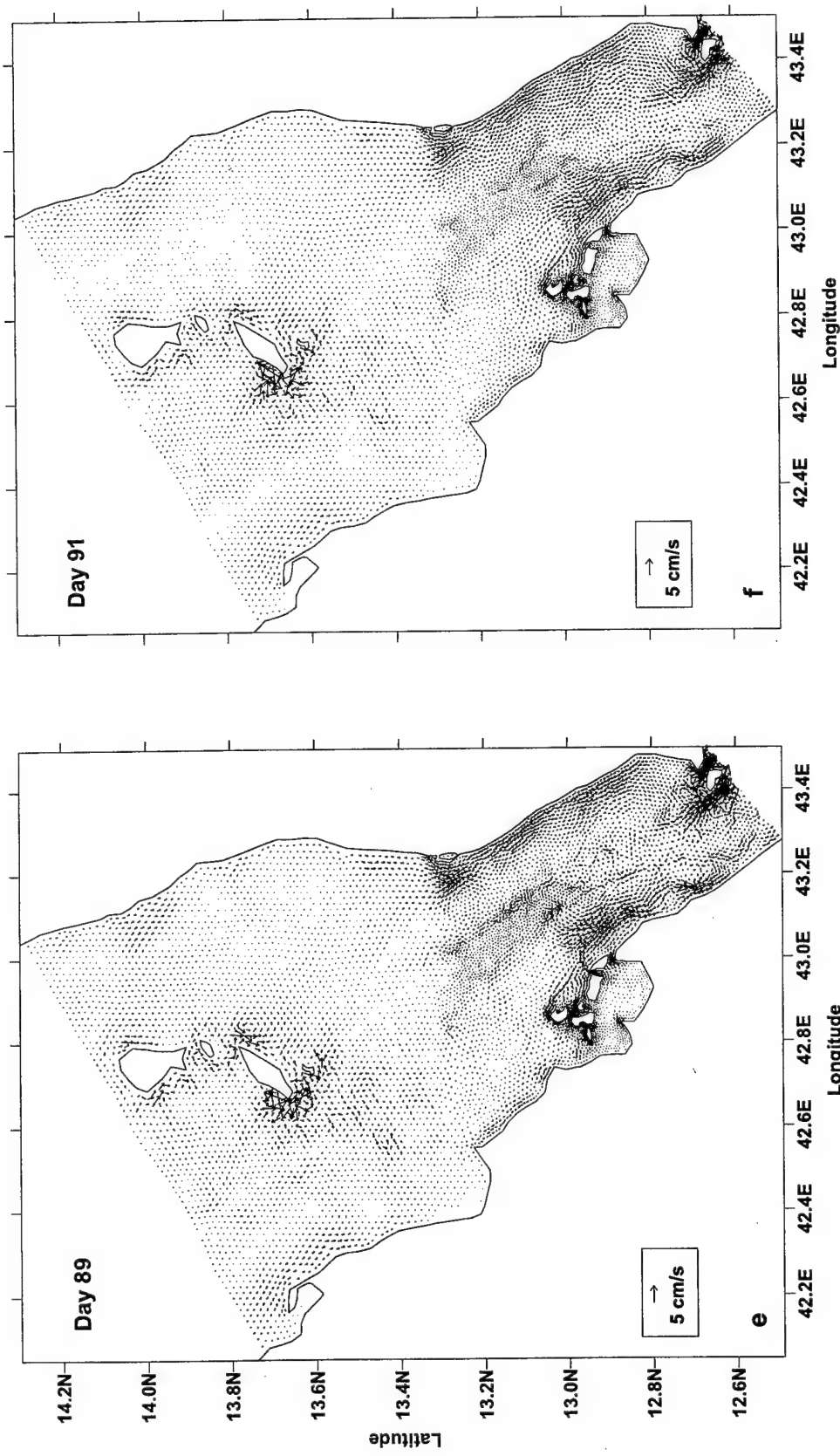


Figure 57. Snapshots of the fluctuating residual at two-day intervals (a) day 81, (b) day 83, (c) day 85, (d) day 87, (e) day 89, (f) day 91, (g) day 93, and (h) day 95.



(Figure 57 cont.)



(Figure 57 cont.)

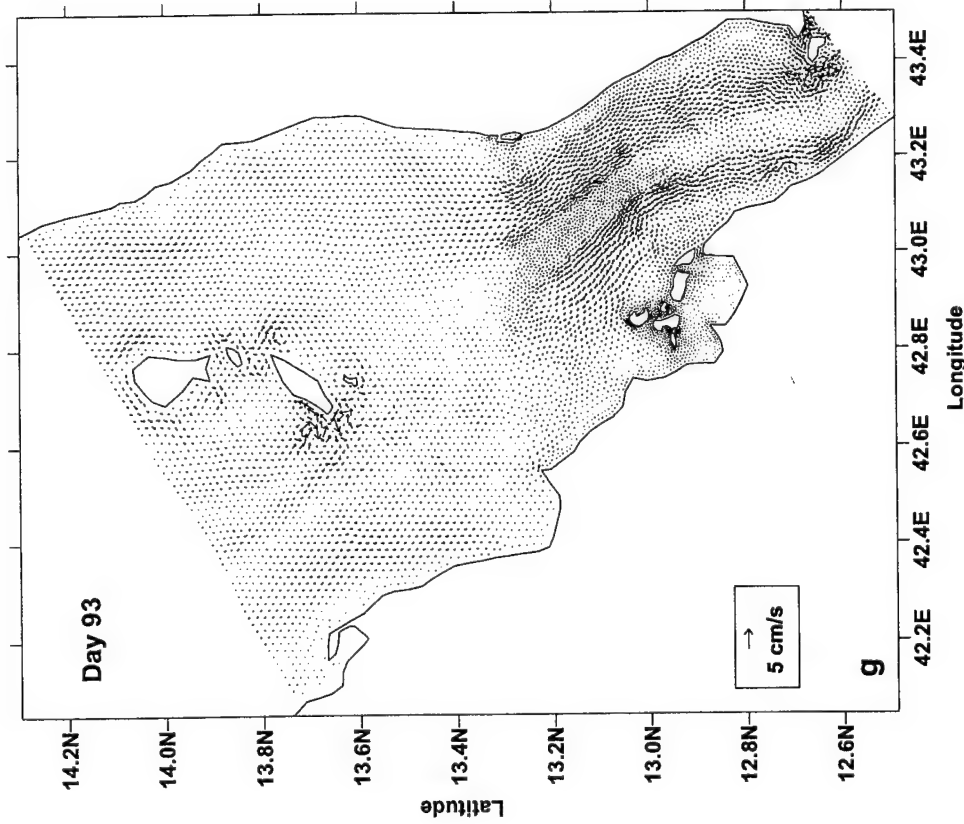
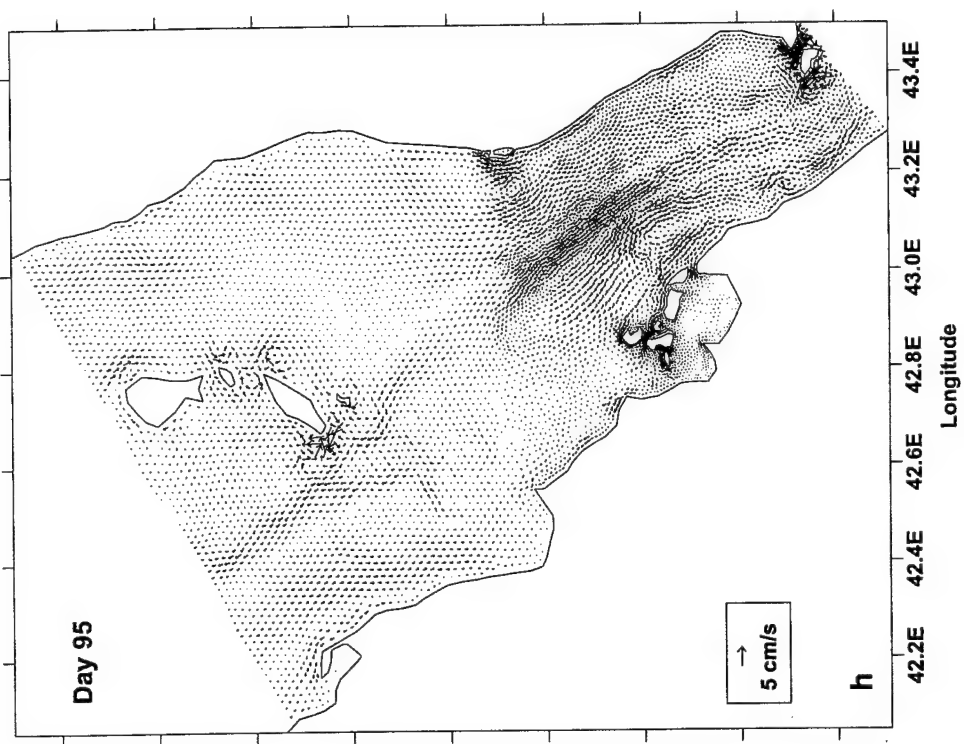


(Figure 57 cont.)

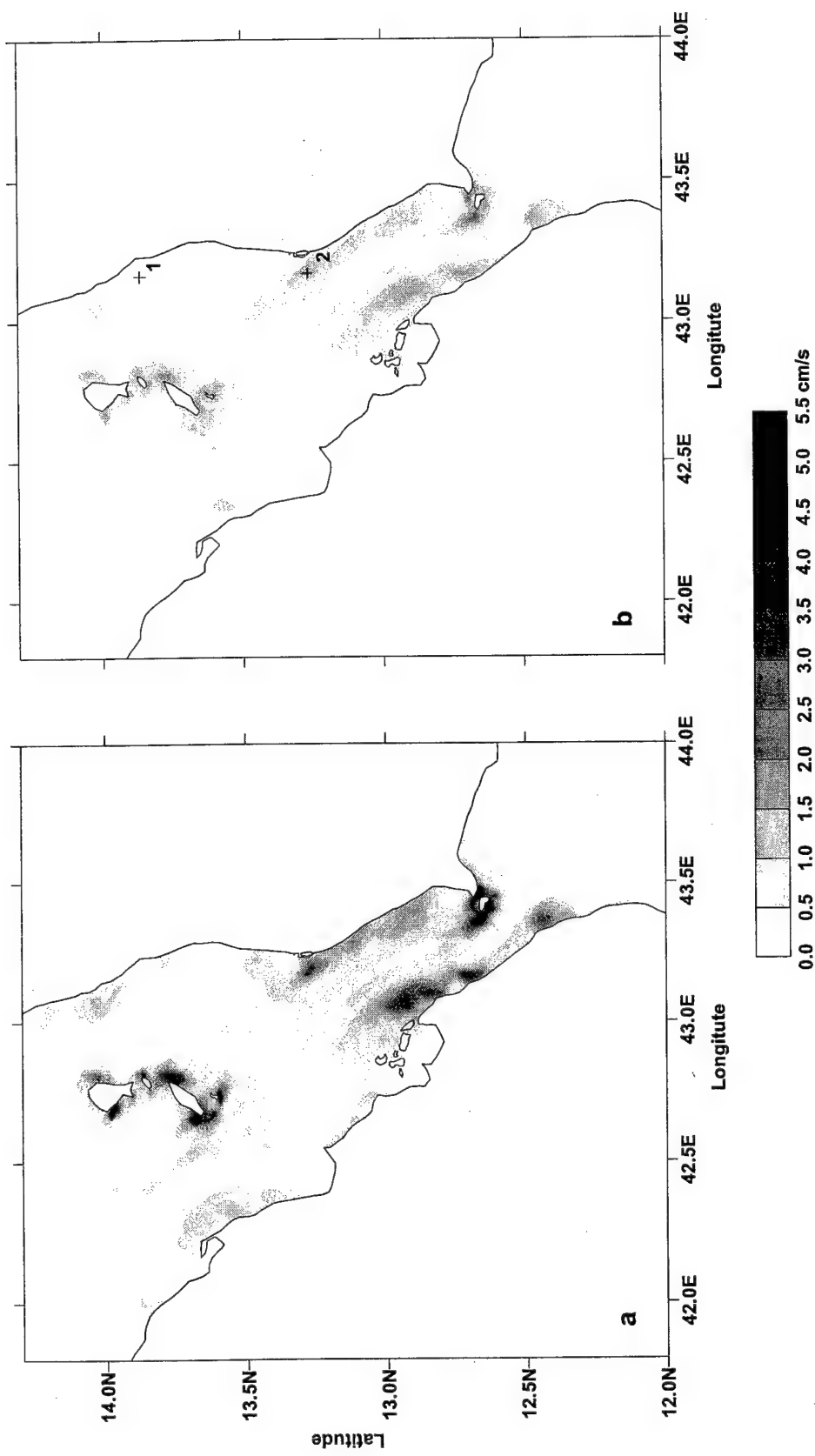


Figure 58. The distribution of the amplitudes of the semimajor axis for (a) the fluctuations generated by the interactions of the  $K_1$  and  $O_1$ , and (b)  $M_{st}$  constituent.

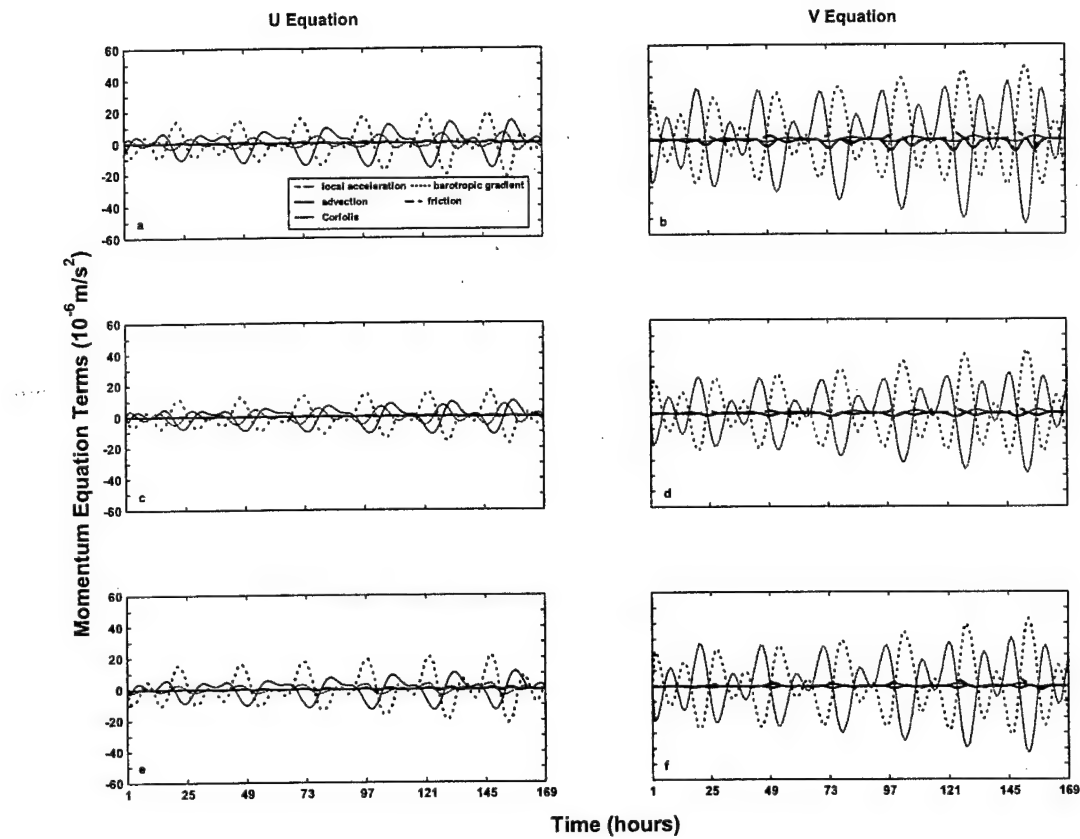


Figure 59. Terms of the momentum equations for the deep-water grid points located near the ADCP moorings (see Figure 1 and Table 10 for the mooring locations) at Perim Narrows (a and b), in the middle of the Strait (C mooring) (c and d), and the Hanish Sill (e and f).

the dominant terms in the along-strait momentum equation, while the pressure gradient is balanced by the Coriolis term and local acceleration (with the latter being generally smaller than the former) in the cross-strait momentum equation. Interestingly, these findings are in agreement with the conclusions, which were reached for the same momentum balances when their terms were evaluated from the data collected near Perim Narrows.

In shallow waters (depths below 50 m), the dominant terms seem to be location dependent. In the parts of the Strait where the residual circulation speeds are small, the barotropic pressure gradient is generally balanced by the Coriolis term in the cross-strait momentum balance (Figure 60a), while the pressure gradient, local acceleration, and friction are dominant terms in the along-strait momentum equation with the advection playing a very small role (Figure 60b). In the areas, where the residual circulation is strong, all terms are generally important with the pressure gradient being the largest one in the cross-strait momentum equation (Figure 60c). In the along-strait momentum balance, the pressure gradient, local acceleration, and friction are the major terms. However, advection, which is smaller than these three, is a much more important term in the momentum balance than where the residual circulation is weak (Figure 60d).

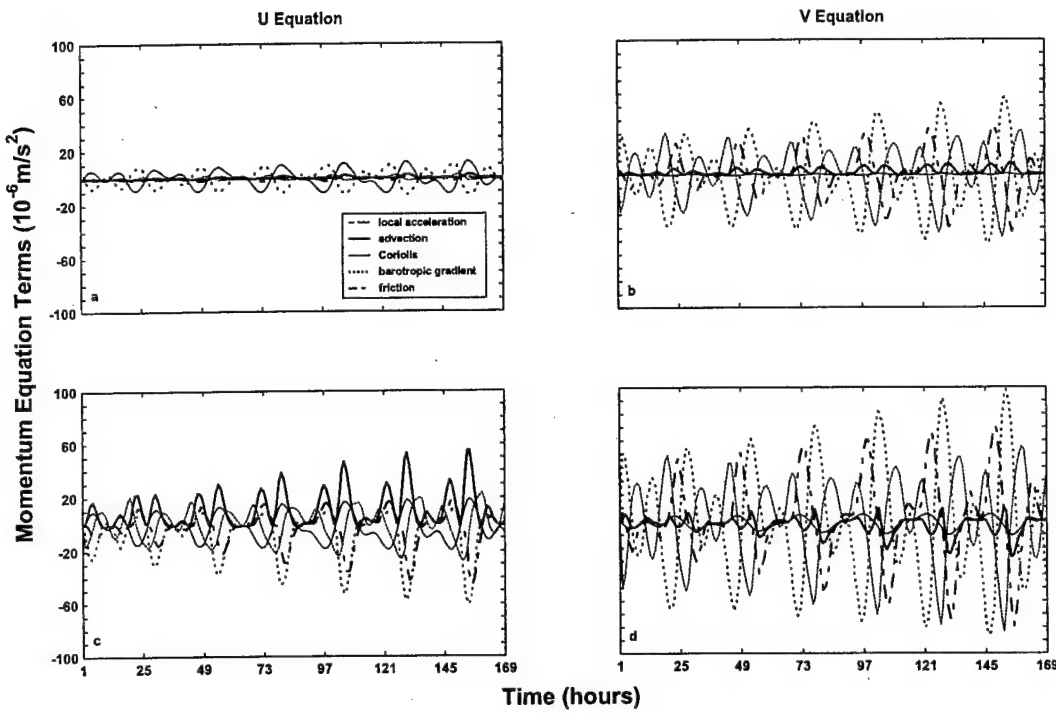


Figure 60. Terms of the momentum equations for the shallow-water grid points (see Figure 58b for their locations): point 1 (a and b) and point 2 (c and d).

### 5.9. Energy flux and dissipation estimates

The vertically integrated energy flux (Kowalik and Proshutinsky, 1993) is given by

$$\bar{F} = (H + \xi) \rho_0 (0.5 |\vec{u}|^2 + g \xi) \vec{u} \quad (15)$$

where  $H$  is the water depth,  $\xi$  is the tidal elevation,  $\rho_0$  is representative seawater density ( $= 1026 \text{ kg/m}^3$ ),  $\vec{u}$  is the current velocity vector, and  $g$  is the acceleration due to gravity. This energy flux includes the contribution of both kinetic and potential energy. In the Bab el Mandab, the flux of the kinetic energy is, on average, one order lower than that of the potential energy.

The average energy flux over a tidal period for the  $K_1$  and  $M_2$  constituents is shown in Figure 61 and 62, respectively. It is very apparent that the fluxes associated with two dominant tidal components display different behavior in the Strait. The  $K_1$  constituent has generally one source of energy, which is the advective flux from the Gulf of Aden into the Strait. The additional contribution of the  $K_1$  energy from the Red Sea proper is negligible because the fluxes associated with this source are three orders of magnitude, smaller than that from the Gulf. In contrast, there are two sources of energy for the  $M_2$  constituent: one is the advective flux from the Gulf of Aden and another is the flux from the Red Sea proper.

Other constituents from the same tidal species have energy sources similar to those of the K<sub>1</sub> and M<sub>2</sub>. However, their magnitudes are smaller, and, for example, the next two strongest constituents O<sub>1</sub> and S<sub>2</sub> have fluxes which, on average, are 38% and 29% of those associated the K<sub>1</sub> and M<sub>2</sub> components, respectively.

Table 9 lists vertically integrated tidal power fluxes normal to two transects that are located near Perim Narrows and the Hanish Sill (see Figure 47 for their locations). All estimates are the net fluxes through the transects with the input flux being positively defined and the output flux being negatively defined. In addition to the K<sub>1</sub> and M<sub>2</sub> fluxes, which are the averages calculated over one tidal cycle, Table 15 lists multiconstituent fluxes, which are obtained by averaging over the 29-day period (29-day) or over 25 hours of the spring or neap tide (spring/neap fluxes). The 29-day fluxes were computed from the tidal predictions over the period of July 1-29, 1995 with all eight constituents included (K<sub>1</sub>, O<sub>1</sub>, P<sub>1</sub>, Q<sub>1</sub>, M<sub>2</sub>, S<sub>2</sub>, N<sub>2</sub>, and K<sub>2</sub>). The spring and neap values are the averages

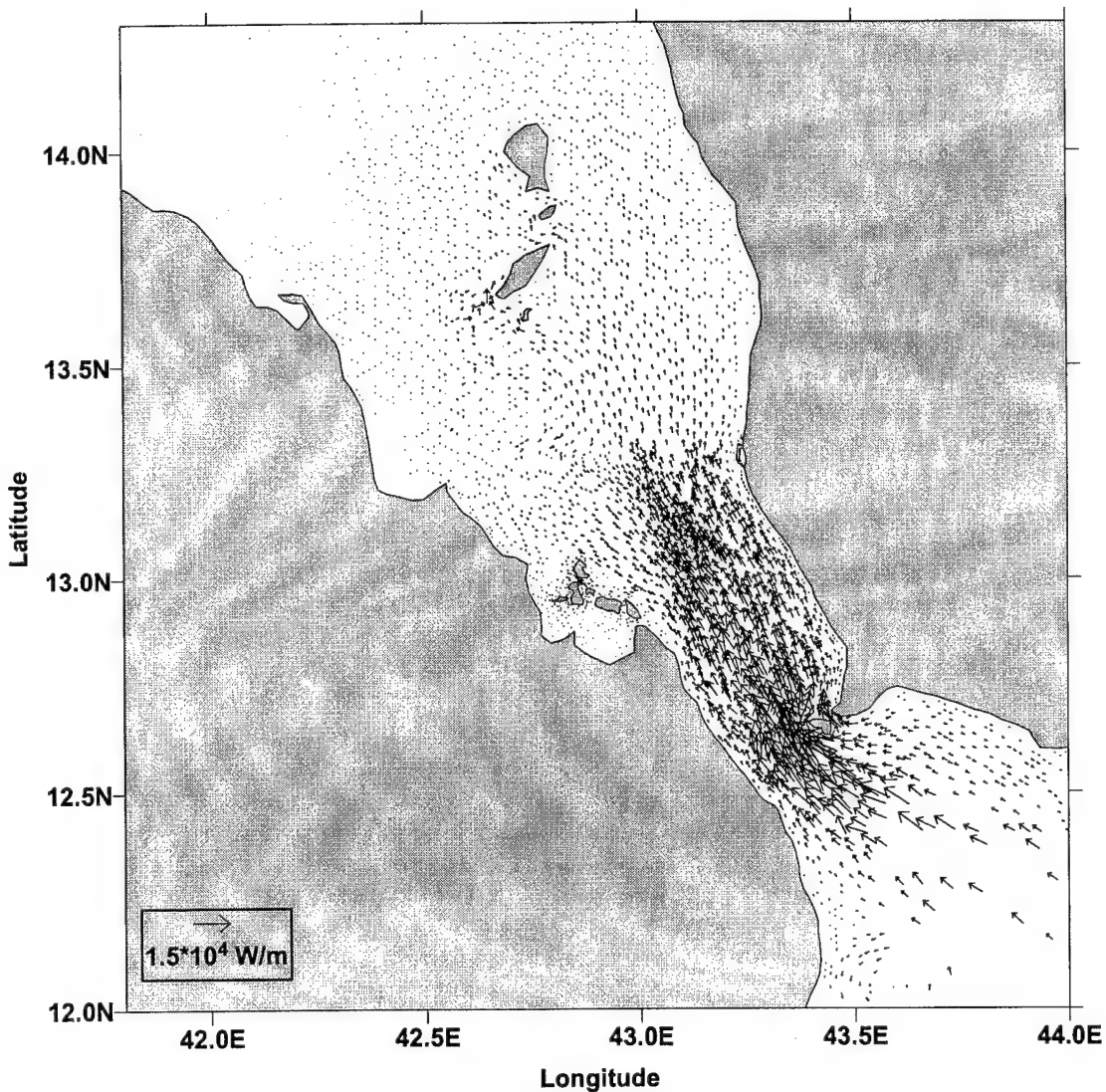


Figure 61. Mean tidal energy flux per unit length for the K<sub>1</sub> constituent.

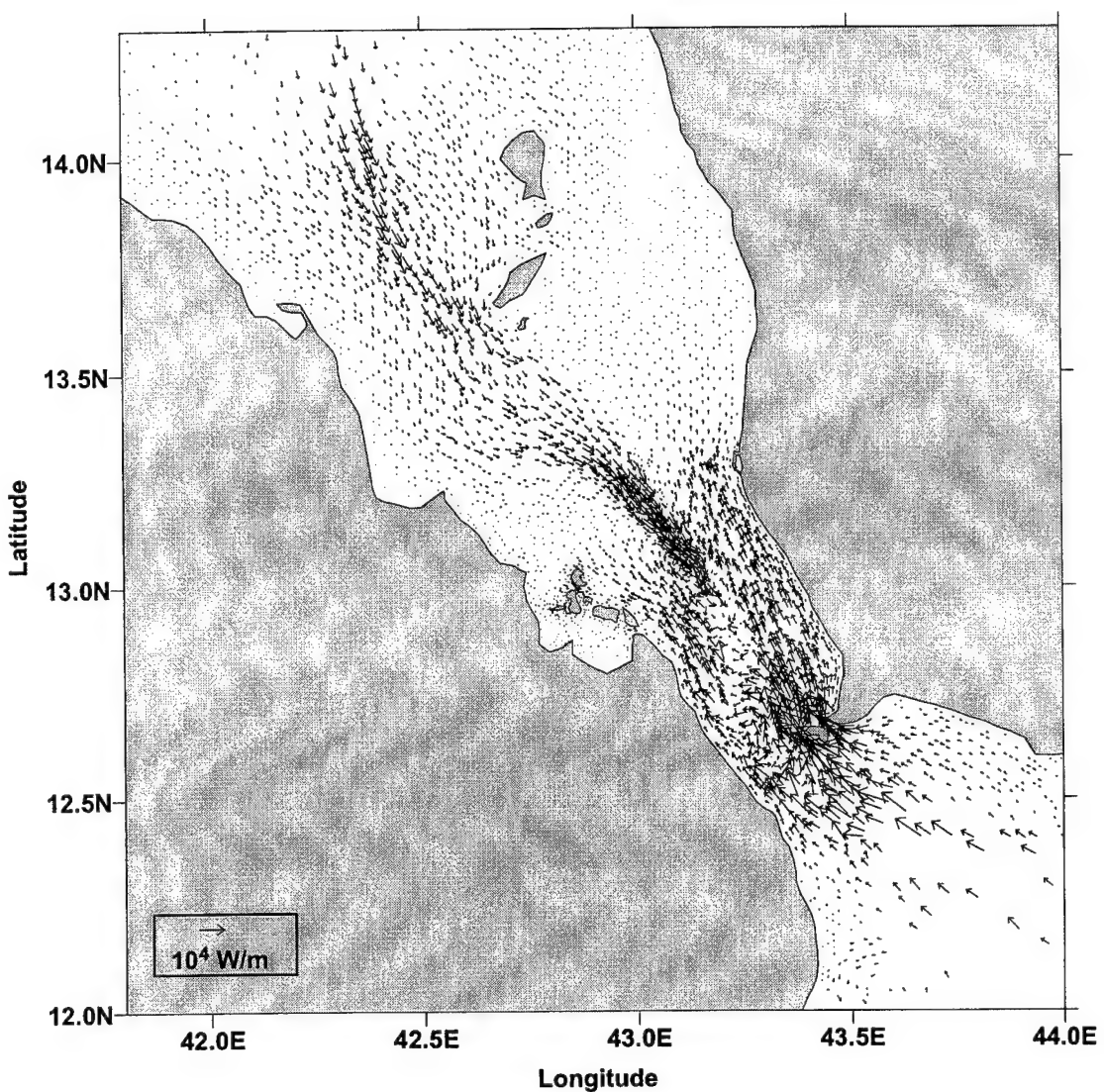


Figure 62. Mean tidal energy flux per unit length for the  $M_2$  constituent.

calculated over 25 hour periods beginning at 00:00 GMT on June 12, 1995 and at 00:00 June 20, 1995, respectively, with all eight constituents included.

Table 9. Vertically integrated power flux (in Gigawatts,  $1 \text{ GW} = 10^9 \text{ Watts}$ ) normal to the transects shown in Figure 46.

Transect	$K_1$	$M_2$	29-day	Spring	Neap
Perim (1)	0.248	0.111	0.730	1.472	0.288
Hanish (2)	- 0.022	0.091	0.065	0.128	- 0.003

The values listed in Table 9 indicate that regardless of the flux type, energy is generally advected in the Strait. The negative (output) net fluxes ( $K_1$  and neap fluxes) are observed only along the Hanish transect and their values are just a small fraction of those transmitted through the Perim Transect. In general, the major part of the barotropic tidal

energy is advected to the Bab el Mandab Strait from the Gulf of Aden. The contribution of energy from the Red Sea is small with the exception of that associated with the  $M_2$  constituent, which is comparable with the  $M_2$  energy input from the Gulf. In addition,

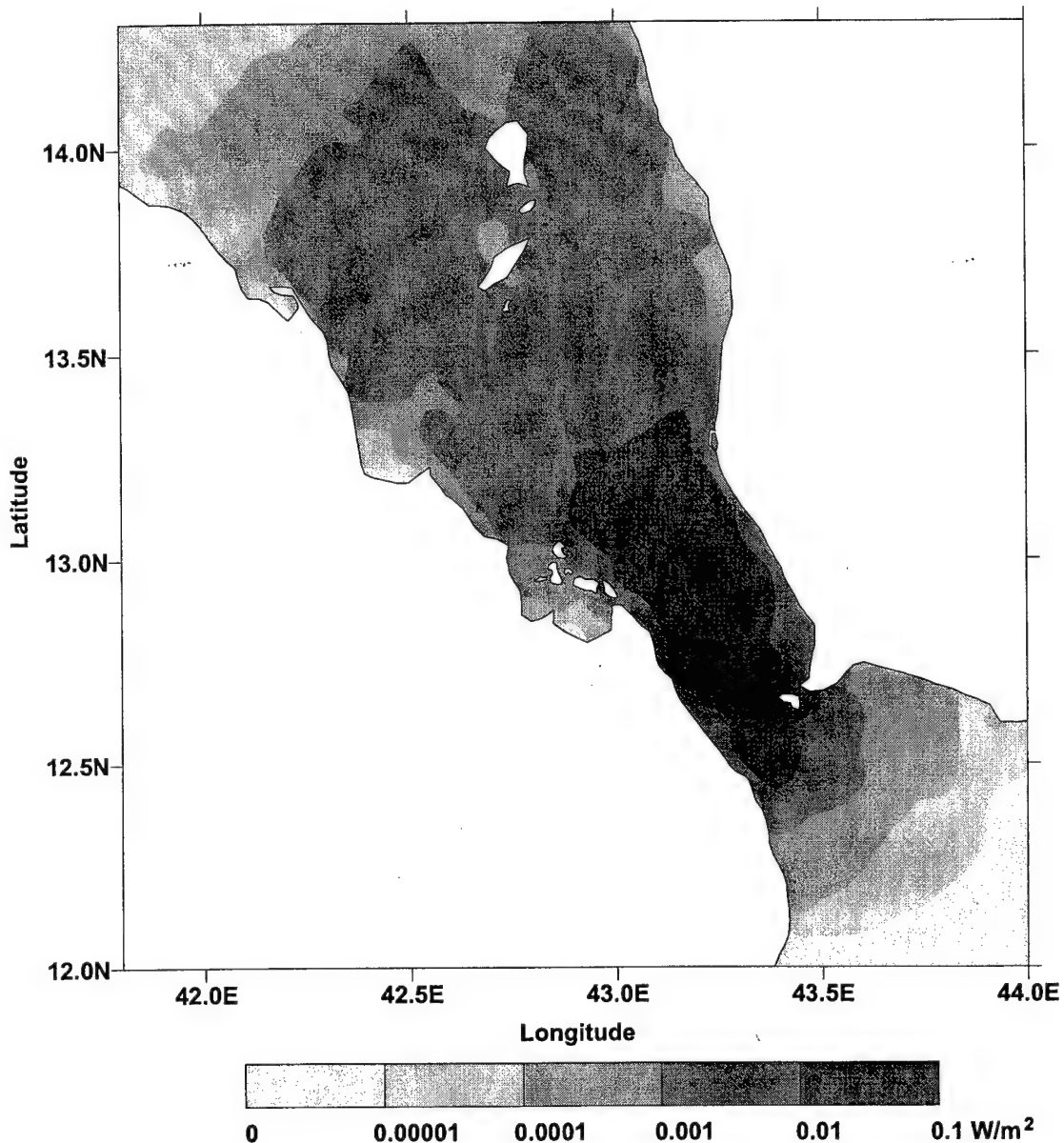


Figure 63. Tidal energy dissipation rate ( $\text{W}/\text{m}^2$ ) for the  $K_1$  constituent.

because of the small output fluxes, almost all tidal energy is dissipated within the Strait. It has to be emphasized here that the model includes only one dissipation mechanism, which is bottom friction (lateral and vertical mixing or energy lost to the generation of internal tides are neglected in the model). When the dissipation process is viewed in terms of the specific constituents, more  $M_2$  energy than  $K_1$  is lost in the study area (98% versus 90% of that which enters). Over the 29-day period, 98% of the energy entering the

Strait is dissipated. The analogous dissipation percentage is observed for the chosen spring tide period, while for the neap tide period, the percentage is slightly lower and equal to 96%. Finally, the dissipation in the polygon encompassed by the chosen transects is estimated as 0.226, 0.199, 0.790, 1.586, and 0.282 GW, respectively, for  $K_1$ ,  $M_2$ , the 29-day and the 25-hour spring and neap periods. To put these numbers in perspective, Candela et al. (1990) estimated, from the data, the net energy flux of the  $M_2$  wave at the Camarinal Sill in the Strait of Gibraltar as  $0.8 \pm 1$  GW; Tejedor et al. (1999) estimated from a model, the  $M_2$  energy dissipation in the same strait as 0.55 GW; and

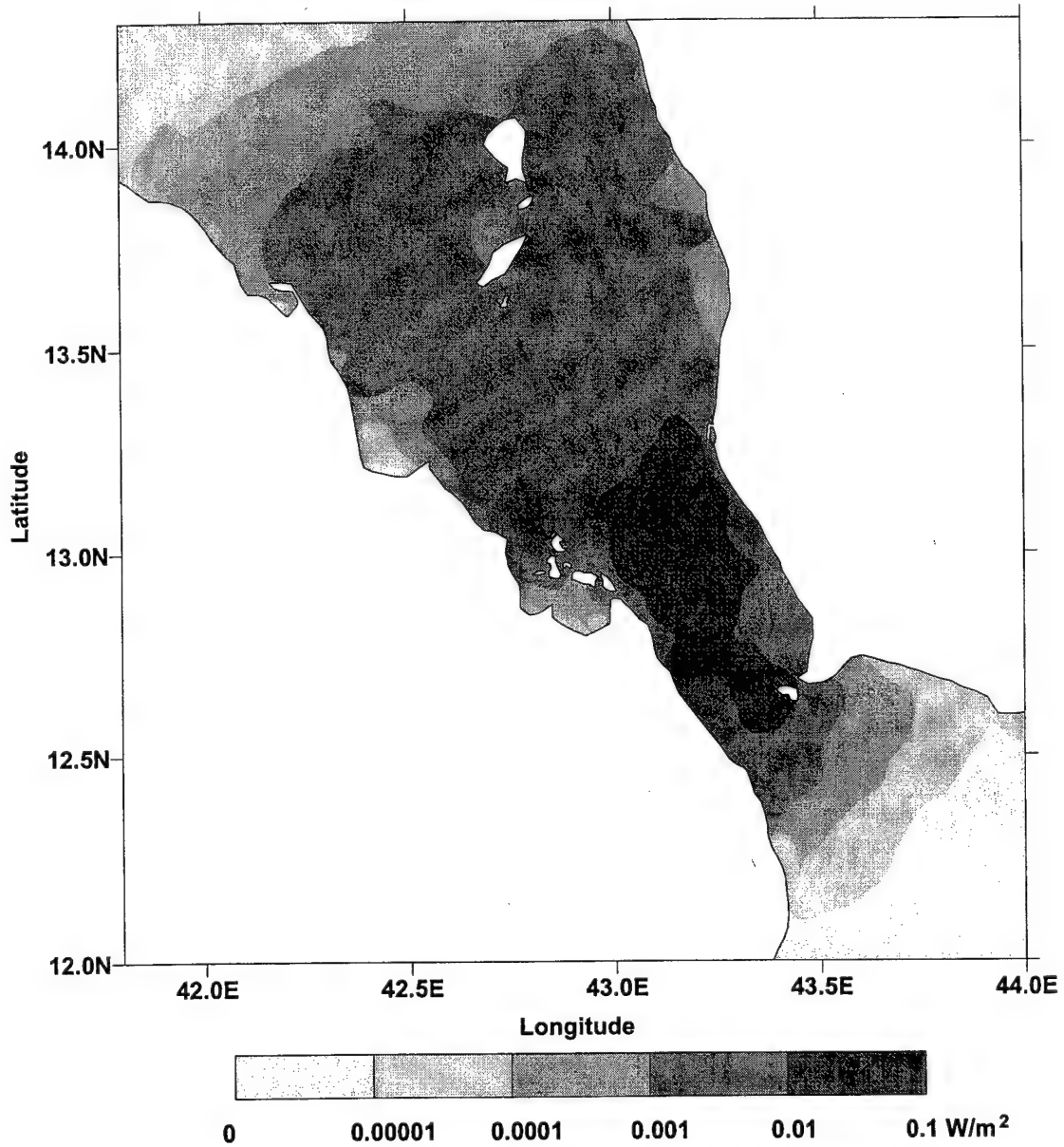


Figure 64. Tidal energy dissipation rate ( $\text{W/m}^2$ ) for the  $M_2$  constituent.

Ray (1993) estimated the work done on the  $M_2$  tide by the lunar-generating forces, which is equal to the worldwide dissipation, to be  $2.5 \pm 0.1$  TW ( $1\text{ TW} = 10^{12}$  Watts).

To investigate further the dissipation process of the  $K_1$  and  $M_2$  waves in the Bab el Mandab Strait, a rate of energy dissipation was computed. This rate was estimated from (Tsimplis et al., 1995, Munk, 1997):

$$d = \frac{1}{T} \int_0^T C_d \rho_o (u^2 + v^2)^{3/2} dt \quad (16)$$

where  $C_d$  is the bottom drag coefficient ( $= 0.003$ ),  $\rho_o$  is the seawater density ( $= 1026 \text{ kg/m}^3$ ),  $u, v$  are the velocity components, and  $T$  is the tidal period.

Figures 63 and 64 display the spatial distribution of the rate of energy dissipation in the Bab el Mandab Strait due to the  $K_1$  and  $M_2$  constituents. The dissipation rate spatial distributions demonstrate that there are similarities in the dissipation pattern of the diurnal and semidiurnal tides. Furthermore, the dissipation process is not uniform in the Strait. The maximum rate of energy dissipation for both tidal components is found in the narrowest part of the study area located between Perim Narrows and the Assab-Mocha line. In this region, it reaches values of or larger than  $0.01 \text{ W/m}^2$  for both tidal components. Farther north, the mean dissipation rate is generally on the order of  $10^{-3} \text{ W/m}^2$ . Integration of the dissipation rate over the area of the Bab el Mandab Strait yields other estimates of the energy dissipation in this region, which are  $0.16 \text{ GW}$  and  $0.12 \text{ GW}$  for the  $K_1$  and  $M_2$  constituents, respectively, and are comparable to those computed from input and output fluxes. Additionally, potential contribution to energy dissipation from nonlinear interactions between different tidal constituents and/or tides and low frequency flow has not been studied in the Bab el Mandab Strait, and this problem would be an interesting topic for future research.

### 5.10. Summary

The barotropic tides in the Bab el Mandab Strait were numerically simulated with the two-dimensional finite element hydrodynamic model named AAdvanced Two-Dimensional Depth-Integrated CIRCulation Model for Shelves, Coasts and Estuaries (ADCIRC-2DDI) developed by Luettich et al., (1992) and Westerink et al. (1994). The model was forced by four diurnal ( $K_1, O_1, P_1, Q_1$ ) and four semidiurnal ( $M_2, S_2, N_2, K_2$ ) tidal constituents whose amplitudes and phases were taken from the World Ocean Tidal (La Provost et al., 1994). In addition, the tidal potential forcing within the model domain was applied for the same eight constituents.

The ADCIRC-2DDI model simulates well the diurnal tidal elevations (small rms values that vary between  $0.9 \text{ cm}$  and  $2.2 \text{ cm}$ ). However, its performance for the semidiurnal tidal elevations is less satisfactory (rms values vary between  $3.0 \text{ cm}$  and  $9.4 \text{ cm}$ ) due to the large errors between observed and computed phases in the region where there is a nodal line for these tides in the Strait. A set of experiments (changes in depth at the model nodes) implies that the phases errors are partly related to the bathymetry. The comparison between observed and computed currents is very satisfactory for both semidiurnal and diurnal constituents because differences between observed and computed current ellipse parameters are small and, for instance, the computed amplitudes of the

semimajor axis are only 20% or less smaller than those estimated from the data, and the phase difference is not larger than 1 hour.

The model amplitudes of the elevation for the diurnal components show a rapid decrease in the along-strait direction and little variation in the cross-strait direction. For instance, the amplitudes of the most energetic diurnal constituent,  $K_1$ , decrease from 36 cm near Perim Narrows to 8 cm near the Hanish Sill. The phases of the diurnal constituents display some variability in the cross-strait direction near the Hanish Islands, but south of these Islands they are nearly constant. Additionally, the model results indicate the presence of the amphidromic systems located north of the Hanish Islands.

For the semidiurnal tides, the amplitudes of the surface tide also display more variations along than across the Strait. Similar to the amplitudes of the diurnal tides, they show rapid decrease in this direction and the amplitudes of the most energetic semidiurnal constituent,  $M_2$ , diminish from their maximum values ( $\sim 45$  cm) near Perim Narrows to their minimum values ( $\sim 1$  cm) observed near Hanish Islands. These minimum values near the Hanish Islands are accompanied by rapid changes in phase for the  $M_2$ ,  $S_2$ , and  $N_2$  constituents, and this configuration of the amplitudes and phases indicate the presence of amphidromic systems for these tidal components.

Barotropic tidal currents generated by the eight constituents have the largest amplitudes of the semimajor axis between Perim Narrows and Assab-Mocha line. Farther north, the amplitudes are reduced, and they are approximately 50% of those observed between Perim Narrows and Assab-Mocha. In addition, the tidal currents are nearly rectilinear in the Strait, and the direction of the maximum flow is generally aligned with the along-strait axis. The strongest tidal currents are generated, as expected, by the  $K_1$  and  $M_2$  components. The amplitudes of the  $K_1$  currents as well as the amplitudes of the currents associated with the  $M_2$  constituent may reach values as large as 40 cm/s at Perim Narrows.

Residual circulation induced by the tidal currents, which are generated by the eight tidal constituents ( $K_1$ ,  $O_1$ ,  $P_1$ ,  $Q_1$ ,  $M_2$ ,  $S_2$ ,  $N_2$ , and  $K_2$ ), is rather weak in the major part of the study area and consists of mean (time-averaged) and fluctuating (deviation from the mean) components. The strongest residual flow speeds are usually found near the islands and in the shallow parts of the region located between Perim Narrows and Assab-Mocha line. The velocities of the mean component averaged over the entire area of the Strait are around 1 cm/s. In general, the mean residual flow contributes little to the overall circulation. In addition, the fluctuating component is dominated by fortnightly oscillations, which are generated by the interactions of the  $K_1$  and  $O_1$  constituents as well as the interaction between the  $M_2$  and  $S_2$  components.

Examination of the momentum balance terms indicates that in the deep parts of the Strait, the tidal dynamics are linear, i.e., the momentum balances are dominated by the linear terms. The elevation gradient, Coriolis term and local acceleration are the dominant terms for the cross-strait balance, while for the along-strait balance, the local acceleration and elevation gradient are the most important ones. However, in shallow waters, the nonlinear terms, such as friction and advection, become as important as the linear terms.

In the Bab el Mandab, the flux of the kinetic energy is, on average, one order lower than that of the potential energy. In general, the mean energy fluxes are small mainly due to nearly  $\sim 90^\circ$  phase difference between tidal velocity and elevation, which

is observed in the major part of the Strait. Furthermore, the distribution of the average energy flux is different for the diurnal and semidiurnal components. The  $K_1$  constituent has generally one source of energy, which is the advective flux from the Gulf of Aden. The additional contribution of the  $K_1$  energy from the Red Sea proper is negligible because the fluxes associated with this source are three orders of magnitude, smaller than that from the Gulf. In contrast, there are two sources of energy for the  $M_2$  constituent: one is the advective flux from the Gulf of Aden and another is the flux from the Red Sea proper. Other constituents from the same tidal species have energy sources similar to those of the  $K_1$  and  $M_2$ . However, their magnitudes are smaller, and, for example, the next two strongest constituents  $O_1$  and  $S_2$  have fluxes which, on average, are 38% and 29% of those associated the  $K_1$  and  $M_2$  components, respectively.

Very small energy fluxes from the Strait to the adjacent basins indicate that almost all tidal energy is dissipated within the Strait. The distribution of the rate of energy dissipation due to bottom friction implies that the major area of dissipation is located between Perim Narrows and the Assab-Mocha line. The energy dissipation, which was estimated from a difference between the output and input fluxes through two transects located at the southern and northern ends of the Strait, is 0.226 GW and 0.199 GW for the  $K_1$  and  $M_2$  constituents, respectively. These estimates are comparable to other estimates of the energy dissipation, which were obtained from the integration of the dissipation rate over the area of the Strait, and they are 0.16 GW and 0.12 GW for the  $K_1$  and  $M_2$  constituents, respectively.

## 6. SUMMARY AND CONCLUSIONS

The Bab el Mandab Strait is located in the southern end of the Red Sea and is its major link with the Gulf of Aden and Indian Ocean. This Strait is also a region where the transition occurs between two noticeably different tidal regimes: the Gulf of Aden, where tidal fluctuations are mixed and have a range in excess of 2 m, and the Red Sea, where the tides are principally semidiurnal and their range is less than 1 m.

Prior to the BAM project, historical observations and descriptions of the tides, especially tidal currents, in the Strait were very limited and generally restricted to its southern end. Extensive surveys carried out between May of 1995 and July of 1997 for the BAM project allowed us to examine in more details tidal characteristics in the Bab el Mandab Strait. Objectives for data analyses were: (1) to identify major tidal constituents in the entire Strait, (2) to examine their variability in the region, and (3) to establish whether seasonal changes in stratification influence the observed tidal currents. Major findings of these analyses concerning the tidal elevation and currents are summarized below.

Within the Strait, subsurface pressure observations indicate that tidal water level fluctuations have a larger range ( $\sim 2$  m) in the southern part than in the northern part where their range is below 1 m. The major tidal constituents of the surface tide are the  $K_1$ ,  $O_1$ , and  $P_1$  components for the diurnal species and the  $M_2$ ,  $S_2$ , and  $N_2$  components for the semidiurnal species. The largest amplitudes among diurnal components are observed for the  $K_1$ , while among semidiurnal constituents, the  $M_2$  is a dominant component. The major changes in amplitudes and phases of these constituents are observed along the Strait. For the diurnal components, the along-strait variability is generally associated with their amplitudes, which decrease from their maximum values observed at the southern end to their minimum values present at the northern end. For the semidiurnal components, both tidal constants display large changes within the Strait. Their amplitudes show a minimum approximately in the middle of the Strait and larger values at Perim Narrows in the south and the Hanish Sill in the north, while the phase distribution implies nearly an  $180^\circ$  difference between these two locations. The different variability of the amplitudes and phases of the semidiurnal and diurnal surface tides generates three different tidal regimes within the Strait: (1) mixed, predominantly semidiurnal in the south, (2) mixed, predominantly diurnal in the middle, and (3) semidiurnal in the northern part.

The tidal currents in the Bab el Mandab Strait are nearly rectilinear and generally aligned with the along-strait axis. They are the most energetic near Perim Narrows. Farther north, the tidal currents fluctuations are still very distinct but their range is smaller. Variance estimated from the observations indicate that the tidal currents are of the mixed type even near the Hanish Sill where the surface tide regime is semidiurnal; however, whether the tidal current regime is predominantly diurnal or semidiurnal it depends on depth and stratification. Similar to fluctuations of the surface tide, the tidal currents are also dominated by the same constituents ( $K_1$ ,  $O_1$ ,  $P_1$ ,  $M_2$ ,  $S_2$ , and  $N_2$ ) among which the  $K_1$  and  $M_2$  generate the most energetic tidal flows. Amplitudes of these constituents have the largest values in the southern part of the Strait and show smaller values farther north. The vertical structure of these constituents is complicated, differs

between semidiurnal and diurnal constituents, and depends on the location and stratification.

There are two different types of stratification in the Strait: (1) a winter stratification regime, which is associated with the two-layer subtidal circulation and is characterized by three-layer structure (two nearly homogenous layers and one pycnocline layer between them), and (2) more variable summer stratification regime, which is observed during the three-layer subtidal circulation period and may have five different layers in the vertical (three nearly homogenous layers and two pycnocline layers). The presence of two different types of stratification in the Strait causes the constituents to have different vertical profiles: one for the winter stratification and another for the summer stratification. All parameters (semimajor axis, semiminor axis, inclination angle, phase) of the tidal current ellipse are influenced by the change in stratification regime; however, the most evident changes are observed in the vertical profiles of the semimajor axis. When these profiles are compared at three different moorings located in a deep channel, which runs along the Strait, the changes are more distinct for the  $K_1$  constituent than those for the  $M_2$  constituent. A noticeable maximum in the pycnocline layer is observed for the  $K_1$  component during the winter stratification period whereas for summer stratification, this maximum is not observed at Perim Narrows and in the middle of the Strait, and it is smaller and present only in the lower pycnocline at the Hanish Sill. At the same time, larger amplitudes of the  $M_2$  semimajor axis in the pycnocline layer for both stratifications are only observed near the Hanish Sill (for the summer stratification, the maximum is located in the lower pycnocline).

Current measurements collected near Perim Narrows also indicate that there is some variability of the ellipse parameters across the Strait. Vertical distributions of these parameters are again different for the summer and winter stratifications, and the major changes are generally associated with the amplitudes of the semimajor axis. Additionally, for the same stratification regime, the changes are more evident for the  $M_2$  constituent. For the winter stratification, its amplitudes, for example, show a distinct maximum in the pycnocline layer in one mooring site but there is no such maximum at another mooring location.

Furthermore, the tidal currents are very coherent with the water level fluctuations for both semidiurnal and diurnal frequencies. The phase difference between the currents and surface tide is  $\sim 90^\circ$  for both frequency bands. The phase lag between the semidiurnal elevations and currents, small differences between current phase, nearly a  $\sim 180^\circ$  phase difference between the elevations at Perim Narrows and the Hanish Sill, and the existence of the nodal zone for the semidiurnal tides (Vercelli, 1925; Defant, 1961) seem to imply that the semidiurnal tidal wave has characteristics of a standing wave in the Bab el Mandab Strait. Based solely on the phase relationship between the elevation and currents, a similar conclusion can be drawn about the diurnal tides; however, such an interpretation can be erroneous because the observed phase difference may be also generated by very variable geometry of the Strait.

Amplitudes of the depth averaged currents as well as the results of the dynamic mode decomposition imply that the tidal currents in the Bab el Mandab Strait are dominated by the barotropic signal. The structure of the barotropic currents in the deep channel and surface tides near Perim Narrows is fairly well explained by a simple momentum balance. To first order, a balance exists in the along-strait direction between

local acceleration and the elevation gradient, while in the cross-strait direction, a balance between local acceleration, Coriolis term, and elevation gradient is observed.

Due to the existence of density variability in the vertical, the tidal currents in the Bab el Mandab Strait also have a baroclinic component. This baroclinic component is primarily of a diurnal period, and the strongest signal is observed in the pycnocline layer. Additionally, this signal is more pronounced for the winter stratification period, and it is very evident at Perim Narrows and the Hanish Sill. Analyses of the data suggest that the baroclinic velocities contain strong contribution from the second and third baroclinic modes at Perim Narrow, and from the first and second modes at the Hanish Sill. However, to interpret what type of baroclinic responses to the tidal forcing are actually present at the Bab el Mandab Strait, more detailed (finer resolution in time and space) observations of density and currents are definitely required considering the fact that this response may have several different forms.

The barotropic tides in the Bab el Mandab Strait were examined in more detail using results from the high-resolution two-dimensional finite element model (ADCIRC-2DDI). The model, which is forced by four diurnal ( $K_1$ ,  $O_1$ ,  $P_1$ ,  $Q_1$ ) and four semidiurnal ( $M_2$ ,  $S_2$ ,  $N_2$ ,  $K_2$ ) tidal constituents, simulates well the diurnal tidal elevations. However, its performance for the semidiurnal tidal elevations is less satisfactory due to the large errors between observed and computed phases in the region where there is a nodal line for these tides in the Strait. The comparison between observed and computed currents is very satisfactory for both semidiurnal and diurnal constituents because differences between observed and computed current ellipse parameters are small and, for instance, the computed amplitudes of the semimajor axis are only 20% or less smaller than those estimated from the data. The overall purpose of this numerical study was: (1) to describe in more detail the distributions of the barotropic tidal elevation and currents within the Strait; (2) to evaluate whether residual circulation generated by the barotropic tidal currents contributes significantly to the overall circulation in this region; (3) to examine which momentum balance terms are dominant; and (4) to estimate energy fluxes and energy dissipation in the Strait. Major findings of the model data analyses are briefly described below.

Similar to the limited data, the model amplitudes of the elevation for the diurnal components show a rapid decrease in the along-strait direction and little variation in the cross-strait direction. The phases of these constituents display some variability in the cross-strait direction near the Hanish Islands, but south of the Islands they are nearly constant. For the semidiurnal tides, the amplitudes of the surface tide also display more variations along than across the Strait. Similar to the amplitudes of the diurnal tides, they show rapid decrease in this direction from their maximum values in the southern part to the minimum values observed near Hanish Islands. These minimum values near the Hanish Islands are accompanied by rapid changes in phase for the  $M_2$ ,  $S_2$ , and  $N_2$  constituents, and this configuration of the amplitudes and phases indicate the presence of amphidromic systems for these tidal components. Furthermore, the barotropic tidal currents generated by these eight constituents have the largest amplitudes of the semimajor axis between Perim Narrows and Assab-Mocha line. Farther north, the amplitudes are reduced, and they are approximately 50% of those observed between Perim Narrows and Assab-Mocha. In addition, the tidal currents are nearly rectilinear in

the Strait, and the direction of the maximum flow is generally aligned with the along-strait axis.

Residual circulation generated by the tidal currents is rather weak in the major part of the study area and consists of mean (time-averaged) and fluctuating (deviation from the mean) components. The strongest residual flow speeds are usually found near the islands and in the shallow parts of the region located between Perim Narrows and Assab-Mocha line. The velocities of the mean component averaged over the entire area of the Strait are around 1 cm/s. In general, the residual flow contributes little to the overall circulation. In addition, the fluctuating component is dominated by fortnightly oscillations, which are generated by the interactions of the  $K_1$  and  $O_1$  constituents as well as the interaction between the  $M_2$  and  $S_2$  components.

Examination of the momentum balance terms indicates that in the deep parts of the Strait, the tidal dynamics are linear, i.e., the momentum balances are dominated by the linear terms. The elevation gradient, Coriolis term and local acceleration are the dominant terms for the cross-strait balance, while for the along-strait balance, the local acceleration and elevation gradient are the most important ones. However, in shallow waters, the nonlinear terms, such as friction and advection, become as important as the linear terms. Therefore, to capture variability of the barotropic tides in the entire Bab el Mandab Strait, one needs to employ a fully nonlinear hydrodynamic set of the momentum equations.

The mean energy fluxes of the  $K_1$  and  $M_2$  constituents are small mainly due to nearly  $\sim 90^\circ$  phase difference between tidal velocity and elevation, which is observed in the major part of the Strait. They are directed from the Gulf of Aden for the  $K_1$  and from the Red Sea proper and Gulf of Aden for the  $M_2$ . Very small energy fluxes from the Strait to the adjacent basins indicate that almost all tidal energy is dissipated within the Strait. The distribution of the rate of energy dissipation due to bottom friction implies that the major area of dissipation is located between Perim Narrows and the Assab-Mocha line. The energy dissipation, which was estimated from a difference between the output and input fluxes through two transects located at the southern and northern ends of the Strait, is 0.226 GW and 0.199 GW for the  $K_1$  and  $M_2$  constituents, respectively. These estimates are comparable to other estimates of the energy dissipation, which were obtained from the integration of the dissipation rate over the area of the Strait, and they are 0.16 GW and 0.12 GW for the  $K_1$  and  $M_2$  constituents, respectively. This agreement between two different estimates of the  $M_2$  energy dissipation is very encouraging and makes the estimate obtained from the first method less questionable considering the fact that the  $M_2$  elevation harmonic constants, which were used to calculate the energy flux through the Hanish transect, are not well simulated by the model.

In conclusion, analyses of the observations as well as analyses of the model results definitely improved our understanding of the tidal frequency motion in the Bab el Mandab Strait. However, at the same time, there are topics that require more research. At this point, the most urgent problems, which need further research, are those associated with the baroclinic tidal motion considering the fact that this motion may influence water mass exchange between the Red Sea and Indian Ocean as it does in the Strait of Gibraltar. Among others, questions, which need to be addressed, are: (1) what is the type of the baroclinic response in the Strait; (2) is there a net tidal transport of the Red Sea waters to the Gulf of Aden and Indian Ocean; (3) how large is the impact of the mean

flow on the distribution of internal modes in the Strait. In addition, the numerical model of the barotropic tides needs to be improved to be a better tool, for instance, for tidal elevation and current predictions in the region. The next step would be an implementation of better bathymetry since as indicated by a set of experiments, bathymetry may be partly responsible for the less satisfactory model performance for the semidiurnal tides.

## REFERENCES

- Armi, L., and D.M. Farmer, 1988. The flow of Mediterranean water through the Strait of Gibraltar. *Prog. Oceanogr.*, vol. 21, 1-105.
- Armi, L., and D.M. Farmer, 1986. Maximal two-layer exchange over a sill and through the combination of a sill and constriction with barotropic flow. *J. Fluid Mech.*, vol. 164, 53-76.
- Bartkovich, A., 1985. Aspects of the tidal variability observed on the southern California continental shelf. *J. Phys. Oceanogr.*, vol. 15, 225-239.
- Beal, L. M., A. Ffield, and A.L. Gordon, 2000. Spreading of Red Sea outflow waters in the Indian Ocean. *J. Geophys. Res.*, vol. 105, 8549-8564.
- Blain C. A., and W.E. Rogers, 1998. Coastal Tide Prediction Using the ADCIRC-2DDI Hydrodynamic Finite Element Model: Model Validation and Sensitivity Analyses in the Southern North Sea/English Channel. Naval Research Laboratory, Stennis Space Center, 92 pp.
- Brandt P., A Rubino, D. Quadfasel, W. Alpers, J. Sellschopp, and H.V. Fiekas, 1999. Evidence for the influence of the Atlantic-Ionian stream fluctuations on the tidally induced internal dynamics in the Strait of Messina. *J. Phys. Oceanogr.*, vol. 29, 1071-1080.
- Brink K.H., 1995. Tidal and lower frequency currents above Fieberling Guyot. *J. Geophys. Res.*, vol. 100, 10,817-10,832.
- Butman, B., M. Noble, D.C. Chapman, and R.C. Beardsley, 1983. An upper bound for the tidally rectified currents at one location on the southern flank of Georgia Bank. *J. Phys. Oceanogr.*, vol. 13, 1452-1460.
- Candela, J., C. D. Winant, and A. Ruiz, 1990. Tides in the Strait of Gibraltar. *J. Geophys. Res.*, vol. 95, 7313-7335.
- Cartwright, D., W. Munk, and B. Zetler, 1969. Pelagic tidal measurements – a suggested procedure for analysis. *EUS*, vol. 50, 472-477.
- Chandon, E., 1930. Sur les mareas de la mer Rouge et du Golfe de Suez. These pres, a la fac. D. scien. D. Paris, Gauthier-Villars et Cie.
- Csanady, G.T., 1976. Mean circulation in shallow seas. *J. Geophys. Res.*, vol. 81, 5389-5399.
- Defant, A., 1961. *Physical Oceanography*, Vol. 2. Pergamon Press, 598 pp.

- Denbo, D.W., and J.S. Allen, 1984. Rotary empirical orthogonal function analysis of current near the Oregon Coast. *J. Phys. Oceanogr.*, vol. 14, 35-46.
- Desaubies, Y.J.F., 1972. Internal waves near the turning point. *Geophys. Fluid Dynamics*, vol. 2, 143-154.
- Di Sarra, A., A. Pace, and E. Salusti, 1987. Long internal waves and columnar disturbance in the Strait of Messina. *J. Geophys. Res.*, vol. 92, 6495-6500.
- Farmer, D.M., and R. Denton, 1985. Hydraulic control of flow over the sill in Observatory Inlet. *J. Geophys. Res.*, vol. 90, 9051-9068.
- Farmer, D.M., and J.D. Smith, 1980. Tidal interaction of stratified flow with a sill in the Knight Inlet. *Deep-Sea Res.*, vol. 27A, 239-254.
- Foremen M.G.G., 1978. Manual for Tidal Currents Analysis and Prediction. *Pac. Mar. Sci. Rep.* 76-6, Institute of Ocean Sciences, Patricia Bay, B.C., Canada, 70 pp.
- Foreman M.G.G., 1977. Manual for Tidal Heights Analysis and Prediction. *Pac. Mar. Sci. Rep.* 77-10, Institute of Ocean Sciences, Patricia Bay, B.C., Canada, 101 pp.
- Foreman M.G.G., R.A. Walters, R.F. Henry, C.P. Keller, and A.G. Dolling, 1995. A tidal model for eastern Juan de Fuca Strait and the southern Strait of Georgia. *J. Geophys. Res.*, vol. 100, 721-740.
- Gargett A.E., 1976. Generation of internal waves in the Strait of Georgia, British Columbia. *Deep-Sea Res.*, vol. 23, 17-32.
- Garrett, C., and B. Petrie, 1981. Dynamical aspects of the flow through the Strait of Belle Isle. *J. Phys. Oceanogr.*, vol. 11, 376-393.
- Gill, A.E., 1982. *Atmosphere-Ocean Dynamics*. Academic Press, 662 pp.
- Gordon, A.L., J.R.E. Lutjeharms, and M.L. Gründlingh, 1987. Stratification and circulation at the Agulhas Retroflection. *Deep-Sea Res.*, vol. 34, 565-599.
- Grenier, R.R., R.A. Luettich, and J.J. Westerink, 1995. A comparison of the nonlinear frictional characteristics of two-dimensional and three-dimensional models of a shallow tidal embayment. *J. Geophys. Res.*, vol. 100, 13,719-13,735.
- Griffa, A., S. Marullo, R. Santolieri, and A. Viola, 1986. Preliminary observations of large-amplitude tidal internal waves near the Strait of Messina. *Contin. Shelf Res.*, vol. 6, 677-687.
- Gründlingh, M.L., 1985. Occurrence of the Red Sea Waters in the Southwestern Indian Ocean. *J. Phys. Oceanogr.*, vol. 15, 207-212.

- Harris, R.A., 1904. Manual of tides. Part IV. Appendices. U.S. Coast and Geod. Surv. Rep., Washington.
- Helfrich, K.R., 1995. Time-dependent flow two-layer hydraulic exchange. *J. Phys. Oceanogr.*, vol. 25, 359-373.
- Hughes B.A., 1969. Characteristics of some internal waves in Georgia Strait. Technical Memorandum 69-2. Defense Research Establishment Pacific, 23 pp.
- Huthnance, J.M., 1973. Tidal asymmetries over the Norfolk sandbanks. *Estuar. Coast. Shelf Sci.*, vol. 1, 89-99.
- Kolar, R.L., W.G. Gray, J.J. Westernik, and R.A. Luettich, 1994. Shallow water modeling in spherical coordinates: equation formulation, numerical implementation, and application. *J. Hydraul. Res.*, vol. 32, 3-24.
- Kowalik, Z., and I. Polyakov, 1998. Tides in the Sea of Okhotsk. *J. Phys. Oceanogr.*, vol. 28, 1389-1409.
- Kowalik, Z., and A.Y. Proshutinsky, 1993. Diurnal tides in the Arctic Ocean. *J. Geophys. Res.*, vol. 98, 16,449-16,469.
- Lacomb, H., and C. Richez, 1982. The regime of the Strait of Gibraltar. In *The Hydrodynamics of Semi-Enclosed Seas*, edited by J.C.J. Nihoul, Elsevier, 13-73.
- Lafuente J.G., J.M. Vargas, F. Plaza, T. Sarhan, J. Candela, and B. Bascheck, 2000. Tides at the eastern section of the Strait of Gibraltar. *J. Geophys. Res.*, vol. 105, 14,197-14,213.
- La Violette, P.E., and R.A. Arnone, 1988. A tide-generated internal form in the western approaches to the Strait of Gibraltar. *J. Geophys. Res.*, vol. 93, 15,653-15,667.
- LeBlond, P.H., and L.A. Mysak, 1978. *Waves in the Ocean*. Elsevier, 602 pp.
- Le Provost, C., 1991. Generation of overtides and compound tides. In *Tidal Hydrodynamics*, edited by B.B. Parker, John Wiley and Sons, 269-296.
- Le Provost, C., M.L. Genco, F. Lyard, P. Vincent, and P. Caneil, 1994. Spectroscopy of the world ocean tides from a finite element hydrodynamics model. *J. Geophys. Res.*, vol. 99, 24,777-24,797.
- Luettich, R.A., J.J. Westerink, and N.W. Scheffner, 1992. ADCIRC: An Advanced Three-Dimensional Circulation Model for Shelves, Coasts and Estuaries, Report 1: Theory and Methodology of ADCIRC-2DDI and ADCIRC-3DL. Dredging Research Program Technical Report DRP-92-6, U.S. Army Engineers Waterways Experiment Station, Vicksburg, MS, 137 pp.

- Lynch, D.R., and W.G. Gray, 1979. A wave equation model for finite element tidal computations. *Comp. Fluid*, vol. 7, 207-228.
- Maillard, C., and G. Soliman, 1986. Hydrography of the Red Sea and exchanges with the Indian Ocean in summer. *Oceanol. Acta*, vol. 9, 249-269.
- Marchuk, D.I., and B.A. Kagan, 1984. *Ocean Tides. Mathematical Models and Numerical Experiment*. Pergamon Press, 292 pp.
- Mass, L.R.M., and J.J.M van Haren, 1987. Observations on the vertical structure of the tidal and inertial currents in the central North Sea. *J. Mar. Res.*, vol. 45, 293-318.
- Munk, W., 1997. Once again: once again – tidal friction, *Prog. Oceanogr.*, vol. 40, 7-35.
- Munk, W., and D.E. Cartwright, 1966. Tidal spectroscopy and prediction. *Phil. Trans. Roy. Soc.*, vol. 259, 533-581.
- Murray, S.P., and W. Johns, 1997. Direct observations of seasonal exchange through the Bab el Mandab Strait. *Geophys. Res. Lett.*, vol. 24, 2557-2560.
- Nakamura, T., T. Awaji, T. Hatayama, and K. Akitomo, 2000. Tidal exchange through the Kurii Strait. *J. Phys. Oceanogr.*, vol. 30, 1622-1644.
- Patzert, W.C., 1974. Seasonal reversal in the Red Sea circulation. In *L'oceanographie physique de la Mer Rouge*, CNEXO, Paris, 191-201.
- Pearson, F., 1990. *Map Projections: Theory and Applications*. CRC Press, Inc., Boca Raton.
- Pettigrew, N.R., and R.A. Hyde, 1990. The structure of the internal bore in the Strait of Gibraltar. In *The Physical Oceanography of Sea Straits*, edited by L.J. Pratt, Kulwer Academic Publishers, 493-508.
- Pugh, D.T., 1987. *Tides, Surges and Mean Sea-Level*. John Wiley and Sons, 472 pp.
- Prandle, D., 1982. The vertical structure of tidal currents. *Geophys. Astrophys. Fluid Dynamics*, vol. 22, 29-49.
- Pratt, L.J., W. Johns, S.P. Murray, and K. Katsumata, 2000. Hydraulic interpretation of direct velocity measurements in the Bab el Mandab. *J. Phys. Oceanogr.*, vol. 29, 2769-2784.
- Prinsenberg, S.J, and E.B. Bennett, 1989. Vertical variations of tidal currents in shallow land fast ice-covered regions. *J. Phys. Oceanogr.*, vol. 19, 1268-1278.

- Ray, R.D., 1993. Global ocean tidal models on the eve of TOPEX/POSEIDON. IEEE Trans. Geosci. Remote Sens., vol. 31, 355-364.
- Reid, R.O., 1990. Water Level Changes. Handbook of Coastal and Ocean Engineering, edited by J. Herbich, Gulf Publishing, Huston, TX.
- Robinson, I.S., 1983. Tidally induced residual flows. In Physical Oceanography of Coastal and Shelf Seas, edited by B. Johns, Elsevier, 321-356.
- Rocha, C., and A. J. Clarke, 1987. Interaction of ocean tides through a narrow single and narrow multiple strait. J. Phys. Oceanogr., vol. 17, 2203-2218.
- Rosenfeld, L.K., 1990. Baroclinic semidiurnal currents over the continental shelf off northern California. J. Geophys. Res., vol. 95, 22,153-22,172.
- Sapia, A., and E. Saluti, 1987. Observations of nonlinear internal solitary wave trains at the northern and southern mouths of the Strait of Messina. Deep-Sea Res., vol. 34A, 1081-1092.
- Siedler, G., 1969. On the fine structure of density and current distribution and its short-time scale in different areas, Prog. Oceanogr., 5, 81-94.
- Smeed, D., 1997. Seasonal variation of the flow in the Strait of Bab el Mandeb, Oceanol. Acta, 20, 773-781.
- Tejedor, L., A. Izquierdo, B.A. Kagan, and D.V. Sein, 1999. Simulation of the semidiurnal tides in the Strait of Gibraltar. J. Geophys. Res., vol. 104, 13,541-13,557.
- Tsimplis, M.N., R. Proctor, and R.A. Flather, 1995. A tow-dimensional tidal model for the Mediterranean Sea. J. Geophys. Res., vol. 100, 1535-1548.
- Thompson, E.F., 1939. Chemical and physical investigations. The exchange of the water between the Red Sea and the Gulf of Aden over the "Sill", John Murray Expedition 1933-34, Scientific Reports, 2, 105.
- Thomson, R.E, and W. S. Huggett, 1980.  $M_2$  baroclinic tides in Johnstone Strait, British Columbia. J. Phys. Oceanogr., vol. 10, 1509-1539.
- Toole, J.M., and B.A. Warren, 1993. A hydrographic section across the subtropical South Indian Ocean, Deep Sea Res., Part 1,40, 1973-2019.
- Valentine, H.R., J.R.E. Lutjeharms, and G.B. Brundrit, 1993. The water mass and volumetry of the southern Agulhas Current region. Deep-Sea Res., vol. 40, 1285-1305.

- Vercelli F., 1931. Le Nuove recherche sulli correnti marine nel Mar Rosso, Annali Idrografici, 12, 1-74.
- Vercelli, F., 1927. Richerche di oceanografia fisica eseguite della R. N. AMMIRAGLIO MAGNAGHI (1923-24), Part IV, La temperatura e la salinita, Annali Idrografici, 11, 1-66.
- Vercelli, F., 1925. Richerche di oceanografia fisica eseguite della R. N. AMMIRAGLIO MAGNAGHI (1923-24), Part I, Correnti e maree, Annali Idrografici, 11, 1-188.
- Wallace, J.M., and R.E. Dickinson, 1972. Empirical orthogonal representation of time series in the frequency domain. Part I: Theoretical considerations. *J. Appl. Meteor.*, vol. 11, 887-892.
- Walters, R.A, 1987. A model for tides and currents in the English Channel and southern North Sea. *Adv. Water Resources*, vol.10, 138-148.
- Walters, R.A, and F.E. Werner, 1989. A comparison of two finite element models of tidal hydrodynamics using a North Sea data set. *Adv. Water Resources*, vol.12, 84-93.
- Werner, F.E., and D.R. Lynch, 1987. Field verification of wave equation tidal dynamics in the English Channel and southern North Sea. *Adv. Water Resources*, vol.10, 115-130.
- Westerink, J.J., C.A. Blain, R.A. Luettich, and N.W. Scheffner, 1994. ADCIRC: An Advanced Three-Dimensional Circulation Model for Shelves, Coasts and Estuaries; Report 2: Users Manual for ADCIRC-2DDI. Dredging Research Program Technical Report, U.S. Army Engineers Waterways Experiment Station, Vicksburg, MS., 156 pp.
- Westerink, J.J., R.A. Luettich, A.M. Baptista, N.W. Scheffner, and P. Farrar, 1992. Tides and storm surge predictions using a finite element model. *J. Hydraul. Eng.*, vol. 118, 1373-1390.
- Westerink, J.J., K.D. Stoltzembach, and J.J. Connor, 1989. General spectral computations of the nonlinear shallow water tidal interactions within the Bight of Abaco. *J. Phys. Oceanogr.*, vol. 19, 1350-1373.
- Wunch, C., 1975. Internal tides in the Ocean. *Rev. Geophys. Space Phys.*, vol. 13, 167-182.
- Wyrtki, K., 1971. Oceanographic Atlas of the International Indian Ocean Expedition, Nat. Sci. Found., Washington, D.C., 531 pp.

Yasuda, H., 1987. Vertical structure of the tidal currents ellipse in a rotating basin. *J. Oceanogr. Soc. Jpn.*, vol. 43, 309-318.

Zimmerman, J.T.F., 1980. Vorticity transfer by tidal currents over an irregular topography. *J.Mar. Res.*, vol. 38, 601-630.

Zimmerman, J.T.F., 1978. Topographic generation of residual circulation by oscillatory (tidal) current. *Geophys. Astrophys. Fluid Dyn.*, vol. 11, 35-47.

## APPENDIX A: DATA SETS

The majority of data sets analyzed originate from a project entitled "Observation and Modeling – an Integrated Study of the Transport through the Strait of Bab el Mandab" (the BAM project) that was primarily designed to investigate subinertial transport and its variability in the Strait. However, instrumentation as well as the time resolution (0.5 h or 1 h) of the collected data also allows investigating higher frequency signals such as tides. In the course of the experiment, which took place between May 1995 and July 1997, currents, subsurface pressure, salinity, and temperature time series were obtained at different locations in the Strait.

The entire project consisted of three deployment phases. Locations of the instruments deployed at the beginning of the project (first phase) are shown in Figure 1. During this phase, 17 Aanderaa and 3 upward-looking ADCP current meters with a sampling interval of 4 m, 12 Seacats, and 5 subsurface pressure gauges were located in the Strait. The majority of the instruments were deployed at the Hanish Sill (mooring line B) and a few kilometers north from Perim Narrows (mooring line A). Moorings along A and B lines were maintained during the second phase; however, for the third phase, only the B line instruments and pressure gauge near the Hanish Sill were redeployed. Tables 10, 11, and 12 summarize deployment information for all phases. These tables contain information only about the instruments with good quality data that were subsequently used for analyses. Prior to the analyses, the subsurface pressure was converted into water level elevations, and the observations from the ADCP current meters were resampled so that the vertical resolution of the data was 5 meters. The depth range of the ADCP observations varied between locations, and it is listed for each instrument in Tables 10, 11, and 12. For some analyses, the north-south and east-west current components were rotated and aligned with the along- and cross-strait axes, and the rotation angles measured anticlockwise from the east were 5°, 40°, and 45° for the observations gathered along the mooring line A, C mooring, and the mooring line B, respectively.

In addition, CTD casts made during the four cruises servicing the experiment moorings were also analyzed. Finally, tidal elevation amplitudes and phases obtained from the International Hydrographic Office were used to analyze changes of tidal elevation parameters within the Bab el Mandab Strait, the Gulf of Aden, and to compare with modeled tidal harmonic constants.

Table 10. Information for instruments deployed during the first phase of the BAM project.

Station	Water Depth (m)	Latitude	Longitude	Start Time	End Time	Depth of Instrument (m)
Pressure Gauges						
G14	3	12°38.50'	43°54.50'	05/31/1995	02/21/1996	3
G89	3	12°43.50'	43°08.00'	06/01/1995	02/21/1996	3
G109	2	12°43.60'	43°28.00'	06/02/1995	02/23/1996	2
G108	3	13°40.50'	42°10.50'	06/04/1995	02/25/1996	3
Seacats						
B2a	162	13°42.47'	42°32.58'	05/27/1995	07/01/1995	27
				05/27/1995	03/29/1996	66
				05/27/1995	03/29/1996	94
				05/27/1995	03/29/1996	117

(Table 10 cont.)

				05/27/1995	03/29/1996	145
Current Meter Moorings						
A0	48	12°43.00'	43°11.48'	05/29/1995	01/05/1996	22
A1	147	12°44.21'	43°13.81'	05/29/1995	11/29/1995	60
				05/29/1995	01/05/1996	100
				05/29/1995	01/05/1996	130
A2b	210	12°45.12'	43°16.89'	05/29/1995	03/31/1996	20 - 190*
				05/30/1995	12/28/1995	204
A3	48	12°46.64'	43°21.15'	06/01/1995	01/05/1996	29
				06/01/1995	01/05/1996	41
B1	87	13°40.56'	42°28.70'	05/28/1995	12/06/1995	23
				05/28/1995	01/05/1996	45
				05/28/1995	01/05/1996	75
B2b	162	13°42.62'	42°32.35'	05/28/1995	03/29/1996	20 - 135*
				05/28/1995	03/27/1996	154
B3	55	13°44.51'	42°36.86'	05/27/1995	11/25/1995	26
				05/27/1995	01/05/1996	49
C	215	13°20.48'	42°54.22'	06/03/1995	04/03/1996	30 - 190*
				06/03/1995	01/08/1996	204

Table 11. Information for instruments deployed during the second phase of the BAM project.

Station	Water Depth (m)	Latitude	Longitude	Start Time	End Time	Depth of Instrument (m)
Pressure Gauges						
G89	3	12°43.50'	43°08.00'	04/08/1996	12/27/1996	3
G108	3	13°40.50'	42°10.50'	03/29/1996	12/02/1996	3
Seacats						
B2a	159	13°42.46'	42°32.54'	04/08/1996	08/14/1996	24
				04/08/1996	11/30/1996	51
				04/08/1996	11/30/1996	63
				04/08/1996	11/30/1996	114
				04/08/1996	11/30/1996	142
Current Meter Moorings						
AA0	44	12°42.49'	43°12.06'	04/06/1996	09/30/1996	37
AA1	165	12°43.26'	43°14.61'	04/06/1996	11/28/1996	20 - 140*
				04/04/1996	11/28/1996	154
AA2b	237	12°43.64'	43°16.60'	04/06/1996	11/30/1996	20 - 210*
AA3	49	12°44.26'	43°19.90'	04/08/1996	11/28/1996	42
B1	83	13°40.52'	42°28.38'	04/09/1996	11/30/1996	41
				04/09/1996	11/30/1996	71
B2b	158	13°42.59'	42°32.35'	04/06/1996	11/30/1996	20 - 140*
B3	51	13°44.40'	42°36.80'	04/09/1996	10/19/1996	23
				04/09/1996	11/24/1996	45

Table 12. Information for instruments deployed during the third phase of the BAM project.

Station	Water Depth (m)	Latitude	Longitude	Start Time	End Time	Depth of Instrument (m)
Pressure Gauges						
G108	3	13°40.50'	42°10.50'	12/02/1996	07/31/1997	3
Seacats						
B2a	162	13°42.51'	42°32.48'	12/02/1996	07/30/1997	32
				12/02/1996	01/02/1997	61

(Table 12 cont.)

				12/02/1996	07/30/1997	89
				12/02/1996	07/30/1997	117
				12/02/1996	07/30/1997	145
Current Meter Moorings						
B2b	162	13°42.57'	42°32.33'	12/02/1996	07/30/1997	20 - 140*
				12/02/1996	07/30/1997	151

\*Upward looking ADCP current meters; the depth range over which data were collected at each instrument is indicated.

## APPENDIX B: CURRENT ELLIPSE PARAMETERS

Table 13. The K<sub>1</sub> ellipse parameters and their 95% errors for A2b mooring and winter stratification.

Depth (m)	Semimajor Axis (cm/s)	Semiminor Axis (cm/s)	Inclination (deg)	Phase (GMT, deg)
20	33.0 ± 1.5	-2.2 ± 0.9	103 ± 2	66 ± 5
25	32.9 ± 2.0	-2.2 ± 1.1	101 ± 2	65 ± 4
30	32.6 ± 2.4	-2.3 ± 0.6	99 ± 1	64 ± 5
35	32.2 ± 2.4	-2.4 ± 0.2	97 ± 1	62 ± 6
40	31.7 ± 1.8	-2.3 ± 0.5	95 ± 2	62 ± 7
45	31.1 ± 1.5	-2.3 ± 0.7	93 ± 3	61 ± 7
50	30.6 ± 1.4	-2.0 ± 1.2	91 ± 4	60 ± 7
55	30.2 ± 1.5	-1.5 ± 1.4	90 ± 4	59 ± 6
60	30.0 ± 1.3	-1.3 ± 1.5	88 ± 4	59 ± 5
65	30.0 ± 1.0	-0.9 ± 1.5	87 ± 4	60 ± 5
70	30.2 ± 0.8	-0.4 ± 1.3	87 ± 3	61 ± 4
75	30.9 ± 0.9	0.1 ± 1.2	87 ± 2	63 ± 4
80	32.0 ± 1.1	0.4 ± 1.2	86 ± 1	65 ± 4
85	33.6 ± 1.0	0.6 ± 1.2	86 ± 2	68 ± 4
90	35.6 ± 0.7	0.6 ± 1.2	86 ± 2	70 ± 4
95	38.0 ± 0.3	0.4 ± 1.3	86 ± 2	73 ± 4
100	40.2 ± 0.6	-0.1 ± 1.2	86 ± 1	76 ± 4
105	42.6 ± 1.3	-0.8 ± 1.2	87 ± 1	78 ± 3
110	44.7 ± 2.1	-1.6 ± 1.1	87 ± 1	80 ± 2
115	46.2 ± 2.9	-2.4 ± 1.0	88 ± 1	82 ± 2
120	47.0 ± 3.5	-2.8 ± 1.0	89 ± 1	83 ± 1
125	46.0 ± 3.4	-2.8 ± 1.3	90 ± 1	84 ± 1
130	43.1 ± 2.7	-2.4 ± 1.3	91 ± 1	84 ± 1
135	38.6 ± 2.0	-1.7 ± 1.1	91 ± 1	81 ± 1
140	33.7 ± 1.8	-1.1 ± 0.7	92 ± 1	76 ± 3
145	30.0 ± 1.6	-0.6 ± 0.5	92 ± 1	70 ± 5
150	27.7 ± 1.1	-0.5 ± 0.2	92 ± 2	64 ± 5
155	26.6 ± 0.8	-0.5 ± 0.3	92 ± 2	60 ± 6
160	26.2 ± 0.7	-0.8 ± 0.5	92 ± 2	58 ± 6
165	25.9 ± 0.8	-1.0 ± 0.5	92 ± 1	57 ± 6
170	25.5 ± 1.0	-1.2 ± 0.5	92 ± 1	57 ± 6
175	24.9 ± 1.2	-1.7 ± 0.4	92 ± 1	56 ± 6
180	24.1 ± 1.5	-2.2 ± 0.5	92 ± 1	55 ± 6
185	23.3 ± 1.6	-2.5 ± 0.6	93 ± 1	54 ± 6
190	22.5 ± 1.7	-2.7 ± 0.5	94 ± 2	53 ± 6
204	13.3 ± 0.3	-1.3 ± 0.4	94 ± 2	69 ± 16

Table 14. The K<sub>1</sub> ellipse parameters and their 95% errors for A2b mooring and summer stratification.

Depth (m)	Semimajor Axis (cm/s)	Semiminor Axis (cm/s)	Inclination (deg)	Phase (GMT, deg)
20	30.9 ± 2.5	-2.1 ± 1.3	97 ± 1	59 ± 2
25	30.6 ± 4.6	-3.4 ± 4.0	97 ± 1	61 ± 2
30	29.8 ± 6.0	-3.6 ± 3.7	99 ± 1	62 ± 4
35	28.8 ± 5.3	-2.9 ± 2.1	101 ± 2	60 ± 4
40	28.7 ± 4.8	-1.6 ± 0.6	103 ± 2	57 ± 4
45	29.2 ± 4.8	-0.4 ± 1.2	103 ± 2	56 ± 3
50	29.6 ± 4.6	0.1 ± 1.7	103 ± 2	55 ± 3
55	29.9 ± 4.2	0.1 ± 1.7	103 ± 3	55 ± 3

(Table 14 cont.)

60	$30.0 \pm 3.7$	$-0.2 \pm 1.4$	$103 \pm 2$	$57 \pm 3$
65	$29.8 \pm 3.1$	$-0.3 \pm 1.8$	$103 \pm 2$	$59 \pm 3$
70	$29.6 \pm 2.3$	$-0.6 \pm 1.9$	$102 \pm 1$	$62 \pm 4$
75	$29.6 \pm 1.6$	$-0.8 \pm 1.9$	$100 \pm 1$	$64 \pm 5$
80	$29.7 \pm 1.2$	$-1.0 \pm 1.3$	$97 \pm 2$	$67 \pm 4$
85	$30.1 \pm 0.9$	$-1.2 \pm 1.0$	$95 \pm 2$	$68 \pm 3$
90	$30.2 \pm 1.0$	$-1.4 \pm 0.7$	$92 \pm 2$	$69 \pm 2$
95	$30.4 \pm 1.2$	$-1.7 \pm 0.5$	$90 \pm 2$	$67 \pm 2$
100	$30.4 \pm 1.1$	$-2.1 \pm 0.1$	$88 \pm 2$	$70 \pm 2$
105	$30.4 \pm 1.0$	$-2.4 \pm 0.7$	$85 \pm 2$	$70 \pm 2$
110	$30.2 \pm 0.8$	$-2.8 \pm 1.1$	$83 \pm 2$	$70 \pm 2$
115	$30.3 \pm 0.6$	$-3.0 \pm 1.2$	$82 \pm 2$	$71 \pm 2$
120	$30.2 \pm 0.5$	$-3.2 \pm 1.6$	$80 \pm 2$	$71 \pm 4$
125	$29.9 \pm 0.8$	$-3.4 \pm 1.7$	$79 \pm 2$	$72 \pm 4$
130	$29.4 \pm 0.7$	$-3.3 \pm 1.3$	$79 \pm 2$	$74 \pm 5$
135	$28.6 \pm 0.5$	$-3.0 \pm 0.8$	$80 \pm 2$	$75 \pm 6$
140	$27.9 \pm 0.3$	$-2.5 \pm 0.5$	$81 \pm 2$	$77 \pm 7$
145	$26.7 \pm 0.2$	$-2.0 \pm 0.9$	$83 \pm 1$	$78 \pm 7$
150	$25.5 \pm 0.4$	$-1.2 \pm 1.0$	$84 \pm 1$	$78 \pm 8$
155	$24.0 \pm 0.8$	$-0.7 \pm 1.2$	$86 \pm 1$	$79 \pm 8$
160	$22.2 \pm 1.2$	$-0.5 \pm 1.2$	$87 \pm 1$	$79 \pm 7$
165	$20.2 \pm 1.4$	$-0.3 \pm 1.0$	$89 \pm 1$	$77 \pm 6$
170	$18.2 \pm 1.3$	$0.1 \pm 0.9$	$91 \pm 2$	$75 \pm 5$
175	$16.3 \pm 1.0$	$0.3 \pm 0.4$	$93 \pm 1$	$72 \pm 5$
180	$14.5 \pm 0.5$	$0.7 \pm 0.2$	$95 \pm 2$	$72 \pm 4$
185	$13.4 \pm 0.1$	$1.0 \pm 0.3$	$96 \pm 1$	$72 \pm 3$
190	$12.2 \pm 0.4$	$1.1 \pm 0.5$	$99 \pm 1$	$72 \pm 4$
204	$8.7 \pm 0.4$	$-0.5 \pm 0.9$	$102 \pm 5$	$81 \pm 10$

Table 15. The  $M_2$  ellipse parameters and their 95% errors for A2b mooring and winter stratification.

Depth (m)	Semimajor Axis (cm/s)	Semiminor Axis (cm/s)	Inclination (deg)	Phase (GMT, deg)
20	$37.3 \pm 1.6$	$5.6 \pm 0.6$	$106 \pm 4$	$192 \pm 1$
25	$37.4 \pm 1.7$	$5.0 \pm 0.7$	$105 \pm 3$	$192 \pm 1$
30	$37.5 \pm 1.6$	$4.2 \pm 1.0$	$104 \pm 2$	$192 \pm 2$
35	$37.7 \pm 1.3$	$3.1 \pm 1.3$	$103 \pm 2$	$193 \pm 2$
40	$37.7 \pm 1.0$	$2.0 \pm 1.6$	$102 \pm 2$	$193 \pm 2$
45	$37.6 \pm 0.8$	$0.9 \pm 1.5$	$100 \pm 1$	$193 \pm 2$
50	$37.5 \pm 0.8$	$-0.4 \pm 1.4$	$99 \pm 1$	$193 \pm 2$
55	$37.3 \pm 0.8$	$-1.6 \pm 1.4$	$97 \pm 1$	$194 \pm 1$
60	$36.9 \pm 0.9$	$-2.7 \pm 1.3$	$96 \pm 1$	$194 \pm 1$
65	$36.6 \pm 1.2$	$-3.6 \pm 1.2$	$94 \pm 1$	$195 \pm 1$
70	$36.3 \pm 1.4$	$-4.4 \pm 1.0$	$92 \pm 1$	$196 \pm 2$
75	$36.1 \pm 1.4$	$-5.1 \pm 1.0$	$91 \pm 1$	$198 \pm 2$
80	$35.6 \pm 1.5$	$-5.3 \pm 0.9$	$89 \pm 1$	$200 \pm 2$
85	$35.0 \pm 1.4$	$-5.2 \pm 0.9$	$88 \pm 1$	$202 \pm 2$
90	$34.1 \pm 1.1$	$-5.0 \pm 1.0$	$86 \pm 1$	$204 \pm 2$
95	$33.0 \pm 0.8$	$-4.4 \pm 0.8$	$86 \pm 1$	$207 \pm 2$
100	$32.2 \pm 0.7$	$-3.6 \pm 0.9$	$85 \pm 1$	$210 \pm 2$
105	$31.5 \pm 0.6$	$-2.8 \pm 1.0$	$85 \pm 1$	$213 \pm 2$
110	$31.0 \pm 0.6$	$-1.9 \pm 1.0$	$86 \pm 2$	$216 \pm 2$
115	$30.3 \pm 0.6$	$-0.9 \pm 1.0$	$87 \pm 1$	$219 \pm 3$

(Table 15 cont.)

120	29.6 ± 0.8	-0.1 ± 1.0	89 ± 1	222 ± 3
125	29.3 ± 1.0	0.4 ± 0.9	91 ± 2	223 ± 3
130	29.4 ± 1.4	0.8 ± 0.8	94 ± 2	223 ± 4
135	29.4 ± 1.7	1.0 ± 0.6	96 ± 3	221 ± 4
140	28.7 ± 2.0	1.2 ± 0.6	97 ± 3	218 ± 4
145	27.7 ± 2.1	1.6 ± 0.5	97 ± 3	213 ± 4
150	26.8 ± 2.1	1.5 ± 0.4	96 ± 2	207 ± 3
155	26.1 ± 2.0	1.1 ± 0.4	94 ± 1	202 ± 2
160	25.8 ± 2.1	0.8 ± 0.5	93 ± 1	198 ± 2
165	25.6 ± 2.2	0.4 ± 0.5	92 ± 1	196 ± 2
170	25.1 ± 2.2	-0.1 ± 0.5	91 ± 1	195 ± 1
175	24.6 ± 2.2	-0.5 ± 0.6	92 ± 1	194 ± 1
180	23.8 ± 2.0	-0.8 ± 0.7	92 ± 2	193 ± 1
185	23.2 ± 1.9	-1.0 ± 0.9	93 ± 3	192 ± 1
190	22.3 ± 1.6	-1.2 ± 0.9	94 ± 4	191 ± 1
204	15.5 ± 0.4	-0.2 ± 0.2	97 ± 3	202 ± 5

Table 16. The  $M_2$  ellipse parameters and their 95% errors for A2b mooring and summer stratification.

Depth (m)	Semimajor Axis (cm/s)	Semiminor Axis (cm/s)	Inclination (deg)	Phase (GMT, deg)
20	37.6 ± 1.0	-1.6 ± 1.1	104 ± 1	196 ± 2
25	35.6 ± 1.3	0.1 ± 1.4	105 ± 1	198 ± 2
30	33.8 ± 0.8	2.0 ± 1.6	105 ± 2	200 ± 3
35	34.0 ± 0.3	3.2 ± 1.5	104 ± 2	202 ± 2
40	35.3 ± 0.2	3.7 ± 1.3	103 ± 1	202 ± 3
45	36.0 ± 0.3	3.8 ± 1.1	102 ± 1	201 ± 4
50	35.8 ± 0.8	3.6 ± 1.0	100 ± 1	199 ± 4
55	35.2 ± 0.8	3.2 ± 1.0	100 ± 1	198 ± 5
60	34.5 ± 1.0	2.6 ± 0.7	99 ± 1	198 ± 4
65	33.8 ± 1.1	1.8 ± 0.4	98 ± 1	199 ± 4
70	33.4 ± 0.9	0.9 ± 0.1	98 ± 1	201 ± 2
75	33.2 ± 0.4	0.1 ± 0.5	97 ± 1	203 ± 1
80	33.3 ± 0.7	-0.9 ± 0.9	95 ± 1	205 ± 1
85	33.4 ± 0.7	-1.7 ± 1.1	94 ± 1	205 ± 1
90	33.4 ± 0.9	-2.2 ± 1.2	93 ± 1	205 ± 1
95	33.3 ± 0.7	-2.8 ± 1.1	93 ± 1	205 ± 2
100	33.1 ± 0.5	-3.2 ± 1.0	92 ± 1	204 ± 2
105	32.6 ± 0.4	-3.6 ± 1.0	92 ± 1	202 ± 3
110	32.1 ± 0.5	-4.1 ± 0.7	92 ± 1	202 ± 2
115	31.3 ± 0.8	-4.6 ± 0.5	91 ± 1	201 ± 2
120	30.7 ± 0.9	-4.9 ± 0.5	91 ± 1	200 ± 1
125	29.9 ± 1.0	-5.2 ± 0.6	91 ± 1	199 ± 1
130	29.2 ± 0.8	-5.3 ± 0.7	90 ± 1	198 ± 1
135	28.3 ± 0.5	-5.1 ± 0.9	90 ± 2	197 ± 1
140	27.3 ± 0.3	-4.6 ± 0.8	88 ± 2	196 ± 2
145	25.9 ± 0.7	-4.2 ± 0.8	87 ± 2	194 ± 2
150	24.6 ± 1.2	-3.5 ± 0.6	86 ± 2	193 ± 2
155	23.1 ± 1.7	-2.7 ± 0.2	85 ± 2	191 ± 2
160	21.5 ± 2.5	-2.0 ± 0.5	85 ± 1	189 ± 2
165	19.9 ± 3.4	-1.3 ± 1.1	86 ± 1	187 ± 2
170	18.2 ± 4.2	-0.7 ± 1.4	87 ± 1	186 ± 3
175	16.6 ± 4.3	-0.1 ± 1.4	87 ± 2	185 ± 3
180	14.9 ± 4.2	0.4 ± 1.3	89 ± 2	184 ± 3

(Table 16 cont.)

185	$13.7 \pm 4.2$	$0.7 \pm 0.9$	$90 \pm 2$	$181 \pm 4$
190	$12.2 \pm 4.1$	$0.8 \pm 0.8$	$91 \pm 3$	$177 \pm 3$
204	$7.4 \pm 0.4$	$0.6 \pm 1.0$	$90 \pm 5$	$177 \pm 11$

Table 17. The  $K_1$  ellipse parameters and their 95% errors for B2b mooring and winter stratification.

Depth (m)	Semimajor Axis (cm/s)	Semiminor Axis (cm/s)	Inclination (deg)	Phase (GMT, deg)
20	$18.4 \pm 0.7$	$-5.4 \pm 1.5$	$131 \pm 3$	$77 \pm 4$
25	$19.0 \pm 0.5$	$-5.0 \pm 1.4$	$133 \pm 2$	$73 \pm 4$
30	$19.7 \pm 0.3$	$-4.7 \pm 1.5$	$133 \pm 2$	$71 \pm 3$
35	$20.5 \pm 0.5$	$-4.3 \pm 1.4$	$133 \pm 2$	$69 \pm 2$
40	$21.7 \pm 0.8$	$-3.5 \pm 1.2$	$134 \pm 2$	$68 \pm 2$
45	$24.0 \pm 1.9$	$-2.0 \pm 1.1$	$134 \pm 2$	$67 \pm 3$
50	$27.3 \pm 2.4$	$-0.4 \pm 1.0$	$134 \pm 3$	$68 \pm 4$
55	$30.9 \pm 3.0$	$0.3 \pm 0.8$	$135 \pm 2$	$70 \pm 5$
60	$33.7 \pm 2.9$	$-0.3 \pm 0.9$	$133 \pm 2$	$75 \pm 6$
65	$33.0 \pm 2.4$	$-0.9 \pm 0.8$	$131 \pm 2$	$79 \pm 6$
70	$27.4 \pm 2.1$	$-0.6 \pm 0.7$	$131 \pm 1$	$80 \pm 2$
75	$19.8 \pm 1.2$	$0.8 \pm 0.8$	$131 \pm 2$	$74 \pm 5$
80	$14.4 \pm 1.3$	$1.9 \pm 1.0$	$129 \pm 4$	$63 \pm 8$
85	$12.1 \pm 1.2$	$1.4 \pm 0.5$	$127 \pm 4$	$52 \pm 8$
90	$10.8 \pm 1.2$	$0.4 \pm 0.4$	$130 \pm 2$	$45 \pm 9$
95	$9.9 \pm 1.5$	$0.4 \pm 0.3$	$137 \pm 1$	$42 \pm 11$
100	$9.3 \pm 1.8$	$0.6 \pm 0.3$	$143 \pm 1$	$41 \pm 13$
105	$9.1 \pm 2.2$	$0.8 \pm 0.4$	$146 \pm 2$	$43 \pm 11$
110	$9.1 \pm 2.0$	$0.6 \pm 0.2$	$148 \pm 3$	$45 \pm 12$
115	$9.2 \pm 1.7$	$0.6 \pm 0.3$	$147 \pm 3$	$46 \pm 12$
120	$9.2 \pm 1.4$	$-0.2 \pm 0.4$	$147 \pm 2$	$49 \pm 10$
125	$9.3 \pm 1.1$	$-0.3 \pm 0.3$	$146 \pm 3$	$51 \pm 8$
130	$9.3 \pm 1.0$	$-0.6 \pm 0.2$	$145 \pm 3$	$53 \pm 6$
135	$9.3 \pm 1.1$	$-0.7 \pm 0.2$	$145 \pm 4$	$54 \pm 7$
154	$7.8 \pm 0.3$	$-0.1 \pm 0.6$	$151 \pm 2$	$51 \pm 7$

Table 18. The  $K_1$  ellipse parameters and their 95% errors for B2b mooring and summer stratification.

Depth (m)	Semimajor Axis (cm/s)	Semiminor Axis (cm/s)	Inclination (deg)	Phase (GMT, deg)
20	$16.2 \pm 1.2$	$-5.4 \pm 1.2$	$119 \pm 3$	$76 \pm 2$
25	$15.6 \pm 2.2$	$-4.2 \pm 1.4$	$122 \pm 4$	$75 \pm 2$
30	$15.1 \pm 2.7$	$-2.9 \pm 1.3$	$124 \pm 2$	$74 \pm 4$
35	$15.0 \pm 2.5$	$-2.0 \pm 1.5$	$125 \pm 4$	$73 \pm 6$
40	$15.0 \pm 1.6$	$-0.9 \pm 2.1$	$122 \pm 10$	$72 \pm 6$
45	$14.5 \pm 1.4$	$0.6 \pm 1.3$	$117 \pm 12$	$67 \pm 2$
50	$14.2 \pm 1.3$	$1.8 \pm 0.4$	$115 \pm 12$	$64 \pm 1$
55	$14.0 \pm 1.9$	$2.4 \pm 0.7$	$110 \pm 5$	$63 \pm 3$
60	$14.3 \pm 2.6$	$3.3 \pm 1.2$	$109 \pm 3$	$65 \pm 4$
65	$14.0 \pm 2.8$	$4.0 \pm 1.0$	$111 \pm 11$	$67 \pm 12$
70	$14.1 \pm 2.8$	$4.4 \pm 1.1$	$119 \pm 14$	$75 \pm 17$
75	$14.8 \pm 3.8$	$4.3 \pm 1.2$	$130 \pm 13$	$84 \pm 17$
80	$15.8 \pm 4.3$	$3.5 \pm 1.0$	$139 \pm 9$	$90 \pm 18$
85	$17.8 \pm 5.0$	$2.6 \pm 0.5$	$143 \pm 5$	$93 \pm 16$
90	$19.7 \pm 4.5$	$1.2 \pm 0.3$	$145 \pm 1$	$93 \pm 17$
95	$20.8 \pm 3.0$	$0.6 \pm 0.1$	$145 \pm 3$	$92 \pm 20$

(Table 18 cont.)

100	$20.3 \pm 1.8$	$0.6 \pm 1.7$	$145 \pm 4$	$90 \pm 22$
105	$19.6 \pm 4.2$	$0.7 \pm 2.2$	$142 \pm 5$	$88 \pm 22$
110	$17.1 \pm 5.9$	$0.3 \pm 1.7$	$137 \pm 5$	$84 \pm 19$
115	$15.1 \pm 6.2$	$-0.3 \pm 1.2$	$133 \pm 3$	$81 \pm 15$
120	$13.1 \pm 4.9$	$-1.1 \pm 0.5$	$132 \pm 2$	$76 \pm 14$
125	$11.5 \pm 2.7$	$-0.9 \pm 0.2$	$135 \pm 3$	$72 \pm 13$
130	$10.7 \pm 1.2$	$-0.1 \pm 0.4$	$141 \pm 1$	$71 \pm 10$
135	$10.5 \pm 0.8$	$-0.8 \pm 0.5$	$146 \pm 2$	$73 \pm 10$
154	$9.1 \pm 0.4$	$1.2 \pm 0.9$	$152 \pm 5$	$94 \pm 18$

Table 19. The  $M_2$  ellipse parameters and their 95% errors for B2b mooring and winter stratification.

Depth (m)	Semimajor Axis (cm/s)	Semiminor Axis (cm/s)	Inclination (deg)	Phase (GMT, deg)
20	$12.4 \pm 0.4$	$-1.0 \pm 1.1$	$120 \pm 5$	$204 \pm 3$
25	$12.7 \pm 0.4$	$-1.0 \pm 1.1$	$123 \pm 4$	$204 \pm 3$
30	$13.0 \pm 0.4$	$-0.9 \pm 1.1$	$124 \pm 4$	$205 \pm 3$
35	$13.4 \pm 0.3$	$-0.9 \pm 1.0$	$125 \pm 4$	$206 \pm 3$
40	$14.1 \pm 0.4$	$-0.9 \pm 0.8$	$125 \pm 4$	$208 \pm 4$
45	$14.9 \pm 0.4$	$-1.0 \pm 0.4$	$126 \pm 4$	$211 \pm 4$
50	$15.7 \pm 0.6$	$-1.0 \pm 0.3$	$128 \pm 4$	$213 \pm 3$
55	$16.2 \pm 1.0$	$-1.1 \pm 0.4$	$130 \pm 3$	$214 \pm 3$
60	$16.6 \pm 1.4$	$-0.8 \pm 0.5$	$130 \pm 2$	$213 \pm 4$
65	$17.9 \pm 2.9$	$-0.7 \pm 0.4$	$131 \pm 3$	$211 \pm 2$
70	$19.0 \pm 1.2$	$-1.1 \pm 0.5$	$132 \pm 3$	$209 \pm 3$
75	$19.5 \pm 0.8$	$-1.3 \pm 0.4$	$134 \pm 2$	$204 \pm 3$
80	$18.9 \pm 1.0$	$-1.0 \pm 0.3$	$135 \pm 1$	$199 \pm 3$
85	$18.0 \pm 1.2$	$-0.5 \pm 0.4$	$137 \pm 1$	$195 \pm 3$
90	$17.3 \pm 0.8$	$-0.3 \pm 0.5$	$138 \pm 1$	$192 \pm 3$
95	$16.8 \pm 0.8$	$-0.1 \pm 0.5$	$139 \pm 2$	$189 \pm 4$
100	$16.3 \pm 0.7$	$0.6 \pm 0.3$	$140 \pm 1$	$188 \pm 4$
105	$15.9 \pm 0.6$	$1.3 \pm 0.2$	$141 \pm 1$	$187 \pm 3$
110	$15.2 \pm 0.6$	$0.6 \pm 0.2$	$142 \pm 1$	$187 \pm 3$
115	$15.1 \pm 0.6$	$1.8 \pm 0.3$	$142 \pm 1$	$187 \pm 2$
120	$14.3 \pm 0.7$	$1.7 \pm 0.3$	$142 \pm 1$	$188 \pm 4$
125	$13.9 \pm 0.7$	$1.6 \pm 0.3$	$143 \pm 1$	$189 \pm 2$
130	$13.6 \pm 0.5$	$1.5 \pm 0.2$	$144 \pm 1$	$189 \pm 2$
135	$13.3 \pm 0.5$	$1.5 \pm 0.2$	$145 \pm 1$	$190 \pm 2$
154	$10.7 \pm 0.8$	$2.3 \pm 0.5$	$152 \pm 5$	$206 \pm 16$

Table 20. The  $M_2$  ellipse parameters and their 95% errors for B2b mooring and summer stratification.

Depth (m)	Semimajor Axis (cm/s)	Semiminor Axis (cm/s)	Inclination (deg)	Phase (GMT, deg)
20	$12.1 \pm 0.7$	$-0.4 \pm 0.3$	$122 \pm 3$	$207 \pm 4$
25	$12.8 \pm 0.7$	$-1.0 \pm 0.7$	$124 \pm 2$	$211 \pm 6$
30	$13.3 \pm 0.8$	$-1.5 \pm 0.5$	$126 \pm 2$	$212 \pm 4$
35	$13.9 \pm 0.3$	$-1.7 \pm 0.1$	$126 \pm 3$	$211 \pm 3$
40	$14.9 \pm 1.0$	$-2.1 \pm 0.3$	$127 \pm 4$	$208 \pm 3$
45	$15.7 \pm 0.6$	$-2.3 \pm 0.5$	$127 \pm 5$	$204 \pm 3$
50	$16.1 \pm 0.4$	$-2.2 \pm 0.9$	$128 \pm 3$	$202 \pm 2$
55	$16.0 \pm 0.4$	$-2.2 \pm 0.9$	$127 \pm 1$	$201 \pm 2$
60	$16.0 \pm 0.8$	$-2.0 \pm 0.4$	$127 \pm 3$	$202 \pm 3$
65	$16.4 \pm 1.6$	$-1.9 \pm 0.3$	$126 \pm 4$	$203 \pm 5$

(Table 20 cont.)

70	16.8 ± 1.9	-1.6 ± 0.4	127 ± 5	204 ± 4
75	17.1 ± 1.7	-1.2 ± 0.4	128 ± 4	204 ± 4
80	17.4 ± 1.2	-0.6 ± 0.2	129 ± 2	205 ± 3
85	17.6 ± 0.7	0.3 ± 0.7	131 ± 1	208 ± 5
90	17.7 ± 0.8	1.4 ± 0.7	135 ± 3	213 ± 9
95	18.3 ± 1.1	1.8 ± 1.1	139 ± 5	219 ± 12
100	18.4 ± 1.1	1.8 ± 1.3	143 ± 5	224 ± 12
105	18.9 ± 0.9	1.7 ± 1.3	145 ± 3	227 ± 10
110	17.6 ± 1.2	1.5 ± 1.3	146 ± 2	229 ± 7
115	16.2 ± 2.6	1.2 ± 1.0	146 ± 2	228 ± 9
120	14.3 ± 3.0	0.9 ± 0.6	144 ± 3	224 ± 12
125	13.2 ± 2.4	0.5 ± 0.2	143 ± 3	218 ± 13
130	12.3 ± 1.6	0.3 ± 0.4	141 ± 1	213 ± 11
135	11.7 ± 1.1	0.5 ± 0.5	140 ± 3	210 ± 8
154	7.7 ± 0.4	0.9 ± 1.0	150 ± 5	215 ± 11

Table 21. The K<sub>1</sub> ellipse parameters and their 95% errors for C mooring and winter stratification.

Depth (m)	Semimajor Axis (cm/s)	Seminor Axis (cm/s)	Inclination (deg)	Phase (GMT, deg)
30	13.1 ± 1.6	-0.6 ± 1.7	127 ± 6	88 ± 9
35	13.1 ± 1.6	-0.2 ± 1.8	125 ± 7	84 ± 9
40	13.1 ± 1.4	0.1 ± 1.7	124 ± 8	78 ± 8
45	13.2 ± 1.2	0.2 ± 1.6	123 ± 9	72 ± 8
50	13.2 ± 0.9	0.2 ± 1.4	121 ± 10	67 ± 8
55	13.5 ± 0.8	-0.1 ± 1.1	120 ± 10	61 ± 9
60	13.6 ± 1.0	-0.3 ± 0.9	120 ± 9	56 ± 11
65	13.6 ± 1.2	-0.4 ± 0.8	119 ± 9	51 ± 13
70	13.4 ± 1.3	-0.3 ± 1.0	118 ± 9	48 ± 14
75	13.4 ± 1.9	0.8 ± 1.2	117 ± 10	48 ± 11
80	13.7 ± 1.9	2.8 ± 1.3	118 ± 8	52 ± 8
85	14.6 ± 1.6	4.8 ± 1.2	122 ± 5	59 ± 8
90	15.5 ± 1.3	6.3 ± 1.2	129 ± 7	67 ± 9
95	16.2 ± 1.1	6.7 ± 1.6	135 ± 8	72 ± 8
100	16.6 ± 1.1	6.6 ± 1.7	139 ± 6	74 ± 5
105	16.5 ± 1.1	6.4 ± 1.5	143 ± 3	76 ± 3
110	16.2 ± 0.9	5.7 ± 1.0	149 ± 3	79 ± 5
115	16.1 ± 0.9	4.2 ± 0.6	153 ± 3	83 ± 7
120	16.1 ± 0.9	2.8 ± 1.3	155 ± 3	85 ± 7
125	15.9 ± 0.9	1.7 ± 1.3	155 ± 3	85 ± 7
130	15.5 ± 0.8	1.4 ± 1.2	153 ± 4	83 ± 6
135	15.0 ± 0.9	1.5 ± 1.1	152 ± 4	80 ± 7
140	14.3 ± 0.9	1.9 ± 1.2	152 ± 4	78 ± 8
145	13.5 ± 0.8	1.9 ± 1.4	152 ± 4	77 ± 10
150	13.0 ± 0.9	1.4 ± 1.7	152 ± 5	78 ± 11
155	12.9 ± 0.9	0.5 ± 1.6	150 ± 6	80 ± 11
160	13.1 ± 1.0	0.5 ± 1.5	146 ± 8	83 ± 10
165	13.5 ± 1.2	-1.4 ± 1.3	141 ± 9	85 ± 9
170	14.1 ± 1.5	-2.0 ± 1.3	134 ± 7	86 ± 9
175	14.8 ± 1.7	-2.3 ± 1.2	129 ± 7	85 ± 8
180	15.3 ± 1.9	-2.4 ± 1.0	124 ± 7	84 ± 7
185	15.7 ± 1.9	-2.3 ± 0.7	121 ± 7	82 ± 7
190	15.9 ± 1.8	-2.1 ± 0.6	119 ± 6	80 ± 6
204	16.6 ± 0.2	-3.1 ± 0.9	109 ± 1	59 ± 4

Table 22. The K<sub>1</sub> ellipse parameters and their 95% errors for C mooring and summer stratification.

Depth (m)	Semimajor Axis (cm/s)	Seminor Axis (cm/s)	Inclination (deg)	Phase (GMT, deg)
30	16.5 ± 0.5	-1.9 ± 0.7	124 ± 2	87 ± 9
35	18.4 ± 0.6	-1.6 ± 0.6	123 ± 1	86 ± 6
40	18.6 ± 1.9	-1.2 ± 1.9	123 ± 2	85 ± 4
45	17.8 ± 3.3	-0.9 ± 1.9	123 ± 2	85 ± 5
50	17.1 ± 3.7	-1.3 ± 2.3	122 ± 2	86 ± 4
55	16.6 ± 3.2	-1.7 ± 2.4	122 ± 3	88 ± 4
60	16.1 ± 2.6	-1.8 ± 2.0	120 ± 4	89 ± 3
65	15.4 ± 2.2	-1.6 ± 1.8	119 ± 5	88 ± 2
70	14.9 ± 2.1	-1.1 ± 1.4	119 ± 5	86 ± 4
75	14.2 ± 2.1	-0.4 ± 0.6	119 ± 5	84 ± 5
80	13.3 ± 1.7	0.3 ± 0.8	120 ± 4	83 ± 6
85	12.4 ± 1.2	0.9 ± 0.9	121 ± 3	83 ± 6
90	11.8 ± 0.8	1.3 ± 1.2	125 ± 2	84 ± 7
95	11.6 ± 0.5	1.4 ± 1.2	130 ± 2	85 ± 6
100	11.7 ± 0.3	1.5 ± 1.2	134 ± 6	87 ± 8
105	12.0 ± 1.0	1.3 ± 1.6	138 ± 8	88 ± 10
110	12.5 ± 2.2	1.0 ± 1.7	141 ± 7	89 ± 9
115	13.0 ± 3.1	1.0 ± 1.2	142 ± 4	90 ± 5
120	13.2 ± 3.3	1.1 ± 1.0	144 ± 1	90 ± 3
125	13.5 ± 3.1	1.6 ± 0.9	146 ± 2	90 ± 3
130	14.0 ± 3.4	1.9 ± 1.0	147 ± 3	90 ± 3
135	14.2 ± 2.8	2.1 ± 1.3	147 ± 1	89 ± 3
140	14.1 ± 2.0	2.4 ± 1.4	147 ± 1	89 ± 5
145	14.0 ± 1.5	2.9 ± 1.3	147 ± 4	89 ± 4
150	14.1 ± 1.7	3.0 ± 0.8	147 ± 8	92 ± 2
155	14.5 ± 1.6	2.4 ± 1.2	146 ± 11	95 ± 2
160	15.1 ± 1.3	1.6 ± 2.4	143 ± 12	96 ± 4
165	15.8 ± 0.9	1.7 ± 3.3	139 ± 12	95 ± 8
170	16.5 ± 0.7	-0.2 ± 2.9	134 ± 11	95 ± 9
175	16.8 ± 0.3	-1.0 ± 2.3	131 ± 11	94 ± 10
180	16.9 ± 0.4	-1.6 ± 1.9	129 ± 10	93 ± 10
185	16.7 ± 0.3	-2.2 ± 1.2	127 ± 8	90 ± 10
190	16.4 ± 0.4	-2.6 ± 0.9	126 ± 6	86 ± 10
204	17.4 ± 1.2	-2.9 ± 0.6	125 ± 1	49 ± 3

Table 23. The M<sub>2</sub> ellipse parameters and their 95% errors for C mooring and winter stratification.

Depth (m)	Semimajor Axis (cm/s)	Seminor Axis (cm/s)	Inclination (deg)	Phase (GMT, deg)
30	18.5 ± 0.5	-0.6 ± 0.3	120 ± 2	237 ± 4
35	18.7 ± 0.6	-0.9 ± 0.3	120 ± 2	235 ± 3
40	18.9 ± 0.7	-1.2 ± 0.4	121 ± 2	233 ± 3
45	19.1 ± 0.7	-1.6 ± 0.5	122 ± 2	231 ± 4
50	19.1 ± 0.8	-2.0 ± 0.6	122 ± 1	229 ± 3
55	18.9 ± 1.0	-2.5 ± 0.5	123 ± 1	227 ± 3
60	18.8 ± 1.3	-3.0 ± 0.5	124 ± 2	225 ± 2
65	18.6 ± 1.7	-3.2 ± 0.7	125 ± 3	223 ± 2
70	18.3 ± 2.2	-3.2 ± 0.9	127 ± 3	222 ± 3
75	17.9 ± 2.6	-2.7 ± 0.8	128 ± 4	222 ± 5
80	17.4 ± 2.6	-2.2 ± 0.6	129 ± 5	223 ± 7
85	17.0 ± 2.2	-1.6 ± 0.7	129 ± 5	223 ± 7

(Table 23 cont.)

90	16.6 ± 1.7	-1.0 ± 0.8	129 ± 5	224 ± 5
95	16.2 ± 1.1	-0.2 ± 0.8	129 ± 5	225 ± 4
100	16.1 ± 0.8	0.8 ± 1.1	130 ± 4	225 ± 3
105	16.2 ± 0.9	1.5 ± 1.5	132 ± 5	225 ± 2
110	16.3 ± 1.3	1.7 ± 1.4	132 ± 6	223 ± 3
115	16.1 ± 1.5	2.0 ± 1.2	132 ± 7	220 ± 4
120	16.0 ± 1.6	2.5 ± 0.9	132 ± 6	218 ± 5
125	16.1 ± 1.5	3.1 ± 0.5	131 ± 5	216 ± 4
130	16.5 ± 1.3	3.6 ± 0.2	129 ± 4	214 ± 3
135	17.0 ± 1.3	3.7 ± 0.3	127 ± 4	214 ± 4
140	17.5 ± 1.4	3.5 ± 0.5	126 ± 4	215 ± 5
145	17.9 ± 1.5	3.1 ± 0.7	126 ± 4	216 ± 5
150	18.0 ± 1.4	2.5 ± 0.7	126 ± 5	216 ± 4
155	17.8 ± 1.4	1.8 ± 0.6	128 ± 5	215 ± 3
160	17.3 ± 1.5	1.3 ± 0.4	129 ± 4	213 ± 2
165	16.6 ± 1.6	1.1 ± 0.3	131 ± 4	211 ± 1
170	16.0 ± 1.8	1.2 ± 0.2	133 ± 3	209 ± 2
175	15.7 ± 2.0	1.5 ± 0.2	136 ± 2	208 ± 2
180	15.4 ± 2.0	1.6 ± 0.1	138 ± 2	207 ± 2
185	15.3 ± 2.0	1.6 ± 0.1	140 ± 1	207 ± 2
190	15.1 ± 2.0	1.4 ± 0.2	141 ± 1	207 ± 2
204	15.4 ± 1.8	1.7 ± 0.4	145 ± 2	159 ± 3

Table 24. The M<sub>2</sub> ellipse parameters and their 95% errors for C mooring and summer stratification.

Depth (m)	Semimajor Axis (cm/s)	Seminor Axis (cm/s)	Inclination (deg)	Phase (GMT, deg)
30	16.6 ± 1.3	-1.1 ± 0.7	125 ± 4	230 ± 14
35	16.5 ± 1.0	-0.8 ± 1.1	127 ± 5	232 ± 14
40	16.4 ± 0.6	-0.7 ± 1.0	129 ± 6	235 ± 15
45	16.2 ± 0.8	-0.9 ± 0.6	129 ± 7	236 ± 16
50	16.4 ± 0.9	-0.7 ± 0.4	128 ± 7	236 ± 15
55	16.5 ± 1.0	-0.4 ± 0.5	128 ± 8	234 ± 14
60	16.4 ± 0.9	-0.2 ± 0.4	128 ± 8	233 ± 13
65	16.4 ± 0.7	-0.3 ± 0.4	129 ± 8	233 ± 13
70	16.3 ± 0.4	-0.6 ± 0.7	130 ± 8	234 ± 14
75	16.1 ± 0.1	-1.0 ± 0.7	131 ± 8	235 ± 14
80	15.9 ± 0.2	-1.4 ± 0.8	132 ± 8	235 ± 15
85	15.9 ± 0.5	-1.6 ± 0.8	133 ± 9	234 ± 16
90	16.0 ± 0.9	-1.7 ± 1.0	133 ± 8	233 ± 16
95	16.2 ± 1.1	-1.8 ± 1.2	133 ± 8	231 ± 15
100	16.4 ± 1.2	-1.8 ± 1.4	132 ± 8	229 ± 14
105	16.5 ± 1.0	-1.6 ± 1.6	131 ± 8	227 ± 13
110	16.4 ± 0.9	-1.4 ± 1.6	131 ± 7	226 ± 13
115	16.3 ± 0.7	-1.0 ± 1.6	130 ± 7	224 ± 14
120	16.1 ± 0.7	-0.6 ± 1.6	130 ± 6	222 ± 14
125	16.0 ± 0.9	-0.2 ± 1.5	129 ± 5	219 ± 15
130	16.0 ± 1.2	0.2 ± 1.5	126 ± 5	216 ± 15
135	16.0 ± 1.0	0.5 ± 1.5	124 ± 6	213 ± 14
140	16.1 ± 0.6	0.7 ± 1.2	122 ± 7	211 ± 15
145	16.1 ± 0.6	0.9 ± 1.0	120 ± 6	210 ± 16
150	16.3 ± 0.4	0.9 ± 1.2	119 ± 5	211 ± 15
155	16.3 ± 0.4	0.7 ± 1.0	120 ± 3	211 ± 15
160	16.0 ± 0.7	0.5 ± 0.5	122 ± 2	213 ± 13

(Table 24 cont.)

165	15.9 ± 0.9	0.2 ± 0.3	124 ± 2	214 ± 14
170	15.6 ± 1.0	0.4 ± 0.5	125 ± 3	213 ± 16
175	15.4 ± 1.0	0.9 ± 0.6	126 ± 3	211 ± 17
180	15.4 ± 0.8	1.3 ± 0.8	128 ± 2	211 ± 17
185	15.3 ± 0.8	1.7 ± 0.9	130 ± 3	211 ± 17
190	15.2 ± 0.7	2.1 ± 1.0	133 ± 3	212 ± 17
204	17.3 ± 0.8	3.8 ± 1.6	137 ± 2	177 ± 3

Table 25. The K<sub>1</sub> ellipse parameters and their 95% errors for AA1 mooring and winter stratification.

Depth (m)	Semimajor Axis (cm/s)	Semiminor Axis (cm/s)	Inclination (deg)	Phase (GMT, deg)
20	28.4 ± 2.5	-0.9 ± 1.4	117 ± 4	83 ± 5
25	30.7 ± 1.7	-0.7 ± 1.2	115 ± 2	86 ± 5
30	30.6 ± 3.7	-0.5 ± 0.5	113 ± 1	85 ± 8
35	30.0 ± 5.9	-0.2 ± 0.1	111 ± 2	85 ± 11
40	29.3 ± 7.4	-0.3 ± 0.2	109 ± 2	85 ± 13
45	28.6 ± 8.0	-0.4 ± 0.4	108 ± 1	85 ± 11
50	27.9 ± 8.2	-0.2 ± 0.6	107 ± 1	85 ± 8
55	27.7 ± 8.1	0.4 ± 0.5	105 ± 2	86 ± 5
60	28.0 ± 6.8	1.2 ± 0.2	105 ± 4	87 ± 2
65	28.6 ± 5.1	2.0 ± 0.2	103 ± 6	86 ± 1
70	29.5 ± 3.8	2.7 ± 0.3	102 ± 7	86 ± 1
75	30.3 ± 2.9	3.0 ± 0.8	100 ± 8	85 ± 1
80	30.9 ± 2.3	2.8 ± 1.5	99 ± 8	84 ± 2
85	31.4 ± 1.5	2.1 ± 2.3	97 ± 8	83 ± 4
90	31.9 ± 0.8	1.2 ± 3.2	96 ± 7	84 ± 5
95	32.8 ± 0.3	0.3 ± 3.4	96 ± 5	85 ± 5
100	34.2 ± 0.8	-0.4 ± 3.3	96 ± 5	87 ± 5
105	36.3 ± 2.7	-0.9 ± 3.1	97 ± 3	90 ± 3
110	38.8 ± 5.0	-1.4 ± 3.0	94 ± 3	94 ± 2
115	41.4 ± 7.3	-1.7 ± 3.2	101 ± 3	97 ± 3
120	43.2 ± 9.5	-1.8 ± 3.3	102 ± 2	99 ± 4
125	43.0 ± 9.2	-1.6 ± 3.0	104 ± 2	100 ± 4
130	41.0 ± 6.3	-1.4 ± 2.9	105 ± 3	101 ± 3
135	38.0 ± 1.7	-1.3 ± 3.4	106 ± 4	101 ± 2
140	34.5 ± 3.2	-1.5 ± 3.3	108 ± 4	98 ± 3
154	27.2 ± 5.8	-3.5 ± 2.1	96 ± 5	89 ± 1

Table 26. The K<sub>1</sub> ellipse parameters and their 95% errors for AA1 mooring and summer stratification.

Depth (m)	Semimajor Axis (cm/s)	Semiminor Axis (cm/s)	Inclination (deg)	Phase (GMT, deg)
20	29.6 ± 3.8	-1.2 ± 1.4	107 ± 3	75 ± 4
25	31.4 ± 4.8	-1.6 ± 0.8	106 ± 2	80 ± 1
30	31.7 ± 4.8	-1.6 ± 0.8	106 ± 2	86 ± 3
35	31.0 ± 5.0	-1.2 ± 1.4	107 ± 2	91 ± 5
40	29.2 ± 4.8	-1.0 ± 1.6	107 ± 4	93 ± 6
45	28.1 ± 4.3	-1.1 ± 1.5	109 ± 6	93 ± 5
50	27.7 ± 3.9	-1.3 ± 1.6	110 ± 8	91 ± 4
55	27.7 ± 3.4	-1.5 ± 1.4	112 ± 8	90 ± 2
60	27.7 ± 3.2	-1.6 ± 1.6	112 ± 6	89 ± 1
65	27.7 ± 3.4	-1.6 ± 1.4	112 ± 5	89 ± 1
70	27.7 ± 3.8	-1.5 ± 2.4	111 ± 4	89 ± 2

(Table 26 cont.)

75	$27.7 \pm 4.0$	$-1.2 \pm 2.8$	$110 \pm 3$	$89 \pm 3$
80	$27.8 \pm 3.7$	$-0.8 \pm 3.1$	$109 \pm 2$	$90 \pm 3$
85	$28.0 \pm 2.9$	$-0.6 \pm 3.1$	$108 \pm 2$	$90 \pm 3$
90	$28.1 \pm 2.2$	$-0.4 \pm 2.6$	$106 \pm 2$	$91 \pm 3$
95	$28.2 \pm 1.4$	$-0.3 \pm 1.8$	$104 \pm 2$	$91 \pm 4$
100	$28.5 \pm 0.8$	$-0.3 \pm 1.1$	$102 \pm 2$	$91 \pm 4$
105	$29.1 \pm 0.5$	$-0.7 \pm 0.4$	$100 \pm 2$	$92 \pm 4$
110	$30.0 \pm 0.7$	$-1.2 \pm 0.9$	$98 \pm 2$	$92 \pm 4$
115	$31.0 \pm 0.9$	$-1.8 \pm 1.3$	$96 \pm 2$	$93 \pm 4$
120	$32.1 \pm 1.1$	$-2.1 \pm 1.3$	$96 \pm 2$	$93 \pm 4$
125	$33.2 \pm 1.1$	$-2.1 \pm 1.4$	$95 \pm 2$	$93 \pm 4$
130	$34.2 \pm 1.1$	$-2.0 \pm 1.7$	$96 \pm 2$	$93 \pm 4$
135	$35.1 \pm 1.2$	$-1.7 \pm 1.8$	$97 \pm 2$	$93 \pm 4$
140	$35.6 \pm 1.2$	$-1.6 \pm 1.6$	$98 \pm 3$	$93 \pm 4$
154	$35.9 \pm 1.6$	$-2.8 \pm 1.0$	$97 \pm 3$	$86 \pm 5$

Table 27. The  $M_2$  ellipse parameters and their 95% errors for AA1 mooring and winter stratification.

Depth (m)	Semimajor Axis (cm/s)	Seminor Axis (cm/s)	Inclination (deg)	Phase (GMT, deg)
20	$38.6 \pm 0.4$	$1.5 \pm 0.6$	$117 \pm 1$	$230 \pm 3$
25	$39.4 \pm 0.5$	$1.5 \pm 0.4$	$116 \pm 1$	$231 \pm 3$
30	$39.5 \pm 0.8$	$1.4 \pm 0.1$	$115 \pm 1$	$231 \pm 3$
35	$38.0 \pm 2.2$	$1.0 \pm 0.1$	$114 \pm 1$	$230 \pm 4$
40	$36.3 \pm 2.9$	$0.6 \pm 0.3$	$113 \pm 1$	$229 \pm 4$
45	$34.8 \pm 3.0$	$0.3 \pm 0.3$	$112 \pm 1$	$229 \pm 4$
50	$33.5 \pm 3.3$	$-0.1 \pm 0.3$	$110 \pm 1$	$227 \pm 5$
55	$32.5 \pm 2.9$	$-0.7 \pm 0.5$	$107 \pm 1$	$225 \pm 5$
60	$31.8 \pm 1.4$	$-1.7 \pm 0.2$	$104 \pm 1$	$224 \pm 5$
65	$31.5 \pm 0.4$	$-2.8 \pm 0.4$	$101 \pm 1$	$224 \pm 4$
70	$31.7 \pm 0.8$	$-3.9 \pm 0.7$	$99 \pm 1$	$224 \pm 4$
75	$32.3 \pm 1.0$	$-4.9 \pm 0.7$	$96 \pm 2$	$226 \pm 5$
80	$33.3 \pm 0.5$	$-5.6 \pm 0.6$	$93 \pm 3$	$228 \pm 4$
85	$34.7 \pm 0.2$	$-5.5 \pm 0.2$	$91 \pm 3$	$230 \pm 4$
90	$36.3 \pm 0.3$	$-5.0 \pm 1.0$	$90 \pm 3$	$233 \pm 3$
95	$37.8 \pm 0.4$	$-4.1 \pm 2.2$	$93 \pm 4$	$235 \pm 1$
100	$39.2 \pm 0.5$	$-3.0 \pm 3.2$	$91 \pm 5$	$236 \pm 1$
105	$40.3 \pm 0.3$	$-1.8 \pm 3.6$	$93 \pm 6$	$238 \pm 3$
110	$40.8 \pm 0.1$	$-0.6 \pm 3.2$	$96 \pm 6$	$240 \pm 5$
115	$40.7 \pm 0.7$	$-0.1 \pm 2.3$	$99 \pm 6$	$241 \pm 7$
120	$40.6 \pm 0.9$	$0.6 \pm 1.2$	$102 \pm 6$	$241 \pm 7$
125	$38.6 \pm 0.2$	$1.4 \pm 0.5$	$106 \pm 6$	$240 \pm 7$
130	$36.1 \pm 0.4$	$2.0 \pm 0.2$	$109 \pm 6$	$237 \pm 5$
135	$33.9 \pm 0.6$	$2.4 \pm 0.2$	$111 \pm 6$	$234 \pm 3$
140	$32.4 \pm 0.5$	$2.5 \pm 0.2$	$113 \pm 5$	$232 \pm 1$
154	$27.0 \pm 1.8$	$-0.1 \pm 1.5$	$108 \pm 1$	$220 \pm 2$

Table 28. The  $M_2$  ellipse parameters and their 95% errors for AA1 mooring and summer stratification.

Depth (m)	Semimajor Axis (cm/s)	Seminor Axis (cm/s)	Inclination (deg)	Phase (GMT, deg)
20	$38.3 \pm 2.7$	$-1.1 \pm 1.1$	$110 \pm 2$	$231 \pm 4$
25	$39.7 \pm 1.3$	$-1.3 \pm 1.2$	$111 \pm 1$	$231 \pm 3$
30	$37.1 \pm 0.8$	$-1.5 \pm 0.7$	$112 \pm 1$	$233 \pm 4$

(Table 28 cont.)

35	$34.1 \pm 1.6$	$-0.8 \pm 0.6$	$113 \pm 1$	$235 \pm 4$
40	$32.3 \pm 2.0$	$0.8 \pm 1.2$	$113 \pm 2$	$235 \pm 4$
45	$31.4 \pm 1.8$	$2.3 \pm 1.6$	$112 \pm 2$	$233 \pm 2$
50	$30.2 \pm 2.0$	$3.2 \pm 1.8$	$110 \pm 2$	$231 \pm 1$
55	$29.6 \pm 2.0$	$3.7 \pm 2.0$	$108 \pm 2$	$231 \pm 1$
60	$29.2 \pm 1.7$	$3.8 \pm 2.3$	$107 \pm 2$	$230 \pm 1$
65	$28.9 \pm 1.4$	$3.6 \pm 2.5$	$107 \pm 2$	$230 \pm 1$
70	$28.7 \pm 1.2$	$3.1 \pm 2.6$	$107 \pm 3$	$230 \pm 1$
75	$28.5 \pm 1.0$	$2.5 \pm 2.6$	$108 \pm 3$	$230 \pm 1$
80	$28.2 \pm 0.9$	$1.7 \pm 2.6$	$108 \pm 3$	$230 \pm 2$
85	$28.1 \pm 0.8$	$0.8 \pm 2.4$	$108 \pm 3$	$231 \pm 2$
90	$27.8 \pm 0.8$	$0.1 \pm 2.0$	$107 \pm 4$	$231 \pm 2$
95	$27.4 \pm 0.8$	$-0.6 \pm 1.6$	$107 \pm 4$	$232 \pm 3$
100	$27.0 \pm 0.9$	$-1.3 \pm 1.3$	$106 \pm 4$	$233 \pm 3$
105	$26.6 \pm 1.0$	$-1.9 \pm 0.8$	$106 \pm 3$	$235 \pm 3$
110	$26.3 \pm 1.2$	$-2.4 \pm 0.5$	$105 \pm 3$	$237 \pm 3$
115	$26.3 \pm 1.6$	$-2.6 \pm 0.5$	$103 \pm 2$	$239 \pm 3$
120	$26.5 \pm 2.0$	$-2.6 \pm 0.7$	$102 \pm 1$	$242 \pm 3$
125	$26.7 \pm 2.4$	$-2.7 \pm 1.1$	$101 \pm 1$	$245 \pm 3$
130	$26.9 \pm 2.6$	$-3.0 \pm 1.3$	$99 \pm 2$	$248 \pm 3$
135	$27.1 \pm 2.7$	$-3.2 \pm 1.6$	$98 \pm 3$	$251 \pm 4$
140	$27.2 \pm 2.9$	$-3.5 \pm 1.7$	$98 \pm 4$	$252 \pm 4$
154	$25.9 \pm 3.9$	$-4.9 \pm 2.0$	$92 \pm 8$	$248 \pm 5$

Table 29. The  $K_1$  ellipse parameters and their 95% errors for AA2b mooring and winter stratification.

Depth (m)	Semimajor Axis (cm/s)	Seminor Axis (cm/s)	Inclination (deg)	Phase (GMT, deg)
20	$28.0 \pm 0.6$	$-1.3 \pm 1.5$	$108 \pm 1$	$75 \pm 1$
25	$28.8 \pm 0.7$	$-1.0 \pm 0.9$	$106 \pm 1$	$75 \pm 3$
30	$29.7 \pm 0.9$	$-0.6 \pm 0.2$	$104 \pm 1$	$75 \pm 5$
35	$29.9 \pm 1.4$	$-0.1 \pm 0.3$	$101 \pm 1$	$73 \pm 6$
40	$30.0 \pm 1.9$	$0.6 \pm 0.3$	$99 \pm 1$	$70 \pm 7$
45	$30.0 \pm 2.9$	$0.6 \pm 0.8$	$99 \pm 1$	$68 \pm 6$
50	$29.9 \pm 3.8$	$0.6 \pm 1.2$	$98 \pm 1$	$66 \pm 5$
55	$29.8 \pm 3.1$	$0.3 \pm 1.7$	$99 \pm 2$	$66 \pm 3$
60	$29.8 \pm 2.4$	$-0.1 \pm 2.3$	$99 \pm 2$	$65 \pm 2$
65	$29.8 \pm 1.3$	$-0.3 \pm 3.2$	$98 \pm 2$	$66 \pm 1$
70	$29.8 \pm 0.2$	$-0.5 \pm 4.1$	$97 \pm 2$	$67 \pm 1$
75	$29.6 \pm 1.0$	$-0.4 \pm 4.3$	$96 \pm 1$	$69 \pm 2$
80	$29.5 \pm 1.8$	$-0.4 \pm 4.6$	$95 \pm 1$	$71 \pm 2$
85	$30.2 \pm 3.3$	$-0.4 \pm 3.8$	$95 \pm 1$	$75 \pm 3$
90	$31.0 \pm 4.7$	$-0.4 \pm 3.1$	$95 \pm 1$	$78 \pm 4$
95	$33.7 \pm 6.3$	$-0.4 \pm 2.3$	$96 \pm 1$	$80 \pm 4$
100	$36.4 \pm 8.1$	$-0.3 \pm 1.6$	$96 \pm 1$	$83 \pm 5$
105	$39.1 \pm 8.0$	$-0.5 \pm 1.3$	$96 \pm 1$	$84 \pm 4$
110	$41.8 \pm 7.9$	$-0.7 \pm 1.0$	$96 \pm 1$	$86 \pm 4$
115	$43.2 \pm 7.0$	$-1.4 \pm 1.4$	$95 \pm 1$	$87 \pm 5$
120	$44.7 \pm 6.2$	$-2.0 \pm 1.9$	$94 \pm 1$	$88 \pm 5$
125	$44.4 \pm 5.4$	$-2.2 \pm 2.0$	$94 \pm 1$	$89 \pm 6$
130	$44.1 \pm 4.5$	$-2.4 \pm 2.2$	$94 \pm 1$	$90 \pm 7$
135	$41.6 \pm 2.9$	$-1.7 \pm 1.3$	$93 \pm 1$	$90 \pm 7$
140	$39.0 \pm 1.4$	$-1.1 \pm 0.3$	$92 \pm 1$	$91 \pm 7$
145	$35.2 \pm 2.3$	$-0.6 \pm 1.1$	$92 \pm 1$	$88 \pm 9$

(Table 29 cont.)

150	$31.5 \pm 3.1$	$-0.2 \pm 1.9$	$91 \pm 1$	$85 \pm 12$
155	$29.5 \pm 2.2$	$-0.5 \pm 1.5$	$90 \pm 1$	$78 \pm 16$
160	$27.6 \pm 1.2$	$-0.9 \pm 1.2$	$89 \pm 1$	$70 \pm 20$
165	$27.3 \pm 1.0$	$-1.0 \pm 0.8$	$88 \pm 1$	$66 \pm 16$
170	$27.1 \pm 0.7$	$-1.7 \pm 0.5$	$87 \pm 1$	$60 \pm 12$
175	$27.0 \pm 0.4$	$-1.7 \pm 0.2$	$87 \pm 1$	$58 \pm 9$
180	$26.9 \pm 0.1$	$-1.8 \pm 0.1$	$86 \pm 1$	$56 \pm 6$
185	$26.5 \pm 0.3$	$-1.6 \pm 0.2$	$85 \pm 1$	$56 \pm 6$
190	$26.0 \pm 0.5$	$-1.4 \pm 0.4$	$85 \pm 1$	$55 \pm 5$
195	$25.5 \pm 0.6$	$-1.2 \pm 0.4$	$85 \pm 1$	$54 \pm 5$
200	$24.9 \pm 0.6$	$-1.0 \pm 0.5$	$84 \pm 2$	$54 \pm 6$
205	$24.4 \pm 0.8$	$-0.6 \pm 0.6$	$84 \pm 1$	$53 \pm 7$
210	$23.8 \pm 1.0$	$-0.3 \pm 0.6$	$84 \pm 1$	$53 \pm 7$

Table 30. The  $K_1$  ellipse parameters and their 95% errors for AA2b mooring and summer stratification.

Depth (m)	Semimajor Axis (cm/s)	Semiminor Axis (cm/s)	Inclination (deg)	Phase (GMT, deg)
20	$28.8 \pm 3.3$	$-0.5 \pm 1.4$	$100 \pm 2$	$59 \pm 2$
25	$29.1 \pm 3.2$	$-1.1 \pm 1.0$	$100 \pm 2$	$63 \pm 2$
30	$29.3 \pm 3.1$	$-1.6 \pm 0.5$	$99 \pm 3$	$68 \pm 2$
35	$29.1 \pm 3.2$	$-0.8 \pm 0.7$	$100 \pm 3$	$68 \pm 2$
40	$28.8 \pm 3.3$	$-0.1 \pm 0.9$	$101 \pm 3$	$69 \pm 2$
45	$29.3 \pm 2.6$	$0.5 \pm 1.0$	$103 \pm 3$	$67 \pm 2$
50	$29.9 \pm 2.0$	$1.1 \pm 1.1$	$104 \pm 4$	$66 \pm 2$
55	$30.1 \pm 2.0$	$0.6 \pm 1.0$	$106 \pm 3$	$66 \pm 2$
60	$30.3 \pm 2.1$	$0.2 \pm 0.8$	$107 \pm 3$	$65 \pm 2$
65	$30.2 \pm 2.0$	$-0.4 \pm 1.6$	$107 \pm 3$	$66 \pm 2$
70	$30.2 \pm 1.9$	$-1.1 \pm 2.4$	$107 \pm 2$	$67 \pm 2$
75	$30.1 \pm 1.8$	$-1.3 \pm 2.6$	$106 \pm 2$	$68 \pm 1$
80	$30.0 \pm 1.7$	$-1.5 \pm 2.9$	$105 \pm 2$	$70 \pm 1$
85	$29.8 \pm 1.6$	$-1.3 \pm 2.5$	$103 \pm 1$	$70 \pm 1$
90	$29.7 \pm 1.4$	$-1.1 \pm 2.0$	$101 \pm 1$	$71 \pm 1$
95	$29.6 \pm 1.6$	$-0.7 \pm 1.7$	$99 \pm 1$	$72 \pm 2$
100	$29.5 \pm 1.8$	$-0.4 \pm 1.2$	$97 \pm 1$	$72 \pm 4$
105	$29.8 \pm 2.3$	$-0.3 \pm 1.0$	$95 \pm 2$	$72 \pm 4$
110	$30.1 \pm 2.8$	$-0.2 \pm 0.8$	$93 \pm 2$	$73 \pm 5$
115	$30.3 \pm 3.3$	$-0.2 \pm 1.2$	$91 \pm 3$	$74 \pm 5$
120	$30.6 \pm 3.7$	$-0.3 \pm 1.5$	$90 \pm 3$	$75 \pm 5$
125	$30.5 \pm 3.7$	$-0.6 \pm 1.7$	$89 \pm 2$	$76 \pm 4$
130	$30.4 \pm 3.8$	$-0.9 \pm 1.9$	$88 \pm 2$	$78 \pm 4$
135	$30.2 \pm 3.8$	$-1.1 \pm 1.7$	$87 \pm 2$	$79 \pm 3$
140	$30.1 \pm 3.8$	$-1.3 \pm 1.4$	$86 \pm 2$	$81 \pm 2$
145	$29.6 \pm 3.3$	$-1.2 \pm 1.2$	$86 \pm 2$	$82 \pm 2$
150	$29.2 \pm 2.9$	$-1.2 \pm 1.0$	$85 \pm 2$	$83 \pm 3$
155	$28.5 \pm 2.6$	$-0.8 \pm 0.7$	$85 \pm 2$	$83 \pm 5$
160	$27.9 \pm 2.3$	$-0.5 \pm 0.4$	$85 \pm 2$	$83 \pm 6$
165	$26.9 \pm 2.8$	$-0.2 \pm 0.4$	$86 \pm 2$	$82 \pm 6$
170	$20.0 \pm 3.3$	$0.1 \pm 0.3$	$86 \pm 2$	$81 \pm 7$
175	$24.7 \pm 3.5$	$0.1 \pm 0.6$	$86 \pm 2$	$78 \pm 6$
180	$23.4 \pm 3.8$	$0.1 \pm 0.9$	$87 \pm 2$	$76 \pm 5$
185	$22.4 \pm 3.4$	$0.2 \pm 1.1$	$88 \pm 2$	$73 \pm 5$
190	$21.4 \pm 3.1$	$0.3 \pm 1.3$	$88 \pm 3$	$71 \pm 4$
195	$20.5 \pm 2.8$	$0.3 \pm 1.4$	$89 \pm 3$	$69 \pm 4$

(Table 30 cont.)

200	$19.6 \pm 2.5$	$0.3 \pm 1.5$	$89 \pm 3$	$67 \pm 4$
205	$19.1 \pm 2.0$	$0.3 \pm 1.4$	$88 \pm 3$	$65 \pm 4$
210	$18.5 \pm 1.6$	$0.4 \pm 1.4$	$88 \pm 2$	$64 \pm 6$

Table 31. The  $M_2$  ellipse parameters and their 95% errors for AA2b mooring and winter stratification.

Depth (m)	Semimajor Axis (cm/s)	Semiminor Axis (cm/s)	Inclination (deg)	Phase (GMT, deg)
20	$33.1 \pm 2.6$	$4.5 \pm 0.1$	$111 \pm 5$	$194 \pm 3$
25	$33.4 \pm 1.8$	$4.7 \pm 0.4$	$110 \pm 4$	$195 \pm 3$
30	$35.0 \pm 1.0$	$4.9 \pm 1.0$	$109 \pm 3$	$196 \pm 3$
35	$35.6 \pm 1.1$	$3.9 \pm 0.9$	$106 \pm 2$	$196 \pm 2$
40	$36.2 \pm 1.3$	$2.5 \pm 1.1$	$104 \pm 2$	$196 \pm 2$
45	$36.0 \pm 1.1$	$1.1 \pm 2.0$	$103 \pm 2$	$196 \pm 2$
50	$35.8 \pm 0.8$	$-0.3 \pm 0.9$	$101 \pm 2$	$195 \pm 1$
55	$35.7 \pm 0.5$	$-1.1 \pm 2.9$	$100 \pm 1$	$195 \pm 2$
60	$35.6 \pm 0.2$	$-1.9 \pm 2.1$	$99 \pm 1$	$194 \pm 2$
65	$35.4 \pm 0.5$	$-2.7 \pm 1.8$	$99 \pm 1$	$195 \pm 1$
70	$35.2 \pm 0.7$	$-3.6 \pm 1.5$	$98 \pm 2$	$195 \pm 1$
75	$34.7 \pm 1.0$	$-4.0 \pm 0.7$	$98 \pm 2$	$196 \pm 1$
80	$34.2 \pm 1.2$	$-4.4 \pm 0.1$	$98 \pm 3$	$197 \pm 1$
85	$33.6 \pm 1.2$	$-4.4 \pm 0.7$	$97 \pm 3$	$199 \pm 1$
90	$33.1 \pm 1.2$	$-4.3 \pm 1.4$	$97 \pm 4$	$201 \pm 2$
95	$32.5 \pm 1.3$	$-4.2 \pm 2.0$	$97 \pm 4$	$204 \pm 4$
100	$31.9 \pm 1.4$	$-4.2 \pm 2.5$	$96 \pm 5$	$207 \pm 5$
105	$31.3 \pm 0.7$	$-4.2 \pm 2.1$	$96 \pm 5$	$211 \pm 4$
110	$30.6 \pm 0.1$	$-4.1 \pm 1.6$	$96 \pm 5$	$214 \pm 3$
115	$30.4 \pm 0.3$	$-3.6 \pm 1.1$	$96 \pm 4$	$218 \pm 2$
120	$30.2 \pm 0.7$	$-3.1 \pm 0.5$	$95 \pm 3$	$222 \pm 1$
125	$30.3 \pm 0.5$	$-1.9 \pm 1.2$	$95 \pm 2$	$225 \pm 1$
130	$30.4 \pm 0.3$	$-0.6 \pm 1.8$	$95 \pm 1$	$227 \pm 1$
135	$29.9 \pm 0.5$	$-0.1 \pm 1.7$	$95 \pm 1$	$225 \pm 3$
140	$29.3 \pm 0.8$	$0.5 \pm 1.7$	$95 \pm 1$	$223 \pm 5$
145	$28.4 \pm 1.3$	$0.9 \pm 1.6$	$94 \pm 1$	$217 \pm 7$
150	$27.4 \pm 1.8$	$1.2 \pm 1.6$	$94 \pm 1$	$211 \pm 8$
155	$27.2 \pm 1.6$	$1.6 \pm 1.3$	$92 \pm 1$	$207 \pm 8$
160	$27.0 \pm 1.3$	$2.0 \pm 1.0$	$91 \pm 1$	$203 \pm 8$
165	$27.1 \pm 1.0$	$1.8 \pm 0.7$	$89 \pm 1$	$201 \pm 8$
170	$27.1 \pm 0.8$	$1.6 \pm 0.3$	$88 \pm 1$	$198 \pm 7$
175	$26.9 \pm 0.6$	$1.2 \pm 0.6$	$87 \pm 1$	$197 \pm 5$
180	$26.6 \pm 0.4$	$0.8 \pm 0.9$	$86 \pm 1$	$196 \pm 4$
185	$26.1 \pm 0.5$	$0.5 \pm 1.0$	$86 \pm 1$	$195 \pm 3$
190	$25.6 \pm 0.5$	$0.1 \pm 1.0$	$85 \pm 1$	$194 \pm 2$
195	$25.0 \pm 0.5$	$-0.2 \pm 1.0$	$85 \pm 1$	$194 \pm 2$
200	$24.4 \pm 0.4$	$-0.4 \pm 0.9$	$84 \pm 1$	$193 \pm 1$
205	$24.1 \pm 0.3$	$-0.5 \pm 0.9$	$83 \pm 1$	$192 \pm 1$
210	$23.7 \pm 0.2$	$-0.6 \pm 0.9$	$83 \pm 1$	$191 \pm 2$

Table 32. The  $M_2$  ellipse parameters and their 95% errors for AA2b mooring and summer stratification.

Depth (m)	Semimajor Axis (cm/s)	Semiminor Axis (cm/s)	Inclination (deg)	Phase (GMT, deg)
20	$37.3 \pm 1.1$	$-2.0 \pm 1.1$	$105 \pm 2$	$200 \pm 3$
25	$36.7 \pm 0.9$	$-0.6 \pm 0.9$	$105 \pm 1$	$201 \pm 3$

(Table 32 cont.)

30	$36.2 \pm 0.7$	$0.8 \pm 0.7$	$105 \pm 1$	$202 \pm 3$
35	$36.4 \pm 0.8$	$2.4 \pm 1.5$	$105 \pm 1$	$202 \pm 3$
40	$36.6 \pm 0.8$	$4.0 \pm 2.3$	$105 \pm 2$	$203 \pm 4$
45	$37.1 \pm 1.2$	$4.2 \pm 2.1$	$104 \pm 2$	$203 \pm 4$
50	$37.6 \pm 1.6$	$4.4 \pm 2.0$	$103 \pm 2$	$203 \pm 4$
55	$37.1 \pm 1.2$	$4.4 \pm 1.6$	$103 \pm 2$	$203 \pm 4$
60	$36.6 \pm 0.8$	$4.4 \pm 1.2$	$102 \pm 2$	$203 \pm 4$
65	$35.6 \pm 0.8$	$4.0 \pm 1.3$	$102 \pm 2$	$203 \pm 4$
70	$34.6 \pm 0.8$	$3.7 \pm 1.3$	$102 \pm 2$	$202 \pm 4$
75	$34.0 \pm 0.6$	$3.1 \pm 1.3$	$103 \pm 2$	$203 \pm 4$
80	$33.3 \pm 0.3$	$2.6 \pm 1.4$	$103 \pm 2$	$203 \pm 4$
85	$33.3 \pm 0.5$	$2.0 \pm 1.4$	$103 \pm 2$	$203 \pm 3$
90	$33.3 \pm 0.7$	$1.3 \pm 1.5$	$103 \pm 2$	$203 \pm 3$
95	$33.1 \pm 0.8$	$0.6 \pm 1.5$	$103 \pm 2$	$203 \pm 3$
100	$32.9 \pm 0.9$	$-0.1 \pm 1.5$	$102 \pm 2$	$203 \pm 3$
105	$32.5 \pm 1.0$	$-0.7 \pm 1.4$	$102 \pm 2$	$203 \pm 3$
110	$32.0 \pm 1.0$	$-1.3 \pm 1.2$	$102 \pm 2$	$202 \pm 3$
115	$31.5 \pm 1.0$	$-1.8 \pm 0.9$	$102 \pm 2$	$201 \pm 3$
120	$30.9 \pm 1.0$	$-2.3 \pm 0.6$	$101 \pm 2$	$200 \pm 3$
125	$30.4 \pm 1.2$	$-2.9 \pm 0.7$	$101 \pm 2$	$200 \pm 3$
130	$29.9 \pm 1.5$	$-3.4 \pm 0.7$	$100 \pm 2$	$200 \pm 3$
135	$29.5 \pm 1.8$	$-3.9 \pm 0.8$	$98 \pm 2$	$199 \pm 3$
140	$29.0 \pm 2.0$	$-4.3 \pm 0.8$	$97 \pm 2$	$199 \pm 3$
145	$28.9 \pm 2.2$	$-4.6 \pm 0.8$	$97 \pm 2$	$199 \pm 3$
150	$28.7 \pm 2.3$	$-4.9 \pm 0.9$	$94 \pm 2$	$198 \pm 3$
155	$28.5 \pm 2.5$	$-5.0 \pm 0.9$	$92 \pm 2$	$198 \pm 3$
160	$28.4 \pm 2.7$	$-5.1 \pm 1.0$	$90 \pm 2$	$197 \pm 4$
165	$27.8 \pm 3.1$	$-5.0 \pm 1.4$	$88 \pm 2$	$195 \pm 4$
170	$27.1 \pm 3.4$	$-4.9 \pm 1.8$	$86 \pm 2$	$193 \pm 4$
175	$26.3 \pm 3.7$	$-4.5 \pm 2.2$	$84 \pm 2$	$190 \pm 3$
180	$25.5 \pm 4.1$	$-4.0 \pm 2.5$	$82 \pm 3$	$188 \pm 3$
185	$24.7 \pm 4.3$	$-3.3 \pm 2.8$	$81 \pm 3$	$185 \pm 3$
190	$23.8 \pm 4.6$	$-2.6 \pm 3.0$	$80 \pm 3$	$183 \pm 3$
195	$23.1 \pm 4.8$	$-2.1 \pm 2.9$	$80 \pm 3$	$181 \pm 4$
200	$22.4 \pm 5.0$	$-1.7 \pm 2.9$	$80 \pm 3$	$179 \pm 4$
205	$22.0 \pm 4.9$	$-1.3 \pm 2.6$	$80 \pm 3$	$177 \pm 4$
210	$21.5 \pm 4.7$	$-1.0 \pm 2.2$	$79 \pm 3$	$176 \pm 4$

Table 33.  $K_1$  and  $M_2$  ellipse parameters and their 95% errors – AA0 mooring.

Constituent	Depth (m)	Semimajor Axis (cm/s)	Seminor Axis (cm/s)	Inclination (deg)	Phase (GMT, deg)
Winter Stratification					
$K_1$	37	$25.7 \pm 0.1$	$-0.5 \pm 1.8$	$114 \pm 3$	$70 \pm 2$
$M_2$		$31.2 \pm 0.8$	$-2.8 \pm 0.6$	$119 \pm 2$	$202 \pm 1$
Summer Stratification					
$K_1$	37	$29.2 \pm 3.5$	$-0.1 \pm 1.8$	$119 \pm 2$	$63 \pm 3$
$M_2$		$34.9 \pm 1.8$	$-2.7 \pm 2.2$	$119 \pm 3$	$211 \pm 4$

Table 34.  $K_1$  and  $M_2$  ellipse parameters and their 95% errors – AA3 mooring.

Constituent	Depth (m)	Semimajor Axis (cm/s)	Seminor Axis (cm/s)	Inclination (deg)	Phase (GMT, deg)
Winter Stratification					
$K_1$	42	$25.7 \pm 1.1$	$-0.9 \pm 0.9$	$104 \pm 3$	$50 \pm 2$
$M_2$		$31.9 \pm 0.8$	$-0.5 \pm 0.6$	$109 \pm 2$	$200 \pm 2$

(Table 34 cont.)

Summer Stratification					
K <sub>1</sub>	42	25.1 ± 1.7	0.3 ± 0.7	105 ± 2	51 ± 2
M <sub>2</sub>		33.1 ± 0.8	-1.0 ± 1.0	109 ± 1	199 ± 2

## APPENDIX C: NUMERICAL DISCRETIZATION OF THE MODEL (ADCIRC-2DD) EQUATIONS

The numerical discretization of the generalized wave continuity equation (GWCE) (equation 13, page 77) and momentum equations (equations 12a and 12b, page 76) is implemented in three stages. First, Galerkin weighted residual statements are developed for the GWCE and momentum equations. Second, the equations are time discretized. A variably weighted three-time-level implicit scheme is used for most linear terms in the GWCE with the nonlinear, Coriolis, and tidal potential terms being treated explicitly, while the time derivative term of the advective terms is evaluated at two known time levels. The weak weighted residual form of the momentum equations are discretized in time using a two-time-level implicit Crank-Nicolson approximation with the exception of the friction and advection terms, which are treated explicitly. The final step in the numerical discretization scheme is approximation of the spatial domain using the finite element method. This involves expending the variable over three-node linear triangles developing discrete equations on an element level. Then the elemental equations are summed over the global domain. The fully discretized system of the model equations (equations 13, 12a, and 12b) are written in matrix notation (Luettich et al., 1992):

$$\sum_{j=1}^N {}^g M_{ij}^{GWCE} {}^g \zeta_j^{k+1} = {}^g P_i^{GWCE} \quad (17a)$$

$$\sum_{j=1}^N {}^g M_{ij}^{1ME} {}^g U_j^{k+1} - \sum_{j=1}^N {}^g M_{ij}^{2ME} {}^g V_j^{k+1} = {}^g P_i^{\lambda ME} \quad (17b)$$

$$\sum_{j=1}^N {}^g M_{ij}^{2ME} {}^g U_j^{k+1} + \sum_{j=1}^N {}^g M_{ij}^{1ME} {}^g V_j^{k+1} = {}^g P_i^{\phi ME} \quad (17c)$$

$$i = 1, \dots, N$$

where  ${}^g M_{ij}^{GWCE}$  is the global banded time-independent system matrix,  ${}^g M_{ij}^{1ME}$  and  ${}^g M_{ij}^{2ME}$  are the global diagonal time-dependent system matrices,  ${}^g P_i^{GWCE}$  is the load vector of known forcing in the GWCE equation,  ${}^g P_i^{\lambda ME}$  and  ${}^g P_i^{\phi ME}$  are the load vectors of known forcing for the momentum equations,  ${}^g \zeta_j^{k+1}$  is the global vector of unknown surface elevations at time level  $k + 1$ ,  ${}^g U_j^{k+1}$  and  ${}^g V_j^{k+1}$  are the vectors of unknown velocity components in the  $\lambda$  and  $\phi$  directions at time level  $k + 1$ ,  $N$  is the total number of nodes.

Elevation boundary conditions are enforced in the discrete form of the GWCE equation and zero velocity boundary conditions are enforced in the discrete momentum equations. The decoupled discrete GWCE and momentum equations lead to sequential solution procedure. At each timestep, the GWCE equation is solved first for the surface water elevation at new time level  $k + 1$ . The discrete momentum equations are solved second and used the elevation values at time level  $k + 1$  computed from the GWCE equation.

## VITA

Ewa Jarosz was born on May 22, 1964, in Olecko, Poland. From 1970 to 1982, she attended the primary and high school in Olecko. In 1983, she entered the University of Gdansk and graduated with the master's degree in physical oceanography in 1989. Between 1990 and 1995, she worked as a teaching and research assistant at the Oceanography Institute of the Gdansk University. In fall of 1995, she enrolled in the master's degree program in the Department of Oceanography and Coastal Sciences at Louisiana State University. In 1997, she graduated with the master's degree in oceanography and coastal sciences. In 1998, she enrolled in the doctoral program at the same department.